
Development of Sensor-based Phenotyping Methods for Ascochyta Blight Resistance Breeding of Chickpea

Author:

Florian TANNER

Supervisors:

A/Prof. Bettina BERGER

Dr. Kenneth CLARKE

Dr. Darren PLETT

Dr. Jennifer DAVIDSON



THE UNIVERSITY
of ADELAIDE

*This thesis is submitted in fulfilment of the requirements
for the degree of Doctor of Philosophy*

in the

School of Agriculture, Food & Wine

May 11, 2023

Declarations

I certify that this work contains no material which has been accepted for the award of any other degree or diploma in my name in any university or other tertiary institution and, to the best of my knowledge and belief, contains no material previously published or written by another person, except where due reference has been made in the text. In addition, I certify that no part of this work will, in the future, be used in a submission in my name for any other degree or diploma in any university or other tertiary institution without the prior approval of the University of Adelaide and where applicable, any partner institution responsible for the joint award of this degree. The author acknowledges that copyright of published works contained within this thesis resides with the copyright holder(s) of those works. I give permission for the digital version of my thesis to be made available on the web, via the University's digital research repository, the Library Search and also through web search engines, unless permission has been granted by the University to restrict access for a period of time.

Signed:

Date:

UNIVERSITY OF ADELAIDE

Abstract

Faculty of Sciences
School of Agriculture, Food & Wine

Doctor of Philosophy

Development of Sensor-based Phenotyping Methods for Ascochyta Blight Resistance Breeding of Chickpea

by Florian TANNER

Increasing pulse production can benefit global nutritional security and improve the sustainability of food production. The breeding of chickpea, the second most widely cultivated pulse, for resistance to *Ascochyta* blight can contribute to this goal, as this fungal disease limits yield in all major growing areas. Applying sensor-based phenotyping to disease resistance breeding programs allows for the rapid, precise, and nondestructive screening of large numbers of plants for improved disease resistance. In this way, the genetic gain can be increased.

Previous studies have demonstrated the use of optical sensors for resistance breeding in other plant-pathosystems, but not yet for *Ascochyta* blight of chickpea. More broadly, the deployment of sensor-based phenotyping to uncontrolled conditions in the field, especially for measuring plant disease, remains a challenge.

Therefore, the objectives of this thesis were (i) to develop sensor-based phenotyping methods for scoring *Ascochyta* blight disease severity in a chickpea breeding program and (ii) to identify within-scale and cross-scale functional resistance components. This was addressed by (a) reviewing the literature on sensor-based phenotyping of plant-pathogen interaction and (b) using an experimental approach in three different growth environments where chickpea and wild relatives were screened under disease pressure.

The main outcomes from approach (a), the literature review, were the identification of potentially suitable sensor technology for *Ascochyta* blight of chickpea as RGB imaging, fluorescence imaging, hyperspectral imaging, and light detection and ranging, and the designation of potential measurable resistance components such as loss of healthy biomass, necrosis, chlorosis, and changes in plant metabolism. The experimental approach was conducted at (b1) single plant scale under controlled conditions in a glasshouse, (b2) at single pot scale in a disease nursery, and (b3) at plot scale in the field.

In the glasshouse (b1), time course RGB imaging and extraction of growth rates in response to infection was a suitable and transferable method for predicting disease, achieving an R^2 of 0.37 to 0.64 on unseen data. In the disease nursery (b2), also using RGB time course imaging derived growth rates, disease severity levels could be classified on unseen data with overall accuracies of 65 - 81 % ($\kappa = 0.43 - 0.59$). For the purpose of early disease detection, infected and non-infected pots could be distinguished using lesion detection with 92.6 % accuracy 30 days after infection in one experiment, and 75.7 % accuracy 42 days after infection in a second experiment. In the field (b3), only single time points of data were acquired with a ground-based phenotyping platform that carried hyperspectral and lidar sensors. Using those single time point data, a general plant stress response expressed in the near infrared spectrum could rank genotypes according to their disease scores with ρ of 0.89.

Across environments (b1) and (b2), models trained on spectral data for early disease detection and prediction of disease severity showed poor transferability to independent data. When hyperspectral data were used to predict disease severity in the glasshouse (b1) and field (b3), the degree of success was significantly impacted by the data preprocessing.

These studies showed that time course RGB imaging to derive growth rate estimates and the measurement of general plant stress responses in the red edge and VNIR spectrum were suitable to assess the severity of *Ascochyta* blight disease for resistance breeding, and demonstrated the use of lesion detection for early detection of the disease. This thesis represents an important step toward supporting disease resistance breeding for *Ascochyta* blight of chickpea and for disease resistance breeding programs of other crops.

Acknowledgements

First I wish to acknowledge and pay respect to the Kaurna people, the traditional owners and custodians of the Adelaide plains, the lands on which I conducted this research.

I give sincere thanks to my supervisors, all of whom have greatly supported me. Trevor Garnett was my first point of contact at the Australian Plant Phenomics Facility and was able to arrange a scholarship for me to provide an opportunity to join the team at The Plant Accelerator. He left the role at the Australian Plant Phenomics facility before I started the project and Bettina Berger became my principal supervisor instead. I want to thank her for her guidance through the technical aspects of the thesis, but more than that, I always felt like she had my back. Darren Plett was the second member of my supervisory team until he changed position in early 2022. During this time, his practical advice and help with data acquisition were important for the completion of this thesis. My third supervisor was Jenny Davidson, whose support was also invaluable. She enabled my thesis by providing access for imaging the breeding program and with her expertise about *Ascochyta* blight, even into her retirement. Ken Clarke became my supervisor after Darren Plett had left, but even before the change of roles, his advice on remote sensing and data analysis was vital to the project.

I am grateful for the support by the University of Adelaide with a Scholarship International, and by The Plant Accelerator with a PhD stipend top-up. I acknowledge the use of the facilities, and scientific and technical assistance of the Australian Plant Phenomics Facility, which is supported by the Australian Government's National Collaborative Research Infrastructure Strategy (NCRIS). Behind the name of the institution there are many people to whom I want to express my gratitude. The expertise accumulated at The Plant Accelerator is the reason why I wanted to come to Adelaide for a PhD. On top of that, the friendly atmosphere made the whole experience enjoyable. Lidia Mischis knows everything there is to know about chickpeas and the greenhouses and was always fast to help, so were the other greenhouse technical officers; George Sainsbury supported this effort enormously by helping with anything relating to data and programming; Chris Brien and Nathaniel Jewell gave statistical advice; Paul Jenkins helped me build the imaging pushcart and had to deal with fallout from my experiments in the greenhouse; Huajian Liu and Andrew Hennessy were my officemates and provided support for the analysis of hyperspectral data; Fiona Norrish lent me her camera in the first year of experiments; Brooke Bruning shared her experience as the previous PhD student at the institution; everyone else on the team who is not listed here by name contributed at the very least indirectly with their company during morning tea.

I also want to thank the people at the South Australian Research and Development Institute (SARDI) who have supported this project, your help was vital. Judith Atieno for collegiality and friendship, Marzena Krysinska-Kaczmarek for reliable technical support regarding inoculation and running the experiments, and Sara Blake, who took over the scoring work performed by Jenny Davidson.

Ben Gruber of KWS was instrumental in securing my position and scholarship by writing a letter of recommendation, for which I am very grateful. Julie Hayes was my independent advisor and made a large contribution to this project by kindly providing chickpea seeds for my first experiment.

My personal network supported me and kept me going by staying interested in my work, but even more so by enjoying fun activities outside of work: my friends in Adelaide and at home, as well as my parents and the rest of my family, all of whom were always there for me.

Lastly, I want to thank Jessica Beaumont for moving to Australia with me and supporting me throughout. I would not have been able to finish the thesis without her support.

Contents

Declarations	iii
Abstract	v
Acknowledgements	vii
List of Included Submitted and Published Manuscripts	xv
1 Introduction	1
1.1 Thesis structure	1
1.2 Background	1
1.2.1 The role of chickpea for global food security	1
1.2.2 Ascochyta blight of chickpea	3
1.2.3 Australian context of chickpea cultivation and AB	4
1.2.4 Breeding chickpea for AB resistance	6
1.2.5 Phenotyping for disease resistance breeding	10
Sensor-based phenotyping to support disease scoring in breed- ing programs	12
Sensor-based measurements of signs and symptoms	12
1.3 Research aims	14
1.4 References	14
2 Literature review: Sensor-based phenotyping of above-ground plant-pathogen interactions	23
2.1 Declarations	24
2.2 Literature review	26
2.2.1 Abstract	26
2.2.2 Background	26
2.2.3 Signs, symptoms and sensors	28
Pathogen signs	28
Symptom: changes in primary metabolism	32
Symptom: changes in secondary metabolism	34
Symptom: necrosis and chlorosis	35
Symptom: thermal energy dissipation	36
Sensing structural changes	37
2.2.4 Discussion	37

Phenotyping plant-pathogen interactions in the field is limited by specificity, canopy structure, and environmental conditions	37
Non-invasive phenotyping of below-ground plant-pathogen interactions remains a challenge	38
Sensor data helps to understand plant-pathogen interactions in more detail	38
Advanced sensors expand the range of perceivable signs and symptoms but require complementary technologies	38
2.2.5 Abbreviations	38
2.2.6 Declarations	38
2.2.7 References	39
3 Time course sensor-based phenotyping can predict Ascochyta blight disease severity in Cicer species	45
3.1 Declarations	46
3.2 Manuscript	48
3.2.1 Abstract	48
3.2.2 Introduction	49
3.2.3 Materials and methods	51
Experimental design	51
Data acquisition	52
RGB image analysis	54
Multispectral image analysis	54
Spatio-temporal modeling	55
Intermediate trait extraction	56
Genotypic and treatment effects	56
Predictive models	57
3.2.4 Results	57
Visual scores	57
Evaluation of low-level trait extraction	59
Smoothed FGCC and lesion count	60
Treatment effects on intermediate traits	60
Disease index classification	63
Early detection of disease	64
3.2.5 Discussion	65
3.2.6 Acknowledgements	68
3.2.6 Data availability	68
3.2.6 Supplementary materials	68
3.2.7 References	77

4	Time course RGB imaging outperforms hyperspectral imaging for chickpea Ascochyta blight severity prediction in the greenhouse	85
4.1	Declarations	86
4.2	Abstract	88
4.3	Introduction	88
4.3.1	Spectroscopy for plant disease phenotyping	88
4.3.2	Related work	90
	Non-imaging spectroscopy	90
	Imaging spectroscopy	92
	Spectroscopy for chickpea AB	94
4.3.3	Research opportunities	94
4.3.4	Research aims	96
4.4	Materials and methods	97
4.4.1	Plant material	97
4.4.2	Infection	97
4.4.3	Experimental design	98
4.4.4	Data acquisition	99
	Imaging	99
	Visual scoring	100
4.4.5	Data processing	100
	RGB data processing	101
	Hyperspectral data processing	101
4.4.6	Analysis of disease indices and extracted traits	103
4.4.7	Early detection of disease	104
4.4.8	Disease index prediction	104
	Disease index prediction with RGB data	104
	Disease index prediction with hyperspectral data	104
4.5	Results	104
4.5.1	Disease indices	104
4.5.2	Projected shoot area	105
4.5.3	Early detection of AB using hyperspectral data	105
4.5.4	Prediction of disease index	107
	Prediction of disease index with RGB image data	107
	Prediction of disease index with hyperspectral data	108
4.6	Discussion	112
4.6.1	Low disease pressure in the greenhouse	112
4.6.2	Full spectrum early detection models were not transferable between experiments	112
4.6.3	RGB-based growth rates are stable predictors for disease indices	113
4.6.4	Perspectives	113
	Ensuring high disease pressure and avoiding cross-contamination	113
	Potential approaches to increase suitability of hyperspectral data	114

4.6.5	Study outcomes in relation to research aims	115
4.7	Conclusion	115
4.8	Data availability	116
4.9	References	116
4.10	Supplementary material	122
5	Prediction of Ascochyta blight damage on field-grown chickpea using lidar and hyperspectral data	127
5.1	Declarations	128
5.2	Abstract	130
5.3	Introduction	130
5.3.1	Field disease screening	130
5.3.2	Sensor-based disease phenotyping in the field	130
5.3.3	Related work	131
	Sensor - based screening of necrotrophic fungi in the field	131
5.3.4	Research opportunities	132
	Considerations and applications for AB screens	132
	Specificity of stress detection in the field	132
5.3.5	Aims of this study	133
5.4	Materials and methods	133
5.4.1	Experimental design	133
5.4.2	Data acquisition	134
5.4.3	Data analysis	136
	Calibration and fusion of hyperspectral and lidar data	136
	Full spectrum hyperspectral data pre-processing	136
	Feature extraction from hyperspectral and lidar data	137
	Learning algorithms and model selection	137
	Feature selection	138
	Analysis of treatment and genotypic effects on PAD scores	138
5.5	Results	138
5.5.1	Visual scoring of AB damage	138
	2020 season	138
	2022 season	139
5.5.2	Exploratory analysis of hyperspectral data	141
5.5.3	Prediction of AB damage	143
5.5.4	Treatment classification	145
5.6	Discussion	149
5.6.1	General discussion	149
5.6.2	Study outcomes in relation to research aims	152
5.7	Conclusion	152
5.8	Acknowledgements	153
5.9	Data availability	153

5.10	COVID-19 impact statement	153
5.11	References	153
5.12	Supplementary material	159
6	Discussion	163
6.1	Discussion structure	163
6.2	Thesis overview	163
6.3	Thesis outcomes	164
6.3.1	Key outcomes	164
	Symptoms of chickpea AB can be measured with imaging sensors	164
	RGB-imaging based growth rates are suitable for prediction for DI	165
	Lesion detection enables early detection of disease	165
	Hyperspectral models are significantly influenced by the choice	
	of pre-processing steps and learning algorithms	166
	Conservative growth may be a resistance mechanism	166
6.4	Perspectives	167
6.4.1	Summarised recommendations for deployment	167
	Recommendations for deployment to nursery disease screens .	167
	Recommendations for deployment to glasshouse disease screens	167
	Recommendations for deployment to field disease screens . . .	167
6.4.2	Summarised recommendations for further research	168
	Application of other sensor technologies	168
	Exploration of trait extraction	169
	Direct selection for sensor-based traits	170
6.5	Significance and implications of research	170
6.6	Conclusion	171
6.7	References	171

List of Included Submitted and Published Manuscripts

Chapter 2

Florian Tanner et al. (2022). "Sensor-based phenotyping of above-ground plant-pathogen interactions". In: *Plant Methods* 18.1. Publisher: BioMed Central, pp. 1–18. ISSN: 17464811. DOI: 10.1186/s13007-022-00853-7. URL: <https://doi.org/10.1186/s13007-022-00853-7>

Chapter 3

Florian Tanner et. al. (2022). "Time course sensor-based phenotyping can predict Ascochyta blight disease severity in Cicer species". [Manuscript submitted for publication].

List of Figures

1.1	Average global yields of chickpea compared to pulses and cereals . . .	2
1.2	Ascochyta blight disease cycle	3
1.3	Plants and seeds of <i>Cicer</i> species	9
1.4	Phenotyping as a network of sensor, vector, environment and data analysis	11
2.1	Signs and symptoms of plant-pathogen interactions	27
2.2	Physical paths of electromagnetic radiation in biological samples . . .	27
3.1	Nursery disease screens	51
3.2	Experimental design	52
3.3	Visual scores	58
3.4	Smoothed fractional green canopy cover	61
3.5	Smoothed number of lesions detected with YOLOv5	62
3.6	Variable importance for classification of disease indices	63
3.7	Early detection results	66
3.8	Fitted values for FGCC for main parts	69
3.9	Fitted values for number of lesions for main parts	70
3.10	Intermediate traits derived from RGB imaging	71
3.11	AUC between 0 and 42 DAI of vegetation indices	72
3.12	Sample pots with varying disease indices	74
4.1	Steps in hyperspectral sensing	89
4.2	Band pair correlation	95
4.3	Size of chickpea and wild relative leaflets	97
4.4	Mini-dome inoculation	98
4.5	Experimental design	99
4.6	Monochrome SWIR images of a hemp plant compared to chickpea plant	100
4.7	Disease indices	105
4.8	Side view images in greenhouse	106
4.9	Smoothed projected shoot area over time	106
4.10	Disease index and trait correlation matrices	109
4.11	Predicted disease indices compared to ground truth	110
4.12	Relative growth rates 7 - 14 DAI	122
5.1	Plots and lesions in 2020 field experiment	134

5.2	Trays in 2022 experiment	135
5.3	Reconstituted RGB image of plot	136
5.4	Percent AB damage per genotype	139
5.5	Treatment effects on percent AB damage	140
5.6	Correlation between reflectance at individual bands	141
5.7	Principal component analysis of spectral data	142
5.8	Feature importance for prediction of PAD in 2020	143
5.9	Feature importance for prediction of PAD in 2022	144
5.10	Feature importance for treatment classification in 2020	146
5.11	Feature importance for treatment classification in 2022	147

List of Tables

1.1	GRDC AB resistance rating scale	7
1.2	Candidate traits involved in resistance	13
2.1	Summary of sensors that have been used for phenotyping PPI	28
2.2	Applications of sensor-based phenotyping of PPI	29
2.3	Suitability of sensors for phenotyping PPI	32
3.1	Extracted low-level traits	55
3.2	Evaluation of visual scores	59
3.3	Correlation between in situ measurements and automated system	60
3.4	Confusion matrices and classification metrics	64
3.5	Genotypic, treatment, and trial effects	73
3.6	Estimated metrics for score classification	75
3.7	Distribution of disease severity classes	76
4.1	Specifications of hyperspectral cameras	100
4.2	Confusion matrices for early detection algorithms	107
4.3	Influence of processing steps on DI prediction performance	111
4.4	Genotypic and treatment effect on scores and traits	123
4.5	Cross-validation results for prediction of DI	124
4.6	Cross-validation results for accuracy of early detection	125
5.1	Hyperspectral cameras in ground-based field phenotyping platform	135
5.2	Between-year PAD score prediction validation results	144
5.3	Between-year treatment classification	148
5.4	Influence of hyperspectral data processing and learning algorithms	160
5.5	Low-level traits extracted from average hyperspectral data and lidar at plot level.	161
5.6	Details and timing of treatments (i) to (v) applied to 2020 plots and treatments (i) to (iii) applied to trays in 2022.	162

List of Abbreviations

AB	Ascochyta Blight
ANOVA	Analysis of Variance
BM	Biomass
CCD	Charge-Coupled Device
Chl-F	Chlorophyll α Fluorescence
CNN	Convolutional Neural Network
CT	Computed Tomography
CV	Cross Validation
cv.	Cultivar
CVR	Cultivar
DAI	Days After Inoculation
DAS	Days After Sowing
DI	Disease Index
ENDVI	Enhanced Normalized Difference Vegetation Index
ETI	Effector-Triggered Immunity
EVI	Enhanced Vegetation Index
ExGI	Excess Green Index
FAIR	Findable Accessible Interoperable Reusable
FAO	Food and Agriculture Organization of the United Nations
FGCC	Fractional Green Canopy Cover
F_m	Maximum Fluorescence
FN	Fortnightly
F_V/F_M	Maximum quantum efficiency of PSII
FWHM	Full Width at Half Maximum
GC	Ground Cover
GCC	Green Chromatic Coordinate
GRVI	Green Red Vegetation Index
GSD	Ground Sample Distance
HPLC	High-Performance Liquid Chromatography
HR	Hypersensitive Response
HSI	Hyperspectral Imaging
HSV	Hue Saturation Value
IR	Infrared
LASSO	Least Absolute Shrinkage and Selection Operator
LDT	Lesion Doubling Time

Lidar	L ight d etection and ranging
MAMP	M icrobe- A ssociated M olecular P attern
MLP-NN	M ulti L ayer P erceptron N eural N etwork
MR	M ean R eflectance
MSAVI	M odified S oil A ddjusted V egetation I ndex
MSR	M odified S imple R atio
MTI	M AMP- T riggered I mmunity
NDVI	N ormalized D ifference V egetation I ndex
NIR	N ear I nfrared
NPQ	N on- P hotochemical Q uenching
OCT	O ptical C oherence T omography
PAD	P ercent A rea D iseased
PAM	P ulse- A mplitude- M odulated
PLSDA	P artial L east S quares D iscriminant A nalysis
PLSR	P artial L east S quares R egression
PMMOV	P epper M ild M ottle V irus
PPI	P lant- P athogen I nteraction
PSRI	P lant S enescence R eflectance I ndex
PSA	P rojected S hoot A rea
PSII	P hotosystem I I
PSM	P lant S econdary M etabolite
px	P ixel
QP	P hotochemical Q uenching
RBF	R adial B asis F unction
RCBD	R andomized C omplete B lock D esign
RENDVI	R ed E dge N ormalized D ifference V egetation I ndex
RF	R andom F orest
RGB	R ed G reen B lue
RGR	R elative G rowth R ate
RMSE	R oot M ean S quare E rror
SARDI	S outh A ustralian R esearch and D evelopment I nstitute
SIPI	S tructure I nsensitive P igment I ndex
SPCSV	S weet P otato C hlorotic S tunt V irus
SPFMV	S weet P otato F eathery M ottle V irus
SR	R ed E dge S imple R atio
STB	S eptoria T ritici B lotch
SV	S ide V iew
SVM	S upport V ector M achine
SWIR	S hort W ave I nfrared
TIR	T hermal I nfrared
TMV	T obacco M osaic V irus
TPA	T he P lant A ccelerator®

TV	Top View
UAV	Uncrewed Aerial Vehicle
UV	Ultraviolet
UV-C	Ultraviolet C
VARI	Green Red VI Vegetation Index
VI	Vegetation Index
VIS	Visible
VNIR	Visible Near Infrared
WLD	Wild Chickpea Relative

Chapter 1

Introduction

1.1 Thesis structure

This thesis is structured into six chapters: two introductory and background chapters, three experimental chapters, and a combined discussion of all chapters. Chapter 1 introduces chickpea and *Ascochyta* blight (AB) and details the specifics of sensor-based phenotyping in the context of resistance breeding. Chapter 2, the second background chapter, contains a review of the literature which was written to explore the utility of various sensors to measure the signs and symptoms of plant-pathogen interactions, expanding on those specific to AB discussed in Chapter 1. This review was published in *Plant Methods* and is included in the same format.

Chapter 3 is the first experimental chapter and describes the development and application of RGB- and multispectral sensor-based phenotyping methods for three years of disease screens of chickpea and wild relatives in outdoor screens of pots. This chapter was submitted for publication and is included in manuscript form. The second experimental chapter (4) focuses on hyperspectral sensors and the search for reflectance features that can quantify the disease severity greenhouse, described in unpublished manuscript form. Sensor-based field phenotyping in the field was performed using a ground-based platform and is discussed in the last experimental chapter (5) in unpublished manuscript form.

A discussion of methods across scales and sensors and a conclusion with recommendations for the deployment of sensor-based phenotyping methods in AB resistance breeding programs and future research are presented in the last chapter (6).

1.2 Background

1.2.1 The role of chickpea for global food security

Chickpea (*Cicer arietinum*, NCBI:txid3827) is a predominantly self-pollinating diploid legume grown primarily for human consumption. In the period between 2010 and 2020, chickpea was the second most produced pulse after common bean (*Phaseolus vulgaris*, NCBI:txid3885) with an average annual global production of 13.1 Mt (FAO-STAT). As a pulse, it contributes to global food security due to its valuable nutritional profile with a protein content of 16-24 % and a high content of essential amino acids

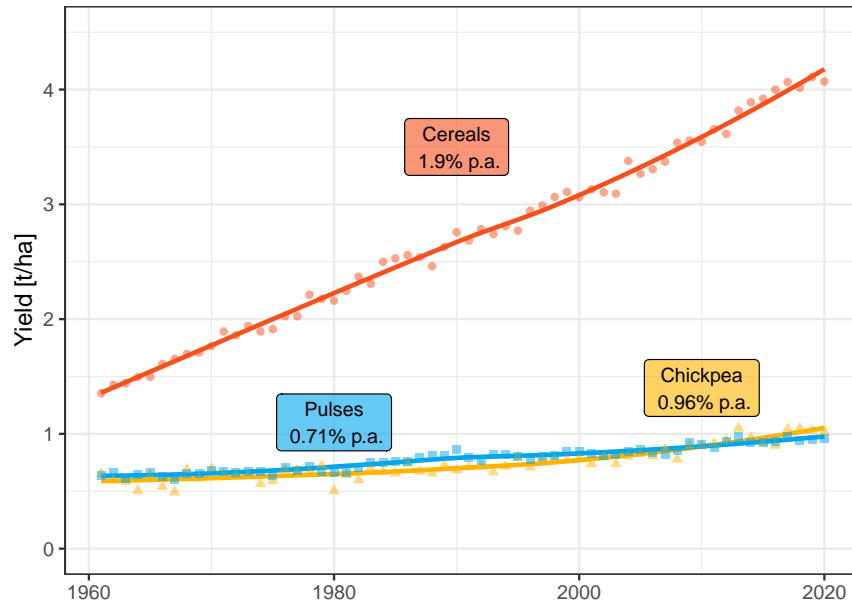


FIGURE 1.1: Average yearly global dry grain yield (points and trend line) and average yearly gains (text boxes) in chickpea compared to total cereals and total pulses. Cereals include 17 primary cereals harvested only for dry grain (Wheat, Maize (corn), Rice, Sorghum, Barley, Rye, Oats, Millet, Triticale, Buckwheat, Fonio, Quinoa, Canary seed, Teff, Mixed grain, Cereals nec.). Pulses include 11 primary pulses harvested solely for dry grain, not oil extraction (*Phaseolus spp.* (beans), *Vicia faba* (broad beans), *Lens esculenta* (lentils), *Cicer arietinum* (chick peas), *Pisum spp.* (peas), *Cajanus spp.* (pigeon peas), *Vigna sinensis* (cow peas), *Vicia sativa* (vetch), *Lupinus spp.* (lupins), *Vigna spp.* (black gram, green gram, mung, etc.), Pulses nec.) (FAOSTAT).

and micronutrients (Varshney et al., 2019; GRDC, 2017; Rawal and Navarro, 2019). In addition, its nitrogen-fixing capability can reduce the environmental impacts of synthetic nitrogen fertilizers. These detrimental impacts include the large primary energy consumption of fertilizer synthesis, the loss of biodiversity caused by eutrophication through runoff, and the emission of nitrous oxide, a powerful greenhouse gas linked to both fertilizer synthesis and eutrophication (Foyer et al., 2016). Despite these potential benefits of pulse cultivation, the realized yields of chickpea and other pulses have not risen at the same rate as those of cereals since the 1960s (Figure 1.1) (Rawal and Navarro, 2019; FAOSTAT; Foyer et al., 2016).

A large gap between potential and realized yields is caused by biotic and abiotic stresses in chickpea cultivation. The main abiotic stresses are drought and heat, and the main biotic stresses include pests and diseases such as *Helicoverpa punctigera* (NCBI:txid27545), Ascochyta blight (AB), Fusarium wilt, and competition from weeds (Rawal and Navarro, 2019). Furthermore, a historic neglect of research focused on the agronomy and breeding of pulse crops in general, and the low genetic variation in chickpea cultivars in particular have limited the potential yield of the crop (Von Wettberg et al., 2018; Foyer et al., 2016). Therefore, the FAO called for a “[...] major

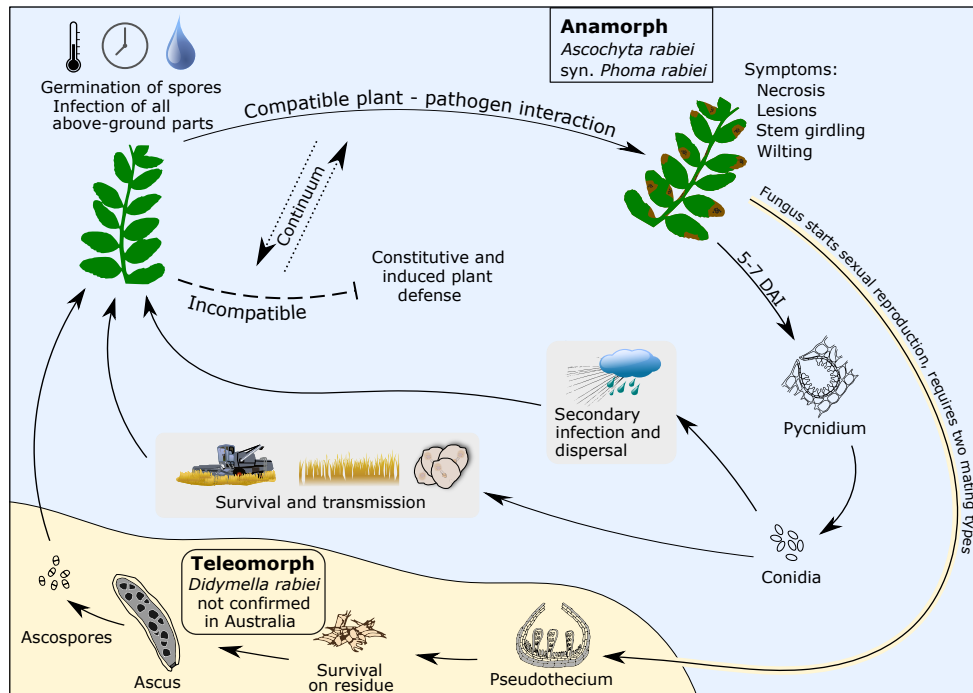


FIGURE 1.2: *Ascochyta* blight disease cycle. The teleomorph form of the fungus, *Didymella rabiei* (yellow background shading), has not been found in Australia except for one study in Western Australia (Galloway and MacLeod, 2003). References for components of the visualization: Ascus after (Trapero-Casas, 1992), Pseudothecium after (Ixitixl, 2012), Pycnidium after (Piepenbring, 2015), Chickpea leaves after (Pulse Australia, 2015), Debris after (Slpfeifer, 2013).

thrust in agricultural research and extension, improving credit availability [to facilitate the adoption of improved varieties and modern agronomic practices], and public investment.” (Rawal and Navarro, 2019). Plant breeding is one of the pathways to contribute to raising both yield stability and yield potential in pulses (Foyer et al., 2016; Jha et al., 2022b).

1.2.2 *Ascochyta* blight of chickpea

AB is one of the main biotic stresses that affect chickpeas and is caused by the necrotrophic fungus *Ascochyta rabiei* (NCBI: txid5454), leading to yield losses in all major growing regions (Pande et al., 2005). Integrated AB disease management includes cultural management through tilling, crop rotation, hygiene, delayed sowing, lower seed rates, increased potassium fertilization under high nitrogen conditions, resistant varieties, and chemical control (Pande et al., 2005).

Host-pathogen interactions Infection of chickpea by *A. rabiei* in its anamorph form can take place at all stages of growth, from seedling stage to generative stage (Figure 1.2) (Pande et al., 2005). Germination of conidia or ascospores occurs 12-48 hours after infection in a temperature range of 5-30 °C with an optimum at 20 °C. Leaf wetness is

essential for a successful infection, optimally for 17 h after infection or longer, which means that the severity and spread of AB depend heavily on environmental conditions (Pande et al., 2005; Sharma and Ghosh, 2016). Conidia germinate and penetrate the host on all aerial parts through stomata, hydathodes, cell junctions, or directly through the cuticle (Ilarslan and Dolar, 2002; Armstrong-Cho et al., 2015). The germination tubes produce a mucilaginous substance that attaches to the surface of the plant and the fungus produces cell-wall lytic compounds and phytotoxins that aid penetration and cause necrosis (Jayakumar et al., 2005; Pande et al., 2005).

During the asexual stage, the fungus forms pycnidia from which conidia are emitted. These spores can cause secondary infections on other plant parts when transmitted by air or water splash (Pande et al., 2005; Sharma and Ghosh, 2016). At seven DAI, necrosis becomes evident and the fungus colonizes the vascular system to spread to the petioles and further throughout the plant (Pande et al., 2005). The necrosis, if severe, can lead to stem breakage which drives yield loss. *A. rabiei* can stay infectious in chickpea debris for eight months, 20 months on stems, and five months on seeds (Pande et al., 2005). However, seed infection can occur for at least 13 years if the seeds are stored at 4 °C (Kaiser, 1997). These estimates of the survival time of the anamorph come from research in tillage farming systems and it is suspected that common Australian no-till farming systems may allow the fungus to survive on standing stubble for longer periods, as has been observed for *Leptosphaeria maculans* in standing canola stubble (McCredden et al., 2018). Dispersal of the spores can occur by seed, by air, and machinery. By these means, virulent isolates are quickly spread throughout growing regions (Mehmood et al., 2017). In contrast, an incompatible host-pathogen can be mediated by two mechanisms, microbe-associated molecular patterns (MAMP) triggered immunity (MTI) and effector-triggered immunity (ETI) (Jha et al., 2022b). Both mechanisms can confer levels of resistance to chickpea.

Pathotypes and mating types Two mating types of the fungus (MAT1-1 and MAT1-2) are required for the fungus to sexually reproduce and enter the teleomorph stage (*Didymella rabiei*) (Figure 1.2) (Jayakumar et al., 2005). The teleomorph can survive on plant residue and produce ascospores that, in turn, can infect live plants (Pande et al., 2005). The fungal isolates are classified into pathotypes based on their ability to cause severe AB on a differential set of host genotypes. Depending on the country, the resolution of this classification is between three to ten groups (Jha et al., 2022b).

1.2.3 Australian context of chickpea cultivation and AB

Chickpea cultivation in Australia In Australia, chickpea is grown due to its price potential and as part of a sustainable crop rotation to maintain soil fertility and structure, and to control cereal root diseases that are caused by sustained cereal cultivation (GRDC, 2017). In the period 2010 - 2020, Australia was the second largest chickpea producer (average annual production of 0.79 Mt) after India (8.90 Mt) (FAOSTAT). Of this production, less than 2 % were estimated to be used domestically, the rest being

exported (ABARES, 2022). Chickpea varieties consist of two types: *desi* and *kabuli* (Figure 1.3). *Desi* types are characterized by small angular dark seeds, pink flowers, thick seed coat, more protein, and less available carbohydrates compared to *kabuli*. *Kabuli* types have larger round seeds with a lighter-colored, thinner seed coating compared to *desi* and white flowers (Vega, 2011). In Australia, 90-95% of chickpeas grown are the *desi* type and most chickpeas are grown in the northern growing region (New South Wales and Queensland). However, most of the Australian *kabuli* production takes place in the southern growing region (Victoria and South Australia) (GRDC, 2017). The main variable costs in chickpea cultivation in Australia are plant protection chemicals and seed inoculants (43% of variable costs) (Rawal and Navarro, 2019). Furthermore, seed costs are a major variable cost because relatively high seed rates and good seed quality are required for a high germination rate and early vigor (GRDC, 2017; Rawal and Navarro, 2019). The demand for Australian pulses, including chickpeas, is projected to increase, mainly from the Indian subcontinent (Collis, 2019). As with other crops, chickpea trade is subject to varying yields across production zones and trade restrictions, for example, a tariff introduced by India in 2017 led to lower production in 2018-2019 (ABC, 2017; Goddard, 2022).

Ascochyta blight in Australia All Australian isolates of *A. rabiei* that have been tested for mating type have consisted of only one type (MAT1-2), which limits the fungus to clonal reproduction (Bar et al., 2021). Without sexual reproduction, the genetic diversity of the pathogen population in Australia is lower compared to other global populations (Bar et al., 2021). Despite this limitation, pathogen adaptation has been observed, aggressive haplotypes have developed through opportunistic mutations, and previously effective host resistance in some cultivars is no longer effective (Mehmood et al., 2017; Bar et al., 2021). Routine screens of *A. rabiei* of current isolates collected annually from growing regions across Australia are performed in controlled environments (Bar et al., 2021). Between 2013 and 2020, 95-200 isolates were screened each year on a set of control genotypes. The percentages of isolates capable of causing severe disease increased from 6.7 % to 36.3 % for cultivar (cv.) Genesis090, from 17.9 % to 51.0 % for cv. PBA HatTrick, from 0 % to 48.3 % for cv. PBA Seamer, and from 0 % to 10.4 % on breeding line ICC3996, a source of resistance for many cultivars (Bar, 2022). Based on the severity of the disease in the genotypes ICC3996, Genesis090, PBA HatTrick and Kyabra, the isolates are grouped into six pathotypes (pathogenicity group 0 = low, to pathogenicity group 5 = high) in Australia (Bar et al., 2021). An introduction of the second mating type into Australia, which is regarded as only a matter of time by some experts, would likely increase the speed of pathogen adaptation to the host (Ford et al., 2022).

Disease management in Australia Due to the lack of resistant cultivars, other disease management options are required. Traditional management methods include delayed sowing, tilling, and lower seed rates. However, they are rarely used as AB

management measures in Australia, as they can limit yield, especially under drought conditions (Davidson, personal communication). Other management options recommended by the Grains Research and Development Corporation (GRDC) include seed treatment with thiram-based fungicides to prevent the spread of the fungus from seed to seedling, a break of at least three years between repeat cropping of chickpea in the same paddock, and a distance of 500 m to neighboring fields where chickpeas were previously planted, which requires the collaboration between farmers (GRDC, 2017). In addition, protective fungicides are used as a control measure. These fungicides protect plants from secondary spread of the disease through rain splash and prevent germination of conidia on wet leaves. The required frequency of fungicide applications depends on the degree of susceptibility of the cultivar and the risk of secondary spread (GRDC, 2017; GRDC, 2020). Current practice in the northern growing region is to spray protective fungicides before rain events after the detection of the first symptoms in the field (Brand, 2019; Fanning, 2022). Due to the generally higher rainfall in the southern growing region, prophylactic sprays 8-10 weeks after sowing followed by sprays at early flowering and during podding are recommended for that region (Davidson, personal communication). A single application of these foliar fungicides costs approximately AU\$35 per hectare for chlorothalonil to AU\$55 per hectare for fludioxonil + pydiflumetofen (Miravis Star, Syngenta, Australia) (Pulse Australia, 2015; Pulse Australia, 2019; CropLife Australia, 2017; PIRSA, 2019; Fanning, 2022).

Resistant varieties could reduce the dependence on fungicide application and the yield-limiting influence of management options such as late sowing and low seed rates. Therefore, breeding for resistance to AB is an important goal for the Australian chickpea industry (GRDC, 2017; Li et al., 2017).

1.2.4 Breeding chickpea for AB resistance

Definitions of plant disease resistance vary depending on the context. A strict definition from the field of plant pathology is: "Resistance reduces pathogen populations while tolerance reduces fitness loss of the host without altering pathogen development." (Fradin and Thomma, 2006). In an agronomic context, the distinction between tolerance and resistance is often lost and plant resistance is defined based on the amount of "economic management" needed to produce an optimum yield beyond what is provided by genetic resistance (Table 1.1) (GRDC, 2019).

The process towards AB resistant cultivars

Breeding for plant resistance requires three steps (Niks et al., 2019):

1. Identification or creation of a source of resistance
2. Evaluation of the resistance
3. Introgression of the resistance into commercial cultivars

TABLE 1.1: GRDC AB resistance rating scale. Resistance is rated based on amount of required economic disease management.

Rating	Management Option Description
9: Resistant	Disease may be found but will be at such a level that no economic management is required, even in instances of high disease pressure.
8: Resistant – Moderately Resistant	—
7: Moderately Resistant	Disease may be observed but no economic management decisions will be required. Preventative sprays not necessary but disease should be monitored. Management of seed quality may be required.
6: Moderately Resistant – Moderately Susceptible	—
5: Moderately Susceptible	In the presence of inoculum and in seasons conducive to disease, the disease will be seen more readily when inspecting the crop. If the disease appears early in the season then an economic management decision (preventative spray) may be appropriate. Later occurrence of the disease may not require any action. Management of seed quality will be required.
4: Moderately Susceptible – Susceptible	—
3: Susceptible	The disease will be easily found in the crop. Management decisions will be required to reduce yield loss and will most probably be economic to do so. Management of seed quality will be required.
2: Susceptible – Very Susceptible	—
1: Very Susceptible	Do not grow this variety if the disease in question is a regular occurrence or risk. The variety in question can be a complete loss if sown and no disease management is applied.

Sources of resistance In addition to mutagenesis and genetic modification, sources of resistance can come from elite lines of other breeding programs, landraces, or wild relatives. Due to bottleneck events in chickpea domestication, the available genetic variation within the cultivar pool is low (Von Wettberg et al., 2018; Varshney et al., 2019; Varshney et al., 2021), and therefore, cultivars or breeding lines are not promising sources of resistance.

However, wild relatives can provide a useful source of variation for multiple agronomic traits, including AB resistance (Von Wettberg et al., 2018). The genus *Cicer* consists of the cultivated chickpea *C. arietinum*, 34 perennial species, and eight wild annual relatives, which are endemic to an area from Turkey to central Asia and areas of Sudan, Egypt, and Ethiopia (Figures 1.3, 4.3) (Upadhyaya et al., 2011). Worldwide, 28 major genebanks hold a collection of more than 1,300 wild accessions alongside more than 90,000 cultivated accessions (Upadhyaya et al., 2011). Within the annual wild relatives, genetic variability for resistance to AB has been reported in *Cicer bijugum* (NCBI:txid90899), *C. judaicum* (NCBI:txid92719), *C. pinnatifidum* (NCBI:txid47088), *C. reticulatum* (NCBI:txid90898), and *C. echinospermum* (NCBI:txid90897) (Newman et al., 2021; Collard et al., 2001; Singh et al., 2015; Singh and Reddy, 1993; Manjunatha et al., 2018). The two closest relatives that can be hybridized directly with chickpea are *C. echinospermum* and *C. reticulatum* (Vega, 2011). A recent collection mission in Turkey largely expanded the pool of available lines of these two species (Von Wettberg et al., 2018) and variation for resistance to AB was found within the collection (Newman et al., 2021).

Evaluation of resistance Signs and symptoms can be measured to predict the quantitative and qualitative effect of the disease on yield (Mahlein, 2016). Signs are an indication of disease by the pathogen and symptoms are the response of the plant to the pathogen (D'Arcy, 2001). Traditionally, visual scoring is used for such an evaluation and detailed guidelines and formalized scoring guides have been published to increase the reliability and accuracy of scoring. For AB resistance breeding in chickpea, a commonly used rating scale evaluates the extent of lesions and stem girdling (Singh, 1981). Multiple adaptations of such rating scales exist both for controlled environment and field experiments. Some of the scales include the percentage of surface area or percentage of individual plants within a group affected by disease symptoms to quantitatively assess symptoms (Kimber, 2003; Chongo et al., 2004; Shtienberg et al., 2006; Armstrong-Cho et al., 2015). Although visual scoring with detailed guidelines by trained and experienced scorers can reliably quantify disease symptoms, it has limitations. First, it depends on human labor and is therefore prone to error and limited in throughput (Bock et al., 2020). Second, the human eye can only spot symptoms when they appear within the visible spectrum (Mahlein, 2016). Third, a traditional ordinal breeding rating scale confines the scoring of symptoms to a semiquantitative level.



FIGURE 1.3: Side view images of *Cicer* plants and top view images of corresponding seeds. a = *Cicer arietinum*, kabuli type; b = *Cicer arietinum*, desi type; c = *Cicer reticulatum*

Another factor to consider in breeding for AB resistance of chickpea is the dependency of resistance on the development stage of the plant. Varieties that do not show symptoms at seedling stage may well be susceptible to infection during the generative phase, which can lead to pod abortion (Elliott, Taylor, and Ford, 2013). Therefore, it is important to define the type of resistance and to acknowledge the limitations of specific screening methods. Seedling resistance can be tested in week-old seedlings in a controlled environment, while adult plant resistance screens require a complete growth cycle and are preferably performed in the field (Reddy, 1984; Garg et al., 2018).

Introgression After the identification and evaluation of a source of resistance, it can be used as a donor genotype to develop resistant cultivars, a process that can be supported by various genomics techniques as reviewed by Jha et al., 2022b. After introgression, further evaluation of the resistance is required to test whether it is effective in the genetic background of high-yielding cultivars.

1.2.5 Phenotyping for disease resistance breeding

The output from research using sensor-based phenotyping has grown exponentially in the past decade (Saint Cast et al., 2022). In the context of disease resistance breeding, phenotyping is required to find sources of resistance and evaluate resistance. A more detailed introduction of the concept of sensor-based phenotyping with a focus on the sensor technology can be found in Section 2.2. Briefly, the use of sensors for phenotyping offers a range of advantages over visual evaluation: objectivity, precision, spectral range, and imaging modalities, and the potential to increase throughput by automation (Simko, Jimenez-Berni, and Sirault, 2017). In this way, sensor-based plant phenotyping can increase the rate of genetic gain by addressing the components of the breeder's formula (1.1) (Araus et al., 2018; Rebetzke et al., 2019).

$$R_t = \frac{ir\sigma_A}{y} \quad (1.1)$$

where R_t is genetic gain over time, i is selection intensity, r is selection accuracy, σ_A is genetic variance, and y is time per cycle. i and σ_A can be increased when a larger number of genotypes can be screened with higher throughput. r can be increased with precise measurements and y can potentially be reduced by early measurements of signs and symptoms enabled by various imaging modalities (Araus et al., 2018; Rebetzke et al., 2019).

Systems for sensor-based phenotyping not only require appropriate sensors, but also rely on a network of supporting expertise and technology to proceed from measurement to knowledge and decision support (Figure 1.4) (Fiorani and Schurr, 2013; Mutka and Bart, 2015).

Data acquisition: Environment, sensor, vector The expression of disease depends on the plant-pathosystem and environment, this informs the choice of sensor (Chapter 2). The environment where the screens are performed is dictated by the application, for example, field disease screens or controlled environment screens. The environment, in turn, influences which sensors and vectors can sensibly be used. Vectors are devices that either bring the sensor to the plant or the plant to the sensor. These can be ground-based phenotyping platforms, aerial platforms, satellites, conveyor belt-based systems, or simple hand-held solutions (Bagley et al., 2020) (Figure 1.4).

Data analysis The goal of sensor data analysis is to retrieve a target trait that is valuable for the selection process, such as resistance components or the severity of the disease (Eeuwijk et al., 2019). This can be achieved through two loosely grouped approaches, deterministic or empirical (Weiss, Jacob, and Duveiller, 2020). Usually, a minimum of preprocessing and calibration is applied to raw sensor data for either approach. Beyond that minimum processing, the deterministic approach focuses on a mechanistic understanding of the plant-pathogen interaction and aims to infer candidate traits from the radiative process (Weiss, Jacob, and Duveiller, 2020). The

advantage of this approach is that such defined resistance components may be transferable from controlled environment to the field (Simko, Jimenez-Berni, and Sirault, 2017; Eeuwijk et al., 2019; Rebetzke et al., 2019). In an empirical approach, the emphasis is not on understanding the mechanism of disease progression, but the target trait is predicted directly from sensor data (Baker et al., 2018; Weiss, Jacob, and Duveiller, 2020). This approach can be supported by emerging machine learning algorithms that work with high-dimensional data (Sperschneider, 2019). The deterministic and empirical approaches to the analysis are not exclusive. An iteration of empirical and mechanistic models can be used to break down complicated phenomena such as disease progression into smaller mechanistic explanations (Baker et al., 2018). After either way of feature extraction, further hierarchical modeling steps can be applied to merge data from multiple environments and multiple time points (Eeuwijk et al., 2019; Tardieu et al., 2017). These steps are correction for spatial and design effects, longitudinal modeling, and modeling environmental effects (Eeuwijk et al., 2019).

Throughout the entire process from data acquisition to analysis, appropriate data and metadata management are important to meet the FAIR (Findable, Accessible, Interoperable, Reusable) data standards (Figure 1.4) (Papoutsoglou et al., 2020).

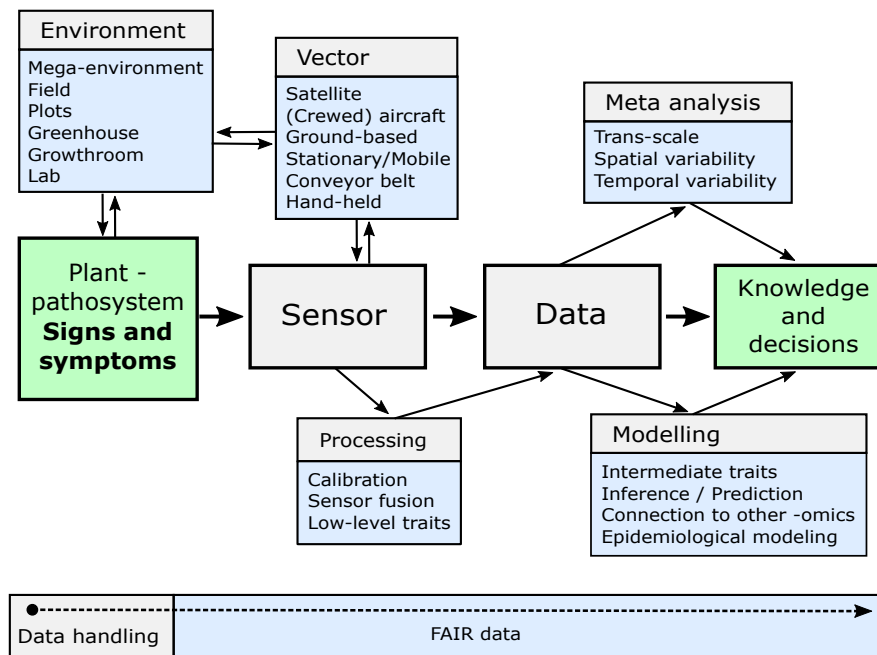


FIGURE 1.4: Phenotyping as a network of sensor, vector, environment, and data analysis. To draw knowledge from sensor data, complementary network components are required. The choice of components is determined by a) the plant- pathosystem and its signs and symptoms and b) the compatibility of the components. At each step, appropriate data and metadata handling are necessary.

Sensor-based phenotyping to support disease scoring in breeding programs

Sensor-based phenotyping has been widely used to directly predict visual disease severity scores to support plant resistance breeding programs. For example, using a MicaSense RedEdge multispectral camera mounted on an uncrewed aerial vehicle (UAV) in the field, disease scores of *Verticillium* wilt of strawberry were predicted with Normalized Difference Vegetation Index (NDVI) (Cockerton et al., 2019). The authors realized a 15-fold increase in scoring speed while maintaining a strong correlation between visual scores and automated scores.

Red, green, blue (RGB) images from handheld cameras were used to predict the severity of *Septoria tritici* blotch (STB) of wheat in field plots. The percentage of affected area was extracted by manual hue, saturation, value (HSV) thresholding. This trait showed a positive linear correlation with visual scores of the area on a 1-9 scale (Walter et al., 2019). Instead of extracting traits, convolutional neural networks were applied directly to RGB images of individual leaves to classify diseases and estimate the severity of the disease in soybean and coffee on ordinal scales (Ghosal et al., 2018; Esgario, Krohling, and Ventura, 2020). For soybeans, eight different stresses could be distinguished with 94 % accuracy and the severity estimates were based on area of explanation in an unsupervised manner (Ghosal et al., 2018). In coffee, four diseases and healthy leaves could be identified with 95 % accuracy and the disease severity class (healthy, very low, low, high, very high) could be predicted with 87 % accuracy.

Sensor-based measurements of signs and symptoms

Chapter 2 contains a review of sensor technology suitable for measuring specific signs and symptoms, Section 4.3.2 contains a discussion of spectroscopy for measuring plant-pathogen interactions, and Section 5.3 focusses on the deployment of the technology to the field. Specific measurements of signs and symptoms have not been performed for AB of chickpea to date with non-invasive sensors. The following paragraph contains a discussion of potentially fitting sensor technology to measure the signs and symptoms of this particular pathosystem.

Phenotyping *A. rabiei* × Chickpea interactions Interactions between *A. rabiei* and chickpea are influenced by constitutive and induced mechanisms of host plant resistance (Pande et al., 2005; Jha et al., 2022a). Although these traits have been largely discovered using invasive measurements, some of them may also be measured or estimated by their spectral properties using non-invasive sensors (Chapter 2). Mechanisms that might be quantified using non-invasive sensor technology are detailed in Table 1.2 and include structural adaptations, constitutive and accumulated phenolic compounds, phytoalexins, reactive oxygen species signaling, hypersensitive response, and organic acid contents (Weigand et al., 1986; Höhl, Pfautsch, and Barz, 1990; Daniel and Barz, 1990; Ilarslan and Dolar, 2002; Jayakumar et al., 2005; Pande et al., 2005; Ahuja, Kissen, and Bones, 2012; Armstrong-Cho et al., 2015; Çağırğan et al., 2011).

TABLE 1.2: Chickpea responses to *A. rabiei* infection. Potential options to measure or estimate the responses using sensor-based non-invasive methods are suggested. All measurements in the referenced studies except visual scoring were performed invasively.

Trait	Measurement	Reference	Potential non-invasive measurement
Phytoalexins (Medicarpin, Mackiain) accumulation	HPLC	Weigand et al., 1986; Daniel and Barz, 1990	Spectral imaging
Browning 2DAI, Hypersensitive response (HR)	Light microscopy	Höhl, Pfautsch, and Barz, 1990	Spectral imaging
Autofluorescence of palisade parenchyma preceding HR	Fluorescence microscopy	Höhl, Pfautsch, and Barz, 1990	Fluorescence imaging
Structural organization of xylem tissues	Light and fluorescence microscopy	Angelini et al., 1993	Tomography, Raman spectroscopy
Polyamine metabolism and peroxidase	Spectrofluometry, Spectrophotometry	Angelini et al., 1993	Spectral imaging
Lesions, girdling, stem breakage	Visual scoring	Pande et al., 2005	RGB imaging, Lidar
Malic acid content	HPLC	Çağirgan et al., 2011	Spectral imaging
Upregulation of peroxidase activity	Spectrophotometry	Kaur, Singh, and Gupta, 2012	Spectral imaging

1.3 Research aims

Current disease screening protocols for AB of chickpea are limited in precision, sensitivity, objectivity, and throughput. The feasibility of predicting visible scores of plant disease severity using both RGB and hyperspectral imaging has been shown for various diseases on different crops, including for AB of chickpea on two cultivars under various fungicide treatments (Zhang, Chen, and Sankaran, 2019). However, this has not been applied in high-throughput testing of genetic resources for breeding chickpea for AB resistance. Furthermore, no screens for resistance component traits that can address the phenotypic plasticity of plant disease due to genotype-environment interactions of host and pathogen have been developed. This left two main aims for this project:

1. Development of sensor-based phenotyping methods to score disease severity in a chickpea breeding program
2. Identification of within-scale and cross-scale functional resistance components

1.4 References

- ABARES (2022). *Crop data underpinning: Australian crop report: June 2022 No. 202*. URL: <https://www.awe.gov.au/abares/research-topics/agricultural-outlook/data#australian-crop-report-data>.
- ABC (Dec. 2017). "Multi-million-dollar pulse export market stunned by new Indian tariff". en-AU. In: *ABC News*. URL: <https://www.abc.net.au/news/rural/2017-12-29/india-imposes-30percent-tariff-on-imported-chickpeas-and-lentils/9290358> (visited on 10/26/2022).
- Ahuja, Ishita, Ralph Kissen, and Atle M. Bones (2012). "Phytoalexins in defense against pathogens". In: *Trends in Plant Science* 17.2. Publisher: Elsevier Ltd, pp. 73–90. ISSN: 13601385. DOI: 10.1016/j.tplants.2011.11.002. URL: <http://dx.doi.org/10.1016/j.tplants.2011.11.002>.
- Angelini, Riccardo et al. (1993). "Involvement of Polyamines, Diamine Oxidase and Peroxidase in Resistance of Chickpea to *Ascochyta rabiei*". In: *Journal of Plant Physiology* 142.6, pp. 704–709. ISSN: 01761617. DOI: 10.1016/S0176-1617(11)80906-5.
- Araus, José Luis et al. (2018). "Translating High-Throughput Phenotyping into Genetic Gain". In: *Trends in Plant Science* 23.5, pp. 451–466. ISSN: 13601385. DOI: 10.1016/j.tplants.2018.02.001.
- Armstrong-Cho, Cheryl et al. (2015). "Characterization of resistance to ascochyta blight of selected wild cicer germplasm". In: *Botany* 93.11, pp. 723–734. ISSN: 19162804. DOI: 10.1139/cjb-2015-0072.

- Bagley, Stuart A. et al. (June 2020). "Low-Cost Automated Vectors and Modular Environmental Sensors for Plant Phenotyping". en. In: *Sensors* 20.11, p. 3319. ISSN: 1424-8220. DOI: 10.3390/s20113319. URL: <https://www.mdpi.com/1424-8220/20/11/3319> (visited on 04/21/2023).
- Baker, Ruth E. et al. (2018). "Mechanistic models versus machine learning, a fight worth fighting for the biological community?" In: *Biology Letters* 14.5, pp. 1–4. ISSN: 1744957X. DOI: 10.1098/rsbl.2017.0660.
- Bar, Ido (2022). "Mapping *Ascochyta rabiei* aggressiveness and understanding the pathogen adaptation to disease management strategies - GRDC". In: URL: <https://grdc.com.au/resources-and-publications/grdc-update-papers/tab-content/grdc-update-papers/2022/02/mapping-ascochyta-rabiei-aggressiveness-and-understanding-the-pathogen-adaptation-to-disease-management-strategies> (visited on 06/03/2022).
- Bar, Ido et al. (2021). "Current population structure and pathogenicity patterns of *Ascochyta rabiei* in Australia". In: *Microbial Genomics* 7.7. ISSN: 20575858. DOI: 10.1099/mgen.0.000627.
- Bock, Clive H. et al. (Dec. 2020). "From visual estimates to fully automated sensor-based measurements of plant disease severity: status and challenges for improving accuracy". In: *Phytopathology Research* 2.1. Publisher: Phytopathology Research, p. 9. ISSN: 2524-4167. DOI: 10.1186/s42483-020-00049-8. URL: <https://phytopatholres.biomedcentral.com/articles/10.1186/s42483-020-00049-8>.
- Brand, Jason (2019). *Growing Pulses in 2019 Webinar: Chickpeas - YouTube*. URL: <https://www.youtube.com/watch?v=-QuR1Es54C4> (visited on 02/12/2020).
- Chongo, G. et al. (2004). "Genetic diversity of *Ascochyta rabiei* in Canada". In: *Plant Disease* 88.1, pp. 4–10. ISSN: 01912917. DOI: 10.1094/PDIS.2004.88.1.4.
- Cockerton, Helen M. et al. (2019). "Identifying *Verticillium dahliae* resistance in strawberry through disease screening of multiple populations and image based phenotyping". In: *Frontiers in Plant Science* 10.July. ISSN: 1664462X. DOI: 10.3389/fpls.2019.00924.
- Collard, B. C.Y. et al. (2001). "Prospecting for sources of resistance to ascochyta blight in wild *Cicer* species". In: *Australasian Plant Pathology* 30.3, pp. 271–276. ISSN: 08153191. DOI: 10.1071/AP01036.
- Collis, Clarisa (2019). *Australian pulse trade at the intersection of five megatrends in world markets | Ground Cover*. URL: <https://groundcover.grdc.com.au/story/6481128/market-megatrends-what-global-appetite-for-australian-pulses/?cs=14005> (visited on 01/07/2020).
- CropLife Australia (2017). "CropLife Australia Fungicide Resistance Management Review Group Fungicide Activity Group Table". In: June, pp. 2–4.
- Daniel, Susanne and Wolfgang Barz (1990). "Elicitor-induced metabolic changes in cell cultures of chickpea (*Cicer arietinum* L.) cultivars resistant and susceptible to *Ascochyta rabiei*". In: *Planta* 182.2, pp. 279–286. ISSN: 0032-0935. DOI: 10.1007/bf00197122.

- D'Arcy (2001). "Illustrated Glossary of Plant Pathology". In: *The Plant Health Instructor*. ISSN: 19359411. DOI: 10.1094/PHI-I-2001-0219-01. URL: <https://www.apsnet.org/edcenter/resources/illglossary/Pages/default.aspx>.
- Eeuwijk, Fred A. van et al. (2019). "Modelling strategies for assessing and increasing the effectiveness of new phenotyping techniques in plant breeding". In: *Plant Science* 282. December 2017. Publisher: Elsevier, pp. 23–39. ISSN: 18732259. DOI: 10.1016/j.plantsci.2018.06.018. URL: <https://doi.org/10.1016/j.plantsci.2018.06.018>.
- Elliott, Vicki L., Paul W. J. Taylor, and Rebecca Ford (2013). "Changes in Foliar Host Reaction to *Ascochyta Rabiei* With Plant Maturity". In: *Journal of Agricultural Science* 5.7. ISBN: 6135381229, pp. 29–35. ISSN: 1916-9752. DOI: 10.5539/jas.v5n7p29.
- Esgario, José G.M., Renato A Krohling, and José A Ventura (Feb. 2020). "Deep learning for classification and severity estimation of coffee leaf biotic stress". In: *Computers and Electronics in Agriculture* 169. July 2019, p. 105162. ISSN: 01681699. DOI: 10.1016/j.compag.2019.105162. URL: <https://linkinghub.elsevier.com/retrieve/pii/S0168169919313225>.
- Fanning, Josh (Oct. 2022). *Effectiveness of curative fungicide strategies and cultivar resistance on the control of Chickpea Ascochyta Blight*. Wagga Wagga, NSW, Australia. FAOSTAT. URL: <https://www.fao.org/faostat/en/#home> (visited on 05/18/2022).
- Fiorani, Fabio and Ulrich Schurr (2013). "Future Scenarios for Plant Phenotyping". In: *Annual Review of Plant Biology* 64.1, pp. 267–291. ISSN: 1543-5008. DOI: 10.1146/annurev-arplant-050312-120137.
- Ford, Rebecca et al. (Oct. 2022). *Panel Discussion*. Wagga Wagga, NSW, Australia.
- Foyer, Christine H. et al. (2016). "Neglecting legumes has compromised human health and sustainable food production". In: *Nature Plants* 2.8. Publisher: Macmillan Publishers Limited, pp. 1–10. ISSN: 2055026X. DOI: 10.1038/NPLANTS.2016.112. URL: <http://dx.doi.org/10.1038/nplants.2016.112>.
- Fradin, Emilie F. and Bart P.H.J. Thomma (2006). "Physiology and molecular aspects of *Verticillium* wilt diseases caused by *V. dahliae* and *V. albo-atrum*". In: *Molecular Plant Pathology* 7.2. ISBN: 1364-3703 (Electronic)\r1364-3703 (Linking), pp. 71–86. ISSN: 14646722. DOI: 10.1111/j.1364-3703.2006.00323.x.
- Galloway, J. and W. J. MacLeod (2003). "*Didymella rabiei*, the teleomorph of *Ascochyta rabiei*, found on chickpea stubble in Western Australia". In: *Australasian Plant Pathology* 32.1, pp. 127–128. ISSN: 08153191. DOI: 10.1071/AP02076.
- Garg, Tosh et al. (2018). "Identification of QTLs for resistance to *Fusarium* wilt and *Ascochyta* blight in a recombinant inbred population of chickpea (*Cicer arietinum* L.)" In: *Euphytica* 214.3. Publisher: Springer Netherlands, pp. 1–11. ISSN: 15735060. DOI: 10.1007/s10681-018-2125-3. URL: <https://doi.org/10.1007/s10681-018-2125-3>.
- Ghosal, Sambuddha et al. (May 2018). "An explainable deep machine vision framework for plant stress phenotyping". In: *Proceedings of the National Academy of Sciences* 115.18. Publisher: Proceedings of the National Academy of Sciences, pp. 4613–4618.

- DOI: 10.1073/pnas.1716999115. URL: <https://www.pnas.org/doi/abs/10.1073/pnas.1716999115> (visited on 12/15/2022).
- Goddard, Nick (Oct. 2022). *Chickpea Production in Australia*. Wagga Wagga, NSW, Australia.
- GRDC (2017). *GRDC: Chickpea Southern Region - GrowNotes™*. Vol. 53. arXiv: 1011.1669v3 Issue: 9 ISSN: 1098-6596. ISBN: 978-85-7811-079-6. DOI: 10.1017/CB09781107415324.004.
- (2019). “GRDC-NVT Disease Resistance Rating Definitions Rusts and Foliar Diseases”. In: pp. 1–2. URL: <https://www.nvtonline.com.au/resource/disease-rating-definitions/>.
- (2020). “2020 South Australian Crop Sowing Guide”. In: December 2019. URL: <https://grdc.com.au/resources-and-publications/all-publications/nvt-crop-sowing-guides/sa-crop-sowing-guide>.
- Höhl, B., M. Pfautsch, and W. Barz (1990). “Histology of Disease Development in Resistant and Susceptible Cultivars of Chickpea (*Cicer arietinum* L.) Inoculated with Spores of *Ascochyta rabiei*”. In: *Journal of Phytopathology* 129.1, pp. 31–45. ISSN: 14390434. DOI: 10.1111/j.1439-0434.1990.tb04287.x.
- Ilarslan, H. and F. S. Dolar (2002). “Histological and ultrastructural changes in leaves and stems of resistant and susceptible chickpea cultivars to *Ascochyta rabiei*”. In: *Journal of Phytopathology* 150.6, pp. 340–348. ISSN: 09311785. DOI: 10.1046/j.1439-0434.2002.00763.x.
- Ixitixl (2012). *Scheme Pseudothecium von Didymella brioniae.png - Wikimedia Commons*. URL: https://commons.wikimedia.org/wiki/File:Scheme_Pseudothecium_von_Didymella_brioniae.png (visited on 02/18/2020).
- Jayakumar, P. et al. (2005). “*Ascochyta* blight of chickpea: Infection and host resistance mechanisms”. In: *Canadian Journal of Plant Pathology* 27.4, pp. 499–509. ISSN: 17152992. DOI: 10.1080/07060660509507251.
- Jha, Uday et al. (Feb. 2022a). “Breeding and Genomics Interventions for Developing *Ascochyta* Blight Resistant Grain Legumes”. In: *International Journal of Molecular Sciences* 23.4. MAG ID: 4213178760, pp. 2217–2217. DOI: 10.3390/ijms23042217.
- Jha, Uday C. et al. (2022b). “Breeding and Genomics Interventions for Developing *Ascochyta* Blight Resistant Grain Legumes”. In: *International Journal of Molecular Sciences* 23.4. ISSN: 14220067. DOI: 10.3390/ijms23042217.
- Kaiser, Walter J. (1997). “Inter- and intranational spread of *ascochyta* pathogens of chickpea, faba bean, and lentil”. In: *Canadian Journal of Plant Pathology* 19.2, pp. 215–224. ISSN: 17152992. DOI: 10.1080/07060669709500556.
- Kaur, Livinder, Varinder P. Singh, and Anil K. Gupta (2012). “Peroxidase: a marker for *Ascochyta* blight resistance in chickpea”. In: *Archives of Phytopathology and Plant Protection* 45.1. ISBN: 0323540090, pp. 42–46. ISSN: 03235408. DOI: 10.1080/03235400903392804.
- Kimber, Rohan (2003). *AB chickpea rating scale*.

- Li, Yongle et al. (2017). "Genome analysis identified novel candidate genes for ascochyta blight resistance in chickpea using whole genome re-sequencing data". In: *Frontiers in Plant Science* 8.March, pp. 1–13. ISSN: 1664462X. DOI: 10.3389/fpls.2017.00359.
- Mahlein, Anne-Katrin (2016). "Present and Future Trends in Plant Disease Detection". In: *Plant Disease* 100.2. arXiv: 1011.1669v3 ISBN: 9780874216561, pp. 1–11. ISSN: 0717-6163. DOI: 10.1007/s13398-014-0173-7.2.
- Manjunatha, L. et al. (2018). "Present status on variability and management of Ascochyta rabiei infecting chickpea". In: *Indian Phytopathology* 71.1. Publisher: Springer India ISBN: 0123456789, pp. 9–24. ISSN: 22489800. DOI: 10.1007/s42360-018-0002-6. URL: <https://doi.org/10.1007/s42360-018-0002-6>.
- McCredde, J. et al. (2018). "Changes in farming practices impact on spore release patterns of the blackleg pathogen, *Leptosphaeria maculans*". In: *Crop and Pasture Science* 69.1, pp. 1–8. ISSN: 18365795. DOI: 10.1071/CP16404.
- Mehmood, Yasir et al. (2017). "Evidence and consequence of a highly adapted clonal haplotype within the Australian ascochyta rabiei population". In: *Frontiers in Plant Science* 8.June. ISSN: 1664462X. DOI: 10.3389/fpls.2017.01029.
- Mutka, Andrew M. and Rebecca S. Bart (2015). "Image-based phenotyping of plant disease symptoms". In: *Frontiers in Plant Science* 5.JAN, pp. 1–8. ISSN: 1664462X. DOI: 10.3389/fpls.2014.00734.
- Newman, Toby E. et al. (2021). "Identification of novel sources of resistance to ascochyta blight in a collection of wild cicer accessions". In: *Phytopathology* 111.2, pp. 369–379. ISSN: 19437684. DOI: 10.1094/PHYTO-04-20-0137-R.
- Niks, R.E. et al. (Mar. 2019). *Breeding crops with resistance to diseases and pests*. The Netherlands: Wageningen Academic Publishers. ISBN: 978-90-8686-328-0. DOI: 10.3920/978-90-8686-882-7. URL: <https://www.wageningenacademic.com/doi/book/10.3920/978-90-8686-882-7>.
- Pande, S. et al. (2005). "Ascochyta blight of chickpea (*Cicer arietinum* L.): a review of biology, pathogenicity, and disease management". In: *Australian Journal of Agricultural Research* 56.4, p. 317. ISSN: 0004-9409. DOI: 10.1071/AR04143. URL: <http://www.publish.csiro.au/?paper=AR04143>.
- Papoutsoglou, Evangelia A. et al. (2020). *Enabling reusability of plant phenomic datasets with MIAPPE 1.1*. Publication Title: New Phytologist ISSN: 0028-646X. ISBN: 0000000327640. DOI: 10.1111/nph.16544.
- Piepenbring, M. (2015). *File:04 03 53 asexual forms, Coelomycetes, Pleosporales, Ascomycota (M. Piepenbring).png - Wikimedia Commons*. URL: [https://commons.wikimedia.org/wiki/File:04_03_53_asexual_forms,_Coelomycetes,_Pleosporales,_Ascomycota_\(M._Piepenbring\).png](https://commons.wikimedia.org/wiki/File:04_03_53_asexual_forms,_Coelomycetes,_Pleosporales,_Ascomycota_(M._Piepenbring).png) (visited on 02/18/2020).
- PIRSA (2019). "Farm Gross Margin and Enterprise Planning Guide". In: URL: https://pir.sa.gov.au/primary_industry/industry_support/farm_gross_margins_and_enterprise_planning_guide.

- Pulse Australia (2015). *APB Chickpea ascochyta blight*. URL: <http://www.pulseaus.com.au/growing-pulses/bmp/chickpea/ascochyta-blight> (visited on 01/10/2020).
- (2019). “2019 season fungicide guide”. In: URL: <http://pulseaus.com.au/growing-pulses/bmp/chickpea/2019-season-fungicide-guide> (visited on 01/22/2020).
- Rawal, V. and D. K Navarro (2019). *The Global Economy of Pulses*. Issue: September 2016. Rome: FAO. ISBN: 978-92-5-109730-4.
- Rebetzke, G. J. et al. (2019). “Review: High-throughput phenotyping to enhance the use of crop genetic resources”. In: *Plant Science* 282. June 2018. Publisher: Elsevier, pp. 40–48. ISSN: 18732259. DOI: 10.1016/j.plantsci.2018.06.017. URL: <https://doi.org/10.1016/j.plantsci.2018.06.017>.
- Reddy, M. V. (1984). “Evaluation of a World Collection of Chickpea Germ Plasm Accessions for Resistance to Ascochyta Blight”. In: *Plant Disease* 68.10, p. 900. ISSN: 0191-2917. DOI: 10.1094/pd-69-900.
- Saint Cast, Clément et al. (Jan. 2022). “Connecting plant phenotyping and modelling communities: lessons from science mapping and operational perspectives”. en. In: *in silico Plants* 4.1. Ed. by Steve Long, diac005. ISSN: 2517-5025. DOI: 10.1093/insilicoplants/diac005. URL: <https://academic.oup.com/insilicoplants/article/doi/10.1093/insilicoplants/diac005/6570881> (visited on 07/20/2022).
- Sharma, Mamta and Raju Ghosh (2016). “An update on genetic resistance of chickpea to ascochyta blight”. In: *Agronomy* 6.1. ISSN: 20734395. DOI: 10.3390/agronomy6010018.
- Shtienberg, D. et al. (2006). “Optimisation of the chemical control of ascochyta blight in chickpea”. In: *Australasian Plant Pathology* 35.6, pp. 715–724. ISSN: 08153191. DOI: 10.1071/AP06069.
- Simko, Ivan, Jose A. Jimenez-Berni, and Xavier R.R. Sirault (2017). “Phenomic approaches and tools for phytopathologists”. In: *Phytopathology* 107.1, pp. 6–17. ISSN: 0031949X. DOI: 10.1094/PHT0-02-16-0082-RVW.
- Singh, K. B. (1981). “Resistance in Chickpeas to *Ascochyta rabiei*”. In: *Plant Disease* 65.7, p. 586. ISSN: 0191-2917. DOI: 10.1094/PD-65-586. URL: http://www.apsnet.org/publications/PlantDisease/BackIssues/Documents/1981Abstracts/PD_65_586.htm.
- Singh, K. B. and M. V. Reddy (May 1993). “Sources of resistance to ascochyta blight in wild Cicer species”. In: *Netherlands Journal of Plant Pathology* 99.3, pp. 163–167. ISSN: 00282944. DOI: 10.1007/BF01974268. URL: <http://link.springer.com/10.1007/BF01974268>.
- Singh, Mohar et al. (2015). “Exploitation of wild annual Cicer species for widening the gene pool of chickpea cultivars”. In: *Plant Breeding* 134.2, pp. 186–192. ISSN: 14390523. DOI: 10.1111/pbr.12254.
- Slpfeifer (2013). *File:Spring Black Stem Disease Cycle.jpg - Wikipedia*. URL: https://en.m.wikipedia.org/wiki/File:Spring_Black_Stem_Disease_Cycle.jpg (visited on 02/19/2020).

- Sperschneider, Jana (2019). "Machine learning in plant–pathogen interactions: empowering biological predictions from field scale to genome scale". In: *New Phytologist*. ISSN: 14698137. DOI: 10.1111/nph.15771.
- Tardieu, François et al. (2017). "Plant Phenomics, From Sensors to Knowledge". In: *Current Biology* 27.15, R770–R783. ISSN: 09609822. DOI: 10.1016/j.cub.2017.05.055.
- Trapero-Casas, A. (1992). "Development of *Didymella rabiei*, the Teleomorph of *Ascochyta rabiei*, on Chickpea Straw". In: *Phytopathology* 82.11, p. 1261. ISSN: 0031949X. DOI: 10.1094/Phyto-82-1261. URL: http://www.apsnet.org/publications/phytopathology/backissues/Documents/1992Abstracts/Phyto82_1261.htm.
- Upadhyaya, Hari D. et al. (2011). "Genomic tools and germplasm diversity for chickpea improvement". In: *Plant Genetic Resources: Characterisation and Utilisation* 9.1. ISBN: 1479262110, pp. 45–58. ISSN: 14792621. DOI: 10.1017/S1479262110000468.
- Varshney, Rajeev K. et al. (2019). "Resequencing of 429 chickpea accessions from 45 countries provides insights into genome diversity, domestication and agronomic traits". In: *Nature Genetics* 51.5. Publisher: Springer US ISBN: 4158801904013, pp. 857–864. ISSN: 15461718. DOI: 10.1038/s41588-019-0401-3. URL: <http://dx.doi.org/10.1038/s41588-019-0401-3>.
- Varshney, Rajeev K. et al. (2021). "A chickpea genetic variation map based on the sequencing of 3,366 genomes". In: *Nature* 599.7886, pp. 622–627. ISSN: 14764687. DOI: 10.1038/s41586-021-04066-1.
- Vega, Marcelino Perez de la (Sept. 2011). *Genetics, Genomics and Breeding of Cool Season Grain Legumes*. CRC Press. ISBN: 978-1-4398-8339-6. DOI: 10.1201/b11407. URL: <https://www.taylorfrancis.com/books/9781439883396>.
- Von Wettberg, Eric J.B. et al. (2018). "Ecology and genomics of an important crop wild relative as a prelude to agricultural innovation". In: *Nature Communications* 9.1. ISBN: 4146701802867. ISSN: 20411723. DOI: 10.1038/s41467-018-02867-z.
- Walter, James et al. (2019). "High-throughput field imaging and basic image analysis in a wheat breeding programme". In: *Frontiers in Plant Science* 10.April, pp. 1–12. ISSN: 1664462X. DOI: 10.3389/fpls.2019.00449.
- Weigand, F. et al. (Mar. 1986). "Accumulation of phytoalexins and isoflavone glucosides in a resistant and a susceptible cultivar of *Cicer arietinum* during infection with *Ascochyta rabiei*". In: *Journal of Phytopathology* 115.3, pp. 214–221. ISSN: 0931-1785. DOI: 10.1111/j.1439-0434.1986.tb00879.x. URL: <http://doi.wiley.com/10.1111/j.1439-0434.1986.tb00879.x>.
- Weiss, M., F. Jacob, and G. Duveiller (2020). "Remote sensing for agricultural applications: A meta-review". In: *Remote Sensing of Environment* 236.August 2019. Publisher: Elsevier, p. 111402. ISSN: 00344257. DOI: 10.1016/j.rse.2019.111402. URL: <https://doi.org/10.1016/j.rse.2019.111402>.
- Zhang, Chongyuan, Weidong Chen, and Sindhuja Sankaran (2019). "High-throughput field phenotyping of *Ascochyta* blight disease severity in chickpea". In: *Crop*

Protection 125.March. Publisher: Elsevier Ltd, p. 104885. ISSN: 02612194. DOI: 10.1016/j.cropro.2019.104885. URL: <https://doi.org/10.1016/j.cropro.2019.104885>.

Çağırğan, M. İlhan et al. (2011). "Assessment of endogenous organic acid levels in Ascochyta blight [*Ascochyta rabiei* (Pass.) Labr.] susceptible and resistant chickpeas (*Cicer arietinum* L.)" In: *Turkish Journal of Field Crops* 16.2, pp. 121–124. ISSN: 13011111.

Chapter 2

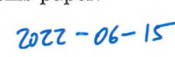
Literature review: Sensor-based phenotyping of above-ground plant-pathogen interactions

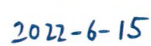
2.1 Declarations

Statement of Authorship

Title of Paper	Sensor-based phenotyping of above-ground plant-pathogen interactions
Publication Status	Published
Publication Details	Tanner, F. et al. (2022). "Sensor-based phenotyping of above-ground plant-pathogen interactions". In: Plant Methods 18.1, pp. 1–18. ISSN: 17464811. DOI: https://doi.org/10.1186/s13007-022-00853-7

Principal Authors

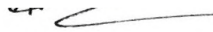

Name of Shared First Author	Florian Tanner
Contribution to the Paper by the Candidate	Conception, Knowledge, Drafting. Performed literature review, wrote manuscript and acted as corresponding author. 300 total estimated research hours.
Overall percentage	35%
Certification	This paper reports on original research I conducted during the period of my Higher Degree by Research candidature and is not subject to any obligations or contractual agreements with a third party that would constrain its inclusion in this thesis. I am the co-primary author of this paper.
Signature	
Date	2022-06-15

Name of Shared First Author	Sebastian Tonn
Contribution to the Paper	Conception, Knowledge, Drafting. Performed literature review and wrote manuscript.
Overall percentage	35%
Signature	
Date	2022-6-15

Co-Author Contributions

By signing the Statement of Authorship, each author certifies that:

- the candidate's stated contribution to the publication is accurate (as detailed above);
- permission is granted for the candidate to include the publication in the thesis; and
- the sum of all co-author contributions is equal to 100% less the candidate's stated contribution.

Name of Co-Author	Jos de Wit
Contribution to the Paper	Conception and Review of Manuscript
Signature	
Date	23-06-2022
Name of Co-Author	Guido Van den Ackerveken
Contribution to the Paper	Conception and Review of Manuscript
Signature	
Date	
Name of Co-Author	Bettina Berger
Contribution to the Paper	Conception and Review of Manuscript
Signature	Digitally signed by Bettina Berger
Date	DN: cn=Bettina Berger, o, ou, email=bettina.berger@adelaide.edu.au, c=AU Date: 2022.06.15 16:25:01 +09'30'
Name of Co-Author	Darren Plett
Contribution to the Paper	Conception and Review of Manuscript
Signature	
Date	27-06-2022

2.2 Literature review

Tanner *et al. Plant Methods* (2022) 18:35
<https://doi.org/10.1186/s13007-022-00853-7>


Plant Methods

REVIEW

Open Access

Sensor-based phenotyping of above-ground plant-pathogen interactions



Florian Tanner^{1*}, Sebastian Tonn^{2†}, Jos de Wit³, Guido Van den Ackerveken², Bettina Berger¹ and Darren Plett¹

Abstract

Plant pathogens cause yield losses in crops worldwide. Breeding for improved disease resistance and management by precision agriculture are two approaches to limit such yield losses. Both rely on detecting and quantifying signs and symptoms of plant disease. To achieve this, the field of plant phenotyping makes use of non-invasive sensor technology. Compared to invasive methods, this can offer improved throughput and allow for repeated measurements on living plants. Abiotic stress responses and yield components have been successfully measured with phenotyping technologies, whereas phenotyping methods for biotic stresses are less developed, despite the relevance of plant disease in crop production. The interactions between plants and pathogens can lead to a variety of signs (when the pathogen itself can be detected) and diverse symptoms (detectable responses of the plant). Here, we review the strengths and weaknesses of a broad range of sensor technologies that are being used for sensing of signs and symptoms on plant shoots, including monochrome, RGB, hyperspectral, fluorescence, chlorophyll fluorescence and thermal sensors, as well as Raman spectroscopy, X-ray computed tomography, and optical coherence tomography. We argue that choosing and combining appropriate sensors for each plant-pathosystem and measuring with sufficient spatial resolution can enable specific and accurate measurements of above-ground signs and symptoms of plant disease.

Keywords: Plant disease, Phenotyping, Imaging sensors, Plant-pathogen interactions, Biotic stress, Signs and symptoms

Background

Worldwide yield losses in major crops due to pathogens and pests are estimated to be 17–30% [1]. In this review, we will focus on plant pathogens, i.e., organisms or biotic agents that can cause disease [2] and not on pests such as insects and nematodes. Plant pathogens belong to various taxa including viroids, viruses, phytoplasmas, bacteria, oomycetes and fungi [3]. When a pathogen interacts with a plant, structural, physical, and biochemical changes can occur in both the plant and the pathogen. Depending on plant genotype, pathogen strain, and environmental

conditions, the outcome of plant-pathogen interactions (PPI) may be disease, a physiological disturbance of the plant [3–5].

Disease resistance breeding and precision agriculture are key strategies to reduce yield losses due to plant disease in a sustainable way. Both rely on detection, identification and quantification of plant disease on various scales. In disease resistance breeding and pre-breeding, PPI are examined at the cell, tissue, whole plant and field plot level. Zooming in to the cell or tissue level can uncover the distinct mechanisms that determine plant resistance or susceptibility, and precise quantification of disease or resistance levels in whole plants or field plots aids the selection of the best genotypes. In precision agriculture, early and precise disease detection in the field enables efficient crop protection, e.g. by targeted

*Correspondence: florian.tanner@adelaide.edu.au

†Florian Tanner and Sebastian Tonn contributed equally to this work

¹ Australian Plant Phenomics Facility, School of Agriculture, Food and Wine, University of Adelaide, Urrbrae, SA, Australia
 Full list of author information is available at the end of the article



© The Author(s) 2022. **Open Access** This article is licensed under a Creative Commons Attribution 4.0 International License, which permits use, sharing, adaptation, distribution and reproduction in any medium or format, as long as you give appropriate credit to the original author(s) and the source, provide a link to the Creative Commons licence, and indicate if changes were made. The images or other third party material in this article are included in the article's Creative Commons licence, unless indicated otherwise in a credit line to the material. If material is not included in the article's Creative Commons licence and your intended use is not permitted by statutory regulation or exceeds the permitted use, you will need to obtain permission directly from the copyright holder. To view a copy of this licence, visit <http://creativecommons.org/licenses/by/4.0/>. The Creative Commons Public Domain Dedication waiver (<http://creativecommons.org/publicdomain/zero/1.0/>) applies to the data made available in this article, unless otherwise stated in a credit line to the data.

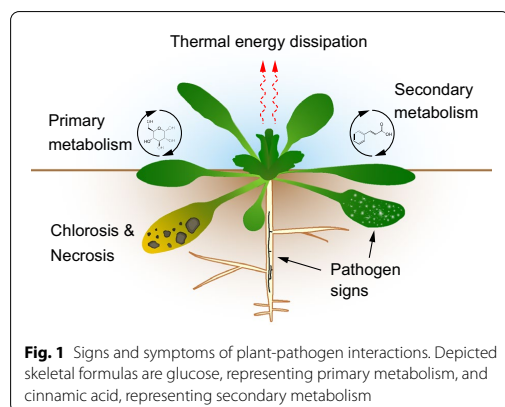
pesticide application or eradication of diseased plants. The challenge to detect and quantify plant disease in an unbiased and precise way initiated the field of plant disease phenotyping [6–8].

In general, “plant phenotyping” describes the study of the manifestation of a genotype under specific environmental conditions [9]. In the context of PPI the phenotype consists of changes that can be described as contrasting indications of disease: signs and symptoms. Whereas these terms were originally used for changes that are visible to the human eye, here we will use them also for changes that can be detected by non-invasive sensors.

Following the American Phytopathological Society (APS) Illustrated Glossary of Plant Pathology, a “symptom” is an indication of disease by reaction of the host [2]. These plant reactions include changes to pigmentation (e.g. necrosis, chlorosis), primary and secondary metabolism, and thermal energy dissipation (Fig. 1). A “sign” is an indication of disease from direct observation of a pathogen or its parts (e.g. sporulation, formation of fruiting bodies, mycelium, bacterial ooze) [2].

While the signs and symptoms are specific for each plant-pathosystem and influenced by environmental conditions, we classify them by their shared characteristics for this review. In practice, signs and symptoms most often do not appear in isolation but occur simultaneously. For example, chlorosis, necrosis, and sporulation may successively co-occur in the same area of an infected leaf.

Phenotyping of PPI can be addressed with invasive methods. For example, colonization of a plant leaf by a pathogen can be detected, classified and quantified by quantitative polymerase chain reaction (qPCR) or for bacterial pathogens by measuring colony-forming units in a homogenate. Such invasive methods can be precise and objective. However, they are necessarily destructive



and limited in speed and scalability, limitations that can be overcome by non-invasive sensors.

Non-invasive sensing offers the possibility of time-course measurements, higher throughput and lower costs [8, 10, 11]. The classic approach for non-invasive phenotyping is visual inspection by humans. This can yield precise and accurate estimates if raters are well trained and appropriate scales are used. However, visual estimates are prone to subjectivity, offer limited speed and scalability, are often qualitative rather than truly quantitative, and are innately limited to the visible spectrum of light [12]. Sensor-based non-invasive phenotyping has the potential to increase throughput and precision, and can detect disease signs and symptoms that are invisible to the human eye [7]. Essentially, non-invasive sensors capture the changes in interactions between electromagnetic radiation and matter (Fig. 2).

The most established sensors for non-invasively measuring PPI are red–green–blue (RGB), hyperspectral, thermal, and fluorescence sensors (Table 1). Less often, monochrome sensors, Raman spectroscopy, and tomographic sensors have been used [6, 13–16].

By focusing here on the biological aspects of disease phenotyping, namely the signs and symptoms, we highlight the sensor-based technologies that are most suitable for specific plant-pathosystems. We group the signs and symptoms into five generalised categories (Fig. 1 and Table 2) to illustrate the common biological processes that underlie sensor-detected signals, to highlight similarities between different plant-pathosystems and to

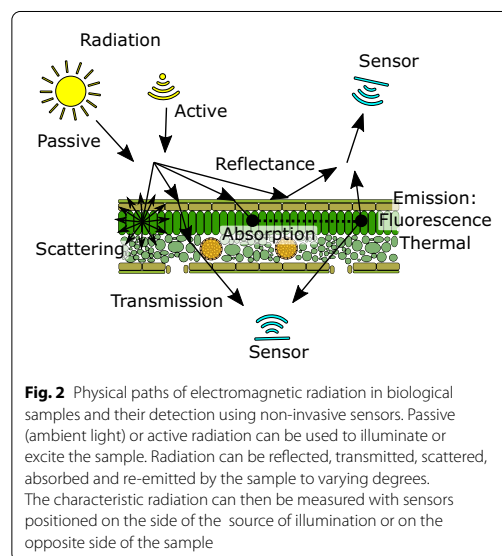


Table 1 Summary of sensors that have been used for phenotyping PPI

Sensor, technology	Imaging/non-imaging	Active/passive	Effect measured	Excitation/illumination wavelengths	Measured wavelengths
Monochrome	Imaging	Mainly active	Reflectance	Variable	Variable
RGB	Imaging	Mainly active, passive at large scale	Reflectance	Variable, usually visible spectrum	Range: ~400–700 nm R: ~600 nm G: ~530 nm B: ~460 nm
Hyperspectral	Both	Mainly active, passive at large scale	Reflectance, transmission	Variable	400–2500 nm
Thermal	Mainly imaging	Passive	Emission	NA	8–15 μ m
Chlorophyll fluorescence (kinetics)	Imaging/non-imaging	Active	Emission	400–700 nm	~650–800 nm
Fluorescence	Imaging/non-imaging	Active	Emission	Mostly 300–400 nm	Mainly 400–700 nm
Raman spectroscopy	Non-imaging	Active	Inelastic scattering of photons (Raman scattering)	Variable, often 785–830 nm [17]	Raman bands, 400–2133 cm^{-1} [18]
Optical coherence tomography	Imaging	Active	Reflectance of coherent light	800–1000 nm or 1200–1400 nm	800–1000 nm or 1200–1400 nm
X-ray computed tomography	Imaging	Active	Attenuation, phase shift	~0.01–0.1 nm	Visible light using scintillator

thereby point out possibilities to transfer and adapt phenotyping solutions (Table 3).

Signs, symptoms and sensors

Pathogen signs

After successful infection, plant pathogens propagate on or inside their host plant, either by rapid replication (e.g. bacteria, viruses) or mycelial growth (fungi, oomycetes) [4]. Quantifying the pathogen, based on signs like spores or mycelium, is a direct measure of plant resistance, defined in a strict sense as the ability of the host to restrict pathogen growth [19]. When a pathogen grows on the surface of the plant, sensors that directly capture the optical changes caused by its physical presence can be used for non-invasive measurement (Table 3).

Powdery mildews are surface-colonizing pathogens representing a variety of obligate biotrophic fungi that can cause disease on various host plants. Growing on the surface, these fungi only penetrate epidermal cells and use haustoria to acquire nutrients. RGB imaging was successfully applied to quantify pathogen signs both for grapevine powdery mildew (*Erysiphe necator*) and cereal powdery mildew infection (*Blumeria graminis* spp.) [20, 21]. In both studies, mycelial growth on detached leaf pieces was imaged in automated phenotyping systems. For grapevine powdery mildew, this system included a movable stage and a DSLR camera [20]. For cereal powdery mildew, a monochrome charge-coupled device (CCD) camera was combined with narrow-bandwidth illumination and a robotic arm system. The

best correlation to visual estimates of infected area was achieved with a simple segmentation algorithm that uses the minimum of the three RGB values [21]. While the throughput of imaging can be easily increased compared to visual scoring for both cereal powdery mildew and grapevine powdery mildew, the preparation of leaf samples remains a bottleneck for these plant-pathosystems.

Unlike powdery mildews, many other filamentous pathogens like fungi and oomycetes form signs on the surface of the host only at the end of the disease cycle, in the form of spore bearing structures. Sporulation of *Cercospora beticola*, a polycyclic necrotrophic ascomycete fungus, occurs on the leaves of infected sugar beet in the area of the necrotic lesions. Hyperspectral microscopy was used to show that sporulation is correlated to an overall decrease in reflectance in the area of lesions in the spectral range of 400–900 nm [22]. However, the advantage of hyperspectral images over RGB images in this study is unclear since the proposed trait is the difference of the integral of reflectance over the entire spectral range of the camera. It would be interesting to know whether the difference in reflectivity over a narrower wavelength range (e.g. one of the RGB channels) could match or improve the quantification of fungal sporulation.

An RGB flatbed scanner was used to assess the interaction between a panel of 335 wheat cultivars and *Mycosphaerella graminicola* (Septoria tritici blotch) [23]. Leaves were collected from a field trial with natural infection and scanned. From the scans the density, size and

Table 2 Applications of sensor-based phenotyping of PPI

Sign/symptom	Plant	Pathogen	Sensor / Vector	Scale	Reference
Pathogen signs	<i>Arabidopsis thaliana</i> , <i>Hordeum vulgare</i>	<i>Fusarium graminearum</i> expressing GFP	Zeiss Stemi-C dissecting microscope with a 470 nm excitation filter and 535 nm emission filter	Whole plants (At), detached spikes (Hv)	[26]
	<i>Beta vulgaris</i> L.	<i>Cercospora beticola</i>	Hyperspectral microscope (PFD V10E), motorized stage	Individual lesions	[22]
	Cereals	<i>Blumeria graminis</i>	Monochrome CCD sensor, 4 channels captured	'Macrobot', robotic arm	[21]
	<i>Nicotiana benthamiana</i>	<i>Phytophthora infestans</i> expressing RFP	Monochrome camera with filter wheel and excitation lights (Patho-Screen imaging system, Phenovation, the Netherlands)	Detached leaves	[28]
	<i>Nicotiana tabacum</i>	<i>Tobacco mosaic virus</i> expressing GFP	RGB camera under UV illumination (Blak-Ray Model B 100AP)	Detached leaves	[27]
	<i>Phaseolus vulgaris</i>	<i>Pseudomonas syringae</i> pv. <i>phaseolicola</i> expressing <i>lux-eYFP</i> operon	nightOWL LB 983 in vivo imaging system (Berthold Technologies, Germany), confocal laser scanning microscope Zeiss LSM 880	Detached leaves	[34]
	<i>Triticum aestivum</i> L.	<i>Fusarium graminearum</i>	X-ray CT, Biomedical Imaging and Therapy beamline (BM10, 05B1.1)	Spikelet	[114]
<i>Vitis</i> spp.	<i>Erysiphe necator</i>	RGB (Nikon D850), automated motorized stage	Individual leaf discs, automated imaging	[20]	
Primary metabolism	<i>Arabidopsis thaliana</i>	<i>Pseudomonas syringae</i>	CF Imager (Technologica Ltd, UK), NPQ, fPSII, Fv/Fm	Individual plants	[149]
	<i>Cucumis melo</i>	<i>Podosphaera xanthii</i>	Open FluorCam 700 MF (Photon System Instruments), NPQ, fPSII	Individual leaves	[54]
	<i>Hordeum vulgare</i>	<i>Blumeria graminis</i> f. sp. <i>hordei</i>	Chlorophyll Fluorometer IMAGING-PAM M-series (Walz, Germany)	Individual leaves	[150]
	<i>Lactuca sativa</i>	<i>Bremia lactucae</i>	Open FluorCam 700 MF (Photon System Instruments), Fv/Fm	Leaf discs	[151]
	<i>Nicotiana benthamiana</i>	Pepper mild mottle virus	FluorCam (Photon System Instruments), NPQ, fPSII	Individual leaves	[152]
	<i>Olea europaea</i>	<i>Xylella fastidiosa</i>	Micro-hyperspectral imager (VNIR model, Headwall Photonics, USA), 400–885 nm, from aircraft 500 m above ground	Orchards	[48]
	<i>Oryza sativa</i>	<i>Rhizoctonia solani</i>	Non-imaging NeoSpectra micro handheld spectrometer (SiWare Systems, Canada), 1348–2551 nm	Individual leaf spots (non-imaging)	[61]
	<i>Solanum tuberosum</i>	<i>Phytophthora infestans</i> , <i>Alternaria solani</i>	Non-imaging field spectrometer SVC HR-1024i (350–2500 nm) (Spectra Vista Corporation, USA)	Individual leaf spots (non-imaging)	[153]

Table 2 (continued)

Sign/symptom	Plant	Pathogen	Sensor / Vector	Scale	Reference
Secondary metabolism	<i>Beta vulgaris</i>	<i>Cercospora beticola</i>	SWIR spectral camera, 970–2500 nm (HySpex SWIR-320 m-e line camera, Norsk Elektro Optikk A/S, Norway)	Detached leaves	[154]
	<i>Citrus sinensis</i> , <i>Citrus paradisi</i>	<i>Candidatus Liberibacter</i> spp.	Non-imaging handheld Raman spectrometer (Resolve spectrometer equipped with 831-nm laser source, Agilent, USA)	Detached leaves	[86, 87, 90]
	<i>Hordeum vulgare</i>	<i>Blumeria graminis f.sp. hordei</i>	UV line scanner, 250–500 nm (Head-wall Photonics)	Detached leaves	[81]
	<i>Nicotiana benthamiana</i>	Pepper mild mottle virus	Excitation with xenon-lamp + BP 340/75, imaging with CCD camera + BP 440/20 and BP 520/20	Individual leaves	[152]
	<i>Triticum aestivum</i>	<i>Puccinia triticina</i> , <i>Blumeria graminis f. sp. tritici</i>	Non-imaging fiber-optic fluorescence spectrometer (IOM GmbH, Germany) combined with 337 nm pulsed N2 laser	Individual leaf spots (non-imaging)	[73]
	<i>Vitis vinifera</i>	<i>Plasmopara viticola</i>	Macroscope (AZ100 multizoom, Nikon), ex. BP 340/26 and em. LP 371	Leaf parts	[69]
Necrosis and chlorosis	<i>Arabidopsis thaliana</i>	<i>Pseudomonas syringae</i>	RGB (Nikon D5200 DSLR)	Seedlings growing in well-plates	[117]
	<i>Arabidopsis thaliana</i>	<i>Sclerotinia sclerotiorum</i>	RGB (USB camera, full HD 1080p) controlled by Raspberry Pi 3 Model B motherboards	Detached leaves	[115]
	<i>Beta vulgaris</i>	<i>Cercospora beticola</i>	RGB (camera Baumer HXG-40), multi-spectral camera (6 bands of 10 nm between 450 and 850 nm, AIRPHEN)	Phenobile 1, 50 distance to canopy top (RGB), hexacopter (multispectral)	[119]
	<i>Triticum aestivum</i>	<i>Mycosphaerella graminicola</i>	RGB (flatbed scanner)	Detached leaves collected from field trial	[23]
	<i>Zea mays</i>	<i>Setosphaeria turcica</i>	RGB	Drone, 6 m above ground	[118, 120]

Table 2 (continued)

Sign/symptom	Plant	Pathogen	Sensor / Vector	Scale	Reference
Thermal energy dissipation	<i>Cucumis sativus</i> L.	<i>Fusarium oxysporum</i> f. sp. <i>cucumerinum</i>	FLIR SC620	Individual leaves	[123]
	<i>Ipomoea batatas</i> L.	Sweet potato feathery mottle virus (SPFMV), Sweet potato chlorotic stunt virus (SPCSV)	Top-view thermal camera (FLIR A615), PlantScreen conveyor system, NaPPI, Helsinki	Whole plant	[132]
	<i>Nicotiana tabacum</i> L.	Tobacco mosaic virus (TMV)	Infrared imager (Agema THV900LW), Cartesian positioning system in imaging chamber	Leaves	[131]
	<i>Olea europaea</i> L.	<i>Verticillium dahliae</i>	Temperature sensor (Apogee IRR-P), Fixed 1 m above canopy	Single tree canopy	[129]
	<i>Olea europaea</i> L.	<i>Verticillium dahliae</i>	Broad-band thermal camera (FLIR SC655) on crewed aircraft	3000 ha, spatial resolution = 62 cm	[130]
Structural changes	<i>Capsicum annuum</i>	<i>Stemphylium lycopersici</i>	Laboratory-OCT system, 4096-pixel line scan camera (spl4096-140 km, Basler)	Single leaves	[134]
	<i>Malus domestica</i>	<i>Marssonina coronaria</i>	Backpack-based OCT system, 2048-pixel line scan camera (spl2048-140 km, Basler, Germany)	Single leaves	[133]
	<i>Solanum tuberosum</i>	<i>Streptomyces scabies</i>	Medical X-ray CT scanner (Toshiba Xvision high-resolution CT scanner)	Single plants	[135]
	<i>Triticum aestivum</i>	<i>Fusarium graminearum</i>	Synchrotron-based phase contrast X-ray imaging with the Biomedical Imaging and Therapy beamline (BM15-BM16) at the Canadian Light Source	Single excised wheat spikes	[114]

Table 3 Suitability of sensors for phenotyping PPI

		RGB	Hyperspectral	Thermal	Fluorescence	Chlorophyll fluorescence (kinetics)	Raman spectroscopy	OCT	X-ray CT
Pathogen signs	Controlled	++	+	–	+	–	–	+	+
	Field	++	+	–	–	–	–	+	–
Primary metabolism	Controlled	–	+	–	–	++	+	–	–
	Field	–	+	–	–	++	+	–	–
Secondary metabolism	Controlled	–	+	–	+	–	+	–	–
	Field	–	+	–	+	–	+	–	–
Necrosis and chlorosis	Controlled	++	++	–	+	+	–	+	+
	Field	++	+	–	+	+	–	+	–
Thermal energy dissipation	Controlled	–	–	++	–	–	–	–	–
	Field	–	–	+	–	–	–	–	–

"Not used/unsuitable" (–), "Preliminary" (+) and "Widely used" (++)

melanisation of pycnidia (signs) as well as lesion size (a symptom) were measured. A Genome-Wide Association Study using the phenotypic data identified 26 chromosome intervals associated with *Septoria tritici* blotch resistance. Sixteen of these loci overlapped with intervals that had already been identified based on visual assessment in previous studies, while ten had not been described before, demonstrating the potential power of quantitative phenotyping [23]. This example also illustrates the benefit of a high resolution, e.g. being able to discriminate single pycnidia to determine density and size, thus overcoming the weakness of low spatial resolution of many field phenotyping methods.

Transgenic pathogen strains that express detectable markers such as fluorescent proteins or bioluminescence conferring enzymes are another alternative to track and quantify pathogen growth directly [24, 25]. Fluorescent proteins have mainly been used to study the infection process in vivo at the cell level using epi-fluorescence or fluorescence confocal laser scanning microscopy. But also at the level of whole plants or seedlings, pathogens expressing fluorescent proteins, including bacteria, fungi, oomycetes and viruses have been used to track, image and quantify infection and colonization [26–31]. Plant autofluorescence and low fluorescent protein signal intensity can hinder imaging at larger scales. Bioluminescence, so far mainly applied in bacteria, generates a light signal without prior excitation, therefore avoiding plant autofluorescence. But the low signal intensity requires imaging with sensitive cameras and extended exposure time in the dark (up to several minutes) [32, 33]. A recent study generated bioluminescent and fluorescent *Pseudomonas syringae* pv. *phaseolicola* [34]. The bioluminescence enabled detection of the bacteria at the leaf scale in a dedicated imaging chamber. Identified colonized plant parts

could then be sampled and further investigated under the fluorescence microscope making use of the expressed fluorescent proteins. Since enzymes producing bioluminescent compounds have also been identified in fungi, such a luminescence based approach might also be feasible to facilitate quantification and examination of fungal infection at the macro- and microscopic level [35]. But all these approaches are restricted by the requirement for both a protocol for genetic transformation of the pathogen of interest and for facilities authorized to carry out experiments with transgenic plant pathogens.

Symptom: changes in primary metabolism

In plant-pathogen interactions, the plant primary metabolism is influenced both by manipulation of the pathogen and the immune response of the plant itself. Pathogen infection may modify source-sink relations in the plant or impair photosynthesis, while plant immune responses require additional resources from the pool of primary metabolites [36–38]. Together this may lead to detectable symptoms based on photosynthetic performance or altered accumulation and allocation of primary metabolites.

Photosynthetic performance can be probed by analyzing chlorophyll *a* fluorescence and the kinetics of chlorophyll *a* fluorescence (Chl-F) [39, 40]. According to the model of photosystem II (PSII) absorbed light energy can take three different paths: (i) drive photosynthesis (photochemical quenching); (ii) dissipate as heat (non-photochemical quenching); (iii) re-emit as fluorescence [39, 41].

Measuring the kinetics of Chl-F, the changes of Chl-F under different light conditions, e.g. before and after a saturating light pulse, allows separation of these components and calculation of diverse parameters that yield information about photosystem II (PSII) photochemistry, electron flux, and CO₂ assimilation [39, 40]. Commonly

used parameters are the maximum quantum efficiency of PSII photochemistry (F_v/F_m), the operating efficiency of PSII photochemistry (F_q'/F_m' or $\Delta F/F_m$), the level of photochemical quenching of PSII (qP or F_q'/F_v') or the level of non-photochemical quenching (NPQ) which estimates the rate constant for heat loss from PSII [40].

With commercially available Chl-F kinetics imaging systems these parameters can be mapped onto imaged leaves or whole plants, enabling identification of spatial heterogeneity that may be linked to localized pathogen infection [42]. Many of the Chl-F parameters (e.g. F_v/F_m , qP, NPQ) are measured on dark-adapted plants and commonly require light sources in close proximity to the plant to provide e.g. a saturating pulse to measure maximum fluorescence (F_m). Therefore, most Chl-F imaging systems are designed for growth chambers or greenhouses where LED panels can provide even illumination and plants can easily be dark adapted [42]. However, there are also field phenotyping systems that include Chl-F imaging with active illumination [43]. Dark adaptation in the field can be achieved by imaging at night or before dawn. But because the sensor needs to be close to the plants, Chl-F imaging with active illumination in the field is limited to ground-based phenotyping platforms which offer limited throughput compared to uncrewed aerial vehicles (UAV).

Analysis of spectral reflectance under sunlight does not require active illumination and is therefore an alternative for probing photosynthesis that is compatible with aerial vectors like UAVs or aircrafts. Spectral reflectance data can be used to build predictive models for photosynthetic parameters like maximum carboxylation rate of Rubisco or to estimate sun-induced chlorophyll fluorescence [44–47]. For example, sun-induced chlorophyll fluorescence, determined from spectral images taken from an aircraft, has successfully been used to estimate disease severity of olive trees infected with the bacterium *Xylella fastidiosa* [48]. But these approaches are technically challenging, both in data acquisition and data analysis, and interpretation is difficult because the relationship of reflectance, canopy geometrical structure, leaf physiology and variation in solar radiation is not fully understood [47, 49, 50]. So far, these challenges limit applications, despite the potential especially for large scale remote sensing of plant stress.

Chlorophyll fluorescence imaging systems with active illumination on the other hand have been used in numerous studies to monitor the effect of pathogen infection on plants [42]. A common response, in many cases prior to visual changes, is the decrease of PSII resulting from a decreased PSII electron transport as well as an increased heat dissipation rate (NPQ). This has also been observed for infections of many biotrophic pathogens like powdery

mildew of wheat and barley (*B. graminis*), powdery mildew of cucurbits (*Podosphaera xanthii*), downy mildew of lettuce (*Bremia lactucae*) and downy mildew of grapevine (*Plasmopara viticola*) [51–54]. These biotrophic pathogens often induce visible symptoms only at late infection stages, thus Chl-F imaging may be particularly useful to visualize and quantify early colonization.

A general drawback of Chl-F imaging is the lack of specificity as photosynthesis and Chl-F are influenced by many biotic and abiotic stress factors alike [55]. This could be partially overcome by taking into account the differences in spatial patterns of Chl-F changes. Patterns induced by localized pathogen infection might be distinguishable from patterns induced by abiotic stresses that affect the whole plant.

While Chl-F provides information about the current productivity of the plant, it does not allow for quantification of the actual concentration of primary metabolites. Changes in accumulation and allocation of sugars, starch, amino acids or proteins can, in principle, also be estimated directly via reflectance spectroscopy or imaging spectroscopy in the visible (VIS, 400–700 nm), near-infrared (NIR, 700–1000 nm) and shortwave infrared (SWIR, 1000–2500 nm) range [56–58]. Such approaches are based on combining non-invasive spectroscopic measurements with biochemical analysis of the same tissue to build predictive models. For example, Ely et al. [56] developed spectra-trait models for leaf starch, glucose, and protein content based on reflectance spectroscopy (500–2400 nm) and biochemical analysis of leaves of eight crop species. However, the usefulness of such models for linking spectral features to metabolic changes during PPI still requires validation.

So far, studies only indicate that reflectance spectroscopy may sense specific changes in primary metabolism during PPI. Gold et al. [59] collected reflectance spectra (400–2400 nm) with a portable non-imaging contact spectrometer from potato leaves at different infection stages of *Phytophthora infestans* or *Alternaria solani*. Using spectra-trait models they estimated pathogen-induced changes in leaf sugar, starch and nitrogen concentration and found increased sugar concentration during the biotrophic, necrotrophic and sporulation phase of *P. infestans*. But these estimates were not validated by chemical analysis and the applied spectra-trait models were originally developed on data from forests and grasslands [60]. Although the study shows clear differences in reflectance spectra between tissue infected with the different pathogens and tissue at different infection stages, the interpretation of these spectral differences remains unclear.

A similar study in rice with healthy and sheath blight (*Rhizoctonia solani*) affected plants found that differential

spectral regions could be linked to absorption features of starch, cellulose and protein content, although they were not chemically validated [57, 61].

Both of these studies used non-imaging spectrometers and found spectral features in the SWIR range to be important for detection of diseased plant tissue. Therefore, imaging SWIR sensors might be particularly useful to not only measure changes to primary metabolites but also to provide spatial information on these changes.

Symptom: changes in secondary metabolism

Plant secondary metabolites (PSM) are a large group of structurally and functionally diverse metabolites that are, as opposed to primary metabolites, considered non-essential for primary functions like photosynthesis, growth and reproduction [62, 63]. Those PSM that are involved in plant immunity are commonly classified into two groups, phytoanticipins and phytoalexins [64]. While phytoanticipins are constitutively produced and stored in plant tissue, phytoalexins are synthesized in response to a pathogen. Members of both groups show *in vitro* antimicrobial and insect-deterrent activity [65].

Independent of their function, PSM can be informative markers for preformed resistance (phytoanticipins), or a symptom of the infection progress, and magnitude or quality of the plant immune response (phytoalexins). Due to their specific absorption and, in some cases, fluorescence spectra they may be detected non-invasively, e.g. by reflectance and fluorescence spectroscopy or imaging [57, 66].

In grapevine, infection with the downy mildew pathogen *Plasmopara viticola* induces the accumulation of stilbenes, a group of phenolic compounds [67]. Pure stilbenes emit a violet-blue fluorescence around 400 nm when excited with UV light (335 nm) [68]. A fluorescence signal with a similar spectrum was imaged in downy mildew infected grapevine leaves at the cell level using confocal laser scanning microscopy, as well as at the tissue level using epifluorescence microscopy [68–70]. Mass spectrometry imaging revealed co-localization of stilbenes with the violet-blue fluorescence signal, suggesting that stilbenes are indeed the source or at least contribute to the observed fluorescence [70]. Since stilbene synthase expression has also been linked to downy mildew resistance, the violet-blue fluorescence may not only enable detection and quantification of downy mildew infection but also allow for the assessment of differences in plant defense responses [71].

Blue (around 440 nm) and green (around 520 nm) fluorescence upon UV excitation has also been described in *Nicotiana benthamiana* infected with Pepper mild mottle virus, likely due to accumulation of the phenolic compound chlorogenic acid, and in wheat infected with leaf

rust (*Puccinia triticina*) or powdery mildew (*Blumeria graminis* f. sp. *Tritici*) [72, 73].

These examples indicate that changes in UV-excited blue and green fluorescence, induced by certain pathogens, is a conserved response across plant species. In fact, it has been described as a general conserved stress response, also to abiotic stresses including drought, nutrient deficiencies and increased UV irradiation [74–77]. Responsible fluorophores in most cases are likely stress-induced soluble and cell wall bound phenolic compounds that fluoresce in the blue-green spectrum [78]. For example, the fluorescent stilbenes accumulate in grapevine leaves also in response to prolonged UV-C irradiation [70]. Consequently, distinction between infections of different pathogens, or between biotic and abiotic stress, might not be possible. This is a critical limitation for phenotyping in field trials, where various stresses can occur simultaneously.

Plant secondary metabolite content of leaves may also be estimated via reflectance spectroscopy [79, 80]. Spectral indices or models for leaf traits like phenolic content have been mostly developed and validated for remote sensing in landscape ecology studies [60, 79]. For example, Kokaly and Skidmore [80] proposed that an absorption feature around 1660 nm is related to content of phenolic compounds in different plant species and showed that in fresh tea leaves (*Camellia sinensis*), this absorption feature correlates with total phenolic compound content.

Only a few studies have combined spectral measurements with biochemical analysis of diseased plants. This is required to link spectral features to physiological processes during PPI. Brugger et al. [81] explored spectral imaging in the UV range (250–400 nm), which is particularly interesting because many plant secondary metabolites involved in stress responses feature absorption maxima in that range. They found in barley infected with powdery mildew (*Blumeria graminis* f. sp. *hordei*) that changes in flavonoid content during the first 5 days of infection correlated with reflectance intensity around wavelengths that match flavonoid absorption spectra. But adverse interaction of the sensor with the required UV light source restrains interpretation of these results. Another study combined spectral imaging in the SWIR range (970–2500 nm) with untargeted metabolic fingerprinting of three different sugar beet genotypes infected with *Cercospora beticola* [82]. Although there were correlations between several secondary metabolites and spectral data, it remains unclear if this correlation is due to direct contribution of these metabolites to the reflectance spectrum. Combining imaging spectroscopy with mass spectrometry imaging could help to provide direct links between specific metabolite groups and spectral features.

Raman spectroscopy is another technology to measure changes in plant secondary metabolism. After excitation of the sample with a laser it measures the inelastic scattering of photons (also called Raman scattering), which can provide both qualitative and quantitative information about the chemical composition of the sample [15, 83]. Raman scattering can be collected with portable non-imaging handheld Raman spectrometers [84, 85] and this approach has been applied to detect viral, bacterial and fungal infections in plants [85–89]. For example, a handheld Raman spectrometer was used to detect *C. liberibacter* spp. infection in citrus trees. Using orthogonal partial least squares discriminant analysis, grapefruit leaves were classified into healthy, infected, and nutrient-deficient categories with 98% accuracy in the training set, but the authors did not validate the classification accuracy in a test set [86, 87]. Infection was associated with increased intensity of the Raman band assigned to lignin and phenolic compounds. Correspondingly, a follow-up study found increased *p*-coumaric acid content in infected leaves, a phenolic compound and lignin precursor whose Raman spectrum matches the disease associated bands [90]. Similar disease associated bands, likely corresponding to phenolic compounds, have also been described for virus infection in wheat, tomato and rose [15, 88, 91]. These studies used non-imaging Raman spectrometers, which only provide point measurements and do not yield any spatial information. But Raman spectroscopy can also be combined with digital imaging so that Raman spectra are recorded for each pixel [92]. This has been explored as a tool for quality and safety inspection in food, pharmaceutical, and biomedical sectors and, for example, to detect watermelon seeds infected by the bacteria *Acidovorax citrulli* [93, 94]. So far, the lengthy image acquisition has restricted the throughput and therefore applications of Raman imaging, but Lee et al. [94] report a relatively fast system that requires 250 s to image an area of five by twenty cm with a spatial resolution of 250 by 1024 pixels. Such systems may already be useful for certain phenotyping challenges, but further reducing the acquisition time would widen the range of possible applications.

Symptom: necrosis and chlorosis

Pathogen-induced chlorosis and necrosis are prominent symptoms of plant disease as they are visually evident and very common. Chlorosis results from changes in pigmentation, mainly the degradation of chlorophyll, and necrosis from the death of cells and tissue. Both may occur locally in lesions, with chlorosis often preceding or surrounding necrotic lesions. Viruses can cause chlorosis in diverse patterns that are often reflected in their name

(e.g. “chlorosis”, “mottle”, “mosaic”, “streak”, “vein clearing”, “yellowing”) [95].

Both chlorosis and necrosis can be induced by specific pathogen-produced metabolites or proteins, e.g. the chlorosis inducing coronatine from *Pseudomonas syringae* or the necrosis and ethylene-inducing peptide 1 (Nep1)-like proteins from *Botrytis cinerea* [96–101]. Particularly pathogens with a necrotrophic life style produce toxins that kill plant cells, by disrupting the plant cell membrane directly or by generating membrane damaging reactive oxygen species [102, 103]. In interactions with viruses and biotrophic pathogens like downy mildews, chlorosis is often induced in later stages of the infection, and chlorophyll degradation appears to be regulated by the same plant genes that control regular leaf senescence [104–106]. The area of chlorotic or necrotic tissue can serve as a good proxy to estimate spread of the pathogen, as well as the impact on yield, depending on plant developmental stage, type of the pathogen and stage of the infection.

While chlorotic tissue has reduced chlorophyll content, necrotic tissue lacks all pigments characteristic for healthy plant tissue. This results in changes of absorption and reflectance in the visible spectrum, evident as color ranging from yellow (chlorosis) to shades of brown to black (necrosis). Besides the lack of pigments, necrotic tissue also differs from healthy tissue in water content and three-dimensional structure due to the collapse of cells. A lower ratio of cell surface to intercellular air space due to a collapse of e.g. the spongy mesophyll leads to reduced reflectance of NIR radiation [107]. Changes in water content in necrotic tissue also impacts SWIR reflectance due to several water absorption peaks in the SWIR range [108, 109]. Consequently, sensors that detect reflectance in the VIS–NIR–SWIR range are useful to quantify chlorosis and necrosis. The contrast between healthy leaf tissue and lesions lacking chlorophyll may be enhanced by imaging the red steady-state chlorophyll fluorescence [110, 111]. The onset of cell death can also be visualised by imaging the increased chlorophyll fluorescence that results from the disassembly of the chloroplast thylakoid membrane in tissue undergoing cell death [112]. Additionally, the changes in plant internal tissue structure that precede and are associated with necrosis and tissue damage can be measured with different tomography methods, e.g. optical coherence tomography (OCT) or X-Ray computed tomography (CT) [113, 114].

In controlled experiments, particularly on samples that are easy to image such as detached leaves, RGB imaging is an established method to track and quantify chlorosis and necrosis. Barbacci et al. [115] combined a detached leaf assay with a setup for automated RGB

image acquisition and analysis to quantify necrotic lesion development on *Arabidopsis* inoculated with *S. sclerotiorum*. This enabled measurement of latency period and lesion doubling time (LDT) at high resolution (measurement every 10 min over 36 h) and of large sample sizes (120–270 leaves per imaging unit). Whereas latency period varied mostly between different *S. sclerotiorum* isolates, LDT was mainly determined by the plant genotype and independent of the inoculated isolate. Using the differences in LDT as a robust indicator of quantitative resistance led to the identification of the nucleotide-binding site leucine-rich repeat gene *LAZ5* as a negative regulator of quantitative resistance to *S. sclerotiorum*. On a similar scale, RGB imaging enabled quantification of chlorosis induced by *P. syringae* in *Arabidopsis* seedlings growing in 48-well plates [116, 117]. The assay was tested in a genome-wide association study to efficiently distinguish between presence and absence of effector-triggered immunity and confirmed the loci of known resistance genes.

In field experiments, necrosis in maize infected by *Setosphaeria turcica* (Northern corn leaf blight) or sugar beet infected by *C. beticola* (Cercospora leaf spot) has been assessed by sensors [118, 119]. Wiesner-Hanks et al. [118, 120] acquired images with a RGB camera mounted on a UAV flying 6 m above a maize field trial. The necrotic lesions captured in these images were manually annotated and used to train a CNN. Combining this CNN with a conditional random field method allowed automated segmentation of the aerial images to identify and quantify lesion area.

In a sugar beet field trial, Jay et al. [119] tested both RGB imaging from a ground-based vehicle and spectral imaging (six bands between 450 and 850 nm) from a UAV to assess *Cercospora* leaf spot severity. They determined the necrotic spot density from RGB images and green fraction from both RGB and spectral images. The image data was compared to visual severity scores given by an expert on a 1–9 scale. Spot density gave a better prediction for low (less severe) visual scores and green area was a better predictor for high visual scores. Consequently, combining these two features as input for a neural network enabled a good prediction of the visual disease scores. Because only the ground-based RGB sensor enabled measuring both of these features, it outperformed the aerial spectral sensor.

Symptom: thermal energy dissipation

Plant-pathogen interactions can result in a change of tissue temperature by affecting energy balance terms such as transpiration or light absorption [121]. These induced changes often precede other symptoms and are characterized by complex spatial and temporal

dynamics. This makes thermal energy dissipation an interesting candidate trait for early detection of disease. PPI can cause an increase in tissue temperature by inducing stomatal closure and vascular occlusion. Conversely, damage to cells and deregulation of stomatal opening can lead to decreased tissue temperature through uncontrolled transpiration [122, 123]. Photosynthetic performance has an influence on plant temperature as well because part of the absorbed light energy, if not emitted as fluorescence or converted in photochemistry, is dissipated as heat in the process of non-photochemical quenching [39].

Temperature can be remotely measured in the thermal infrared spectrum (TIR, 8000–15,000 nm) with radiometric sensors [124]. This technology has long been applied to measure abiotic stresses, particularly drought stress which is associated with an increased canopy temperature [125, 126]. Multiple plant-pathosystems have also been studied with thermal sensors [127].

Vascular pathogens that grow within the xylem of host plants can cause occlusion of the vascular system due to both their own growth and the plant responses to the pathogens. This can lead to symptoms similar to drought stress, as the hydraulic conductivity is inhibited by the occlusion [128]. In a field experiment, the crown temperature of olive trees under natural infection with *Verticillium dahliae*, a vascular fungal pathogen, was measured with infrared temperature sensors (Apogee IRR-P) mounted 1 m above the trees. The temperature was positively correlated with *Verticillium* wilt disease severity levels across multiple sites [129]. The same authors validated and vastly increased the throughput of their methods by mounting a broad-band thermal camera (FLIR SC655) on a crewed aircraft and flying it over 3000 ha of olive orchards [130].

The measurement of plant thermal energy dissipation is not easy to measure in the field as environmental effects and the influence of other stresses decrease specificity of the measurements. Therefore, many studies of plant thermal energy dissipation are performed in controlled environments.

An abscisic-acid-induced stomatal closure in leaves of cucumber infected with the vascular pathogen *Fusarium oxysporum* f. sp. *Cucumerinum* could be detected by an increase in temperature with a FLIR SC620 digital infrared camera in a controlled environment [123]. The maximum temperature of leaves of infected plants was reached nine days after infection. The authors also observed a fast decrease of temperature ten days after infection and attributed it to uncontrolled water loss due to cell damage. Eleven days after infection, leaf temperature rose again which was attributed to dehydration of the leaves.

Virus-plant interactions can also influence tissue temperature. Tobacco infected with tobacco mosaic virus shows a fast increase in leaf temperature at the initial infection site preceding a hypersensitive response. This increase in temperature is due to stomatal closure which is induced by salicylic acid accumulation. The same areas of the leaves later appear as necrotic lesions [131]. Changes in leaf temperature were also observed in sweet potato upon infection with two different viruses, Sweet potato feathery mottle virus (SPFMV) and Sweet potato chlorotic stunt virus (SPCSV) [132]. In this controlled environment experiment, leaf temperature was measured with a top-view thermal camera (FLIR A615) and differed between healthy plants, plants infected with SPFMV, and plants co-infected with both viruses. Higher temperatures were associated with higher disease severity scores [132].

Sensing structural changes

Preliminary studies using tomographic sensors for phenotyping PPI have been performed in various plant-pathosystems. As these sensors measure spatially resolved attenuation, refractive index variation and scattering strength inside tissue, they can be useful to non-invasively study internal structural changes which can allow for early detection and potentially identification of disease [113, 114, 133, 134]. Besides measuring internal plant and pathogen structure, X-ray CT scanning also provides the option to measure through substrate and was used to study changes in root morphology of potato affected by *Streptomyces scabies* [135].

Synchrotron based phase contrast X-ray CT was used to measure differences in tissue degradation in wheat caused by *Fusarium graminearum* [114]. A known resistance mechanism to this fungus is the inhibition of fungal colonization from spikelet to spikelet inside the rachis internode. Traditional histological studies to quantify this type of resistance require destructive sampling. The tissue degradation leads to increased tissue porosity, which makes it possible to sense the pathogen spread by changes in X-ray attenuation.

Leaves of apple trees infected with *Marssonina coronaria* were measured with a custom-built backpack-based OCT sensor in the field [133]. Disease progression causes an enlarged gap between epidermis and palisade parenchyma that could be sensed by a reduction in back-scattering. The presence of infection was confirmed using Loop-mediated isothermal amplification, a nucleic-acid based technique [133]. Authors from the same group applied similar techniques in leaves of *Capsicum annuum* infected with *Stemphylium lycopersici* [134].

These studies show the potential of tomographic sensors for early detection of disease as well as phenotyping of below ground structures.

Discussion

Phenotyping plant-pathogen interactions in the field is limited by specificity, canopy structure, and environmental conditions

Signs and symptoms are easier to measure in a controlled environment where plant material can be accessed from multiple angles at close proximity and under optimal illumination. Yet field phenotyping is a requirement for most disease resistance breeding programs and precision agriculture.

Traits identified in controlled environments at small scales such as lesion size or sporulation, may, in some cases, be transferrable to the field [7, 136, 137]. For example, Northern corn leaf blight causes large and obvious lesions on maize plants, a symptom that was measured on RGB images taken from a UAV at 6 m altitude [118, 120]. This way, the relative area of necrotic maize tissue could be measured with high throughput.

However, it is technically more demanding to measure signs and symptoms under field conditions. Multiple biotic and abiotic stresses can affect plants simultaneously and lead to a loss of specificity. For example, chlorosis may be caused both by a pathogen or abiotic stress. In a canopy, plants or plant parts can shade each other from the sensors, especially in tall growing crops where lower plant parts are covered. Applying sensors from a distance, e.g. when mounted on UAVs, can result in a lack of spatial resolution. Also, natural radiation influences sensor-based measurements and can confound the measurement of signs and symptoms.

The effect of natural radiation can be controlled either by numerical correction during the data analysis, or by shading during the data acquisition, but both approaches are difficult due to the spatial and temporal variation of natural radiation. The technical limitations involving spatial resolution and natural radiation could be overcome partly by ground-based phenotyping platforms that carry sensors close to the canopy and offer a compromise between throughput and accuracy. For example, ground-based RGB imaging outperformed aerial RGB imaging for assessing *Cercospora* leaf spot in a sugar beet field trial [119]. The ground-based platform offered higher spatial resolution and artificial illumination which enabled measuring necrotic spot size and density, traits that could not be measured with the aerial platform. The specificity of measurements could potentially be further improved by sensor fusion, the integration of data from multiple sources [138, 139]. A combination of functional

plant traits derived from hyperspectral imaging (400–885 nm) and a thermal imaging sensor mounted on an aircraft enabled early detection of *Xylella fastidiosa*, a xylem-bound bacterial pathogen of olive trees [48].

These examples illustrate that it is feasible to increase throughput while maintaining accuracy also under field conditions. But it is critical that the challenges of specificity, canopy architecture, spatial resolution and natural radiation are considered and addressed with new solutions like improved sensor and vector technology or sensor fusion.

Non-invasive phenotyping of below-ground plant-pathogen interactions remains a challenge

Phenotyping of PPI below ground is still in an early stage of development as in-soil non-invasive phenotyping is difficult. Using invasive sampling and RGB imaging, changes of morphological root characteristics could be detected on soybean infected with *Fusarium* species and on alfalfa affected by *Phymatotrichopsis* root rot [140, 141]. Tomographic sensors are an option to measure PPI on roots growing in substrate in pots non-invasively [135]. With new X-ray CT scanners that are installed in automated phenotyping facilities, this method may become more accessible [142–144].

Sensor data helps to understand plant-pathogen interactions in more detail

Sensor-based phenotyping is commonly deployed to substitute traditional visual disease scores, for example to rank a genotype on a spectrum from resistant to susceptible in comparison with other genotypes [12]. Yet sensor-based phenotyping can capture the sum of processes that underlie PPI in more detail than what is reflected in traditional disease severity scores. To understand which specific PPI related changes influence the detected signals, sensor data needs to be linked with in situ measurements, particularly in the case of advanced sensors. This has been shown successfully in two studies that linked disease induced accumulation of phenolic compounds to specific Raman bands in Raman spectroscopy [90] and flavonoids to UV absorption features in spectral imaging [81]. Establishing and confirming such links will allow to non-invasively measure diverse aspects of PPI simultaneously and to transfer those findings between pathosystems and environments.

Advanced sensors expand the range of perceivable signs and symptoms but require complementary technologies
Implementation of sensor technology for phenotyping of PPI allows for measurement of a wide range of signs and symptoms (Table 2). Plant metabolites may be detected

with spectroscopic methods, and internal plant and pathogen structures can be detected with tomographic methods [15, 18]. Fluorescence imaging, possibly with tagged pathogens, and chlorophyll fluorescence imaging are other promising approaches for measuring pathogen growth and photosynthetic parameters. To build useful phenotyping systems, any improvements and innovation in sensor technology need to be matched with appropriate facilities, vector technology, data management and data analysis methods. In those fields, constant improvement is pivotal, such as increased payload of UAVs, addition of active illumination to ground-based phenotyping platforms, automation of indoor phenotyping systems, implementation of FAIR data standards and new machine learning methods for analysis [11, 145–148]. Integration of the resulting phenotypes with other-omics data can enable a more comprehensive interpretation of sensor data and will eventually lead to a deeper understanding of plant-pathogen interactions.

Abbreviations

CCD: Charge-coupled device; Chl-F: Chlorophyll *a* fluorescence; CNN: Convolutional neural network; CT: Computed tomography; FAIR: Findable, accessible, interoperable, reusable; F_m : Maximum fluorescence; F_v/F_m : Maximum quantum efficiency of PSII; IR: Infrared; LDT: Lesion doubling time; NIR: Near-infrared; NPQ: Non-photochemical quenching; OCT: Optical coherence tomography; PAM: Pulse-amplitude-modulated; PMMoV: Pepper mild mottle virus; PPI: Plant-pathogen interaction; PSII: Photosystem II; PSM: Plant secondary metabolite; qP: Photochemical quenching; RGB: Red–green–blue; SPSCV: Sweet potato chlorotic stunt virus; SPFMV: Sweet potato feathery mottle virus; SWIR: Shortwave-infrared; TIR: Thermal infrared; TMV: Tobacco mosaic virus; UAV: Uncrewed aerial vehicle; UV: Ultraviolet; UV-C: Ultraviolet C; VIS: Visible.

Authors' contributions

FT and ST analyzed references and drafted the manuscript; DP, BB, GA, and JW revised manuscript. All authors read and approved the final manuscript.

Funding

FT is supported by the University of Adelaide with a Scholarship International, and by The Plant Accelerator with a PhD stipend top-up. BB, DP and FT acknowledge the use of the facilities, and scientific and technical assistance of the Australian Plant Phenomics Facility, which is supported by the Australian Government's National Collaborative Research Infrastructure Strategy (NCRIS). ST and JW are supported by the PathoView project (16293) granted to GA, a TTW partnership project that is funded by Rijk Zwaan (de Lier, Netherlands) and the Dutch Research Council (NWO).

Availability of data and materials

Data sharing not applicable to this article as no datasets were generated or analysed during the current study.

Declarations

Ethics approval and consent to participate

Not applicable.

Consent for publication

Not applicable.

Competing interests

The authors declare that they have no competing interests.

Author details

¹Australian Plant Phenomics Facility, School of Agriculture, Food and Wine, University of Adelaide, Urrbrae, SA, Australia. ²Department of Biology, Plant-Microbe Interactions, Utrecht University, 3584CH Utrecht, The Netherlands. ³Department of Imaging Physics, Delft University of Technology, Lorentzweg 1, 2628 CJ Delft, The Netherlands.

Received: 29 June 2021 Accepted: 8 February 2022

Published online: 21 March 2022

References

- Savary S, Wilcoquet L, Pethybridge SJ, Esker P, McRoberts N, Nelson A. The global burden of pathogens and pests on major food crops. *Nat Ecol Evol*. 2019;3:430–9. <https://doi.org/10.1038/s41559-018-0793-y>.
- D'Arcy CJ. Illustrated glossary of plant pathology. *Plant Heal Instr*. 2001. <https://doi.org/10.1094/PHI-I-2001-0219-01>.
- Nijs RE, Parlevliet JE, Lindhout P, Bai Y. Breeding crops with resistance to diseases and pests. The Netherlands: Wageningen Academic Publishers; 2019.
- Agrios GN. How pathogens attack plants. In: *Plant pathology*. Amsterdam: Elsevier; 2005. p. 175–205.
- Agrios GN. Environmental factors that cause plant diseases. *Plant Pathol*. 2005. <https://doi.org/10.1016/b978-0-08-047378-9.50016-6>.
- Mutka AM, Bart RS. Image-based phenotyping of plant disease symptoms. *Front Plant Sci*. 2015;5:1–8. <https://doi.org/10.3389/fpls.2014.00734>.
- Simko I, Jimenez-Berni JA, Sirault XRR. Phenomic approaches and tools for phytopathologists. *Phytopathology*. 2017;107:6–17. <https://doi.org/10.1094/PHYTO-02-16-0082-RVW>.
- Mahlein AK, Oerke EC, Steiner U, Dehne HW. Recent advances in sensing plant diseases for precision crop protection. *Eur J Plant Pathol*. 2012;133:197–209. <https://doi.org/10.1007/s10658-011-9878-z>.
- Furbank RT, Tester M. Phenomics—technologies to relieve the phenotyping bottleneck. *Trends Plant Sci*. 2011;16:635–44. <https://doi.org/10.1016/j.tplants.2011.09.005>.
- Singh A, Ganapathysubramanian B, Singh AK, Sarkar S. Machine learning for high-throughput stress phenotyping in plants. *Trends Plant Sci*. 2016;21:110–24. <https://doi.org/10.1016/j.tplants.2015.10.015>.
- Sperschneider J. Machine learning in plant–pathogen interactions: empowering biological predictions from field scale to genome scale. *New Phytol*. 2019. <https://doi.org/10.1111/nph.15771>.
- Bock CH, Barbedo JGA, Del Ponte EM, Bohnenkamp D, Mahlein A-K. From visual estimates to fully automated sensor-based measurements of plant disease severity: status and challenges for improving accuracy. *Phytopathol Res*. 2020;2:9. <https://doi.org/10.1186/s42483-020-00049-8>.
- Sankaran S, Mishra A, Ehsani R, Davis C. A review of advanced techniques for detecting plant diseases. *Comput Electron Agric*. 2010;72:1–13. <https://doi.org/10.1016/j.compag.2010.02.007>.
- Mahlein A-K. Present and future trends in plant disease detection. *Plant Dis*. 2016;100:1–11. <https://doi.org/10.1007/s13398-014-0173-7>.
- Farber C, Mahnke M, Sanchez L, Kurouski D. Advanced spectroscopic techniques for plant disease diagnostics. A review. *TrAC Trends Anal Chem*. 2019;118:43–9. <https://doi.org/10.1016/j.trac.2019.05.022>.
- Oerke EC. Precision agriculture for sustainability. In: Stafford J, editor. *Precision agriculture for sustainability*. Routledge: Taylor & Francis; 2019.
- Payne WZ, Kurouski D. Raman-based diagnostics of biotic and abiotic stresses in plants. A review. *Front Plant Sci*. 2021. <https://doi.org/10.3389/fpls.2020.616672>.
- Sylvain T, Cecile LG. Disease identification: a review of vibrational spectroscopy applications. *Compr Anal Chem*. 2018;80:195–225. <https://doi.org/10.1016/bs.coac.2018.03.005>.
- Restif O, Koella JC. Concurrent evolution of resistance and tolerance to pathogens. *Am Nat*. 2004. <https://doi.org/10.1086/423713>.
- Bierman A, LaPlumm T, Cadle-Davidson L, Gadoury D, Martinec D, Sappkota S, et al. A high-throughput phenotyping system using machine vision to quantify severity of grapevine powdery mildew. *Plant Phenomics*. 2019;2019:1–13. <https://doi.org/10.34133/2019/9209727>.
- Lück S, Strickert M, Lorbeer M, Melchert F, Backhaus A, Kilias D, et al. 'MacroBot'—an automated segmentation-based system for powdery mildew disease quantification. *Plant Phenomics*. 2020. <https://doi.org/10.1101/2020.03.16.993451>.
- Oerke EC, Leucker M, Steiner U. Sensory assessment of *Cercospora beticola* sporulation for phenotyping the partial disease resistance of sugar beet genotypes. *Plant Methods*. 2019;15:1–12. <https://doi.org/10.1186/s13007-019-0521-x>.
- Yates S, Mikaberidze A, Krattinger SG, Abrouk M, Hund A, Yu K, et al. Precision phenotyping reveals novel Loci for quantitative resistance to *Septoria tritici* Blotch. *Plant Phenomics*. 2019;2019:1–11. <https://doi.org/10.34133/2019/3285904>.
- Lorang JM, Tuori RP, Martinez JP, Sawyer TL, Redman RS, Rollins JA, et al. Green fluorescent protein is lighting up fungal biology. *Appl Environ Microbiol*. 2001;67:1987–94. <https://doi.org/10.1128/aem.67.5.1987-1994.2001>.
- Kassem II, Splitter GA, Miller S, Rajashekara G. Let there be light! Bioluminescent imaging to study bacterial pathogenesis in live animals and plants. *Biolumin Fundam Appl Biotechnol*. 2014;3:119–45.
- Skadsen RW, Hohn TM. Use of *Fusarium graminearum* transformed with *gfp* to follow infection patterns in barley and *Arabidopsis*. *Physiol Mol Plant Pathol*. 2004;64:45–53. <https://doi.org/10.1016/j.pmpp.2004.04.003>.
- Chapman S, Faulkner C, Kaiserli E, Garcia-Mata C, Savenkov EI, Roberts AG, et al. The photoreversible fluorescent protein iLOV outperforms GFP as a reporter of plant virus infection. *Proc Natl Acad Sci*. 2008;105:20038–43. <https://doi.org/10.1073/pnas.0807551105>.
- Domazakis E, Wouters D, Visser RGF, Kamoun S, Joosten MHAJ, Vleeshouwers VGAA. The ELR-SOBIR1 complex functions as a two-component receptor-like kinase to mount defense against *Phytophthora infestans*. *Mol Plant Microbe Interact*. 2018;31:795–802. <https://doi.org/10.1094/mpmi-09-17-0217-r>.
- Wang K, Kang L, Anand A, Lazarovits G, Mysore KS. Monitoring in planta bacterial infection at both cellular and whole-plant levels using the green fluorescent protein variant GFPuv. *New Phytol*. 2007;174:212–23. <https://doi.org/10.1111/j.1469-8137.2007.01999.x>.
- Fujie M, Takamoto H, Kawasaki T, Fujiwara A, Yamada T. Monitoring growth and movement of *Ralstonia solanacearum* cells harboring plasmid pRSS12 derived from bacteriophage φRSS1. *J Biosci Bioeng*. 2010;109:153–8. <https://doi.org/10.1016/j.jbiosc.2009.07.012>.
- Hupp S, Rosenkranz M, Bonfig K, Pandey C, Roitsch T. Noninvasive phenotyping of plant-pathogen interaction: consecutive in situ imaging of fluorescing *Pseudomonas syringae*, plant phenolic fluorescence, and chlorophyll fluorescence in *Arabidopsis* leaves. *Front Plant Sci*. 2019;10:1239. <https://doi.org/10.3389/fpls.2019.01239>.
- Du H, Wen C, Zhang X, Xu X, Yang J, Chen B, et al. Identification of a Major QTL (qRRs-10.1) that confers resistance to *Ralstonia solanacearum* in pepper (*Capsicum annuum*) using SLAF-BSA and QTL mapping. *Int J Mol Sci*. 2019;20:5887. <https://doi.org/10.3390/ijms20235887>.
- Xu X, Rajashekara G, Paul PA, Miller SA. Colonization of tomato seedlings by bioluminescent *Clavibacter michiganensis* subsp. *michiganensis* under different humidity regimes. *Phytopathology*. 2012;102:177–84. <https://doi.org/10.1094/phyto-03-11-0090>.
- Soldan R, Sanguankiatichai N, Bach-Pages M, Bervoets I, Huang WE, Preston GM. From macro to micro: a combined bioluminescence-fluorescence approach to monitor bacterial localization. *Environ Microbiol*. 2020. <https://doi.org/10.1111/1462-2920.15296>.
- Kotlobay AA, Sarkisyan KS, Mokrushina YA, Marcet-Houben M, Serbrovskaya EO, Markina NM, et al. Genetically encodable bioluminescent system from fungi. *Proc Natl Acad Sci*. 2018;115:12728–32. <https://doi.org/10.1073/pnas.1803615115>.
- Berger S, Sinha AK, Roitsch T. Plant physiology meets phytopathology: plant primary metabolism and plant pathogen interactions. *J Exp Bot*. 2007;58:4019–26. <https://doi.org/10.1093/jxb/erm298>.
- Bolton MD. Primary metabolism and plant defense—fuel for the fire. *Mol Plant Microbe Interact*. 2009;22:487–97. <https://doi.org/10.1094/mpmi-22-5-0487>.
- Rojas CM, Senthil-Kumar M, Tzin V, Mysore KS. Regulation of primary plant metabolism during plant-pathogen interactions and its contribution to plant defense. *Front Plant Sci*. 2014. <https://doi.org/10.3389/fpls.2014.00017>.

39. Baker NR. Chlorophyll fluorescence: a probe of photosynthesis in vivo. *Annu Rev Plant Biol.* 2008;59:89–113. <https://doi.org/10.1146/annurev.arplant.59.032607.092759>.
40. Murchie EH, Lawson T. Chlorophyll fluorescence analysis: a guide to good practice and understanding some new applications. *J Exp Bot.* 2013;64:3983–98. <https://doi.org/10.1093/jxb/ert208> PMID: 23913954.
41. Butler WL. Energy distribution in the photochemical apparatus of photosynthesis. *Annu Rev Plant Physiol.* 1978;29:345–78. <https://doi.org/10.1146/annurev.pp.29.060178.002021>.
42. Pérez-Bueno ML, Pineda M, Barón M. Phenotyping plant responses to biotic stress by chlorophyll fluorescence imaging. *Front Plant Sci.* 2019;10:1135. <https://doi.org/10.3389/fpls.2019.011135>.
43. Virlet N, Sabermanesh K, Sadeghi-Tehran P, Hawkesford MJ. Field scanner: an automated robotic field phenotyping platform for detailed crop monitoring. *Funct Plant Biol.* 2017;44:143. <https://doi.org/10.1071/fp16163>.
44. Rascher U, Alonso L, Burkart A, Cilia C, Cogliati S, Colombo R, et al. Sun-induced fluorescence—a new probe of photosynthesis: first maps from the imaging spectrometer HyPlant. *Glob Chang Biol.* 2015;21:4673–84. <https://doi.org/10.1111/gcb.13017>.
45. Silva-Perez V, Molero G, Serbin SP, Condon AG, Reynolds MP, Furbank RT, et al. Hyperspectral reflectance as a tool to measure biochemical and physiological traits in wheat. *J Exp Bot.* 2018;69:483–96. <https://doi.org/10.1093/jxb/erx421>.
46. Aasen H, Wittenberghe V, Medina S, Damm A, Goulas Y, Wieneke S, et al. Sun-induced chlorophyll fluorescence II: review of passive measurement setups, protocols, and their application at the leaf to canopy level. *Remote Sens.* 2019;11:927. <https://doi.org/10.3390/rs11080927>.
47. Meacham-Hensold K, Fu P, Wu J, Serbin S, Montes CM, Ainsworth E, et al. Plot-level rapid screening for photosynthetic parameters using proximal hyperspectral imaging. *J Exp Bot.* 2020;71:2312–28. <https://doi.org/10.1093/jxb/eraa068>.
48. Zarco-Tejada PJ, Camino C, Beck PSA, Calderon R, Hornero A, Hernández-Clemente R, et al. Previsual symptoms of *Xylella fastidiosa* infection revealed in spectral plant-trait alterations. *Nat Plants.* 2018;4:432–9. <https://doi.org/10.1038/s41477-018-0189-7>.
49. Pinto F, Celesti M, Acebron K, Alberti G, Cogliati S, Colombo R, et al. Dynamics of sun-induced chlorophyll fluorescence and reflectance to detect stress-induced variations in canopy photosynthesis. *Plant Cell Environ.* 2020;43:1637–54. <https://doi.org/10.1111/pce.13754>.
50. Dechant B, Ryu Y, Badgley G, Zeng Y, Berry JA, Zhang Y, et al. Canopy structure explains the relationship between photosynthesis and sun-induced chlorophyll fluorescence in crops. *Remote Sens Environ.* 2020;241: 111733. <https://doi.org/10.1016/j.rse.2020.111733>.
51. Csefalvay L, Di Gaspero G, Matouš K, Bellin D, Ruperti B, Olejníčková J. Pre-symptomatic detection of *Plasmopara viticola* infection in grapevine leaves using chlorophyll fluorescence imaging. *Eur J Plant Pathol.* 2009;125:291–302. <https://doi.org/10.1007/s10658-009-9482-7>.
52. Kuckenber J, Tartachnyk I, Noga G. Temporal and spatial changes of chlorophyll fluorescence as a basis for early and precise detection of leaf rust and powdery mildew infections in wheat leaves. *Precis Agric.* 2009;10:34–44. <https://doi.org/10.1007/s11119-008-9082-0>.
53. Brugger A, Behmann J, Paulus S, Luigs HG, Kuska MT, Schramowski P, et al. Extending hyperspectral imaging for plant phenotyping to the UV-range. *Remote Sens.* 2019;11:1–11. <https://doi.org/10.3390/rs11121401>.
54. Polonio A, Pineda M, Bautista R, Martínez-Cruz J, Pérez-Bueno ML, Barón M, et al. RNA-seq analysis and fluorescence imaging of melon powdery mildew disease reveal an orchestrated reprogramming of host physiology. *Sci Rep.* 2019;9:1–16. <https://doi.org/10.1038/s41598-019-44443-5>.
55. Lichtenthaler HK, Rinderle U. The role of chlorophyll fluorescence in the detection of stress conditions in plants. *C R C Crit Rev Anal Chem.* 1988;19:529–85. <https://doi.org/10.1080/15476510.1988.10401466>.
56. Ely KS, Burnett AC, Lieberman-Cribbin W, Serbin SP, Rogers A. Spectroscopy can predict key leaf traits associated with source–sink balance and carbon–nitrogen status. *J Exp Bot.* 2019;70:1789–99. <https://doi.org/10.1093/jxb/erz061>.
57. Curran PJ. Remote sensing of foliar chemistry. *Remote Sens Environ.* 1989;30:271–8. [https://doi.org/10.1016/0034-4257\(89\)90069-2](https://doi.org/10.1016/0034-4257(89)90069-2).
58. Serbin SP, Singh A, Mcneil BE, Kingdon CC, Townsend PA. Spectroscopic determination of leaf morphological and biochemical traits for northern temperate and boreal tree species. *Ecol Appl.* 2014;24:1651–69. <https://doi.org/10.1890/13-2110.1>.
59. Gold KM, Townsend PA, Chlus A, Herrmann I, Couture JJ, Larson ER, et al. Hyperspectral measurements enable pre-symptomatic detection and differentiation of contrasting physiological effects of late blight and early blight in potato. *Remote Sens.* 2020;12:286. <https://doi.org/10.3390/rs12020286>.
60. Wang Z, Chlus A, Geygan R, Ye Z, Zheng T, Singh A, et al. Foliar functional traits from imaging spectroscopy across biomes in eastern North America. *New Phytol.* 2020;228:494–511. <https://doi.org/10.1111/nph.16711>.
61. Conrad AO, Li W, Lee D-Y, Wang G-L, Rodriguez-Saona L, Bonello P. Machine learning-based presymptomatic detection of rice sheath blight using spectral profiles. *Plant Phenomics.* 2020;2020:1–10. <https://doi.org/10.34133/2020/8954085>.
62. Theis N, Lerdau M. The evolution of function in plant secondary metabolites. *Int J Plant Sci.* 2003;164:593–102. <https://doi.org/10.1086/374190>.
63. Kessler A, Kalske A. Plant secondary metabolite diversity and species interactions. *Annu Rev Ecol Syst.* 2018;49:115–38. <https://doi.org/10.1146/annurev-ecolsys-110617-062406>.
64. Bednarek P. Chemical warfare or modulators of defence responses—the function of secondary metabolites in plant immunity. *Curr Opin Plant Biol.* 2012;15:407–14. <https://doi.org/10.1016/j.cpb.2012.03.002>.
65. Piasecka A, Jedrzejczak-Rey N, Bednarek P. Secondary metabolites in plant innate immunity: conserved function of divergent chemicals. *New Phytol.* 2015;206:948–64. <https://doi.org/10.1111/nph.13325>.
66. García-Plazaola JL, Fernández-Marin B, Duke SO, Hernández A, López-Arbeloa F, Becerril JM. Autofluorescence: biological functions and technical applications. *Plant Sci.* 2015;236:136–45. <https://doi.org/10.1016/j.plantsci.2015.03.010>.
67. Pezet R, Gindro K, Viret O, Spring J-L. Glycosylation and oxidative dimerization of resveratrol are respectively associated to sensitivity and resistance of grapevine cultivars to downy mildew. *Physiol Mol Plant Pathol.* 2004;65:297–303. <https://doi.org/10.1016/j.pmpp.2005.03.002>.
68. Bellow S, Latouche G, Brown SC, Poutaraud A, Cerovic ZG. In vivo localization at the cellular level of stilbene fluorescence induced by *Plasmopara viticola* in grapevine leaves. *J Exp Bot.* 2012;63:3697–707. <https://doi.org/10.1093/jxb/ers060> PMID: 22412183.
69. Bellow S, Latouche G, Brown SC, Poutaraud A, Cerovic ZG. Optical detection of downy mildew in grapevine leaves: daily kinetics of autofluorescence upon infection. *J Exp Bot.* 2012;64:333–41. <https://doi.org/10.1093/jxb/ers338> PMID: 23213137.
70. Becker L, Bellow S, Carré V, Latouche G, Poutaraud A, Merdinoglu D, et al. Correlative analysis of fluorescent phytoalexins by mass spectrometry imaging and fluorescence microscopy in grapevine leaves. *Anal Chem.* 2017;89:7099–106. <https://doi.org/10.1021/acs.analchem.7b01002>.
71. Claffi M, Paolacci AR, Paolucci M, Alicandri E, Bigini V, Badiani M, et al. Transcriptional regulation of stilbene synthases in grapevine germplasm differentially susceptible to downy mildew. *BMC Plant Biol.* 2019. <https://doi.org/10.1186/s12870-019-2014-5>.
72. Pineda M, Gáspár L, Morales F, Szigeti Z, Barón M. Multicolor fluorescence imaging of leaves—a useful tool for visualizing systemic viral infections in plants. *Photochem Photobiol.* 2008;84:1048–60. <https://doi.org/10.1111/j.1751-1097.2008.00357.x>.
73. Bürling K, Hunsche M, Noga G. Use of blue–green and chlorophyll fluorescence measurements for differentiation between nitrogen deficiency and pathogen infection in winter wheat. *J Plant Physiol.* 2011;168:1641–8. <https://doi.org/10.1016/j.jplph.2011.03.016>.
74. Lichtenthaler HK, Miehé JA. Fluorescence imaging as a diagnostic tool for plant stress. *Trends Plant Sci.* 1997;2:316–20. [https://doi.org/10.1016/s1360-1385\(97\)89954-2](https://doi.org/10.1016/s1360-1385(97)89954-2).
75. Lang M, Lichtenthaler HK, Sowinska M, Heisel F, Miehé JA. Fluorescence imaging of water and temperature stress in plant leaves. *J Plant Physiol.* 1996;148:613–21. [https://doi.org/10.1016/S0176-1617\(96\)80082-4](https://doi.org/10.1016/S0176-1617(96)80082-4).
76. Hídeg É, Juhász M, Bornman JF, Asada K. The distribution and possible origin of blue–green fluorescence in control and stressed barley leaves. *Photochem Photobiol Sci.* 2002;1:934–41. <https://doi.org/10.1039/b201919g>.

77. Heisel F, Sowinska M, Miehé JA, Lang M, Lichtenthaler HK. Detection of nutrient deficiencies of maize by laser induced fluorescence imaging. *J Plant Physiol.* 1996;148:622–31. [https://doi.org/10.1016/S0176-1617\(96\)80083-6](https://doi.org/10.1016/S0176-1617(96)80083-6).
78. Lang M, Stober F, Lichtenthaler HK. Fluorescence emission spectra of plant leaves and plant constituents. *Radiat Environ Biophys.* 1991;30:333–47. <https://doi.org/10.1007/bf01210517>.
79. Couture JJ, Singh A, Rubert-Nason KF, Serbin SP, Lindroth RL, Townsend PA. Spectroscopic determination of ecologically relevant plant secondary metabolites. *Methods Ecol Evol.* 2016;7:1402–12. <https://doi.org/10.1111/2041-210x.12596>.
80. Kokaly RF, Skidmore AK. Plant phenolics and absorption features in vegetation reflectance spectra near 1.66 μm . *Int J Appl Earth Obs Geoinf.* 2015;43:55–83. <https://doi.org/10.1016/j.jag.2015.01.010>.
81. Brugger A, Schramowski P, Paulus S, Steiner U, Kersting K, Mahlein AK. Spectral signatures in the UV range can be combined with secondary plant metabolites by deep learning to characterize barley–powdery mildew interaction. *Plant Pathol.* 2021;70:1572–82. <https://doi.org/10.1111/ppa.13411>.
82. Arens N, Backhaus A, Döll S, Fischer S, Seiffert U, Mock HP. Non-invasive presymptomatic detection of *Cercospora beticola* infection and identification of early metabolic responses in sugar beet. *Front Plant Sci.* 2016;7:1–14. <https://doi.org/10.3389/fpls.2016.01377>.
83. Butler HJ, Ashton L, Bird B, Cinque G, Curtis K, Dorney J, et al. Using Raman spectroscopy to characterize biological materials. *Nat Protoc.* 2016;11:664–87. <https://doi.org/10.1038/nprot.2016.036>.
84. Gupta S, Huang CH, Singh GP, Park BS, Chua N-H, Ram RJ. Portable Raman leaf-clip sensor for rapid detection of plant stress. *Sci Rep.* 2020. <https://doi.org/10.1038/s41598-020-76485-5>.
85. Farber C, Bryan R, Paetzold L, Rush C, Kurouski D. Non-invasive characterization of single-, double- and triple-viral diseases of wheat with a hand-held Raman spectrometer. *Front Plant Sci.* 2020;11:1–7.
86. Sanchez L, Pant S, Xing Z, Mandadi K, Kurouski D. Rapid and non-invasive diagnostics of Huanglongbing and nutrient deficits on citrus trees with a handheld Raman spectrometer. *Anal Bioanal Chem.* 2019;411:3125–33. <https://doi.org/10.1007/s00216-019-01776-4>.
87. Sanchez L, Pant S, Mandadi K, Kurouski D. Raman spectroscopy vs quantitative polymerase chain reaction in early stage Huanglongbing diagnostics. *Sci Rep.* 2020;10:10101. <https://doi.org/10.1038/s41598-020-67148-6>.
88. Mandrille L, Rotunno S, Miozzi L, Vaira AM, Giovannozzi AM, Rossi AM, et al. Nondestructive Raman spectroscopy as a tool for early detection and discrimination of the infection of tomato plants by two economically important viruses. *Anal Chem.* 2019;91:9025–31. <https://doi.org/10.1021/acs.analchem.9b01323>.
89. Egging V, Nguyen J, Kurouski D. Detection and identification of fungal infections in intact wheat and sorghum grain using a hand-held Raman spectrometer. *Anal Chem.* 2018;90:8616–21. <https://doi.org/10.1021/acs.analchem.8b01863>.
90. Dou T, Sanchez L, Irigoyen S, Goff N, Niraula P, Mandadi K, et al. Biochemical origin of Raman-based diagnostics of Huanglongbing in grapefruit trees. *Front Plant Sci.* 2021. <https://doi.org/10.3389/fpls.2021.680991>.
91. Farber C, Bryan R, Paetzold L, Rush C, Kurouski D. Non-invasive characterization of single-, double- and triple-viral diseases of wheat with a hand-held Raman spectrometer. *Front Plant Sci.* 2020. <https://doi.org/10.3389/fpls.2020.01300>.
92. Stewart S, Priore RJ, Nelson MP, Treado PJ. Raman imaging. *Annu Rev Anal Chem.* 2012;5:337–60. <https://doi.org/10.1146/annurev-anchem-062011-143152>.
93. Lohumi S, Kim MS, Qin J, Cho B-K. Raman imaging from microscopy to macroscopy: quality and safety control of biological materials. *TRAC Trends Anal Chem.* 2017;93:183–98. <https://doi.org/10.1016/j.trac.2017.06.002>.
94. Lee H, Kim M, Qin J, Park E, Song Y-R, Oh C-S, et al. Raman hyperspectral imaging for detection of watermelon seeds infected with *Acidovorax citrulli*. *Sensors.* 2017;17:2188. <https://doi.org/10.3390/s17102188>.
95. Agrios GN. Plant diseases caused by viruses. *Plant Pathol.* 2005. <https://doi.org/10.1016/b978-0-08-047378-9.50020-8>.
96. Bender CL. Chlorosis-inducing phytotoxins produced by *Pseudomonas syringae*. *Eur J Plant Pathol.* 1999;105:1–12. <https://doi.org/10.1023/A:1008692227307>.
97. Ciuffetti LM, Manning VA, Pandelova I, Betts MF, Martinez JP. Host-selective toxins, Ptr ToxA and Ptr ToxB, as necrotrophic effectors in the Pyrenophora tritici-repentis-wheat interaction. *New Phytol.* 2010;187:911–9. <https://doi.org/10.1111/j.1469-8137.2010.03362.x>.
98. Chakravarthy S, Worley JN, Montes-Rodriguez A, Collmer A. *Pseudomonas syringae* pv. tomato DC3000 polymutants deploying coronatine and two type III effectors produce quantifiable chlorotic spots from individual bacterial colonies in *Nicotiana benthamiana* leaves. *Mol Plant Pathol.* 2018;19:935–47. <https://doi.org/10.1111/mpp.12579>.
99. Van Kan JAL. Licensed to kill: the lifestyle of a necrotrophic plant pathogen. *Trends Plant Sci.* 2006;11:247–53. <https://doi.org/10.1016/j.tplants.2006.03.005>.
100. Oome S, Raaymakers TM, Cabral A, Samwel S, Böhm H, Albert I, et al. Nep1-like proteins from three kingdoms of life act as a microbe-associated molecular pattern in *Arabidopsis*. *Proc Natl Acad Sci.* 2014;111:16955–60. <https://doi.org/10.1073/pnas.1410031111>.
101. Hutchison ML, Tester MA, Gross DC. Role of biosurfactant and ion channel-forming activities of syringomycin in transmembrane ion flux: a model for the mechanism of action in the plant-pathogen interaction. *Mol Plant Microbe Interact.* 1995. <https://doi.org/10.1094/mpmi-8-0610>.
102. Seidl MF, Van Den Ackerveken G. Activity and phylogenetics of the broadly occurring family of microbial Nep1-like proteins. *Annu Rev Phytopathol.* 2019;57:367–86. <https://doi.org/10.1146/annurev-phyto-082718-100054>.
103. Möbius N, Hertweck C. Fungal phytotoxins as mediators of virulence. *Curr Opin Plant Biol.* 2009;12:390–8. <https://doi.org/10.1016/j.pbi.2009.06.004>.
104. Espinoza C, Medina C, Somerville S, Arce-Johnson P. Senescence-associated genes induced during compatible viral interactions with grapevine and *Arabidopsis*. *J Exp Bot.* 2007;58:3197–212. <https://doi.org/10.1093/jxb/erm165>.
105. Seo J-K, Kim M-K, Kwak H-R, Choi H-S, Nam M, Choe J, et al. Molecular dissection of distinct symptoms induced by tomato chlorosis virus and tomato yellow leaf curl virus based on comparative transcriptome analysis. *Virology.* 2018;516:1–20. <https://doi.org/10.1016/j.virol.2018.01.001>.
106. Wang Y, Tan J, Wu Z, Vandenlangenberg K, Wehner CT, Wen C, et al. STAYGREEN, STAY HEALTHY: a loss-of-susceptibility mutation in the STAYGREEN gene provides durable, broad-spectrum disease resistances for over 50 years of US cucumber production. *New Phytol.* 2019;221:415–30. <https://doi.org/10.1111/nph.15353>.
107. Slaton MR, Raymond Hunt E, Smith WK. Estimating near-infrared leaf reflectance from leaf structural characteristics. *Am J Bot.* 2001;88:278–84. <https://doi.org/10.2307/2657019>.
108. Wilson RH, Nadeau KP, Jaworski FB, Tromberg BJ, Durkin AJ. Review of short-wave infrared spectroscopy and imaging methods for biological tissue characterization. *J Biomed Opt.* 2015;20:30901. <https://doi.org/10.1117/1.JBO.20.3.030901>.
109. Kim MD, Zhang H, Zhou H, Du T, Wu Q, Mockler CT, et al. Highly sensitive image-derived indices of water-stressed plants using hyperspectral imaging in SWIR and histogram analysis. *Sci Rep.* 2015;5:15919. <https://doi.org/10.1038/srep15919>.
110. Chaerle L, Hagenbeek D, Bruyne ED, Der Straeten DV. Chlorophyll fluorescence imaging for disease-resistance screening of sugar beet. *Plant Cell Tissue Organ Cult.* 2007;91:97–106. <https://doi.org/10.1007/s11240-007-9282-8>.
111. Macioszek KV, Wielanek M, Morkunas I, Ciereszko I, Kononowicz KA. Leaf position-dependent effect of *Alternaria brassicicola* development on host cell death, photosynthesis and secondary metabolites in *Brassica juncea*. *Physiol Plant.* 2020;168:601–16. <https://doi.org/10.1111/pp1.12998>.
112. Landeo Villanueva S, Malvestiti MC, van Ieperen W, Joosten MHAJ, van Kan JAL. Red light imaging for programmed cell death visualization and quantification in plant–pathogen interactions. *Mol Plant Pathol.* 2021;22:361–72. <https://doi.org/10.1111/mpp.13027>.

113. Wijesinghe RE, Lee S-Y, Ravichandran NK, Shirazi MF, Kim P, Jung H-Y, et al. Biophotonic approach for the characterization of initial bitter-rot progression on apple specimens using optical coherence tomography assessments. *Sci Rep*. 2018. <https://doi.org/10.1038/s41598-018-33791-3>.
114. Brar GS, Karunakaran C, Bond T, Stobbs J, Liu N, Hucl PJ, et al. Showcasing the application of synchrotron-based X-ray computed tomography in host-pathogen interactions: the role of wheat rachilla and rachis nodes in Type-II resistance to *Fusarium graminearum*. *Plant Cell Environ*. 2019;42:509–26. <https://doi.org/10.1111/pce.13431>.
115. Barbacci A, Navaud O, Mbengue M, Barascud M, Godiard L, Khafif M, et al. Rapid identification of an *Arabidopsis* NLR gene as a candidate conferring susceptibility to *Sclerotinia sclerotiorum* using time-resolved automated phenotyping. *Plant J*. 2020. <https://doi.org/10.1111/tpj.14747>.
116. Laflamme B, Middleton M, Lo T, Desveaux D, Guttman DS. Image-based quantification of plant immunity and disease. *Mol Plant Microbe Interact*. 2016;29:919–24. <https://doi.org/10.1094/mpmi-07-16-0129-ta>.
117. Martel A, Lo T, Desveaux D, Guttman DS. A high-throughput, seedling screen for plant immunity. *Mol Plant Microbe Interact*. 2020;33:394–401. <https://doi.org/10.1094/MPMI-10-19-0295-TA>.
118. Wiesner-Hanks T, Wu H, Stewart E, DeChant C, Kaczmar N, Lipson H, et al. Millimeter-level plant disease detection from aerial photographs via deep learning and crowdsourced data. *Front Plant Sci*. 2019;10:1–11. <https://doi.org/10.3389/fpls.2019.01550>.
119. Jay S, Comar A, Benicio R, Beauvois J, Dutartre D, Daubige G, et al. Scoring *Cercospora* leaf spot on sugar beet: comparison of UGV and UAV phenotyping systems. *Plant Phenomics*. 2020;2020:1–18. <https://doi.org/10.34133/2020/945123>.
120. Wiesner-Hanks T, Stewart EL, Kaczmar N, DeChant C, Wu H, Nelson RJ, et al. Image set for deep learning: field images of maize annotated with disease symptoms. *BMC Res Notes*. 2018;11:440. <https://doi.org/10.1186/s13104-018-3548-6>.
121. Jones HG, Rotenberg E. Energy, radiation and temperature regulation in plants. In: eLS. Hoboken: Wiley; 2011. <https://doi.org/10.1002/9780470015902.a0003199.pub2>.
122. Chaerle L, Leinonen I, Jones HG, Van Der Straeten D. Monitoring and screening plant populations with combined thermal and chlorophyll fluorescence imaging. *J Exp Bot*. 2007;58:773–84. <https://doi.org/10.1093/jxb/erl257>.
123. Wang M, Ling N, Dong X, Zhu Y, Shen Q, Guo S. Thermographic visualization of leaf response in cucumber plants infected with the soil-borne pathogen *Fusarium oxysporum* f. sp. cucumerinum. *Plant Physiol Biochem*. 2012;61:153–61. <https://doi.org/10.1016/j.plaphy.2012.09.015>.
124. Brooker G. Introduction to sensors for ranging and imaging. London: Institution of Engineering and Technology; 2009.
125. Jackson RD, Idso SB, Reginato RJ, Pinter PJ. Canopy temperature as a crop water stress indicator. *Water Resour Res*. 1981;17:1133–8. <https://doi.org/10.1029/WR017i004p01133>.
126. Pinter PJ, Fry KE, Guinn G, Mauney JR. Infrared thermometry: a remote sensing technique for predicting yield in water-stressed cotton. *Agric Water Manag*. 1983;6:385–95. [https://doi.org/10.1016/0378-3774\(83\)90057-4](https://doi.org/10.1016/0378-3774(83)90057-4).
127. Nilsson HE. Remote sensing and image analysis in plant pathology. *Annu Rev Phytopathol*. 1995;33:489–527. <https://doi.org/10.1146/annurev.phyto.33.1.489>.
128. Yadeta KA, Thomma BPHJ. The xylem as battleground for plant hosts and vascular wilt pathogens. *Front Plant Sci*. 2013;4:1–12. <https://doi.org/10.3389/fpls.2013.00097>.
129. Calderón R, Navas-Cortés JA, Lucena C, Zarco-Tejada PJ. High-resolution airborne hyperspectral and thermal imagery for early detection of Verticillium wilt of olive using fluorescence, temperature and narrow-band spectral indices. *Remote Sens Environ*. 2013;139:231–45. <https://doi.org/10.1016/j.rse.2013.07.031>.
130. Calderón R, Navas-Cortés JA, Zarco-Tejada PJ. Early detection and quantification of Verticillium wilt in olive using hyperspectral and thermal imagery over large areas. *Remote Sens*. 2015;7:5584–610. <https://doi.org/10.3390/rs70505584>.
131. Chaerle L, Van CW, Messens E, Lambers H, Van Montagu M, Van Der Straeten D. Presymptomatic visualization of plant-virus interactions by thermography. *Nat Biotechnol*. 1999;17:813–6. <https://doi.org/10.1038/11765>.
132. Wang L, Poque S, Valkonen JPT. Phenotyping viral infection in sweet-potato using a high-throughput chlorophyll fluorescence and thermal imaging platform. *Plant Methods*. 2019;15:1–14. <https://doi.org/10.1186/s13007-019-0501-1>.
133. Lee J, Lee SY, Wijesinghe RE, Ravichandran NK, Han S, Kim P, et al. On-field in situ inspection for Marssonina coronaria infected apple blotch based on non-invasive bio-photonic imaging module. *IEEE Access*. 2019;7:148684–91. <https://doi.org/10.1109/ACCESS.2019.2946388>.
134. Ravichandran NK, Wijesinghe RE, Shirazi MF, Park K, Lee SY, Jung HY, et al. In vivo monitoring on growth and spread of gray leaf spot disease in capsicum annum leaf using spectral domain optical coherence tomography. *J Spectrosc*. 2016. <https://doi.org/10.1155/2016/1093734>.
135. Han L, Dutilleul P, Prasher SO, Beaulieu C, Smith DL. Assessment of common scab-inducing pathogen effects on potato underground organs via computed tomography scanning. *Phytopathology*. 2008;98:1118–25. <https://doi.org/10.1094/PHYTO-98-10-1118>.
136. Rebetzke GJ, Jimenez-Berni J, Fischer RA, Deery DM, Smith DJ. Review: high-throughput phenotyping to enhance the use of crop genetic resources. *Plant Sci*. 2019;282:40–8. <https://doi.org/10.1016/j.plantsci.2018.06.017>.
137. van Eeuwijk FA, Bustos-Korts D, Millet EJ, Boer MP, Kruijer W, Thompson A, et al. Modelling strategies for assessing and increasing the effectiveness of new phenotyping techniques in plant breeding. *Plant Sci*. 2019;282:23–39. <https://doi.org/10.1016/j.plantsci.2018.06.018>.
138. Pauli D, Chapman SC, Bart R, Topp CN, Lawrence-Dill CJ, Poland J, et al. The quest for understanding phenotypic variation via integrated approaches in the field environment. *Plant Physiol*. 2016;172:622–34. <https://doi.org/10.1104/pp.16.00592>.
139. Weiss M, Jacob F, Duveiller G. Remote sensing for agricultural applications: a meta-review. *Remote Sens Environ*. 2020;236: 111402. <https://doi.org/10.1016/j.rse.2019.111402>.
140. Mattupalli C, Seethepalli A, York LM, Young CA. Digital imaging to evaluate root system architectural changes associated with soil biotic factors. *Phytophysics*. 2019;3:102–11. <https://doi.org/10.1094/PHYTO-08-12-0207-R>.
141. Arias MMD, Leandro LF, Munkvold GP. Aggressiveness of *Fusarium* species and impact of root infection on growth and yield of soybeans. *Phytopathology*. 2013;103:822–32. <https://doi.org/10.1094/PHYTO-08-12-0207-R>.
142. APPE Automated Phenotyping System. <https://www.plantphenomics.org.au/technologies/#greenhouses>. Accessed 28 Apr 2021.
143. Controlled Environment Phenotyping Facility (CEPF). <https://ag.purdue.edu/cepf/>. Accessed 31 Mar 2021.
144. PhenoConveyor-Plant Phenomics Research Center (PPRC). http://pprcen.njau.edu.cn/Research/R_D_Platforms.htm. Accessed 31 Mar 2021.
145. Wilkinson MD, Dumontier M, Aalbersberg IJJ, Appleton G, Axton M, Baak A, et al. Comment: the FAIR guiding principles for scientific data management and stewardship. *Sci Data*. 2016;3:1–9. <https://doi.org/10.1038/sdata.2016.18>.
146. Ferentinos KP. Deep learning models for plant disease detection and diagnosis. *Comput Electron Agric*. 2018;145:311–8. <https://doi.org/10.1016/j.compag.2018.01.009>.
147. Singh AK, Ganapathysubramanian B, Sarkar S, Singh A. Deep learning for plant stress phenotyping: trends and future perspectives. *Trends Plant Sci*. 2018;23:883–98. <https://doi.org/10.1016/j.tplants.2018.07.004>.
148. Papoutsoglou EA, Faria D, Arend D, Arnaud E, Athanasiadis IN, Chaves I, et al. Enabling reusability of plant phenomic datasets with MIAPPE 1.1. *New Phytol*. 2020. <https://doi.org/10.1111/nph.16544>.
149. De Torres ZM, Littlejohn G, Jayaraman S, Studholme D, Bailey T, Lawson T, et al. Chloroplasts play a central role in plant defence and are targeted by pathogen effectors. *Nat Plants*. 2015;1:15074. <https://doi.org/10.1038/nplants.2015.74>.
150. Brugger A, Kuska MT, Mahlein A-K. Impact of compatible and incompatible barley—*Blumeria graminis* f. sp. hordei interactions on chlorophyll fluorescence parameters. *J Plant Dis Prot*. 2017. <https://doi.org/10.1007/s41348-017-0129-1>.

151. Bauriegel E, Brabandt H, Gärber U, Herppich WB. Chlorophyll fluorescence imaging to facilitate breeding of *Bremia lactucae*-resistant lettuce cultivars. *Comput Electron Agric.* 2014;105:74–82. <https://doi.org/10.1016/j.compag.2014.04.010>.
152. Pineda M, Olejníčková J, Cséfalvay L, Barón M. Tracking viral movement in plants by means of chlorophyll fluorescence imaging. *J Plant Physiol.* 2011;168:2035–40. <https://doi.org/10.1016/j.jplph.2011.06.013>.
153. Gold KM, Townsend PA, Herrmann I, Gevens AJ. Investigating potato late blight physiological differences across potato cultivars with spectroscopy and machine learning. *Plant Sci.* 2020;295: 110316. <https://doi.org/10.1016/j.plantsci.2019.110316>.
154. Arens N, Backhaus A, Döll S, Fischer S, Seiffert U, Mock H-P. Non-invasive Presymptomatic Detection of *Cercospora beticola* Infection and Identification of Early Metabolic Responses in Sugar Beet. *Front Plant Sci.* 2016. <https://doi.org/10.3389/fpls.2016.01377>.

Publisher's Note

Springer Nature remains neutral with regard to jurisdictional claims in published maps and institutional affiliations.

Ready to submit your research? Choose BMC and benefit from:

- fast, convenient online submission
- thorough peer review by experienced researchers in your field
- rapid publication on acceptance
- support for research data, including large and complex data types
- gold Open Access which fosters wider collaboration and increased citations
- maximum visibility for your research: over 100M website views per year

At BMC, research is always in progress.

Learn more biomedcentral.com/submissions



Chapter 3

Time course sensor-based phenotyping can predict Ascochyta blight disease severity in Cicer species

3.1 Declarations

Statement of Authorship

Title of Chapter	Time course sensor-based phenotyping can predict Ascochyta blight disease severity in Cicer species
Publication Status	Written in a manuscript style, to be submitted
Publication Details	Manuscript to be submitted to <i>Journal of Experimental Botany</i>

Principal Author

Name of Principal Author	Florian Tanner
Contribution to the Paper by the Candidate	Conception, Experimentation, Analysis, Drafting.
Overall percentage Certification	80%
Signature	This paper reports on original research I conducted during the period of my Higher Degree by Research candidature and is not subject to any obligations or contractual agreements with a third party that would constrain its inclusion in this thesis. I am the primary author of this paper.
Date	2022-12-08

Co-Author Contributions

By signing the Statement of Authorship, each author certifies that:

- the candidate's stated contribution to the publication is accurate (as detailed above);
- permission is granted for the candidate to include the publication in the thesis; and
- the sum of all co-author contributions is equal to 100% less the candidate's stated contribution.

Name of Co-Author	Judith Atieno
Contribution to the Paper	Conception, Drafting, Experimentation
Signature	
Date	09/12/2022

Name of Co-Author	Sara Blake
Contribution to the Paper	Experimentation, Performed Visual Scoring in 2021 and 2022
Signature	
Date	09/12/2022

Name of Co-Author	Marzena Krysinska-Kaczmarek
Contribution to the Paper	Experimentation
Signature	
Date	December 08, 2022
Name of Co-Author	Christopher Boyce
Contribution to the Paper	Conceived Lesion Detection Algorithm
Signature	
Date	December 08, 2022
Name of Co-Author	Chris Brien
Contribution to the Paper	Advice on Split Plot Design and Longitudinal Analysis
Signature	
Date	
Name of Co-Author	Kenneth Clarke
Contribution to the Paper	Drafting, Analysis
Signature	
Date	December 08, 2022
Name of Co-Author	Darren Plett
Contribution to the Paper	Conception
Signature	
Date	December 08, 2022
Name of Co-Author	Jennifer Davidson
Contribution to the Paper	Conception, Experimentation, Performed Visual Scoring in 2020 and 2021
Signature	
Date	<i>JUD - 10/12/22</i>
Name of Co-Author	Bettina Berger
Contribution to the Paper	Conception, Drafting
Signature	
Date	December 08, 2022

3.2 Manuscript

1 Time course sensor-based phenotyping can predict *Ascochyta*
2 blight disease severity in *Cicer* species

3 Florian Tanner^{1*}, Judith Atieno^{2,3}, Sara Blake^{2,3}, Marzena Krysinska-Kaczmarek³,
4 Chris Boyce⁴, Chris Brien¹, Kenneth Clarke¹, Darren Plett¹, Jennifer Davidson^{2,3},
5 and Bettina Berger¹

6 ¹Australian Plant Phenomics Facility, School of Agriculture, Food & Wine,
7 University of Adelaide, Adelaide, SA, Australia

8 ²School of Agriculture, Food & Wine, University of Adelaide, Adelaide, SA,
9 Australia

10 ³South Australian Research and Development Institute, Adelaide, SA, Australia

11 ⁴School of Computer Science, University of Adelaide, Adelaide, SA, Australia

12 *Corresponding author. Email: florian.tanner@adelaide.edu.au

13 Abstract

14 *Ascochyta* blight is a widely occurring chickpea fungal disease that can cause severe yield
15 loss. Breeding the crop for resistance requires a high-throughput evaluation of plant-pathogen
16 interactions in genotypes that can serve as sources of resistance. Current practice for the
17 evaluation is human visual scoring of disease symptoms, which is limited in throughput and
18 precision. Here, we developed open-source sensor-based phenotyping methods using RGB and
19 multispectral imaging to measure resistance components and predict disease severity classes in
20 chickpea and wild relatives grown outdoors over three seasons. Pots were imaged over time from
21 a ground-based platform, providing 86,792 RGB and 8,199 multispectral images. Lesion count
22 was estimated with YOLOv5 object detection (F1 score = 0.27 - 0.30), fractional green canopy
23 cover was estimated from RGB images, and vegetation indices were extracted from multispectral
24 images. A model trained on growth rates normalized to control genotypes could predict disease
25 severity classes with an accuracy of 65 - 81 % ($\kappa = 0.43 - 0.59$) on unseen independent data
26 from three different seasons. The developed methods provide a pathway to predict visual disease
27 severity scores and support the breeding of crops for disease resistance. They may also be used to
28 characterize disease progression, to find underlying resistance mechanisms, and for early disease
29 detection.

1 Introduction

Chickpea (*Cicer arietinum*) is an important food legume with an average global production of 13.13 Mt per year in the period from 2010 to 2020 [1]. During that period, Australia was the second largest producer after India with an average yearly production of 0.79 Mt [1]. Ascochyta blight (AB), caused by the necrotroph fungus *Ascochyta rabiei* (syn. *Phoma rabiei*, NCBI:txid5454), is a major yield-limiting biotic stress for chickpea [2]. After successful infection, the fungus induces necrosis on all above-ground plant parts, including leaves, stems, and pods. Necrotic lesions on leaves and stems cause defoliation and stem breakage. Combined, the symptoms can lead to severe quantitative and qualitative yield loss [3]. Currently, there are no cultivars available in Australia that are resistant to prevalent isolates, leading farmers to rely on multiple applications of fungicides [4, 5]. Breeding for disease resistance is an economically and environmentally sustainable option to decrease the reliance on fungicides, but requires large-scale disease screening of genetic resources within the cultivated species itself and also within its wild relatives [6–8]. Resistant candidate genotypes have previously been reported in wild relatives of chickpea, including *Cicer bijugum*, *C. judaicum*, *C. pinnatifidum*, *C. reticulatum*, and *C. echinospermum* [9–12]. Multiple resistance mechanisms to AB are known, including physical barriers [13], constitutive and accumulated phenolic compounds [14], phytoalexins [15–17], reactive oxygen species signaling [14, 18], and hypersensitive response [3].

Phenotyping for disease resistance Traditionally, disease severity is visually evaluated by experts who judge the extent of signs and symptoms using defined rating scales [19]. This approach is limited by potential human error, subjectivity, and the innate restriction to the visible light spectrum [20]. Instead of visual scoring, sensor-based phenotyping has the potential to increase precision, throughput, and extend the range of perceptible signs and symptoms beyond visible light [21]. In this way, specific signs and symptoms can be quantified and used to judge the resistance as well as predict disease severity scores. However, this remains difficult under field conditions [22, 23].

Extraction of phenotypic data from sensor data Several processing steps are involved to extract phenotypic data from sensor data [22]. At a minimum, sensor data need to be calibrated to incident radiation, which can vary when imaging outside, spectral channels need to be aligned, and regions of interest need to be assigned. These still fairly raw data can be used in deep learning approaches to directly predict a response variable of interest; however, this can limit the explainability and transferability of the models [24]. A further step in the analysis can be the extraction of features from the measured data, so-called low-level traits which include canopy cover, estimated biomass, vegetation indices, and the morphology of signs and symptoms of disease (Table 1) [22, 23, 25, 26]. From these low-level traits measured at individual time points, intermediate traits such as the timing of defined phenotypic stages, dose-response curves, or area-under-the-curve traits can be extracted in a next step [27]. To estimate the treatment and genetic effects on traits, the effects need to then be distinguished from spatial and longitudinal noise [26].

66 **Sensor-based field phenotyping for necrotic pathogens** For necrotic pathogens including *A.*
67 *rabiei*, major resistance components that contribute to field resistance are the latency period after
68 infection before lesions appear, the total lesion and pycnidia production which drives secondary
69 infections, and the ability to maintain healthy biomass under disease pressure [3, 28]. To estimate
70 these traits, lesion count and biomass need to be measured over time, which requires non-destructive
71 techniques. Plant biomass can be measured accurately and non-destructively by 3D reconstruction
72 of plant material [29]. A simpler alternative is to estimate plant biomass by measuring canopy
73 cover or vegetation indices that represent plant health [30, 31]. For chickpea, biomass was shown to
74 closely correlate with fresh biomass (Berger, unpublished data). All these options for the estimation
75 of biomass have been successfully performed in the field [32].

76 The detection of necrotic lesions in the field is less common, but has successfully been performed
77 using RGB imaging from a drone on maize infected with Northern Leaf Blight with object detection
78 algorithms [33, 34]. However, Northern Leaf Blight lesions on corn are larger (10 - 50 mm) than
79 the leaf lesions of chickpea AB (< 5 mm). Another successful example was the detection of *Cer-*
80 *cospora* leaf spot lesions on sugar beet. As these lesions are smaller (2 to 5 mm), a ground-based
81 phenotyping platform had to be used to achieve a high spatial resolution [35]. On soybeans infected
82 with *Cercospora sojina*, lesion count, lesion size, and percentage diseased leaf area were measured
83 using an ImageJ macro based on thresholding [36]. The authors were able to achieve near-perfect
84 correlations with manually measured ground truth, but destructive sampling of individual leaves
85 and controlled imaging had to be used.

86 **Sensor based field phenotyping for AB** Sensor-based phenotyping has also been applied to
87 AB in the field [37]. Zhang et al. tested multiple fungicides on two infected chickpea genotypes and
88 imaged the plots from an octacopter with a thermal camera, a five-band multispectral camera, and
89 a modified RGB camera that captured the infrared channel instead of the red channel. Traits were
90 extracted for individual imaging timepoints and the correlation with visual scores on a scale from
91 one to nine was tested. Depending on the stage of growth of the plants, the traits with the highest
92 absolute correlation coefficients were percentage of canopy coverage ($r = 0.35 - 0.82$), Normalized
93 Difference Vegetation Index (NDVI) ($r = 0.61 - 0.72$), Green Normalized Difference Vegetation Index
94 (GNDVI) ($r = 0.52 - 0.69$), Normalized Difference Red Edge Index (NDRE, also RENDVI) ($r = 0.34$
95 $- 0.67$), and mean canopy temperature from thermal cameras ($r = 0.32 - 0.81$) (Table 1) [37]. This
96 study showed the suitability of sensor-based phenotyping of AB in the field, but also highlighted
97 the need to account for temporal variation along the developmental stages as the various traits had
98 different importance depending on the imaging time point.

99 The objectives of this study were to develop sensor-based phenotyping methods to support AB
100 resistance breeding and for early detection of AB. We measured canopy cover, lesion count, and
101 vegetation indices over time and extracted intermediate traits. These were used to define resistance
102 components and to classify disease scores into three categories (High, Medium, Low).



Figure 1: Nursery disease screens, main part with pots in rows of four is shown.

103 2 Materials and methods

104 2.1 Experimental design

105 A selection of chickpea genotypes (*Cicer arietinum*) and wild relatives (*Cicer reticulatum* and *Cicer*
106 *echinospermum*), were screened for resistance to AB in semi-controlled outdoor conditions. The
107 screens took place on the Waite Campus of the University of Adelaide (34°58'12.0"S 138°38'24.0"E)
108 in the seasons 2020, 2021, and 2022. Five seeds per pot were sown on 2020-06-18, 2021-06-16, and
109 2022-06-08, respectively, and grown in Van Schaik's Bio Gro soil mix (Bio Gro Pty Ltd., Mount
110 Gambier, South Australia) in pots with 2.1 l volume and a diameter of 155 mm (Figure 1). The
111 pots themselves were placed on a sandy layer above the top soil in a netted terrace. Each pot was
112 thinned to four plants after emergence at 46 days after sowing (DAS) in 2020, 30 DAS in 2021, and
113 36 DAS in 2022 (Figure 2). The pots were arranged in rows with a width of four pots and grown in a
114 randomized complete block design with three replicates per genotype and treatment. Irrigation was
115 performed with an overhead system that was scheduled on demand depending on the environmental
116 conditions.

117 In 2021 and 2022, a subset of 30 genotypes each was grown with disease-infected treatment
118 and a control that was not infected and treated with chlorothalonil fungicide (Bravo Weather Stik,
119 Syngenta Crop Protection, 720 g^l⁻¹ applied at 10 ml per pot) to prevent cross-infection from infected
120 pots. Fungicide was applied on the day of infection of the other pots, 22 days after infection (DAI),
121 and 43 DAI in 2021. The same fungicide treatment was applied in 2022 at -1 DAI, 21 DAI, 28 DAI
122 and 44 DAI (Figure 2). Three replicates of each genotype and treatment combination were grown
123 in a split-unit design, resulting in a total of 180 pots each; the treatments were assigned to the main
124 units and the genotypes to the subunits. These subsets, including fungicide controls, were used to
125 develop the screening methods specific for AB. Instead of being placed in rows of four, these pots
126 were spaced further apart in rows of three to avoid overlap of neighboring plant material (Figure 2).

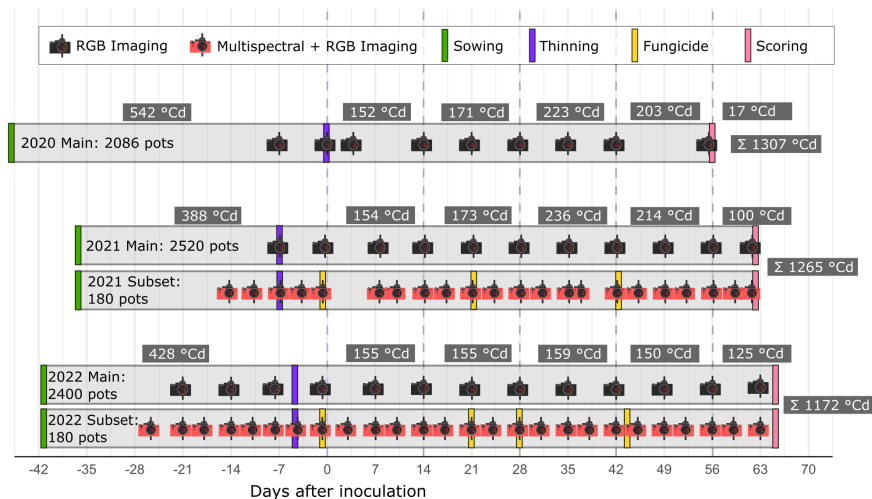


Figure 2: Experimental design for all experiments, mean daily temperature sums per period are shown, calculated with a base temperature of 0 °C. The periods stretch from sowing until inoculation, 0 to 14 DAI, 14 to 28 DAI, 28 to 42 DAI, 42 to 56 DAI, and from 56 DAI until scoring.

127 **Plant material** The screened genotypes were grouped into five categories: Australian varieties,
 128 wild *Cicer* accessions from a collection mission in eastern Turkey [38], breeding and research material
 129 from ICARDA’s Food Legume Improvement Program (FLIP) [39], landraces from the N.I. Vavilov
 130 Research Institute of Plant Industry and introgression lines (Supplementary Table 7). Cultivars
 131 Howzat (susceptible to AB) and Genesis090 (moderately susceptible to AB) were included as controls
 132 [9, 40, 41].

133 **Inoculation and fungal material** Each pot was inoculated with 3 ml of spore suspension of
 134 *A. rabiei* isolate 16CUR018 (collected from cultivar Genesis090 in Curyo, Victoria, Australia in
 135 2016) with a concentration of 1×10^6 spores per ml and surfactant Tween 20 (0.01%) (Merck Pty
 136 Ltd.) [42]. The inoculum was sprayed onto the plants using a commercial hand sprayer (Hardi,
 137 Australia). Two passes in opposite directions were made while walking along the rows of pots. After
 138 inoculation, plants were continuously misted for 30 seconds every 30 minutes for the entire season to
 139 enable polycyclic infection. Misting was temporarily interrupted after rain events. Inoculation was
 140 carried out on 2020-08-03 (46 DAS), 2021-07-20 (37 DAS), and 2022-07-19 (41 DAS) (Figure 2).

141 2.2 Data acquisition

142 Scoring

143 Experts scored visual symptoms of the disease 56 DAI in 2020, 62 DAI in 2021, and 65 DAI in
 144 2022, without knowing the treatment or genotype (Figure 2). The four plants per pot were scored
 145 simultaneously on a scale from 0 - 100 % for four traits: percentage of broken main stems, percentage

146 of main stems with lesions, percentage of diseased side branches, and percentage of diseased leaf area
147 [19, 43]. The four traits were then averaged to form a Disease Index (DI) which can take any value
148 between 0 and 100, where 0 corresponds to a pot free of symptoms and 100 corresponds to a pot with
149 dead plants. For the purpose of classification of disease scores and supporting breeding decisions
150 with the developed screening methods, pots were grouped into three categories based on disease
151 index. $DI > 80$ was considered as material to be rejected (High DI), $DI \leq 80$ to $DI > 40$ was
152 considered acceptable (Medium DI) and $DI \leq 40$ was considered as elite material (Low DI). To
153 investigate the repeatability of scoring, 28 pots representative of the range of genotype groups and
154 disease severity were each scored twice independently by two expert raters in 2021. The overall
155 accuracy and Cohen's κ for the overlap of the score categories between each combination of scorer
156 and round of scoring were then calculated as a measure of repeatability [44].

157 **Imaging**

158 **RGB imaging** The plants were imaged at multiple time points throughout the season using a
159 ground-based phenotyping pushcart built from T-slot aluminium profiles (Figure 2). The cart was
160 pushed along the rows of pots on C-shaped steel rails. RGB images were taken with a digital single-
161 lens reflex camera (2020: Canon EOS 1300D, 2021 & 2022: Canon EOS 1500D) mounted on the
162 aluminium frame at a nadir angle at a height of 1.4 m. The camera settings were as follows: An
163 18-55 mm kit lens at 18 mm focal length (29 mm full frame equivalent), ISO = 200 or 400 depending
164 on light conditions, aperture = f/8, automatic white balance, shutter speed adjusted automatically
165 according to light conditions, format = 14 bit raw (cr2 format). The height of the pushcart combined
166 with the sensor resolution resulted in a ground sample distance of 0.26 mm / pixel (px) width for
167 the Canon EOS 1300D and a ground sample distance of 0.23 mm / px width for the Canon EOS
168 1500D (Supplementary Figure 12).

169 **Multispectral imaging** The subset experiments of 2021 and 2022 were additionally imaged with
170 a multispectral camera (RedEdge-3, MicaSense, Seattle, WA, USA) with a spatial resolution of 1280
171 * 960 px, resulting in a ground sample distance of 0.78 mm / px width (Figure 2). The camera
172 records five spectral channels between visible (VIS) and near-infrared (NIR) with center wavelengths
173 of 475, 560, 668, 717, and 840 nm and respective bandwidths of 20, 20, 10, 10, and 40 nm.

174 **Imaging in automated phenotyping system** In the season of 2021, 831 pots were selected to
175 represent the range of disease severities and plant species and were imaged in an automated phe-
176 notyping system (The Plant Accelerator, <http://www.plantphenomics.org.au/services/accelerator/>)
177 immediately after scoring (2021-09-21 to 2021-09-23). The imaging system is described in detail by
178 Atieno et al. [45]. Briefly, multi angle RGB-images are taken and LemnaGrid (LemnaTec, Ger-
179 many) software is used to measure projected shoot area (PSA), which has been shown to closely
180 correlate with shoot biomass (Berger, unpublished data). In addition, fractional green canopy cover
181 (FGCC) was measured as described in section 2.3. In a next step, the accuracy of the in situ FGCC
182 estimates from the DSLR camera was evaluated by a correlation analysis with the measurements
183 from the automated phenotyping system.

184 2.3 RGB image analysis

185 **Raw development and pre-processing** Conversion of raw data to RGB raster images (png
186 format) was performed using RawTherapee version 5.8 applying lens correction, automatic white
187 balance and dynamic range compression to address lighting differences resulting from shading and
188 cloud cover [46]. The images were cropped to the individual pots by manually adjusting a mask on
189 which the positions of the pots could be detected using Inkscape version 1.1 [47].

190 **Foreground segmentation** Next, pot images were segmented into foreground and background
191 pixels, where healthy plant material was classified as foreground, and soil and diseased plant pixels
192 were classified as background. A training set containing 20 images from different time points was
193 annotated using the software GIMP version 2.10.14 [48]. A multilayer perceptron neural network
194 (MLP-NN) was then trained on the RGB values of annotated foreground pixels and a kernel of 3×3
195 neighboring pixels, resulting in a total of 27 values for each pixel [49]. The training and segmentation
196 was performed using Python version 3.8.10 packages `scipy` (v1.7.1), `numpy` (v1.21.2) and `OpenCV`
197 (v4.5.2) [50–53]. As a next step, erosion followed by dilation with a 3×3 kernel was applied. To
198 exclude non-plant material, connected component-analysis with a size threshold of 150 pixels for
199 the Canon EOS 1500D and a threshold of 110 pixels for the Canon EOS 1300D was applied. The
200 predicted binary masks were evaluated based on visual inspection. Finally, FGCC was calculated as
201 the ratio of foreground pixels to total pot pixels (Table 1) [31].

202 **Lesion detection** The YOLOv5 (v6.2) object detection algorithm was used for lesion detection
203 on processed png images [54]. A total of 1500 images from the 2021 dataset were annotated with
204 bounding boxes marking the locations of the lesions using the `labelImg` version 1.8.6 tool [55].
205 Training data was randomly chosen from both inoculated and fungicide-treated pots, stratified by
206 date and annotated without knowledge of genotype, imaging time point, and treatment. Of the
207 training images, 37% contained lesions. The data was split into training and validation set with
208 an 80:20 split. An additional test set of 2020 data containing 300 images was annotated. Multiple
209 network architectures were trained on the training set and evaluated with the validation set from
210 2021 based on the F1 metric. The medium-sized 5m.pt architecture was chosen as a compromise
211 between speed and performance. Finally, the network was evaluated on the unseen data from 2020.
212 The networks were trained for a maximum of 600 epochs, and hyperparameters were set to default.
213 All training was performed on a local machine with a Nvidia Quadro P1000 GPU. Then the lesion
214 detection was applied to all datasets and the number of lesions was extracted.

215 2.4 Multispectral image analysis

216 The images were pre-processed and calibrated to incident radiation at each imaging date using the
217 Python `imageprocessing` library provided by Micasense [56]. As the imaging distance was fixed to
218 1.4 m, spatial alignment of the five spectral channels was achieved by hard-coding the offset between
219 each channel and merging all channels into one tiff file. Semantic segmentation was performed with
220 MLP-NN classifiers trained on the five pixel values for all channels for each date. For the 2021

Table 1: Extracted low-level traits from RGB camera and RedEdge 5-band multispectral camera.

Abbreviation	Trait	Equation	Citation
Extracted from RGB camera			
FGCC	Fractional Green Canopy Cover	$\frac{n_{foreground\ pixels}}{n_{total\ pixels}}$	[31]
n lesions	Number of lesions	As detected with YOLOv5	[54]
Vegetation indices extracted from RedEdge 5-band camera			
ENDVI	Enhanced Normalized Difference Vegetation Index	$\frac{(NIR-Green)-(2\times Blue)}{(NIR+Green)+(2\times Blue)}$	[57]
GNDVI	Green Normalized Difference VI	$\frac{(NIR-Green)}{(NIR+Green)}$	[58]
NGRDI	Normalized Green-Red Difference Index	$\frac{(Green-Red)}{(Green+Red)}$	[60]
NDVI	Normalized Difference VI	$\frac{(NIR-Red)}{(NIR+Red)}$	[61]
RENDVI	Red Edge Normalized Difference VI	$\frac{(NIR-RedEdge)}{(NIR+RedEdge)}$	[58]

221 data, an individual classifier was trained for each imaging date for which the training data was
 222 made up of 1000 foreground and background pixels from the specific imaging date, as well as 100
 223 foreground and background pixels from each of the dates, resulting in a total of 6400 training pixels
 224 per date. Segmentation was evaluated on the basis of accuracy using a 70:30 train-test split. For the
 225 segmentation of the entire dataset of 2022, a single pixel classifier that was trained for the imaging
 226 date 35 DAI in 2021 was used and evaluated by examining the predicted masks.

227 **Feature extraction** After segmentation, the reflectance of foreground pixels was averaged and
 228 vegetation indices (VI) ENDVI, GNDVI, NGRDI, NDVI and RENDVI were calculated (Table 1)
 229 [57–61]. To evaluate the agreement of semantic segmentation between RGB and multispectral sensor,
 230 FGCC from both sensors was compared.

231 2.5 Spatio-temporal modeling

232 All statistical analyses were performed using R version 4.2.1 [62]. Pots where the maximum FGCC
 233 over all timepoints did not exceed a value of 0.05 were considered to not have germinated and removed
 234 before spatio-temporal modeling. Spatio-temporal analysis was implemented in the `statgenHTP`
 235 v1.0.5 package for all extracted intermediate traits [26, 63, 64]. In a first step, each pot was considered
 236 individually over time and outliers identified by local regression were removed. The parameters for
 237 the individual pot outlier removal were chosen based on visual inspection of the splines. A smoothing
 238 parameter of 0.8 and a confidence interval of 4 were used for each feature of the subset parts of the
 239 experiments. For the main parts, a smoothing parameter of 0.8 and confidence interval sizes of 2.5 for

240 FGCC and 3.5 for number and size of lesions were used for 2022, and a confidence interval size of 2.5
 241 for all traits in the main parts was used in 2020 and 2021. Where more than 25% of pot observations
 242 at a single time point were flagged as outliers, the entire imaging time point was removed from the
 243 analysis for the respective trait. Next, a two-dimensional P-spline was fitted for spatial modeling
 244 at each time point and lastly, longitudinal splines with 5 knots for the main experiment parts and
 245 10 knots for the fungicide treated experimental subsets were fitted to the spatially corrected data
 246 for each pot. The fitted splines were then used to extract intermediate traits [26]. In addition to
 247 the manual outlier removal that was applied before fitting the models, a rule-based outlier removal
 248 was applied to the modeled time-course of the individual experiments. For the main parts in 2020,
 249 2021 and 2022, pots that did not exceed an FGCC of 0.03 at 0 DAI were removed from the analysis
 250 to account for non-germinated pots. Due to the proximity of the pots in the main parts where the
 251 pots were grown in rows of four, overlapping plant material was observed from neighboring pots in
 252 the late stages of growth. To remove the pots where a high FGCC was reached only due to overlap
 253 from neighboring pots towards later growth stages, pots that met two conditions were also removed:
 254 (i) an average FGCC of less than 0.08 between 7 and 28 DAI and (ii) an average FGCC of more
 255 than 0.12 after 28 DAI. For the subset parts in 2021 and 2022, little overlap was observed due to
 256 the spacing of the pots. Therefore, the only outliers that were removed were all pots that did not
 257 exceed a maximum of 0.05 for the fitted FGCC over the entire time, accounting for non-germinated
 258 pots.

259 2.6 Intermediate trait extraction

260 After visual inspection of the fitted FGCC splines from the subset experimental part of 2021, eight
 261 intermediate traits were extracted from the fitted splines for the RGB data (Supplementary Figure
 262 10). The relative change of FGCC ($RGR = 100 \times \frac{FGCC_2 - FGCC_1}{FGCC_1}$) over four biweekly periods
 263 (RGR_{0-14} , RGR_{14-28} , RGR_{28-42} , RGR_{42-56}) was chosen to represent the plant response (Figure
 264 4) [31, 65, 66]. The number of days until the first maximum of the spline after inoculation was defined
 265 as the Breaking Day when FGCC starts to decline. An additional relative growth rate (RGR_{crit})
 266 was then defined as the change between FGCC on the average Breaking Day of control cultivars
 267 Howzat and Genesis090 within each experimental subset and FGCC 14 days after the Breaking Day.

268 The Latent Period until the appearance of lesions, defined as days after infection until a minimum
 269 of three lesions are detected on the leaves, was calculated from the fitted splines for the number of
 270 lesions. A threshold of three lesions rather than a single lesion was chosen to limit the amount of
 271 false positives.

272 For each of the vegetation indices, FGCC and the number of lesion, the area under the curve
 273 (AUC) of the splines was estimated by integrating the daily modeled values between 0 and 42 DAI
 274 ($Trait_{AUC} = \sum_{dai=0}^{42} Trait_{dai}$) [67].

275 2.7 Genotypic and treatment effects

276 To estimate the effects of genotype and treatment on intermediate traits in the subset experimental
 277 parts, mixed models were fitted using the R package `statgenGxE` [68] version 1.0.5 with treatment

278 (T) and treatment by year of trial (T:Y) as fixed effects and the rest including genotype (G) as
 279 random effects.

$$y = T + T : Y + (1|G) + (1|G : T) + (1|G : T : Y)$$

280 2.8 Predictive models

281 **Disease index classification** The models were developed and evaluated in the `tidymodels` ver-
 282 sion 1.0.0 framework [69]. The score category of each pot was predicted using intermediate traits
 283 from each RGB-only, multispectral-only, and both sensors combined. A multilayer perceptron neu-
 284 ral network classifier (MLP-NN) and logistic regression classifier were tested and evaluated based
 285 on estimated area under the receiver operating characteristic curve (ROC AUC) from five-fold CV
 286 with five repeats. To determine the variable importance of traits for the prediction of disease index
 287 classes, 500 random forest models with different random seeds were fitted to the subset datasets of
 288 2021 and 2022 individually. Permutation-based variable importance scores, based on the decrease in
 289 model performance when the variable is randomly shuffled, were then extracted for all models using
 290 the `vip` v0.3.2 package [70–72].

291 **Early detection of infection** Predictive models to distinguish fungicide treated pots from in-
 292 fected pots as early as possible were trained on the daily values of the modeled traits FGCC, number
 293 of lesions, and the five vegetation indices in increments of two days. Hence, the naive model at 0
 294 DAI included seven predictors from 0 DAI. The model at 2 DAI included the predictors from both
 295 0 DAI and 2 DAI. Each subsequent model included the traits from previous dates as predictors, as
 296 well as the most recent ones. A MLP-NN was trained on the data from the individual years after a
 297 dimensionality reduction to seven principal components and tested on the respective opposite year.
 298 Permutation testing was used to evaluate whether the algorithms performed significantly better than
 299 a random classifier.

300 3 Results

301 3.1 Visual scores

302 Most pots that did not receive fungicide showed high disease indices, with a large proportion of pots
 303 completely dead at the time of scoring in the three years of main parts (Figure 3, Supplementary
 304 Table 7). The control cultivars Howzat and Genesis090 were scored consistently throughout the
 305 main parts of the three seasons, with average disease indices (\pm standard deviation) of 98 ± 5 ,
 306 94 ± 11 , 90 ± 11 for Howzat and 68 ± 13 , 76 ± 7 , 57 ± 3 for Genesis090 in 2020, 2021 and 2022,
 307 respectively. In the infected pots of the subset parts, Howzat was scored 100 ± 0 in 2021 and 73 ± 10
 308 in 2022 and Genesis090 was scored 84 ± 11 in 2021 and 59 ± 14 in 2022, indicating that the disease
 309 pressure was lower in 2022 than in 2021. The candidate resistant accession WLD085 consistently
 310 achieved the lowest mean DI across all genotypes in all experiments where it was included (2020
 311 main: $\bar{DI} = 13 \pm 11$, 2021 Main: $\bar{DI} = 8 \pm 7$, 2022 Main: $\bar{DI} = 15 \pm 5$, 2022 Subset: $\bar{DI} = 8 \pm 2$). The

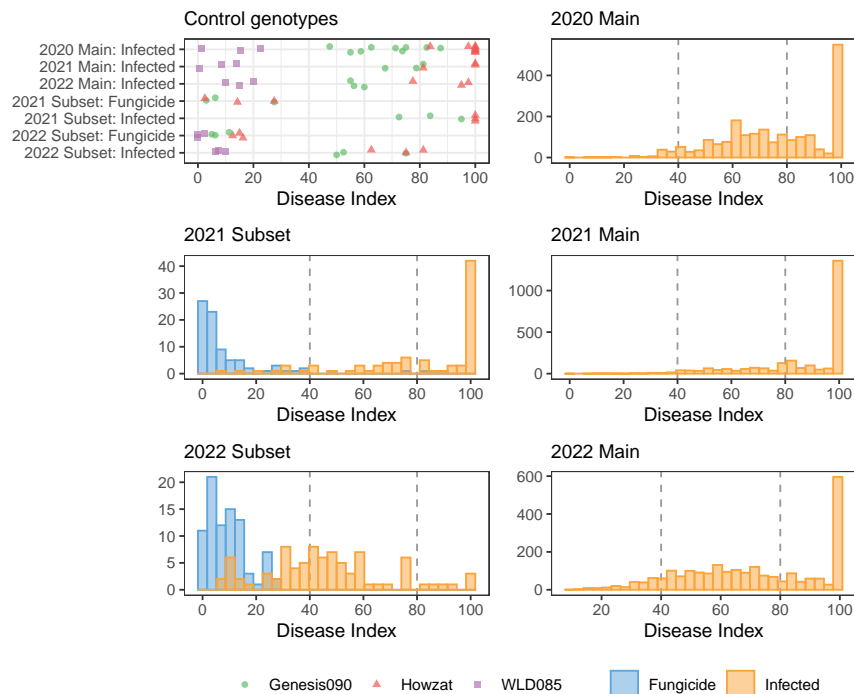


Figure 3: Histograms of scores for all disease screens and dot plot of disease indices of control genotypes Genesis090 and Howzat and candidate resistant genotype WLD085 (not included in 2021 subset). Dashed lines represent cut-offs for score categories (High DI, Medium DI, Low DI).

312 fungicide treatment was not able to completely prevent AB infection in both years with treatment
 313 averages of 81 ± 24 for infected pots and 11 ± 19 for pots treated with fungicides in 2021 and 46 ± 23
 314 for infected pots and 9 ± 7 for fungicide-treated pots in 2022. All interaction effects of genotype,
 315 treatment and year as well as main effects were significant for the disease indices (Supplementary
 316 Table 5).

317 **Repeatability of visual scoring** Within-scorer repeatability was high with overall accuracies of
 318 96 % ($\kappa = 0.93$) for scorer A and 96 % ($\kappa = 0.89$) for scorer B, but the between-scorer repeatability
 319 was lower with accuracies ranging from 75 % ($\kappa = 0.47$) to 79 % ($\kappa = 0.55$) (Table 2).

Table 2: Accuracies and Cohen’s κ for repeated scoring. 28 pots were scored independently twice by two different expert raters. All three classes of scores (Low, Medium, High) were represented.

Truth	Estimate	Accuracy	κ
Within scorer			
Scorer A, Round 1	Scorer A, Round 2	96.43 %	0.93
Scorer B, Round 1	Scorer B, Round 2	96.43 %	0.89
Between scorer			
Scorer A, Round 1	Scorer B, Round 1	75.00 %	0.48
Scorer A, Round 1	Scorer B, Round 2	75.00 %	0.48
Scorer A, Round 2	Scorer B, Round 1	75.00 %	0.47
Scorer A, Round 2	Scorer B, Round 2	78.57 %	0.55

3.2 Evaluation of low-level trait extraction

FCCC can be estimated both with RGB and multispectral data The accuracy of semantic segmentation of multispectral images for the 2021 data was 91 % for the first imaging date (27 DAS \equiv -7 DAI) and then ranged between 96 and 98 % for the remaining imaging time points. For multispectral data from 2022 and RGB data, semantic segmentation was only evaluated visually based on predicted masks. Pearson’s correlation coefficients between FGCC derived from the RGB camera and the multispectral camera were 0.97 and 0.98 in 2021 and 2022, respectively. This indicates that even under difficult lighting conditions, both RGB and multispectral camera can accurately estimate FGCC.

In situ measurements of FGCC are strongly correlated to plant shoot area Out of the 831 plants that were imaged in the automated phenotyping system after scoring in the 2021 season, 661 belonged to the main experimental set and 170 belonged to the subset and were chosen to test the accuracy of the in situ imaging. PSA and FGCC derived from both images in the nursery and images in the automated phenotyping system were all strongly and significantly correlated (Table 3). In an unrelated previous calibration experiment of the automated phenotyping system using *cv.* Genesis090 at various growth stages, a Pearson correlation of 0.99 between fresh weight and PSA was observed (Berger, unpublished data). These combined results indicate that in situ measurements of FGCC can be used to estimate chickpea shoot biomass.

Table 3: Pearson correlations between low-level traits measured in an automated phenotyping system ('PSA' and 'FGCC controlled') with FGCC measured in situ. (***) indicates $p < 0.001$, Adjustment = Holm).

Trait	PSA	FGCC controlled	FGCC in situ
Main: PSA	1	—	—
Main: FGCC controlled	0.92***	1	—
Main: FGCC in situ	0.83***	0.88***	1
Subset: PSA	1	—	—
Subset: FGCC controlled	0.90***	1	—
Subset: FGCC in situ	0.86***	0.91***	1

338 **Lesion detection** The network for lesion detection achieved an F1-score of 0.27 on the validation
 339 set from 2020, and an F1-score of 0.30 on the validation set from 2021 that each consisted of 300
 340 images. Based on these metrics and visual examination of the predicted lesions, the detection is
 341 not very accurate but the method can still provide an estimate that would not easily be achievable
 342 with human vision (Figure 5, Supplementary Figure 9). The training time for the network was
 343 approximately 37 hours in 345 epochs, and the prediction time for one image was approximately
 344 0.05 seconds. This detection speed which would allow for real-time detection in the field.

345 3.3 Smoothed FGCC and lesion count

346 In both years that the fungicide treatment trial was conducted, a reduced average growth rate of
 347 FGCC was observed for infected pots compared to non-infected pots (Figure 4). This reduction
 348 was stronger where the disease score class was higher. In 2022, the average reduction of growth
 349 of FGCC in infected pots was not as pronounced as in 2021 and only started later in the season.
 350 Similarly, the development of lesions started later in 2022 on average compared to 2021, consistent
 351 with that year's lower disease pressure indicated by scores of control genotypes. In 2021, the high
 352 DI class showed the earliest and fastest development of lesion. The average Breaking Day of the
 353 control cultivars was 16 DAI in 2021 and 32 DAI in 2022, delaying the period for RGR_{crit} by 16
 354 days in 2022. In the main experimental parts, the average Breaking Day of the control genotypes
 355 was 16 DAI in 2020, 18 DAI in 2021, and 28 DAI in 2022 (Supplementary Figure 9).

356 3.4 Treatment effects on intermediate traits in subset experiments

357 There was significant genotype by treatment by year interaction for the traits Breaking Day and
 358 NGRDI AUC. Both traits relating to lesion production, Latent Period and Lesion AUC, as well
 359 as RGR_{28-42} and ENDVI AUC showed significant treatment by year and genotype by treatment
 360 interaction. RGR_{14-28} and RGR_{42-56} showed significant genotype by treatment interaction but no
 361 significant treatment by year interaction. No significant effects were observed for RGR_{0-14} . For
 362 RGR_{crit} , only the main genotypic and treatment effects were significant. For the remaining vegeta-

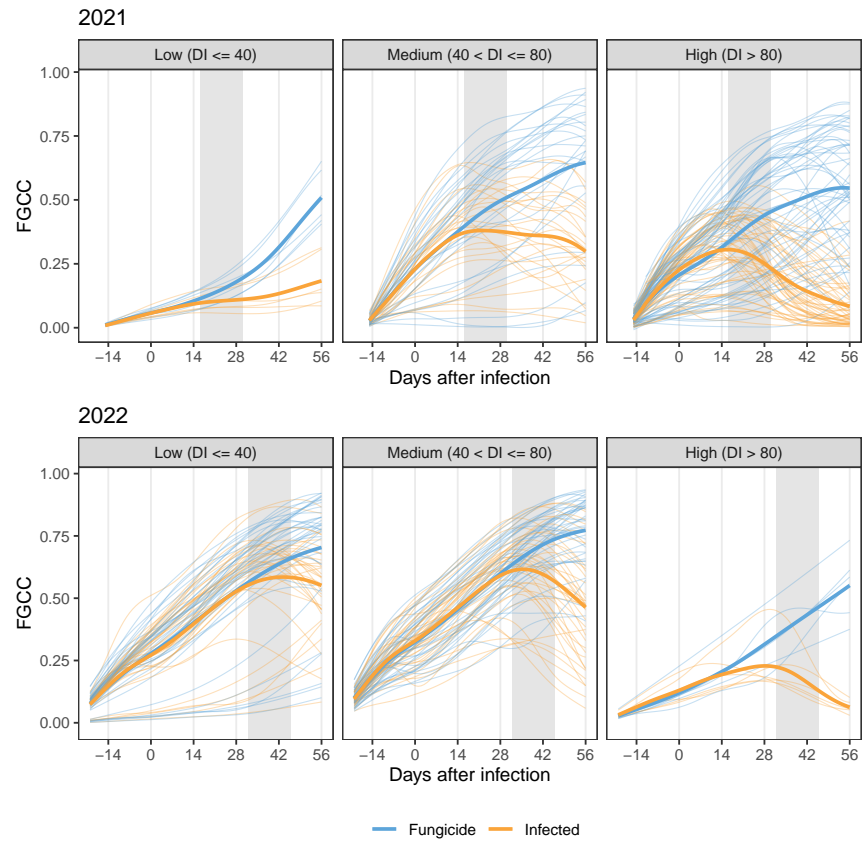


Figure 4: Smoothed fractional green canopy cover (FGCC) for pots in subset experiment, grouped by disease severity class. Individual lines represent individual pots and thick lines represent the group average. Shaded area corresponds to the 14 days after the respective mean breaking day of control genotypes Howzat and Genesis090 (RGR_{crit}).

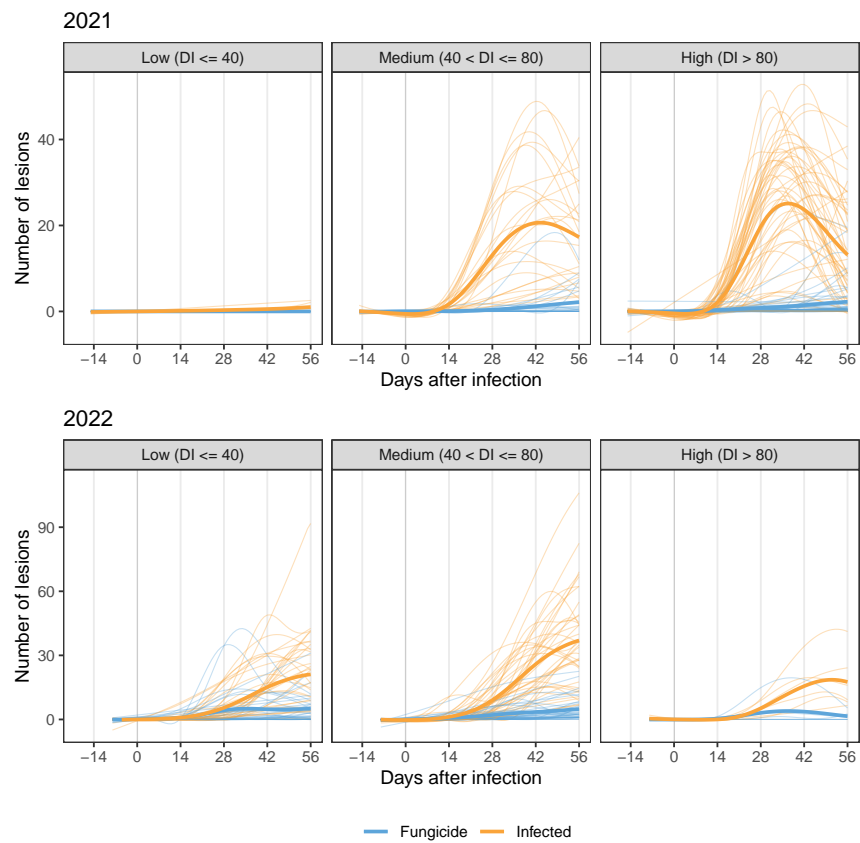


Figure 5: Smoothed number of lesions detected with YOLOv5 for pots in subset experiment, grouped by disease severity class. Individual lines represent individual pots and thick lines represent the group average. Note different y-axes for the seasons.

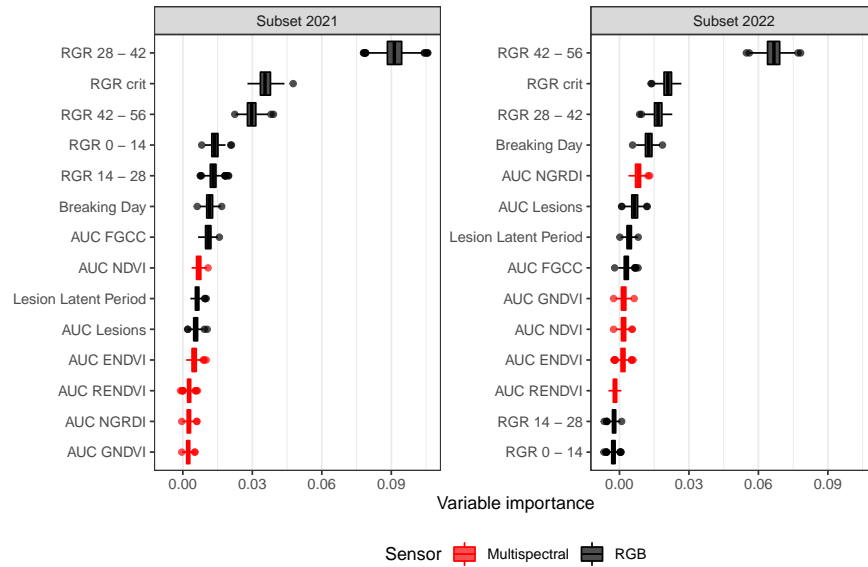


Figure 6: Permutation based variable importance for classification of disease index class, based on permutation in 500 random forest models trained on infected subset within each season.

363 tion indices AUC (GNDVI, NDVI, RENDVI), there were significant treatment by year interactions
 364 and genotypic main effects (Supplementary Figures 10 and 11, Supplementary Table 5).

365 3.5 Disease index classification

366 **Growth rates are the most important predictors for disease index classes** For the subset
 367 in 2021, RGR_{28-42} was the most important predictor for score classification, followed by RGR_{crit}
 368 (Figure 6). In 2022, the most important variable was RGR_{42-56} , again followed by RGR_{crit} . The
 369 higher importance of the later period in 2022 compared to 2021 is consistent with the mean Breaking
 370 Day of the control genotypes that occurred 16 days later. As RGR_{crit} was the second most important
 371 variable in both years and showed a significant positive Pearson correlation with the respective most
 372 important growth rate within each year (2021: 0.90, 2022: 0.95), RGR_{crit} was chosen to train a
 373 simple classification model.

374 **Application of trained score classifiers to the main experimental part** The logistic re-
 375 gression model estimating the score class based on RGR_{crit} was trained on infected pots from the
 376 fungicide-treated experimental subset from both years ($n = 160$) and then applied to the main exper-
 377 imental parts of 2020, 2021 and 2022 (Table 4). The linear decision boundaries of the model returned
 378 the class 'High DI' for values of $RGR_{crit} \leq -20$, the class 'Low DI' for values of $RGR_{crit} > 10$ and
 379 the class 'Medium DI' for all values of RGR_{crit} between -20 and 10. The accuracies achieved when

Table 4: Confusion matrices and classification metrics for the prediction of score groups of the main experimental parts with a classifier trained only on the infected pots of subset experiments from 2021 and 2022.

	Low DI	Medium DI	High DI
2020 Main: Accuracy = 72.46 %, $\kappa = 0.50$			
Predicted: Low DI	40	142	13
Predicted: Medium DI	72	838	266
Predicted: High DI	1	59	577
2021 Main: Accuracy = 80.97 %, $\kappa = 0.59$			
Predicted: Low DI	44	142	4
Predicted: Medium DI	15	421	230
Predicted: High DI	1	81	1547
2022 Main: Accuracy = 65.48 %, $\kappa = 0.43$			
Predicted: Low DI	137	239	68
Predicted: Medium DI	93	792	230
Predicted: High DI	0	105	465

380 applying the classifier to the main experimental subsets were 72.46 % ($\kappa = 0.50$) for data from 2020,
 381 80.97 % ($\kappa = 0.59$) for 2021, and 65.48 % ($\kappa = 0.43$) in 2022 (Table 4).

382 **Estimated within-year disease index classification performance** For the data from 2021,
 383 the within-year disease score classification performance estimated by cross-validation was similar
 384 whether MLP-NN or logistic regression models were used and whether spectral data was included
 385 or not (Supplementary Table 6). All the models where RGB-derived traits were included achieved
 386 an estimated accuracy > 80%, irrespective of model choice and inclusion of spectral data. However,
 387 when using only the spectral traits, the estimated model performance decreased to an accuracy of
 388 $63 \pm 2\%$. When using only RGR_{crit} , an estimated accuracy of $72 \pm 2\%$ was achieved. For the data
 389 from 2022, the simple model based on RGR_{crit} outperformed all other classifiers with an estimated
 390 accuracy of $68 \pm 2\%$, showing the transferrability of this model and confirming the results of the
 391 analysis of variable importance within the experiments (Figure 6).

392 3.6 Early detection of disease

393 The cross-validation performance of the early detection classifiers showed that infected and non-
 394 infected plants can be discriminated with > 90% accuracy from 18 DAI in 2021. The estimated
 395 performance in 2022 is worse, with the best models only reaching accuracies of > 80% 42 DAI
 396 (Figure 7). An analysis of variable importance at the respective dates showed that the number of
 397 lesions had the highest importance for the classification. For both years, the three most important
 398 variables were the lesions counts of the respective most recent three time points (that is, 18, 16,
 399 14 DAI in 2021; 42, 40 and 38 DAI in 2022). Therefore, a simple classifier based on the presence

400 of three or more lesions was included in the evaluation of between-year prediction accuracy. When
401 testing the trained classifiers on the respective opposite seasons, the presence of three or more lesions
402 was the most accurate classifier for both years. It showed a consistent upward trend from 12 DAI in
403 2021 and 20 DAI in 2022. In 2021, a maximum accuracy of 92.6% was reached 30 DAI, plateauing
404 until 38 DAI and then declining again. In 2022, a maximum accuracy of 75.7% was reached 42 DAI.
405 Classifiers based on RGB and spectral data were less consistent, with RGB-only data performing
406 best in both years (Figure 7).

407 4 Discussion

408 **Limitations of data acquisition** Spectral measurements in the field are affected by incident ra-
409 diation [73]. Varying imaging times on individual imaging days lead to shading and harsh contrasts
410 in some of the images (Supplementary Figure 12). This was addressed by preprocessing the RGB
411 sensor data with dynamic range compression but should ideally be controlled for during the acquisi-
412 tion, for example by using a dedicated ground-based phenotyping platform to provide shading and
413 artificial illumination. The subset part of 2022 was imaged before sunrise when lighting was diffuse,
414 and better binary segmentation for the multispectral images was achieved. Unlike the subset part in
415 2021, where multispectral segmentation classifiers had to be adjusted for each imaging time point,
416 a single classifier trained on data 2021-08-24 (35 DAI) was sufficient for all imaging time points in
417 2022.

418 Another limitation during data acquisition was the proximity of pots in the main parts of 2020,
419 2021 and 2022 that led to overlap of plant material between neighboring pots visible from the top view
420 perspective (Figure 1). This issue was partially addressed by developing a rule-based outlier removal
421 procedure that detects pots where FGCC only rises late in the season due to neighboring pots.
422 However this procedure cannot identify pots where FGCC in regularly growing pots is influenced by
423 the neighbors. To improve data acquisition, the pots should be sufficiently spaced.

424 The YOLOv5 algorithm for lesion counting performed well enough to provide a useful trait, but
425 would likely benefit from more training data and higher image quality with higher spatial resolution.
426 Either annotating more training data or transfer learning might further improve the detection of
427 lesions [74–76].

428 **Smoothing and trait extraction** In this study, spatio-temporal modeling was applied to esti-
429 mate genotypic and treatment effects. Spatio-temporal modeling for sensor-based phenotyping is
430 an active area of research and there are multiple approaches [26, 27, 77]. For the chosen method
431 using `statgenHTP`, a minimum of seven imaging time points is required [64]. The required imaging
432 and preprocessing for that amount of timepoints is labor intensive, but can compensate for outliers
433 caused by data acquisition and experimental design.

434 Although more labor intensive, another advantage of longitudinal data for measuring AB severity
435 in chickpea is the ability to estimate key phenotypic stages (Breaking Day) that can be used to
436 normalize seasonal differences in disease progression and compare with control genotypes (RGR_{crit}).
437 Furthermore, small differences in the early response to the disease can be detected when measuring

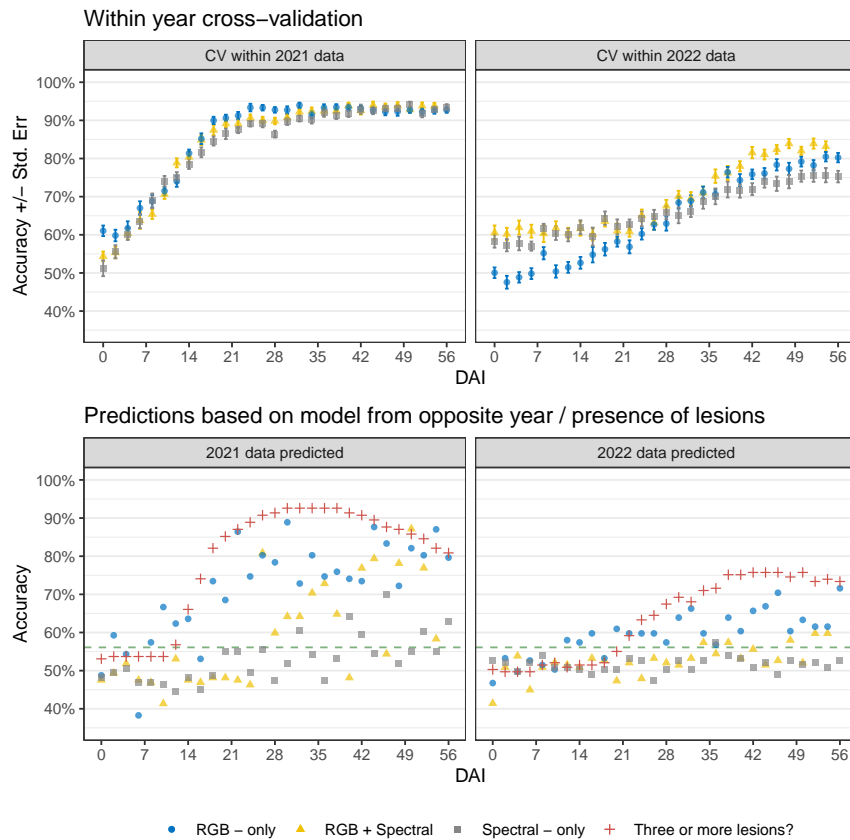


Figure 7: The upper panel shows within year cross-validation results. Mean and standard error from five repeats of five-fold cross-validation is shown for models trained on data up to the respective DAI, based on RGB and spectral traits. The lower panel shows the accuracy of predictions derived from the model trained on the entire data from the opposite year, as well as the accuracy of predictions based on the presence of three or more lesions. Dashed green line in lower panel represents the significance threshold, points that lie above it have a 95% chance of having performed better than a random classifier.

438 over time, and these differences can be useful to breeders given the quantitative nature of resistance
439 to AB. In the germplasm that was screened in this study, a large proportion had died by the time
440 of visual scoring, particularly within the Wild *Cicer* and Introgression genotypes in 2020 and the
441 Vavilov set in 2021 (Supplementary Table 7). When only few or only end point measurements are
442 performed, no matter whether visual scoring or imaging, partial resistance expressed in the early
443 response to infection may be missed.

444 A potentially infinite number of intermediate traits can be extracted from the splines fitted to
445 FGCC, number of lesions, and VI. We chose intermediate traits based on visual inspection of the
446 splines of the 2021 subset, but more options are available for trait extraction [64, 77].

447 **Perspectives** Traits extracted from RGB imaging worked better than those from multispectral
448 imaging for both early detection and disease index class prediction, but so far, trait extraction from
449 multispectral images was limited to AUC traits. It is possible that other traits extracted from
450 VI could improve classification, as NDVI at a single time point had high predictive power for AB
451 disease severity scores in a study of the effects of fungicide on field-grown chickpea [37]. Therefore,
452 more trait extraction and feature selection needs to be performed. Measurements of FGCC from
453 multispectral and RGB camera were highly correlated (2021: $r = 0.97$, 2022: $r = 0.98$), meaning
454 that growth rates could have also been derived from the multispectral images alone.

455 The period from 28-56 DAI was most important for disease class prediction, offering a potential
456 simplification of the data acquisition process by only measuring at a few select time points. However,
457 this would forfeit the ability to fit longitudinal splines. Currently, detection of lesions does not
458 contribute to the prediction of the disease class; however, the detection of three or more lesions was
459 the best criterion to differentiate between fungicide-treated and infected pots. Incorporating lesion
460 detection for the prediction of disease class could be an option to increase specificity in non-controlled
461 field screens, where other stressors may influence growth rates [35].

462 At this stage, the cropping and assignment of positions to individual pots had to be performed
463 manually; this was the major bottleneck for data acquisition. To speed up data acquisition, a fixed
464 gantry or cable-driven system or dedicated ground-based phenotyping devices could be used for
465 better identification and positioning of pots. Such systems could also improve the lighting with
466 active illumination and shading [73]. Optimising the experimental design for imaging by spacing the
467 pots further apart might increase the accuracy of scores class prediction. The estimation of growth
468 rates could be improved by using 3D biomass estimates instead of FGCC. While we argue that more
469 research is needed concerning the trait extraction especially for multispectral data, deep learning
470 could offer an alternative approach by skipping trait extraction and using sensor data directly for
471 the target trait prediction [24].

472 As a tool for breeding, the sensor-based methods were benchmarked on their ability to predict
473 classes of visual scores; however, they are not intended as a replica of visual scoring. Instead, selec-
474 tions may be made based directly on quantitative traits such as growth rates and lesion development.

475 In summary, the proposed methods offer a way to improve screening for resistance to *Ascochyta*
476 blight in chickpeas, which may increase genetic gain in breeding programs. The methods make
477 it easier to measure and identify resistance components that would be difficult to measure with

478 human vision alone. Due to the exclusive use of affordable sensors combined with free and open-
479 source software tools, the barrier to entry for uptake and adoption of the methods to other host-
480 pathosystems is low.

481 **Acknowledgments**

482 **General**

483 FT acknowledges the use of the facilities, and scientific and technical assistance of the Australian
484 Plant Phenomics Facility, which is supported by the Australian Government's National Collaborative
485 Research Infrastructure Strategy (NCRIS). FT acknowledges the provision and advice for use of the
486 spectral camera by Ramesh Raja Segaran (Unmanned Aircraft Research Facility), the support of
487 Paul Jenkins (Australian Plant Phenomics Facility) in the design of the imaging pushcart, and the
488 suggestion of dynamic range compression for image pre-processing by Gert Kootstra (Wageningen
489 University and Research).

490 **Author contributions**

491 B.B., D.P., J.D., J.A and F.T. conceived the idea for the paper. F.T. conducted the imaging, analysed
492 the data and wrote the manuscript. J.A. performed revisions of the manuscript. The experiments
493 were led by M.K-K.. C. Boyce implemented the lesion detection algorithm. J.D. and S.B. performed
494 visual scoring. C. Brien advised on split-unit design and longitudinal smoothing. K.C., D.P., B.B.,
495 J.D. provided supervision and performed revisions of the manuscript. All authors reviewed the
496 manuscript.

497 **Funding**

498 FT is supported by the University of Adelaide with a Scholarship International, and by The Plant Ac-
499 celerator with a PhD stipend top-up. Diseased chickpeas were provided by GRDC Project UOA2005-
500 011RTX.

501 **Conflicts of interest**

502 The author(s) declare(s) that there is no conflict of interest regarding the publication of this article.

503 **Data availability**

504 Data, code, and trained weights for lesion detection are available at [https://github.com/FCTanner/
505 ab_screen_methods](https://github.com/FCTanner/ab_screen_methods)

506 **Supplementary Materials**

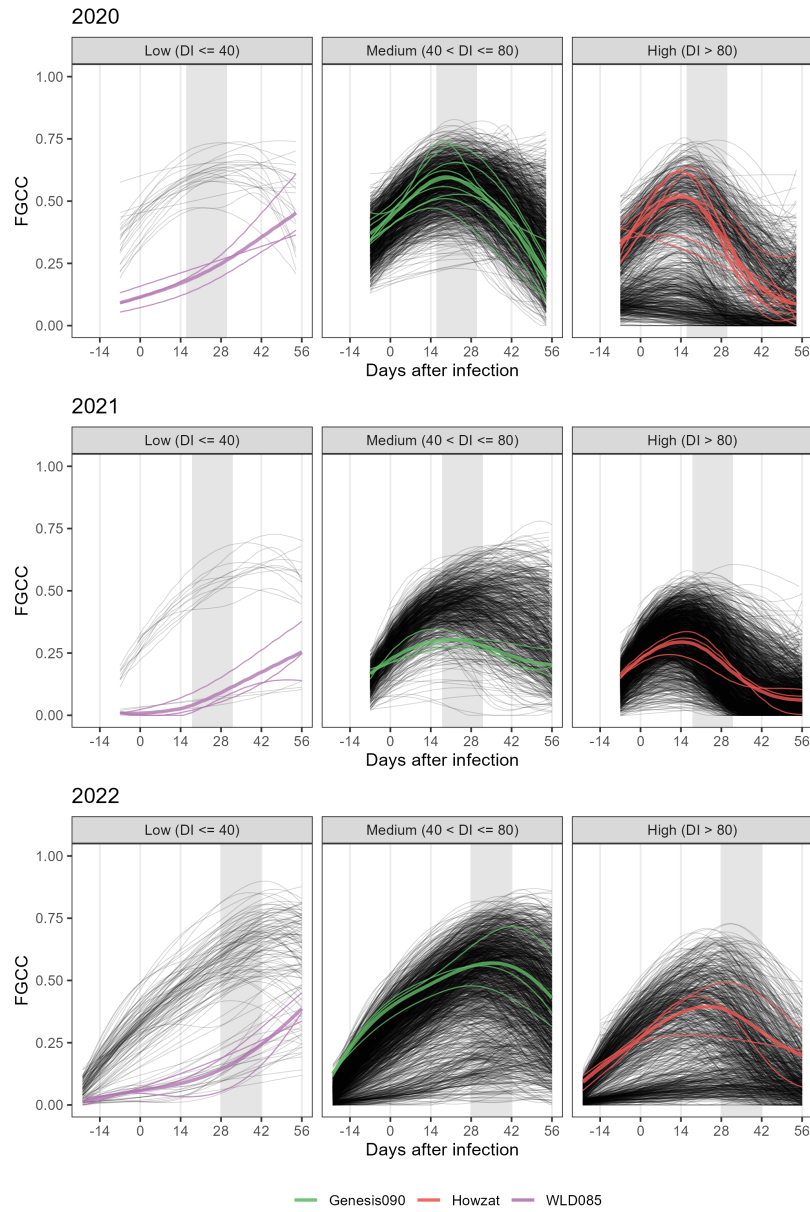


Figure 8: Fitted values for FGCC for main parts in each season, grouped by disease severity class. Individual lines represent individual pots, control genotypes are highlighted by color and the mean of the control genotypes is indicated as a thicker line. Shaded area represents the 14 days following the mean Breaking Day of Howzat and Genesis090 in each respective season.

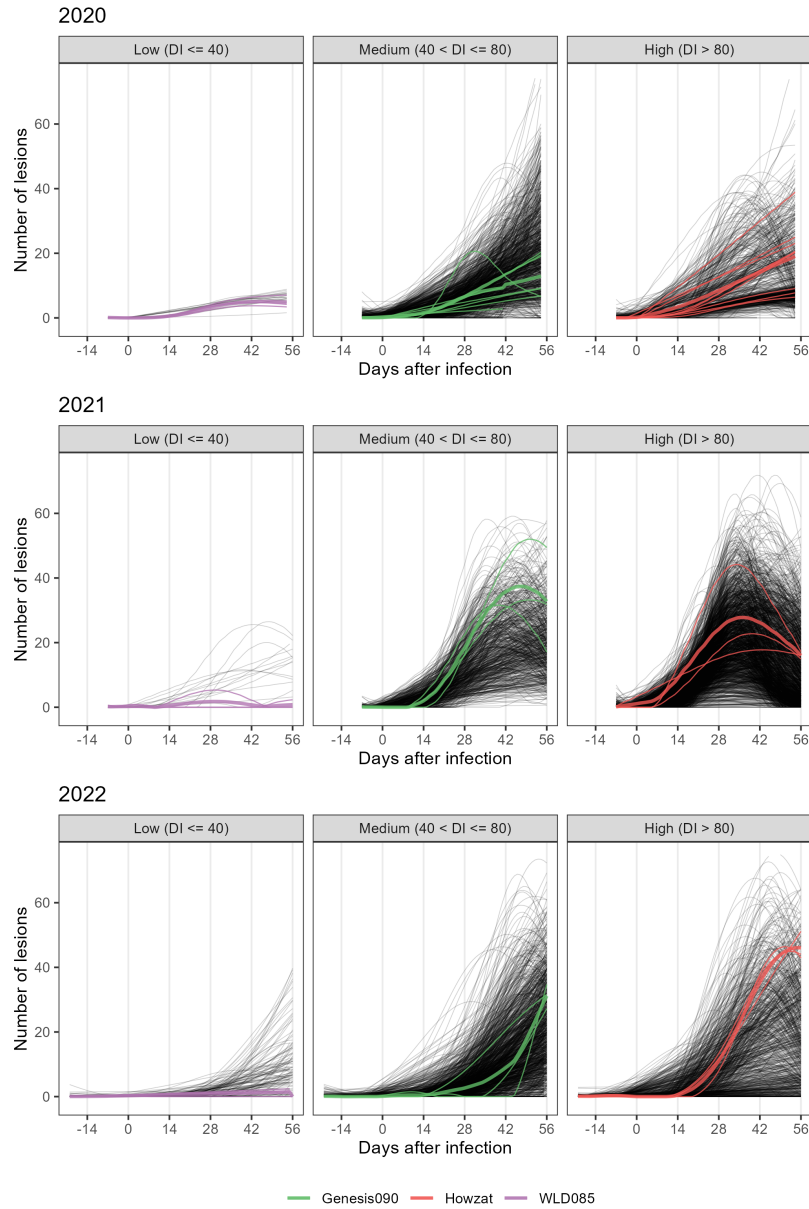


Figure 9: Fitted values for number of lesions for main parts in each season, grouped by disease severity class. Individual lines represent individual pots, control genotypes are highlighted by color and the mean of the control genotypes is indicated as a thicker line.

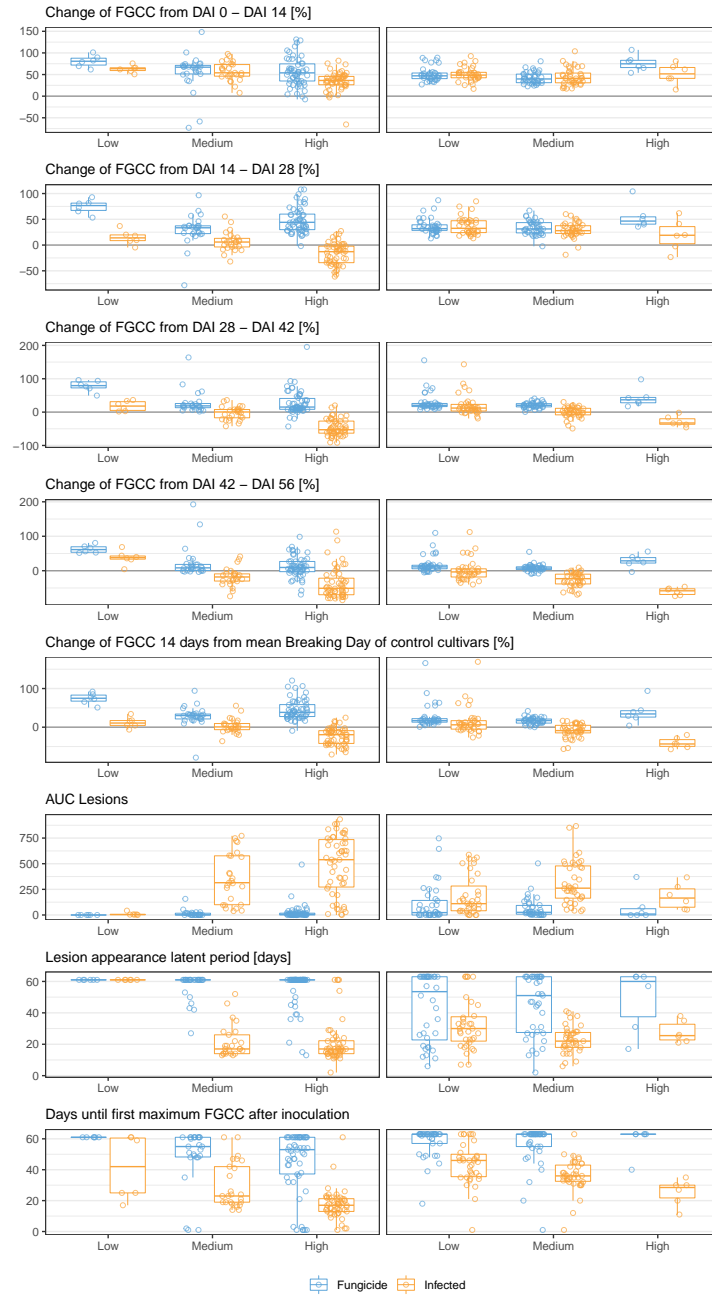


Figure 10: Intermediate traits derived from RGB imaging per score group and treatment. Dots represent individual pots.

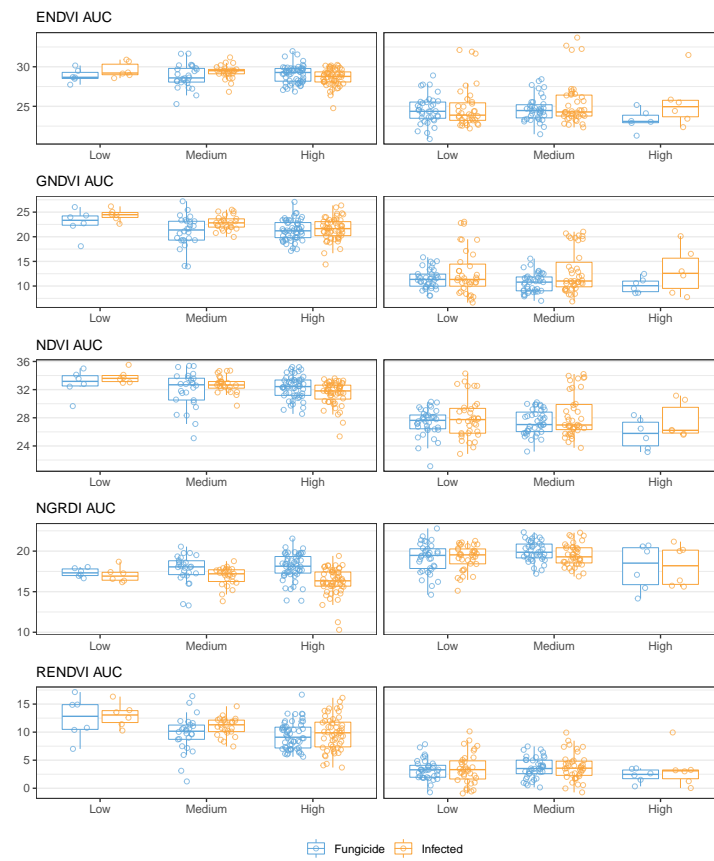


Figure 11: AUC between 0 and 42 DAI of vegetation indices per score group and treatment. Dots represent individual pots.

Table 5: P-value for effects of genotype (G), treatment (T), year of trial (Y), and respective interactions.

Trait	T	G	T:Y	G:T	G:T:Y
Visual score					
Disease Index	<0.001	<0.001	<0.001	<0.001	0.011
RGB					
Breaking Day	<0.001	<0.001	<0.001	<0.001	0.046
Latent Period	<0.001	<0.001	<0.001	<0.001	0.095
Lesions AUC	<0.001	<0.001	<0.001	<0.001	0.503
RGR_{0-14}	0.554	0.875	0.314	0.847	0.083
RGR_{14-28}	0.338	0.028	0.597	0.038	1.000
RGR_{28-42}	<0.001	<0.001	0.001	0.010	1.000
RGR_{42-56}	<0.001	<0.001	0.063	<0.001	1.000
RGR_{crit}	<0.001	0.004	0.133	0.137	0.291
Multispectral					
ENDVI AUC	0.027	<0.001	<0.001	0.008	0.313
GNDVI AUC	<0.001	<0.001	<0.001	0.293	0.919
NDVI AUC	0.132	<0.001	<0.001	0.204	0.358
NGRDI AUC	<0.001	<0.001	<0.001	0.029	0.001
RENDVI AUC	0.277	<0.001	<0.001	0.313	0.873

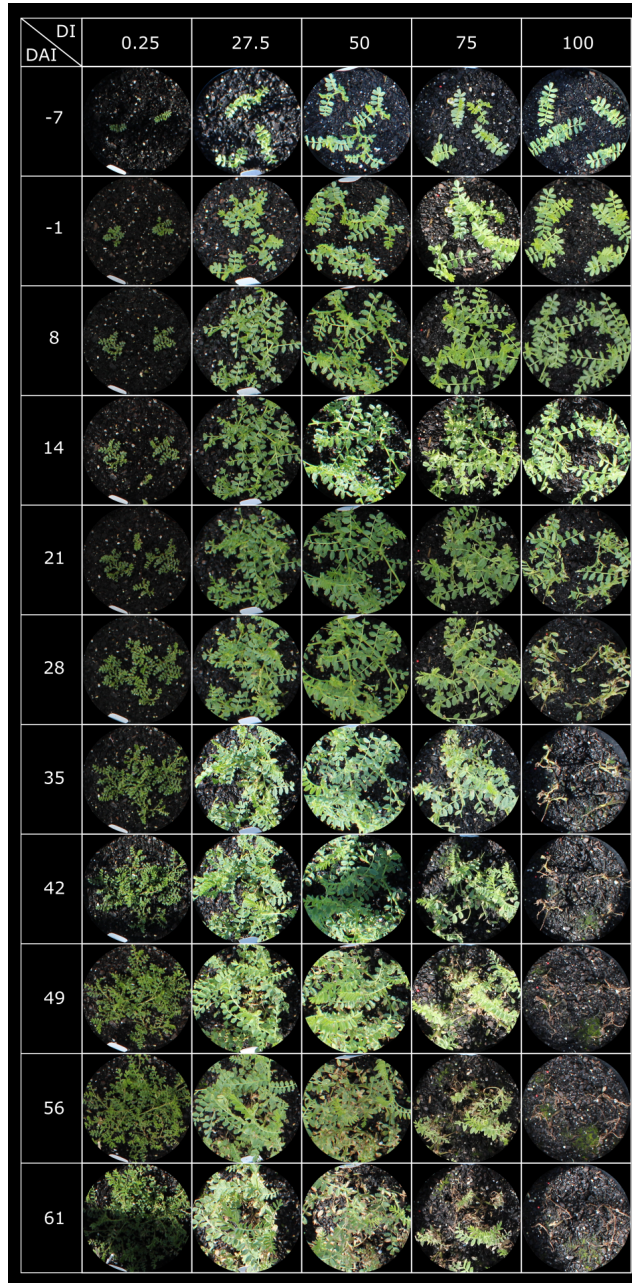


Figure 12: Images of five sample pots with varying disease indices over eleven time points, data from subset in 2021 where lighting was uneven.

Table 6: Estimated ROC AUC, F1 score and accuracy for score classification using intermediate traits for infected subsets. Standard error from 5-fold CV with 5 repeats within each season is shown.

Predictors	Model	ROC AUC	F1 score	Accuracy
2021				
RGB + VI	MLP - NN	0.86 ± 0.02	0.77 ± 0.02	0.81 ± 0.02
RGB + VI	Logistic Regression	0.89 ± 0.02	0.75 ± 0.03	0.8 ± 0.02
RGB - only	MLP - NN	0.85 ± 0.02	0.74 ± 0.03	0.82 ± 0.02
RGB - only	Logistic Regression	0.86 ± 0.02	0.76 ± 0.03	0.82 ± 0.02
VI - only	MLP - NN	0.67 ± 0.02	0.46 ± 0.03	0.53 ± 0.02
VI - only	Logistic Regression	0.71 ± 0.03	0.58 ± 0.03	0.63 ± 0.02
RGR_{crit} - only	Logistic Regression	0.81 ± 0.02	0.68 ± 0.03	0.72 ± 0.02
2022				
RGB + VI	MLP - NN	0.67 ± 0.03	0.59 ± 0.03	0.61 ± 0.03
RGB + VI	Logistic Regression	0.76 ± 0.03	0.63 ± 0.03	0.65 ± 0.02
RGB - only	MLP - NN	0.61 ± 0.03	0.52 ± 0.03	0.55 ± 0.02
RGB - only	Logistic Regression	0.71 ± 0.02	0.56 ± 0.02	0.6 ± 0.02
VI - only	MLP - NN	0.54 ± 0.03	0.47 ± 0.03	0.48 ± 0.03
VI - only	Logistic Regression	0.48 ± 0.02	0.39 ± 0.02	0.43 ± 0.02
RGR_{crit} - only	Logistic Regression	0.79 ± 0.02	0.67 ± 0.03	0.68 ± 0.02

Table 7: Distribution of disease severity class per experiment, treatment and genotype group.

Genotypes	Treatment	Low DI	Medium DI	High DI	Total pots
2020 Main					
Cultivar	Infected	5.7 % (83)	66 % (966)	28.3 % (415)	1464
FLIP	Infected	21.4 % (27)	59.5 % (75)	19 % (24)	126
Introgression	Infected	0 % (0)	3.3 % (3)	96.7 % (87)	90
Wild cicer	Infected	0.8 % (3)	0.8 % (3)	98.4 % (378)	384
2021 Main					
Cultivar	Infected	0 % (0)	22.2 % (2)	77.8 % (7)	9
FLIP	Infected	3.2 % (56)	34.9 % (611)	61.9 % (1084)	1751
Introgression	Infected	1.9 % (1)	17 % (9)	81.1 % (43)	53
Vavilov	Infected	0.1 % (1)	2.9 % (20)	96.9 % (658)	679
Wild cicer	Infected	41.7 % (5)	41.7 % (5)	16.7 % (2)	12
2021 Subset					
Cultivar	Fungicide	92.9 % (65)	2.9 % (2)	4.3 % (3)	70
Cultivar	Infected	5.3 % (4)	30.7 % (23)	64 % (48)	75
Wild cicer	Fungicide	100 % (14)	0 % (0)	0 % (0)	14
Wild cicer	Infected	35.7 % (5)	14.3 % (2)	50 % (7)	14
2022 Main					
Cultivar	Infected	28.7 % (27)	61.7 % (58)	9.6 % (9)	94
FLIP	Infected	10 % (148)	56.8 % (838)	33.2 % (489)	1475
Introgression	Infected	13.7 % (30)	62.1 % (136)	24.2 % (53)	219
Other	Infected	18.5 % (5)	77.8 % (21)	3.7 % (1)	27
Vavilov	Infected	2 % (1)	52.9 % (27)	45.1 % (23)	51
Wild cicer	Infected	8 % (36)	24.3 % (110)	67.7 % (306)	452
2022 Subset					
Cultivar	Fungicide	100 % (72)	0 % (0)	0 % (0)	72
Cultivar	Infected	40.5 % (30)	54.1 % (40)	5.4 % (4)	74
Wild cicer	Fungicide	100 % (13)	0 % (0)	0 % (0)	13
Wild cicer	Infected	63.6 % (7)	9.1 % (1)	27.3 % (3)	11

References

- [1] FAOSTAT. [Online]. Available: <https://www.fao.org/faostat/en/#home> (visited on 05/18/2022).
- [2] A. K. Basandrai, D. Basandrai, S. Pande, M. Sharma, S. K. Thakur, and H. L. Thakur, *Ascochyta blights of grain legumes*, B. Tivoli, A. Baranger, F. J. Muehlbauer, and B. M. Cooke, Eds. Dordrecht: Springer Netherlands, 2007, Publication Title: *Ascochyta blights of grain legumes*, ISBN: 978-1-4020-6064-9. DOI: 10.1007/978-1-4020-6065-6. [Online]. Available: http://link.springer.com/10.1007/978-1-4020-6065-6_8.
- [3] S. Pande *et al.*, "Ascochyta blight of chickpea (*Cicer arietinum* L.): A review of biology, pathogenicity, and disease management," *Australian Journal of Agricultural Research*, vol. 56, no. 4, p. 317, 2005, ISSN: 0004-9409. DOI: 10.1071/AR04143. [Online]. Available: <http://www.publish.csiro.au/?paper=AR04143>.
- [4] Y. Mehmood *et al.*, "Evidence and consequence of a highly adapted clonal haplotype within the Australian *Ascochyta rabiei* population," *Frontiers in Plant Science*, vol. 8, no. June, 2017, ISSN: 1664462X. DOI: 10.3389/fpls.2017.01029.
- [5] GRDC, "2020 South Australian Crop Sowing Guide," no. December 2019, 2020.
- [6] L. Manjunatha, P. R. Saabale, A. K. Srivastava, G. P. Dixit, L. B. Yadav, and K. Kumar, "Present status on variability and management of *Ascochyta rabiei* infecting chickpea," *Indian Phytopathology*, vol. 71, no. 1, pp. 9–24, 2018, Publisher: Springer India ISBN: 0123456789, ISSN: 22489800. DOI: 10.1007/s42360-018-0002-6. [Online]. Available: <https://doi.org/10.1007/s42360-018-0002-6>.
- [7] Y. Li *et al.*, "Genome analysis identified novel candidate genes for *Ascochyta* blight resistance in chickpea using whole genome re-sequencing data," *Frontiers in Plant Science*, vol. 8, no. March, pp. 1–13, 2017, ISSN: 1664462X. DOI: 10.3389/fpls.2017.00359.
- [8] R. Niks, J. Parlevliet, P. Lindhout, and Y. Bai, *Breeding crops with resistance to diseases and pests*. The Netherlands: Wageningen Academic Publishers, Mar. 2019, ISBN: 978-90-8686-328-0. DOI: 10.3920/978-90-8686-882-7. [Online]. Available: <https://www.wageningenacademic.com/doi/book/10.3920/978-90-8686-882-7>.
- [9] T. E. Newman *et al.*, "Identification of novel sources of resistance to *Ascochyta* blight in a collection of wild *Cicer* accessions," *Phytopathology*, vol. 111, no. 2, pp. 369–379, 2021, ISSN: 19437684. DOI: 10.1094/PHYTO-04-20-0137-R.
- [10] B. C. Collard, P. K. Ades, E. C. Pang, J. B. Brouwer, and P. W. Taylor, "Prospecting for sources of resistance to *Ascochyta* blight in wild *Cicer* species," *Australasian Plant Pathology*, vol. 30, no. 3, pp. 271–276, 2001, ISSN: 08153191. DOI: 10.1071/AP01036.
- [11] M. Singh *et al.*, "Exploitation of wild annual *Cicer* species for widening the gene pool of chickpea cultivars," *Plant Breeding*, vol. 134, no. 2, pp. 186–192, 2015, ISSN: 14390523. DOI: 10.1111/pbr.12254.

- [12] K. B. Singh and M. V. Reddy, "Sources of resistance to ascochyta blight in wild Cicer species," *Netherlands Journal of Plant Pathology*, vol. 99, no. 3, pp. 163–167, May 1993, ISSN: 00282944. DOI: 10.1007/BF01974268. [Online]. Available: <http://link.springer.com/10.1007/BF01974268>.
- [13] H. Ilarslan and F. S. Dolar, "Histological and ultrastructural changes in leaves and stems of resistant and susceptible chickpea cultivars to *Ascochyta rabiei*," *Journal of Phytopathology*, vol. 150, no. 6, pp. 340–348, 2002, ISSN: 09311785. DOI: 10.1046/j.1439-0434.2002.00763.x.
- [14] P. Jayakumar, Y. T. Gan, B. D. Gossen, T. D. Warkentin, and S. Banniza, "Ascochyta blight of chickpea: Infection and host resistance mechanisms," *Canadian Journal of Plant Pathology*, vol. 27, no. 4, pp. 499–509, 2005, ISSN: 17152992. DOI: 10.1080/07060660509507251.
- [15] F. Weigand, J. Köster, H. C. Weltzien, and W. Barz, "Accumulation of phytoalexins and isoflavone glucosides in a resistant and a susceptible cultivar of *Cicer arietinum* during infection with *Ascochyta rabiei*," *Journal of Phytopathology*, vol. 115, no. 3, pp. 214–221, Mar. 1986, ISSN: 0931-1785. DOI: 10.1111/j.1439-0434.1986.tb00879.x. [Online]. Available: <http://doi.wiley.com/10.1111/j.1439-0434.1986.tb00879.x>.
- [16] S. Daniel and W. Barz, "Elicitor-induced metabolic changes in cell cultures of chickpea (*Cicer arietinum* L.) cultivars resistant and susceptible to *Ascochyta rabiei*," *Planta*, vol. 182, no. 2, pp. 279–286, 1990, ISSN: 0032-0935. DOI: 10.1007/bf00197122.
- [17] I. Ahuja, R. Kissen, and A. M. Bones, "Phytoalexins in defense against pathogens," *Trends in Plant Science*, vol. 17, no. 2, pp. 73–90, 2012, Publisher: Elsevier Ltd, ISSN: 13601385. DOI: 10.1016/j.tplants.2011.11.002. [Online]. Available: <http://dx.doi.org/10.1016/j.tplants.2011.11.002>.
- [18] C. Armstrong-Cho, M. M. Lulsdorf, P. Hashemi, and S. Banniza, "Characterization of resistance to ascochyta blight of selected wild cicer germplasm," *Botany*, vol. 93, no. 11, pp. 723–734, 2015, ISSN: 19162804. DOI: 10.1139/cjb-2015-0072.
- [19] K. B. Singh, "Resistance in Chickpeas to *Ascochyta rabiei*," *Plant Disease*, vol. 65, no. 7, p. 586, 1981, ISSN: 0191-2917. DOI: 10.1094/PD-65-586. [Online]. Available: http://www.apsnet.org/publications/PlantDisease/BackIssues/Documents/1981Abstracts/PD_65_586.htm.
- [20] C. H. Bock, J. G. A. Barbedo, E. M. Del Ponte, D. Bohnenkamp, and A.-K. Mahlein, "From visual estimates to fully automated sensor-based measurements of plant disease severity: Status and challenges for improving accuracy," *Phytopathology Research*, vol. 2, no. 1, p. 9, Dec. 2020, Publisher: Phytopathology Research, ISSN: 2524-4167. DOI: 10.1186/s42483-020-00049-8. [Online]. Available: <https://phytopatholres.biomedcentral.com/articles/10.1186/s42483-020-00049-8>.
- [21] A.-K. Mahlein, "Present and Future Trends in Plant Disease Detection," *Plant Disease*, vol. 100, no. 2, pp. 1–11, 2016, arXiv: 1011.1669v3 ISBN: 9780874216561, ISSN: 0717-6163. DOI: 10.1007/s13398-014-0173-7.2.

- [22] A. M. Mutka and R. S. Bart, “Image-based phenotyping of plant disease symptoms,” *Frontiers in Plant Science*, vol. 5, no. JAN, pp. 1–8, 2015, ISSN: 1664462X. DOI: 10.3389/fpls.2014.00734.
- [23] I. Simko, J. A. Jimenez-Berni, and X. R. Sirault, “Phenomic approaches and tools for phytopathologists,” *Phytopathology*, vol. 107, no. 1, pp. 6–17, 2017, ISSN: 0031949X. DOI: 10.1094/PHYTO-02-16-0082-RVW.
- [24] R. E. Baker, J. M. Peña, J. Jayamohan, and A. Jérusalem, “Mechanistic models versus machine learning, a fight worth fighting for the biological community?” *Biology Letters*, vol. 14, no. 5, pp. 1–4, 2018, ISSN: 1744957X. DOI: 10.1098/rsbl.2017.0660.
- [25] F. A. van Eeuwijk *et al.*, “Modelling strategies for assessing and increasing the effectiveness of new phenotyping techniques in plant breeding,” *Plant Science*, vol. 282, no. December 2017, pp. 23–39, 2019, Publisher: Elsevier, ISSN: 18732259. DOI: 10.1016/j.plantsci.2018.06.018. [Online]. Available: <https://doi.org/10.1016/j.plantsci.2018.06.018>.
- [26] D. M. Pérez-Valencia *et al.*, “A two-stage approach for the spatio-temporal analysis of high-throughput phenotyping data,” *Scientific Reports*, vol. 12, no. 1, pp. 1–16, 2022, Publisher: Nature Publishing Group UK ISBN: 4159802206, ISSN: 2045-2322. DOI: 10.1038/s41598-022-06935-9. [Online]. Available: <https://doi.org/10.1038/s41598-022-06935-9>.
- [27] L. Roth, M. X. Rodríguez-Álvarez, F. van Eeuwijk, H. P. Piepho, and A. Hund, “Phenomics data processing: A plot-level model for repeated measurements to extract the timing of key stages and quantities at defined time points,” *Field Crops Research*, vol. 274, no. October, 2021, ISSN: 03784290. DOI: 10.1016/j.fcr.2021.108314.
- [28] J. E. Parlevliet, “Components of Resistance that Reduce the Rate of Epidemic Development,” en, *Annual Review of Phytopathology*, vol. 17, no. 1, pp. 203–222, Sep. 1979, ISSN: 0066-4286, 1545-2107. DOI: 10.1146/annurev.py.17.090179.001223. [Online]. Available: <https://www.annualreviews.org/doi/10.1146/annurev.py.17.090179.001223> (visited on 07/29/2022).
- [29] J. D. C. Walter, J. Edwards, G. McDonald, and H. Kuchel, “Estimating Biomass and Canopy Height With LiDAR for Field Crop Breeding,” *Frontiers in Plant Science*, vol. 10, no. September, 2019, ISSN: 1664462X. DOI: 10.3389/fpls.2019.01145.
- [30] R. N. Lati, S. Filin, and H. Eizenberg, “Robust Methods for Measurement of Leaf-Cover Area and Biomass from Image Data,” en, *Weed Science*, vol. 59, no. 2, pp. 276–284, Jun. 2011, ISSN: 0043-1745, 1550-2759. DOI: 10.1614/WS-D-10-00054.1. [Online]. Available: https://www.cambridge.org/core/product/identifier/S0043174500020403/type/journal_article (visited on 11/20/2022).
- [31] A. Patrignani and T. E. Ochsner, “Canopeo: A powerful new tool for measuring fractional green canopy cover,” *Agronomy Journal*, vol. 107, no. 6, pp. 2312–2320, 2015, ISSN: 14350645. DOI: 10.2134/agronj15.0150.

- [32] C. Xie and C. Yang, "A review on plant high-throughput phenotyping traits using UAV-based sensors," en, *Computers and Electronics in Agriculture*, vol. 178, p. 105 731, Nov. 2020, ISSN: 0168-1699. DOI: 10.1016/j.compag.2020.105731. [Online]. Available: <https://www.sciencedirect.com/science/article/pii/S0168169919320046> (visited on 12/12/2022).
- [33] T. Wiesner-Hanks *et al.*, "Image set for deep learning: Field images of maize annotated with disease symptoms," *BMC Research Notes*, vol. 11, no. 1, p. 440, Dec. 2018, ISSN: 1756-0500. DOI: 10.1186/s13104-018-3548-6. [Online]. Available: <https://bmresnotes.biomedcentral.com/articles/10.1186/s13104-018-3548-6>.
- [34] B. Richey and M. V. Shirvaikar, "Deep learning based real-time detection of northern corn leaf blight crop disease using YoloV4," vol. 1173606, no. April 2021, p. 5, 2021, ISBN: 9781510643093, ISSN: 1996756X. DOI: 10.1117/12.2587892.
- [35] S. Jay *et al.*, "Scoring Cercospora Leaf Spot on Sugar Beet: Comparison of UGV and UAV Phenotyping Systems," *Plant Phenomics*, vol. 2020, pp. 1–18, Aug. 2020, Publisher: American Association for the Advancement of Science (AAAS) ISBN: 2643-6515, ISSN: 2643-6515. DOI: 10.34133/2020/9452123. [Online]. Available: <https://spj.sciencemag.org/journals/plantphenomics/2020/9452123/>.
- [36] S. C. McDonald, J. Buck, and Z. Li, "Automated, image-based disease measurement for phenotyping resistance to soybean frogeye leaf spot," *Plant Methods*, vol. 18, no. 1, p. 103, Aug. 2022, ISSN: 1746-4811. DOI: 10.1186/s13007-022-00934-7. [Online]. Available: <https://doi.org/10.1186/s13007-022-00934-7> (visited on 09/01/2022).
- [37] C. Zhang, W. Chen, and S. Sankaran, "High-throughput field phenotyping of Ascochyta blight disease severity in chickpea," *Crop Protection*, vol. 125, no. March, p. 104 885, 2019, Publisher: Elsevier Ltd, ISSN: 02612194. DOI: 10.1016/j.cropro.2019.104885. [Online]. Available: <https://doi.org/10.1016/j.cropro.2019.104885>.
- [38] E. J. Von Wettberg *et al.*, "Ecology and genomics of an important crop wild relative as a prelude to agricultural innovation," *Nature Communications*, vol. 9, no. 1, 2018, ISBN: 4146701802867, ISSN: 20411723. DOI: 10.1038/s41467-018-02867-z.
- [39] M. C. Saxena, "Food Legumes in the Mediterranean Type of Environment and ICARDA's Efforts in Improving their Productivity," *Nitrogen Fixation by Legumes in Mediterranean Agriculture*, pp. 11–23, 1988, ISBN: 9789401071192. DOI: 10.1007/978-94-009-1387-5_2.
- [40] R. Raman *et al.*, "Genome-Wide Association Analyses Track Genomic Regions for Resistance to Ascochyta rabiei in Australian Chickpea Breeding Germplasm," *Frontiers in Plant Science*, vol. 13, 2022, ISSN: 1664-462X. [Online]. Available: <https://www.frontiersin.org/articles/10.3389/fpls.2022.877266> (visited on 11/27/2022).
- [41] S. Blake, "2022 South Australia Pulse Variety Disease Guide," PIRSA, SARDI, Tech. Rep., 2022. [Online]. Available: https://pir.sa.gov.au/___data/assets/pdf_file/0020/386102/pulse_variety_disease_guide_2022.pdf.

- [42] I. Bar, *Whole Genome Sequencing of Ascochyta rabiei Isolates*, original-date: 2017-07-18T23:36:46Z, Oct. 2019. [Online]. Available: https://github.com/IdoBar/A_rabiei_WGS_analysis (visited on 11/14/2022).
- [43] R. Kimber, *AB chickpea rating scale*, 2003.
- [44] J. Cohen, “A Coefficient of Agreement for Nominal Scales,” en, *Educational and Psychological Measurement*, vol. 20, no. 1, pp. 37–46, Apr. 1960, Publisher: SAGE Publications Inc, ISSN: 0013-1644. DOI: 10.1177/001316446002000104. [Online]. Available: <https://doi.org/10.1177/001316446002000104> (visited on 11/16/2022).
- [45] J. Atieno *et al.*, “Exploring genetic variation for salinity tolerance in chickpea using image-based phenotyping,” *Scientific Reports*, vol. 7, no. 1, pp. 1–11, 2017, Publisher: Springer US, ISSN: 20452322. DOI: 10.1038/s41598-017-01211-7. [Online]. Available: <http://dx.doi.org/10.1038/s41598-017-01211-7>.
- [46] *RawTherapee v5.8*, 2022. [Online]. Available: <https://github.com/Beep6581/RawTherapee>.
- [47] *Inkscape — Draw Freely*, May 2021. [Online]. Available: <https://inkscape.org>.
- [48] The GIMP Development Team, *GNU Image Manipulation Program (GIMP)*, 2020. [Online]. Available: <https://www.gimp.org>.
- [49] J. Adams, Y. Qiu, Y. Xu, and J. C. Schnable, “Plant segmentation by supervised machine learning methods,” *The Plant Phenome Journal*, vol. 3, no. 1, pp. 1–11, Jan. 2020, ISSN: 2578-2703. DOI: 10.1002/ppj2.20001. [Online]. Available: <https://onlinelibrary.wiley.com/doi/10.1002/ppj2.20001>.
- [50] T. pandas development team, *Pandas-dev/pandas: Pandas*, Feb. 2020. DOI: 10.5281/zenodo.3509134. [Online]. Available: <https://doi.org/10.5281/zenodo.3509134>.
- [51] F. Pedregosa *et al.*, “Scikit-learn: Machine Learning in {P}ython,” *Journal of Machine Learning Research*, vol. 12, pp. 2825–2830, 2011.
- [52] G. Bradski, “The OpenCV Library,” *Dr. Dobb’s Journal of Software Tools*, 2000.
- [53] C. R. Harris *et al.*, “Array programming with {NumPy},” *Nature*, vol. 585, no. 7825, pp. 357–362, Sep. 2020, Publisher: Springer Science and Business Media {LLC}. DOI: 10.1038/s41586-020-2649-2. [Online]. Available: <https://doi.org/10.1038/s41586-020-2649-2>.
- [54] J. Redmon, S. Divvala, R. Girshick, and A. Farhadi, “You Only Look Once: Unified, Real-Time Object Detection,” in *Proceedings of the IEEE Conference on Computer Vision and Pattern Recognition (CVPR)*, Jun. 2016.
- [55] Tzutalin, *LabelImg. Git code*, 2015. [Online]. Available: <https://github.com/tzutalin/labelImg> (visited on 05/12/2022).
- [56] Micasense, *Imageprocessing*, 2022. [Online]. Available: <https://github.com/micasense/imageprocessing>.
- [57] *ENDVI*. [Online]. Available: <https://maxmax.com/endvi.htm> (visited on 03/17/2022).

- [58] A. A. Gitelson, Y. J. Kaufman, and M. N. Merzlyak, "Use of a green channel in remote sensing of global vegetation from EOS-MODIS," *Remote Sensing of Environment*, vol. 58, no. 3, pp. 289–298, Dec. 1996, Publisher: Elsevier, ISSN: 00344257. DOI: 10.1016/S0034-4257(96)00072-7. [Online]. Available: <https://linkinghub.elsevier.com/retrieve/pii/S0034425796000727>.
- [59] A. A. Gitelson, Y. J. Kaufman, R. Stark, and D. Rundquist, "Novel algorithms for remote estimation of vegetation fraction," *Remote Sensing of Environment*, vol. 80, no. 1, pp. 76–87, 2002, ISSN: 00344257. DOI: 10.1016/S0034-4257(01)00289-9.
- [60] C. J. Tucker, "Red and photographic infrared linear combinations for monitoring vegetation," *Remote Sensing of Environment*, vol. 8, no. 2, pp. 127–150, May 1979, ISSN: 00344257. DOI: 10.1016/0034-4257(79)90013-0. [Online]. Available: <https://linkinghub.elsevier.com/retrieve/pii/0034425779900130>.
- [61] J. W. Rouse Jr, R. H. Haas, J. A. Schell, and D. W. Deering, "Monitoring vegetation systems in the Great Plains with ERTS," in *Third Earth Resources Technology Satellite-1 Symposium: Section AB. Technical presentations*, vol. 1, 1973, p. 309.
- [62] R Core Team, *R: A Language and Environment for Statistical Computing*, Place: Vienna, Austria, 2022. [Online]. Available: <https://www.r-project.org/>.
- [63] M. X. Rodríguez-Álvarez, M. P. Boer, F. A. van Eeuwijk, and P. H. Eilers, "Correcting for spatial heterogeneity in plant breeding experiments with P-splines," *Spatial Statistics*, vol. 23, pp. 52–71, Mar. 2018, Publisher: Elsevier B.V., ISSN: 22116753. DOI: 10.1016/j.spasta.2017.10.003.
- [64] E. J. Millet *et al.*, *statgenHTP: High Throughput Phenotyping (HTP) Data Analysis*, 2021. [Online]. Available: <https://CRAN.R-project.org/package=statgenHTP> (visited on 12/02/2021).
- [65] S. P. Klassen, G. Ritchie, J. Frantz, D. Pinnock, and B. Bugbee, "Real-Time Imaging of Ground Cover: Relationships with Radiation Capture, Canopy Photosynthesis, and Daily Growth Rate," in Oct. 2003, pp. 1–14. DOI: 10.2134/asaspecpub66.c1. [Online]. Available: <http://doi.wiley.com/10.2134/asaspecpub66.c1>.
- [66] N. Al-Tamimi *et al.*, "Salinity tolerance loci revealed in rice using high-throughput non-invasive phenotyping," *Nature Communications*, vol. 7, 2016, ISSN: 20411723. DOI: 10.1038/ncomms13342.
- [67] M. J. Pringle, "Robust prediction of time-integrated NDVI," *International Journal of Remote Sensing*, vol. 34, no. 13, pp. 4791–4811, 2013, Publisher: Taylor and Francis Ltd., ISSN: 13665901. DOI: 10.1080/01431161.2013.782117.
- [68] B.-J. van Rossum, *statgenGxE: Genotype by Environment (GxE) Analysis*, 2021. [Online]. Available: <https://cran.r-project.org/package=statgenGxE>.
- [69] M. Kuhn and H. Wickham, *Tidymodels: A collection of packages for modeling and machine learning using tidyverse principles*. 2020. [Online]. Available: <https://www.tidymodels.org>.

- [70] B. M. Greenwell and B. C. Boehmke, “Variable Importance Plots—An Introduction to the vip Package,” *The R Journal*, vol. 12, no. 1, pp. 343–366, 2020. [Online]. Available: <https://doi.org/10.32614/RJ-2020-013>.
- [71] J. Li *et al.*, “Principal variable selection to explain grain yield variation in winter wheat from features extracted from UAV imagery,” *Plant Methods*, vol. 15, no. 1, p. 123, Nov. 2019, ISSN: 1746-4811. DOI: 10.1186/s13007-019-0508-7. [Online]. Available: <https://doi.org/10.1186/s13007-019-0508-7> (visited on 08/15/2022).
- [72] B. Gregorutti, B. Michel, and P. Saint-Pierre, “Correlation and variable importance in random forests,” en, *Statistics and Computing*, vol. 27, no. 3, pp. 659–678, May 2017, ISSN: 1573-1375. DOI: 10.1007/s11222-016-9646-1. [Online]. Available: <https://doi.org/10.1007/s11222-016-9646-1> (visited on 08/19/2022).
- [73] R. Xu and C. Li, “A Review of High-Throughput Field Phenotyping Systems: Focusing on Ground Robots,” en, *Plant Phenomics*, vol. 2022, pp. 1–20, Jun. 2022, ISSN: 2643-6515. DOI: 10.34133/2022/9760269. [Online]. Available: <https://spj.sciencemag.org/journals/plantphenomics/2022/9760269/> (visited on 08/03/2022).
- [74] J. Sperschneider, “Machine learning in plant–pathogen interactions: Empowering biological predictions from field scale to genome scale,” *New Phytologist*, 2019, ISSN: 14698137. DOI: 10.1111/nph.15771.
- [75] K. Weiss, T. M. Khoshgoftaar, and D. D. Wang, *A survey of transfer learning*. Springer International Publishing, 2016, vol. 3, Publication Title: Journal of Big Data Issue: 1 ISSN: 21961115, ISBN: 4-05-370160-0. DOI: 10.1186/s40537-016-0043-6.
- [76] J. G. A. Barbedo, “Impact of dataset size and variety on the effectiveness of deep learning and transfer learning for plant disease classification,” *Computers and Electronics in Agriculture*, vol. 153, no. July, pp. 46–53, 2018, Publisher: Elsevier, ISSN: 01681699. DOI: 10.1016/j.compag.2018.08.013. [Online]. Available: <https://doi.org/10.1016/j.compag.2018.08.013>.
- [77] C. Brien, N. Jewell, S. J. Watts-Williams, T. Garnett, and B. Berger, “Smoothing and extraction of traits in the growth analysis of noninvasive phenotypic data,” *Plant Methods*, vol. 16, no. 1, pp. 1–21, 2020, Publisher: BioMed Central, ISSN: 17464811. DOI: 10.1186/s13007-020-00577-6. [Online]. Available: <https://doi.org/10.1186/s13007-020-00577-6>.

Chapter 4

**Time course RGB imaging
outperforms hyperspectral imaging
for chickpea *Ascochyta* blight
severity prediction in the
greenhouse**

4.1 Declarations

Statement of Authorship

Title of Chapter	Time-course RGB imaging outperforms hyperspectral imaging for chickpea <i>Ascochyta</i> blight severity prediction in the greenhouse
Publication Status	Unpublished and unsubmitted work written in a manuscript style
Publication Details	Unpublished and unsubmitted

Principal Author

Name of Principal Author	Florian Tanner
Contribution to the Paper by the Candidate	Conception, Knowledge, Experimentation, Analysis, Drafting. Performed experiments, analysed data, wrote manuscript.
Overall percentage Certification	80% This paper reports on original research I conducted during the period of my Higher Degree by Research candidature and is not subject to any obligations or contractual agreements with a third party that would constrain its inclusion in this thesis. I am the primary author of this paper.
Signature	
Date	2022-12-09

Co-Author Contributions

By signing the Statement of Authorship, each author certifies that:

- the candidate's stated contribution to the publication is accurate (as detailed above);
- permission is granted for the candidate to include the publication in the thesis; and
- the sum of all co-author contributions is equal to 100% less the candidate's stated contribution.

Name of Co-Author	Marzena Krysinska-Kaczmarek
Contribution to the Paper	Conception and Experimentation: Inoculum preparation and inoculation
Signature	
Date	December 09, 2022

Name of Co-Author	Chris Brien
Contribution to the Paper	Experimental Design and Statistical Analysis
Signature	
Date	
Name of Co-Author	Prabhakaran Sambasivam
Contribution to the Paper	Conception: Advice on greenhouse experimentation, inoculation and scoring
Signature	
Date	11/12/2022
Name of Co-Author	Huajian Liu
Contribution to the Paper	Hyperspectral Data Analysis: Advice on merging sensor data, semantic segmentation
Signature	
Date	December 09, 2022
Name of Co-Author	Darren Plett
Contribution to the Paper	Conception
Signature	
Date	December 12, 2022
Name of Co-Author	Kenneth Clarke
Contribution to the Paper	Hyperspectral Data Analysis and Review of Manuscript
Signature	
Date	December 09, 2022
Name of Co-Author	Jennifer Davidson
Contribution to the Paper	Conception and Review of Manuscript, Advice on experimental design and scoring
Signature	
Date	12/12/22
Name of Co-Author	Bettina Berger
Contribution to the Paper	Conception and Review of Manuscript
Signature	
Date	December 09, 2022

4.2 Abstract

Hyperspectral imaging can be used for the prediction of disease severity and early detection of diseases in plants to support resistance breeding and precision agriculture. So far, it has not been applied to chickpea and *Ascochyta* blight, a disease caused by the necrotrophic fungus *Ascochyta rabiei* (Pass.) Labr. (syn. *Phoma rabiei*). Here, we imaged two experiments of greenhouse-grown chickpea plants infected with *A. rabiei* in an automated phenotyping system with hyperspectral and RGB sensors for three weeks after inoculation. We developed regression models to predict disease indices, as well as classification models to distinguish infected from noninfected plants as early as possible. Testing the models in cross-validation, the longitudinal traits extracted from the RGB data resulted in a much more transferable model, achieving a validation $R^2 = 0.64$ compared to the best hyperspectral imaging-based model that only achieved a validation $R^2 = 0.02$. Early detection algorithms based on hyperspectral data reached estimated accuracies of 71% at 12 days after infection in 2020 to 78% at 9 DAI in 2021 in cross-validation. However, the classifiers trained on hyperspectral data were not transferable from the training experiment to the validation experiment, where they only achieved accuracies of 42% to 54%, no better than random classifiers. This study demonstrates the suitability of RGB time course imaging derived traits for the prediction of the severity of *Ascochyta* blight disease in greenhouse-grown chickpea plants and the challenges and limitations of hyperspectral models for both severity prediction and disease detection.

4.3 Introduction

4.3.1 Spectroscopy for plant disease phenotyping

Hyperspectral sensing can be applied to guide integrated disease management in precision agriculture, identify sources of resistance in breeding programs and to examine the biochemical interactions between plants and pathogens (Chapter 2) (Mahlein et al., 2018). The fine spectral resolution and extended spectral range of hyperspectral sensors can enable the measurement of such specific interactions (Brugger et al., 2021; Mahlein et al., 2018). Therefore, hyperspectral sensing can support breeding by detecting small differences in quantitative resistance and potentially detecting resistance mechanisms (Mahlein et al., 2018). If automated phenotyping systems are used, hyperspectral sensing has, as other sensor-based methods, the potential to increase throughput, thereby allowing a larger number of plants to be screened. Several plant-pathogen interactions and host resistance mechanisms that are known for chickpea AB could potentially be detected using hyperspectral sensing, including polyamine metabolism, malic acid content, and up-regulation of peroxidase activity (Chapter 1). Hyperspectral sensing can be distinguished into imaging (2D, 3D) and non-imaging (1D) techniques, where imaging techniques can consider the spatial variability and separate plant material from background material, whereas non-imaging

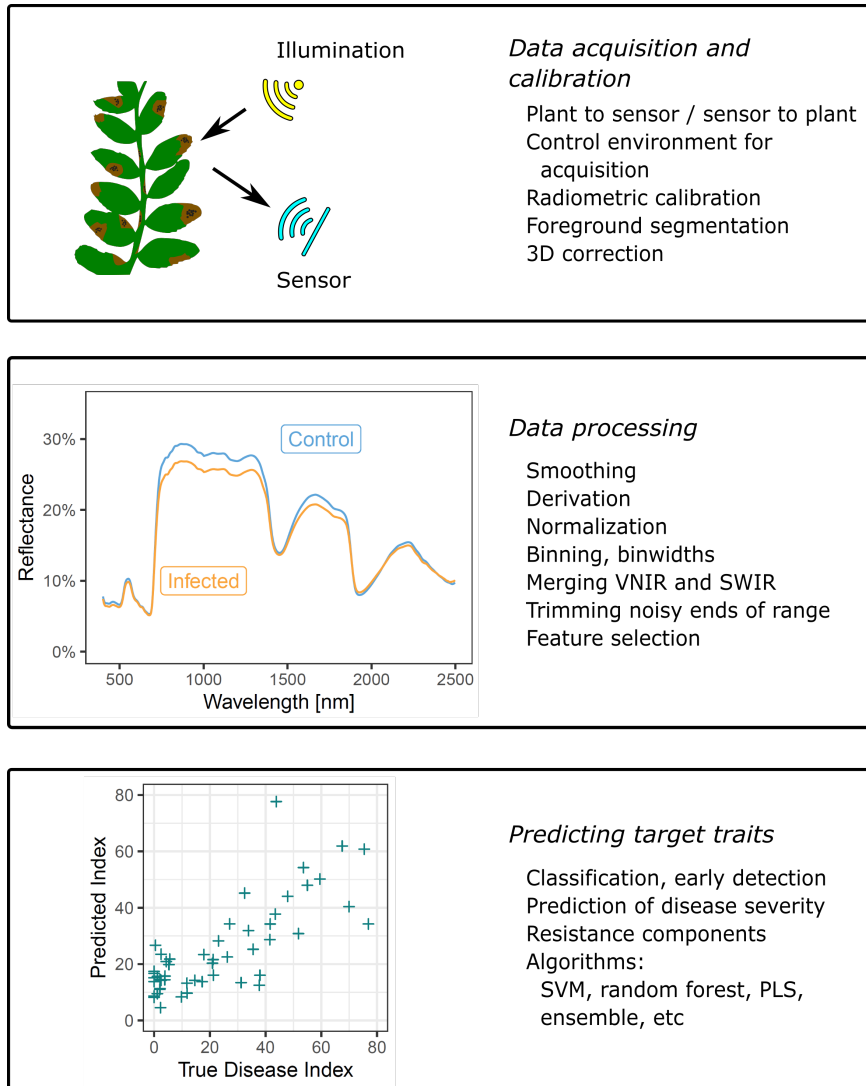


FIGURE 4.1: Steps in hyperspectral sensing from data acquisition to trait prediction. Especially the steps in data processing and target trait prediction require subjective user choices that can influence the results.

spectroscopy can only measure the average reflectance of an entire scene. The non-imaging approach can either be proximal or contact sensing, whereby contact sensing requires manual fixing of the leaves (Fernando Emiliano Romero Galvan et al., 2022). The application of hyperspectral sensing, in particular imaging, is currently limited by the required complex technical setup including cameras and illumination as well as the analysis workflow. The data processing (Figure 4.1) regularly requires subjective user choices that can have a large influence on the results of the analysis (Paulus and Mahlein, 2020; Hennessy, Clarke, and Lewis, 2020).

4.3.2 Related work

Non-imaging spectroscopy

Contact spectroscopy In contact spectroscopy, the sensor is brought close to the sample with a probe tip. Four potato genotypes inoculated by leaf plug with *Phytophthora infestans* were measured daily over the course of one week after inoculation with a leaf-clip high-spectral-resolution SVC HR-1024i (350–2500 nm) field spectroradiometer (Spectra Vista Corporation, Schenectady, NY, USA) (Gold et al., 2020b). The spectral reaction between an R-gene transformed cultivar and its non-transformed counterpart was similar, whereby the transformed cultivar had a stronger reaction in the VNIR region. Despite genotypic difference in spectral response, detection accuracy with a random forest (RF) classifier did not depend strongly on the inclusion of genotypic information, at both control vs pre-symptomatic timepoints (83.41 % vs 84.83 %) and control vs postsymptomatic timepoints (82.65 % vs 81.74 %). Three different feature selection algorithms identified similar wavebands across VIS, VNIR, and SWIR regions that were important for the detection of disease. It was recommended to include the SWIR region bands for robust detection models due to the stability of the spectral response to infection, which remained consistent across cultivars. The metabolic and physiological changes that were suggested to be linked to spectral response were water content, nitrogen content, and total phenolics content. Phenolic content and water content are also affected in chickpea affected by AB, making these traits interesting candidates for detection (Table 1.2). No disease severity prediction was conducted as plants with low severity were excluded from the study and no significant differences between the cultivars were observed, despite the inclusion of a transformed plant containing a copy of an R-gene from a potato wild relative.

The wavebands related to water content also played a role in the classification between rice plants treated with mock-inoculation and inoculation of *Rhizoctonia solani* (rice sheath blight) (Conrad et al., 2020). Only one day after inoculation, the treatments could be distinguished with 86.1 % accuracy. The authors used contact sensing in only the SWIR range with a NeoSpectra micro handheld spectrometer (SiWare Systems, La Canada, CA, USA; 1348–2551 nm; 16 nm spectral resolution) and found informative bands linked to moisture, starch, cellulose and protein content (Chapter 2).

In pot-grown peanuts (*Arachis hypogaea* L.) infected with *Athelia rolfsii*, leaf-clip spectrometry between 200 - 1100 nm (Handheld Jaz spectrometer, 0.46 nm optical resolution, Ocean Optics, Dunedin, FL, USA) was performed and disease severity was classified in three different models (a) Binary classification: Healthy and Severe, (b) Three-class model: Healthy, Mild, Severe, and (c) Five-class model: Healthy, Presymptomatic, Lesion only, Mild, Severe (Wei et al., 2021). The choice of learning algorithms had significant impact on the classification accuracy, depending on the number of classes. Various feature selection algorithms chose similar important bands in VIS, Red-edge and NIR region related to chlorophyll and carotenoid content. This study highlights the importance of choice of learning algorithm and underlines the

advantage of ensemble feature selection for robust waveband selection. Even though daily spectral measurements were taken, the time course data was only considered insofar that each plant was visually rated at each measurement day, thereby providing a disease class label for each timepoint. A similar approach to time series data analysis was chosen by Gold et al., 2020b and has the advantage of normalisation for disease development between experiments. However, it makes the classification completely dependent on ground-truthing by visual scoring.

Contact spectroscopy has also been applied to tree diseases. Leaves of lemon myrtle trees (*Backhousia citriodora*) affected by *Austropuccinia psidii* were scanned with a non-imaging spectroradiometer (Spectral Evolution PSR+ 3500) resampled to a resolution of 10 nm between 350 - 2500 nm (Heim et al., 2018). High classification accuracy between (i) healthy, non-treated trees, (ii) treated and (iii) diseased, untreated trees were achieved. A major influence of derivation of the spectra was observed, classification accuracy increased from 78 % ($\kappa = 0.68$) for primary spectra to 95 % ($\kappa = 0.92$) for first-order derivatives, again highlighting the importance of pre-processing steps. It is possible that factors unrelated to the disease may have increased the reported detection accuracy, as treatment (i) was sampled at a different location compared to treatments (ii) and (iii). Important features for the classification were identified in VIS, VNIR, and SWIR regions linked to necrosis, chlorosis, water content, and general plant stress.

In a study comparing the spectral response of potato to infection with two different pathogens (*Phytophthora infestans* and *Alternaria solani*), successful presymptomatic distinction (Accuracy = 80 %) between the diseases was achieved with a contact spectrometer (SVC HR-1024i; 350–2500 nm; Spectra Vista Corporation, Schnectady, NY, USA) (Gold et al., 2020a). This study indicates that disease-specific detection is possible with contact spectrometry.

Proximal spectroscopy does not require contact of the sample and probe tip of the sensor. This can increase throughput but may reduce data quality because non-plant materials present in the scene is also measured alongside the material of interest. In one such study, measurements of wheat infected with powdery mildew in the field were taken both at flowering and filling from 1 m above the canopy with a handheld non-imaging spectrometer (FieldSpec Handheld 2, Analytical Spectral Devices, Boulder, CO, USA, 325–1075 nm) (Ziheng Feng et al., 2021). In addition, a FLIR T650sc thermal infrared camera (FLIR Systems, Inc., Wilsonville, OR, USA) was used to derive canopy temperature parameters and RGB-image based texture features. Data fusion of spectral vegetation indices with temperature and texture parameters improved the prediction of a disease index, showing that multimodal sensing can improve disease severity prediction. The authors found that RF regression performed better than support vector machine (SVM) and partial least squares (PLS) regression, once more highlighting the influence of learning algorithms. Even though two timepoints were measured, the results were pooled and only differentiated by the visually scored disease severity at

the respective time points. It is possible that spectral signatures related to the growth stage of the plants, not only the disease development, influenced the prediction results.

In an attempt at transferring results from contact spectrometry to proximal spectrometry, a non-imaging leaf clip spectrometry (350 - 2500 nm, FieldSpec 4 Hi-Res, ASD Inc., Boulder, CO, USA) with active illumination was used on wild rocket (*Diplotaxis tenuifolia*) infected with three different soil-borne pathogens (*Rhizoctonia solani*, *Sclerotium rolfsii*, and *Sclerotinia sclerotiorum*) under greenhouse conditions (Angelica Galieni et al., 2022). Vegetation indices were calculated from wavebands that were selected with a random forest feature selection approach. These vegetation indices were then evaluated on canopy-level reflectance in a more natural growing environment with the same non-imaging spectrometer with only sunlight as illumination. Significant rank correlations of indices formed from bands largely in the VIS spectral region as well as one index from the SWIR region were observed with visual disease severity scores in both environments. However, all calculated vegetation indices were also significantly correlated with leaf area and dry matter, which questions whether the spectral regions are biotic stress-specific, let alone pathogen-specific. It would be interesting to see how an imaging spectrometer with which foreground reflectance could be separated from background reflectance would perform at the canopy level. No classification of causal pathogens was attempted. However, this study showed the option of scaling up contact spectrometry to proximal spectrometry and estimating general disease severity of wild rocket with non-invasive hyperspectral sensors at canopy level. This provides a way for automated stress recognition in the field. A further field using proximal spectroscopy study for *Septoria tritici* blotch, a disease of wheat characterized by necrotic lesion, is discussed in Chapter 5 Section 5.3.3 (Yu et al., 2018).

Imaging spectroscopy

Imaging of individual leaves Zhang et al., 2022 imaged detached rice leaves from a field infected with *Xanthomonas campestris* pv. *Oryzae* (Rice bacterial blight) with an imaging spectrograph (ImSpector V10E; Spectral Imaging Ltd., Oulu, Finland; 413 - 1016 nm; 473 bands) and a EMCCD camera (Raptor EM285CL, Raptor Photonics limited, Larne, United Kingdom). Time course 2D data was collected over eight time points, but the spectra were simply averaged over time and space for prediction of lesion proportion and infection status. In a two-stage deep learning algorithm, infection status could be classified with 92 % accuracy and proportion of lesions predicted with an R^2 of 0.96 on validation data. High classification accuracy and lesion proportion were achieved, but it is not clear whether the time course nature of the data provided an advantage as no comparison to using individual time points was made.

Extending the usual spectral range to the UV range, a change in flavonoid content until 5 DAI of barley leaves infected with *Blumeria graminis* f. sp. *hordei* could be linked with corresponding wavebands (Brugger et al., 2021). The leaves were detached and imaged with a Hyperspec UV-VIS-Interline CCD Sensor (Headwall Photonics,

Bolton, MA, USA; 240–500 nm; spectral resolution of 1.4 nm). This study shows that wavebands beyond the usual spectral range of 400 - 2500 nm can be useful for measuring specific plant-pathogen interactions (Chapter 2).

Detached leaves of sugar beet infected with *Cercospora beticola* were imaged with a HySpex SWIR-320m-e line camera (Norsk Elektro Optikk A/S, Skedsmokorset, Norway; 970–2,500 nm; Spectral resolution 6 nm) four days after infection from 1 m distance (Arens et al., 2016). Genotypic differences of leaf metabolite content depending on the level of resistance were found by mass spectrometry. High correlations of the metabolite contents to spectral data were found (R^2 from 0.71 to 0.94), indicating that HSI is a suitable technology for screening plant genotypes for resistance based on specific metabolite contents.

Working on the same plant-pathosystem (Sugar beet - *Cercospora beticola*), but imaging at an even closer distance, an overall decrease in reflectance in the spectral range between 400 - 900 nm was shown to be correlated with sporulation (Oerke, Leucker, and Steiner, 2019). This was demonstrated by using hyperspectral microscopy of individual lesions with a spectral line scanner (Spectral camera PFD V10E, Spectral Imaging Ltd., Oulu, Finland).

Aerial imaging Olive trees infected with *Verticillium dahliae* were imaged with a hyperspectral (VNIR model; Headwall Photonics, Fitchburg, MA, USA; 400–885 nm; 260 bands; 40 cm GSD) and a thermal sensor from an aircraft at 500 m altitude (Zarco-Tejada et al., 2018). The disease could be detected with 81.0 % accuracy ($\kappa = 0.61$) when functional traits from both sensors were combined (Pigment-, Structure-, Fluorescence and Temperature-based Functional Traits). The omission of fluorescence and thermal traits only slightly decreased the accuracy to 78.5 % ($\kappa = 0.56$). However, when instead of functional traits, standard vegetation indices were used, the accuracy decreased to 65.4 % ($\kappa = 0.29$). This shows the advantage of sensor fusion but even more so the importance of translating reflectance measurements into functional traits related to the plant-pathosystem (York, 2019).

Aerial imaging spectroscopy datasets were gathered from olive trees infected by *Verticillium dahliae* (Calderón, Navas-Cortés, and Zarco-Tejada, 2015) and *Xylella fastidiosa* Zarco-Tejada et al., 2018. These two datasets were combined and it was shown that functional spectral traits can accurately distinguish the two diseases (98 %, $\kappa = 0.7$), even though the symptoms of the diseases are visually similar when observed in the field (Poblete et al., 2021). This study showed that disease-specific detection can be achieved.

For the viral disease Grapevine Leafroll-associated Virus Complex 3 (GLRaV-3), accurate early disease detection was possible with aircraft-based imaging spectroscopy data (AVIRIS - NG, 380 to 2510 nm range) (Fernando Emiliano Romero Galvan et al., 2022). At a subsampled ground sampling distance of 3 m, an accuracy of 87 % ($\kappa = 0.73$) was achieved for distinguishing pixels labelled as (a) non-infected and (b) infected but asymptomatic. The authors thereby showed that the disease can

be recognised not only at close range, but also at high throughput. However, no discussion whether the same wavelengths as discovered in previous studies using proximal and contact sensing were useful or sufficient for detection. Therefore, it is not possible to hypothesize whether the same mechanisms were responsible for causing the spectral changes that allowed the classification in each environment.

Spectroscopy for chickpea AB

One study reported the use of spectroscopy for disease severity prediction of chickpea AB (Zhang, Chen, and Sankaran, 2019). A non-imaging leaf clip spectroradiometer (SVC HR-1024i; 350–2500 nm; Spectra Vista Corporation, Schenectady, NY, USA) was used to measure reflectance on three leaves from each of multiple plots of two chickpea genotypes exposed to AB infection and various fungicide treatments at 11 and 19 DAI. Due to the varying efficacy of the fungicides and genotypic effects, a range of disease severity was observed across the plots and visually rated on a scale of 1-9. The reflectance was normalized, binned to a bin width of 10 nm, and the three measurements per plot were averaged. Then, vegetation indices were extracted, of which many showed significant correlation with the disease rating. The highest absolute Pearson correlation coefficients for vegetation indices were $r = 0.51$ 11 days after infection (DAI) with Modified Red Edge Simple Ratio (MRESR) and $r = 0.60$ 19 DAI with Anthocyanin Reflectance Index (ARI2). Additionally, candidate features were extracted using the least absolute shrinkage and selection operator (LASSO). Using a linear regression model with the 14 features selected by LASSO as predictors, correlation coefficients of $r = 0.71$ on 11 DAI and $r = 0.73$ on 19 DAI were achieved. The selected bins were at 670, 680, 730, 770, 1220, 1230, 1241, 1251, 1260, 1271, 1281, 1380, 1391, and 1660 nm. No hypothesis was proposed as to why these wavelengths were selected by the algorithm except for the inclusion of bands in the red and red edge region that are used for many vegetation indices. Feature selection was performed with LASSO, but this algorithm runs the risk of random selection of correlated predictors, meaning that it should be validated on an independent test set, especially in situations with high multicollinearity such as hyperspectral data (Figures 4.2, 5.6) (James et al., 2013). Although the metrics were reported from an unseen test set from the same experiment, it would be interesting to see how the features transfer to an independent experiment. In addition, it is not clear how the three sampled leaves were chosen and how the reflectance at the entire canopy level would perform to estimate severity.

4.3.3 Research opportunities

Whole plant hyperspectral imaging The use of contact non-imaging spectroscopy is well established for measuring plant-pathogen interactions and high disease detection accuracies have been achieved (Section 4.3.2; Chapter 2). However, it is not yet clear how well the technology translates to proximal and imaging spectroscopy. The imaging spectroscopy that has been performed to date has been largely at canopy scale

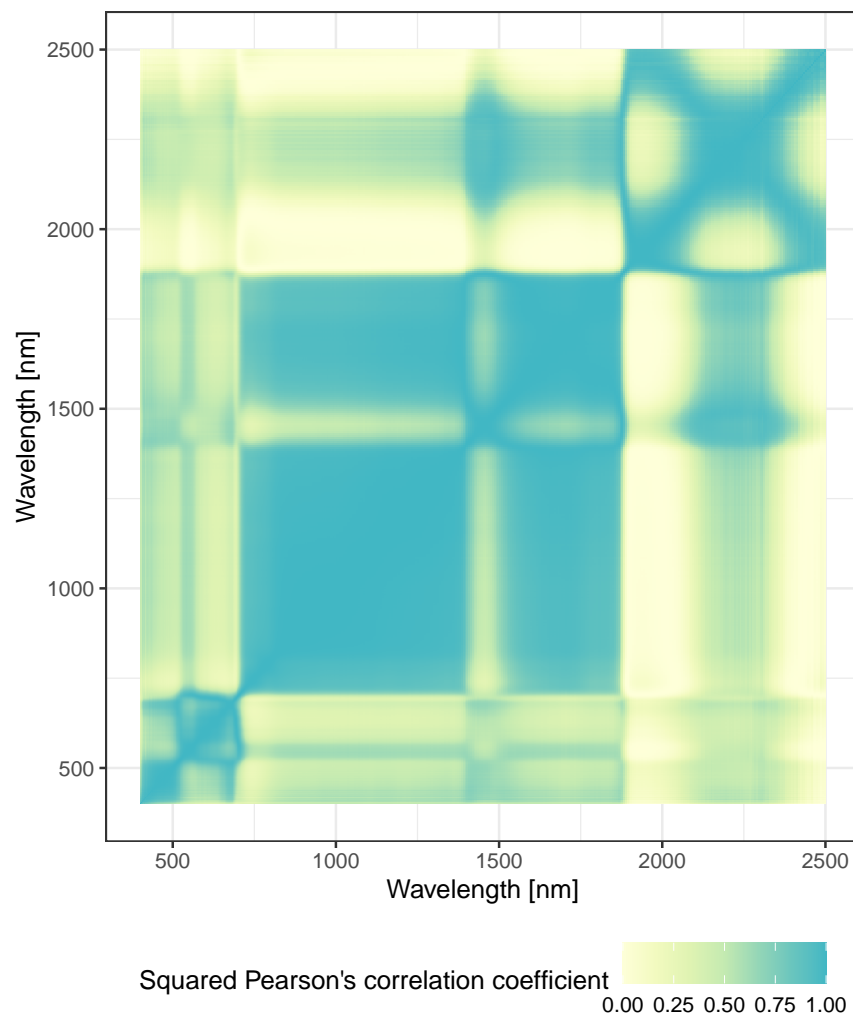


FIGURE 4.2: Symmetric matrix displaying the squared Pearson's correlation coefficient between reflectance at distinct wavelengths ($n = 710$). Data from average reflectance in 2020.

of tree crops (Zarco-Tejada et al., 2018; Poblete et al., 2021) or on detached or fixed plant parts at close range (Oerke et al., 2016; Oerke, Leucker, and Steiner, 2019; Zhang et al., 2022). An exception is the study by Fernando Emiliano Romero Galvan et al., 2022, where grapevines were imaged from the air (Paragraph 4.3.2). This leaves a research opportunity for whole-plant time course imaging spectroscopy for plant-pathogen interactions.

Time course hyperspectral imaging A few studies have performed time course spectroscopy, however the data has often been aggregated by disease rating (Gold et al., 2020b; Ziheng Feng et al., 2021; Wei et al., 2021) or averaged over time (Zhang et al., 2022). An opportunity would be to consider the development over time or reduce dimensionality of the entire dataset rather than averaging (Dorrepaal, Malegori, and Gowen, 2016).

Detecting genotypic differences Often, the only goal of the studies employing spectroscopy is the (early) detection of infected samples compared to non-infected samples. Less work is available that aims to measure genotypic differences and predict disease severity.

Examining influence of pre-processing and learning algorithms Many studies do not apply systematic comparisons of pre-processing and learning algorithms, even though their influence is well documented (Heim et al., 2018; Wei et al., 2021; Hennessy, Clarke, and Lewis, 2020).

Opportunities for AB in particular Specifically for AB of chickpea, no HSI has been performed so far to my knowledge. Yet, multiple functional spectral traits that have also been found to be important in other plant-pathosystems may be relevant for chickpea AB, for example water and phenolic content (Table 1.2).

4.3.4 Research aims

This study aimed to predict disease indices of chickpea AB with whole plant time course imaging using hyperspectral and multi-angle RGB sensors and compare the sensor suitability. Additionally, the possibility of early disease detection with hyperspectral data was evaluated. For both prediction of disease indices and early detection, the influence of hyperspectral data pre-processing steps and learning algorithms on prediction performance was examined.

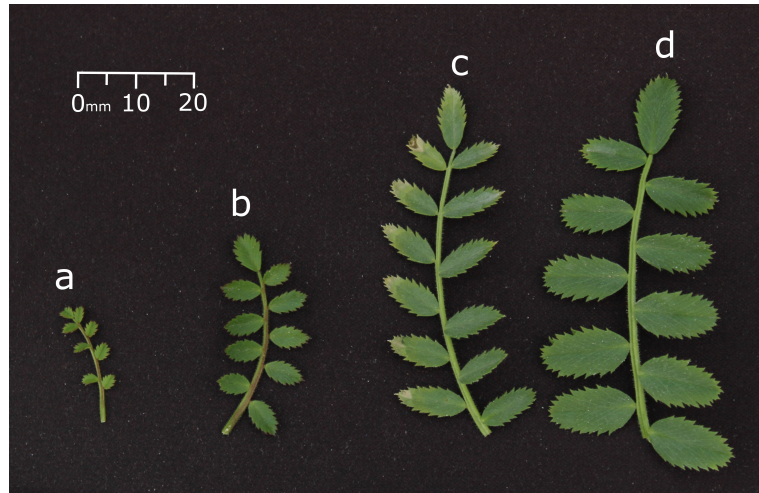


FIGURE 4.3: Leaves of fully mature chickpea and wild relatives. a = *Cicer echinospermum*, b = *Cicer reticulatum*, c and d = *Cicer arietinum*

4.4 Materials and methods

4.4.1 Plant material

Multiple commercial chickpea cultivars (CVR477, CVR480, CVR481, CVR484) with varying degrees of resistance and a candidate resistant wild relative *C. reticulatum* accession (WLD085) were grown in two different experiments carried out in a greenhouse in 2020 and 2021 (Figure 4.3). A third experiment was conducted in 2021 but was not considered for the analysis because cross-infection occurred in non-infected plants. The genotypes were chosen to represent different resistance ratings from sowing guides and based on their performance in disease screens performed in pots in outdoor conditions (GRDC, 2016; GRDC, 2017) (Chapter 3). Two control genotypes were also included in the screens. Cv. Howzat serves as a routine very susceptible control, and cv. Genesis090 is a moderately susceptible cultivar (Raman et al., 2022; Blake, 2022). Two seeds per pot were sown in draining pots (19.5 cm height \times 14.9 cm diameter, 2.5 l volume) containing Van Schaik's Bio Gro soil mix (Bio Gro Pty Ltd., Mount Gambier, South Australia) and thinned to a single plant 10 days after sowing (Figure 4.5).

4.4.2 Infection

To establish AB infection, plants were inoculated 14 days after sowing following the mini-dome protocol with clear plastic cups (Chen, McPhee, and Muehlbauer, 2005). Each plant was sprayed with 2 ml of *A. rabiei* isolate 16CUR018 (collected from cv. Genesis090 in Curyo, Victoria, Australia in 2016) spore suspension at a concentration of 1×10^5 spores per ml using a hand sprayer (Bar, 2019). The inoculum was prepared with surfactant Tween 20 (0.01%) (Merck Pty Ltd.). Control plants were sprayed with water and surfactant. After inoculation, the plants were immediately covered with



FIGURE 4.4: Mini-dome inoculation. Plants are covered with inverted transparent plastic cups to ensure high humidity after inoculation.

inverted transparent plastic cups (Figure 4.4). In 2020, cups with a volume of 500 ml were left on the plants for 24 hours and in 2021, cups with a volume of 1 l were used for 48 hours (Figure 4.5).

4.4.3 Experimental design

All experiments were carried out in greenhouses at the Australian Plant Phenomics Facility, University of Adelaide. Temperatures were set to a maximum of 21 °C and high humidity was ensured by running a humidifier on demand at varying intervals. However, temperature fluctuated in both experiments due to ambient temperatures and the humidity could not be reliably controlled. The experiment in 2020 was carried out with five replicates in a randomized complete block design (RCBD) created with the `dae` package (Brien et al., 2020). In 2021, the experiment was carried out with six replicates in a split-unit design created using the `agricolae` version 1.3.5 package (Felipe de Mendiburu and Muhammad Yaseen, 2020). The designs were created in the R versions 3.6.3 and 4.2.1 computing environment, respectively (R Core Team, 2022). In 2020, all plants were sown on 2020-04-28 and in 2021, the wild accession WLD085 was sown on 2021-05-04, 7 days before the cultivars (sown 2021-05-11) (Figure 4.5). The wild accession was sown earlier to account for differences in germination rate and early plant development and to ensure a more uniform plant size at the time of inoculation.

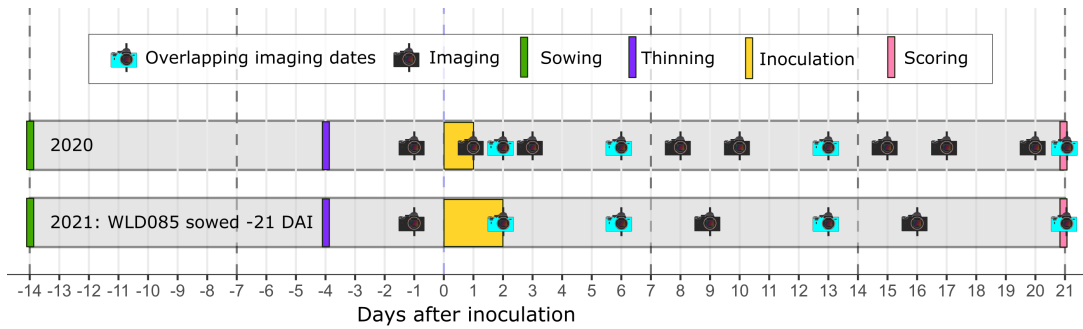


FIGURE 4.5: Experimental design with sowing, imaging, thinning, inoculation, and scoring dates. All imaging timepoints were used for longitudinal smoothing of RGB data and extraction of intermediate traits for the prediction of DI. The overlapping imaging dates 2, 6, 13, 21 DAI were used to evaluate early detection algorithms. In 2021, the wild accession WLD085 was sown seven days before the other plants (-21 DAI) due to its slower germination and early growth.

4.4.4 Data acquisition

Imaging

Imaging was performed at 12 time points in 2020 (-1, 1, 2, 3, 6, 8, 10, 13, 15, 17, 20, 21 days after inoculation (DAI)) and at 7 time points in 2021 (-1, 2, 6, 9, 13, 16, 21 DAI) in an automated phenotyping system (Figure 4.5). The system that was used at The Plant Accelerator® (Australian Plant Phenomics Facility, University of Adelaide) is based on a conveyor belt that automatically delivers pots to imaging chambers, including RGB and hyperspectral sensors (Scanalyzer3D, LemnaTec GmbH, Germany).

RGB imaging The RGB image chamber is equipped with four cameras (AlliedVision Prosilica GT) and four white LED panels for illumination (Gardasoft VTR4-W-28-ETH-NC). The cameras are positioned at nadir angle, side view, and two additional angled side views (close and far). When the pots arrive at the imaging chamber, they are automatically lifted onto a platform and a topview image is taken. The platform with the plant is then turned in five incremental steps of 35 degrees. At each step the three side view cameras take images, leading to a total of 19 images capturing 18 side views and one top view (Figure 4.8).

Hyperspectral imaging The hyperspectral imaging (HSI) chamber contains two hyperspectral line-scan cameras that cover a wavelength range of 400 - 2,500 nm, and a halogen light array for equal illumination. The NIR range is covered by a SpecimFX10 camera (Specim, Finland) and the SWIR range is covered by a Specim SWIR 3 camera (Specim, Finland) (Table 4.1). Top view images were taken with both hyperspectral cameras (Figure 4.6). The imaging system has a ground sampling distance (GSD) of 1.96 mm per pixel in VNIR data and 2.37 mm per pixel in SWIR data, leading to low

TABLE 4.1: Specifications of hyperspectral cameras in automated phenotyping system at The Plant Accelerator®.

Specification	Specim FX10	Specim SWIR 3
Spectral range	397 - 1,005 nm	979 - 2,587 nm
Number of bands	448	288
Full Width at Half Maximum (FWHM)	5.5 nm	12 nm
Spatial resolution	512 * 335 px	384 * 296 px
Ground Sample Distance (GSD)	1.96 mm	2.37 mm
Scanning speed	50 mm/s	50 mm/s
Exposure time	37.00 ms	9.60 ms
Frame rate	26.66	22.42

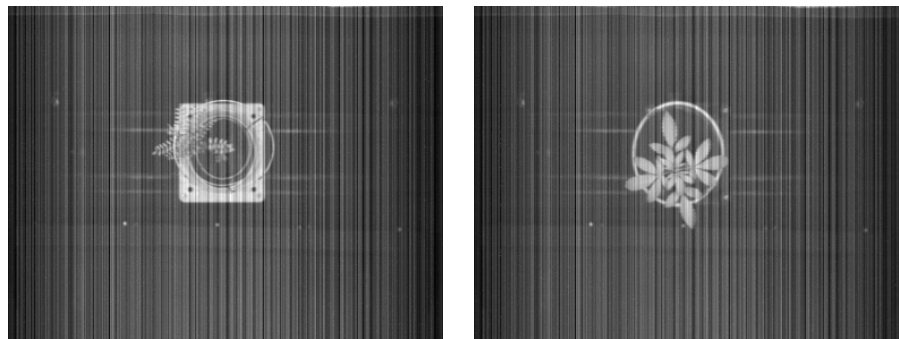


FIGURE 4.6: Monochrome images from Specim SWIR 3 camera of a hemp plant compared to chickpea plant. Left: Chickpea plant. Right: Hemp plant (used with permission from Alison Gill). The small chickpea leaflets are covered by only a few pixels each.

coverage of the leaflets, in particular for the *C. reticulatum* accession WLD085 (Figures 4.3 4.6). The scanning speed for both cameras was fixed at 50 mm/s.

Visual scoring

The disease symptoms were visually scored 21 DAI for percentage of broken main stems, percentage of main stems with lesions, percentage of diseased side branches and percentage of diseased leaf area, as described in Chapter 3. The mean of these four scores was taken to calculate a disease index. This index can take any value between 0 and 100, where 0 indicates no signs or symptoms of disease and 100 indicates a dead plant.

4.4.5 Data processing

Except for the RGB image analysis that was performed with proprietary LemnaTec software (LemnaGrid), all data analysis was performed using Python version 3.8.8 and R version 4.2.1 (R Core Team, 2022; Van Rossum, 2020). The functions and packages used are cited in the respective parts of the Methods section. Data were visualized

using the packages `ggplot2` version 3.3.6 and `ggstatsplot` version 0.9.4 (Wickham, 2016; Patil, 2021).

RGB data processing

LemnaTec proprietary image analysis Nearest-neighbor segmentation was used to distinguish foreground and background pixels, followed by erosion and dilation to fill areas. Projected shoot area (PSA) was then calculated as the sum of plant pixels of the top view (TV) camera angle and plant pixels from two images from each of the three side view cameras (SV , SV_{close} , SV_{far}). The difference between the two side view angles that were used to calculate PSA was 140 degrees.

Trait extraction PSA was smoothed over time using the `statgentHTP` version 1.0.5 package by fitting a spline with 5 knots to the longitudinal data of each plant (for more details on smoothing and trait extraction, see Chapter 3). From the fitted splines, the following intermediate traits were extracted. PSA at 0, 7, 14 and 21 DAI, relative growth rate (RGR) and absolute growth rate (AGR) between two time points (t_1 , t_2) (Brien et al., 2020). The chosen periods for the growth rates were 0 to 7 DAI, 7 to 14 DAI, and 14 to 21 DAI (Figure 4.9).

$$PSA = TV + SV_0 + SV_{140} + SV_{close_0} + SV_{close_{140}} + SV_{far_0} + SV_{far_{140}}$$

$$AGR_{t_1-t_2} = \frac{PSA_{t_2} - PSA_{t_1}}{t_2 - t_1}$$

$$RGR_{t_1-t_2} = \frac{\ln(PSA_{t_2}) - \ln(PSA_{t_1})}{t_2 - t_1}$$

Hyperspectral data processing

Pre-processing of the hyperspectral data consists of multiple steps (Figure 4.1) (Paulus and Mahlein, 2020). Up until the merging of VNIR and SWIR sensor data, the process was performed separately for each camera due to the slightly different imaging angle and the different spatial resolution of the cameras (Hennessy, Clarke, and Lewis, 2020). To remove noise at the extremes of the spectral range, the data were limited to a range of 400 to 2500 nm. Multiple algorithms for pre-processing were tested and the resulting processed data were tested as input for models in cross-validation (Figure 4.1).

Reading and calibrating The raw hyperspectral data were read and calibrated to black and white reference panels with the functions `read_hyper_data()` and `calibrate_hyper_data()` from the `appf_toolbox_v0` (Liu, 2020).

Segmentation of foreground pixels Training data for a classifier that can predict foreground and background pixels were created using false-color images of VNIR and SWIR data each. A total of 20 false-color images were randomly selected to represent the respective variety of imaged time points, genotypes, fungal isolates, and disease progressions for each experiment. These false-color images were loaded into the open source GNU Image Manipulation Program (GIMP) version 2.10.14 and binary masks of foreground pixels and selected background pixels were created using the Quick Mask tool (The GIMP Development Team, 2020). A Python script was then used to extract the hyperspectral pixel values corresponding to the marked pixels from the raw data using the `numpy` package and functions from the `appf_toolbox_v0` (Van Rossum, 2020; Liu, 2020; Harris et al., 2020).

A radial basis function (RBF) support vector machine (SVM) classifier for semantic segmentation was trained with a total of 10,000 randomly selected pixels from each foreground and background extracted from the annotated masks. A 70:30 train-test split was used, and the kernel and regularization parameter of the SVM classifier were optimized using a grid search. The trained classifier was applied to the entire dataset to predict and extract foreground pixels. Packages `pandas` version 1.3.4, `OpenCV` version 4.0.1 and `scikit-learn` version 1.0.1 were used (team, 2020; Pedregosa et al., 2011; Bradski, 2000).

Averaging reflectance of foreground pixels The pixel values of all foreground pixels for each pot were averaged and matched with the experimental design using the `tidyverse` version 1.3.2 collection of packages (Wickham et al., 2019).

Smoothing The average reflectance of each entry was smoothed along the spectrum with a Savitzky-Golay filter implemented in the `prospectr` version 0.2.4 package (Stevens and Ramirez-Lopez, 2020; Savitzky and Golay, 1964). For VNIR and SWIR data, the windowlength and polynomial order were chosen based on visual inspection of the smoothed graphs. A window length of 19 with a third-degree polynomial function was used for the VNIR data. For the SWIR data, the chosen window length was nine, also combined with a third-degree polynomial function. The window length was set to a higher number for VNIR due to the higher number of bands and the smaller band width (Table 4.1). In the case where derivatives of the reflectance were calculated, the smoothing step was integrated as a lagged difference with a gap size chosen based on the desired bin width. To combine VNIR and SWIR data, an overlap of the range of wavelengths is required. Savitzky-Golay filtering cuts off the outer edges of the spectral range because half the windowlength is required to calculate the outmost value. Therefore, the outer edges of the spectrum were padded with smoothed values from a shorter windowlength of five. This ensured overlap between the ranges of VNIR and SWIR data.

Sensor selection Both data exclusively from the VNIR sensor and combined data from both VWIR and SWIR sensors were tested as input for the algorithms.

Combining VNIR and SWIR data For full spectrum analysis, VNIR and SWIR data were combined by fitting a linear least squares model to the reflectance values of the last five wavelengths of the VNIR range (994.65, 996.06, 997.47, 998.88, 1000.29 nm) to predict the reflectance at 1002.18 nm, which is the wavelength of the first used band from the SWIR sensor. The difference between the predicted reflectance at 1002.18 nm and the measured reflectance at 1002.18 nm was then added to the SWIR data to normalize the entire range of SWIR data (Liu, personal communication).

Spectral binning Due to the full width at half maximum (FWHM) of the sensors that spans multiple bands and the optical properties of the plant tissue, adjacent spectral bands carry redundant information (Figure 4.2) (Moghimi, Yang, and Marchetto, 2018). To minimize autocorrelation and reduce the number of predictors, multiple neighboring bands can be averaged, so called binning (Lowe, Harrison, and French, 2017). Here, spectral binning was performed per sensor with the bin width chosen based on the FWHM of each sensor (Table 4.1). Two bin sizes were tested in the modeling pipeline, binning at FWHM and binning at double FWHM. Binning at FWHM reduced the total number of spectral bands from 710 to 233 and binning at double FWHM reduced the spectral bands to 117.

Normalization Due to differences in illumination that can exist even under controlled conditions, normalization of reflectance data was tested (Pu et al., 2012). The reflectance of the plant material at each band was divided by the mean reflectance over all bands.

Calculation of derivatives Gapped second and first derivatives were calculated from unsmoothed data. This was implemented with the `gapDer` function from the `prospectr` package. A window length of 11 and a gap size of 9 were used. Savitzky-Golay smoothing is performed at the given window length, followed by calculation of derivatives under the given gap size (Stevens and Ramirez-Lopez, 2020; Savitzky and Golay, 1964).

4.4.6 Analysis of disease indices and extracted traits

The genotypic and treatment effects on the disease indices and extracted traits were examined with analysis of variance. Where the effects were significant, pairwise differences were analyzed with Tukey Honest Significant Differences, implemented in the R package `agricolae` (Felipe de Mendiburu and Muhammad Yaseen, 2020).

4.4.7 Early detection of disease

The processed hyperspectral data were used to classify infected and non-infected plants at each imaging time point. Random forest (RF) and radial basis function support-vector machine (SVM) classifiers were trained and evaluated using `tidymodels` version 0.2.0 framework and `ranger` version 0.13.1, `kernlab` version 0.9-30 (Kuhn and Wickham, 2020; Karatzoglou, Smola, and Hornik, 2022; Wright and Ziegler, 2017). Five-fold cross-validation (CV) with five repeats was used to evaluate each model's performance within the individual experiments. To evaluate whether the model performed better than a random classifier, the accuracies achieved in cross-validation were compared to the accuracies that random classifiers achieved on the same samples with a t-test. This information was used to choose the best algorithm made up of a pre-processing pipeline and a learning algorithm for each imaging time point. The respective best algorithms within each year were then trained on the entire dataset for that year and tested on the full dataset from the other year where the imaging dates overlapped, which were 2, 6, 13, and 21 DAI (Figure 4.5).

4.4.8 Disease index prediction

Disease index prediction with RGB data

All traits extracted from RGB data were tested for their correlation with the disease index and both a simple linear regression model containing only the traits with the highest correlation to the disease index and a RF model containing all extracted traits as predictors were tested. Same as for the early detection, the algorithms were first evaluated within each year with five-fold CV with five repeats and then tested on the respective opposite year using a model trained on the entire data.

Disease index prediction with hyperspectral data

Disease indices were predicted using hyperspectral data from 21 DAI, the day of scoring. RF, SVM, and PLS regression were used.

4.5 Results

4.5.1 Disease indices

In general, the disease pressure in both experiments was low (Figure 4.7). There were significant genotypic effects on the DI only in 2021 (Supplementary Table 4.4). The wild accession WLD085, which was sown a week before the cultivars, had a significantly lower DI than CVR477 and CVR484, and CVR480 had a significantly lower DI than CVR484. No significant differences in DI were observed in 2020. Although the included control genotypes have differing variety resistance ratings (Howzat = susceptible to AB, Genesis090 = moderately susceptible to AB), no significant differences between their DI were observed in either year (Blake, 2022).

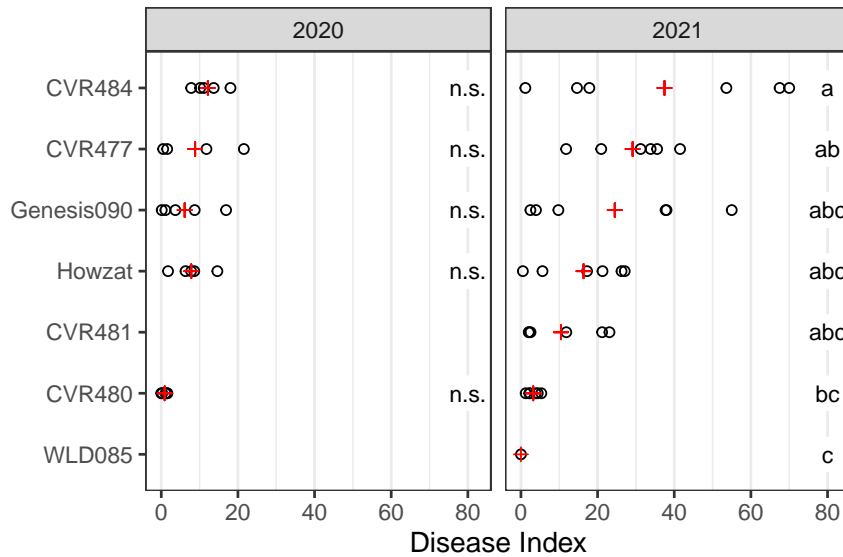


FIGURE 4.7: Disease indices of infected plants in greenhouse experiments in 2020 and 2021. Black dots indicate individual pots and red crosses indicate the mean disease indices. Accessions CVR481 and WLD085 were not grown in 2020. Letters indicate groups where pairwise comparisons are significantly different at $\alpha = 0.05$ within each year. n.s. = non-significant.

4.5.2 Projected shoot area

Overall, the wild accession WLD085 was much smaller compared to the *C. arietinum* accessions, despite the earlier sowing date (Figures 4.9 and 4.8). In response to inoculation, some genotypes showed a slowing of growth. This is reflected in a reduced RGR_{7-14} (Supplementary Figure 4.12). Interaction effects between genotype and treatment on RGR_{7-14} were significant in both experiments (Supplementary Table 4.4).

4.5.3 Early detection of AB using hyperspectral data

Using hyperspectral data, the infected plants could be distinguished from the non-infected plants 2 DAI with estimated accuracies (\pm standard deviation) of $62\% \pm 12\%$ in 2020 and $72\% \pm 12\%$ in 2021. The best discrimination between infected and non-infected plants was reached 17 DAI in 2020 ($72\% \pm 11\%$) and 9 DAI after infection in 2021 ($78\% \pm 9\%$) (Supplementary Table 4.6). On average over all imaging time points, the estimated detection accuracy was lower in 2020 with 63% than in 2021 with 74% , possibly due to the overall lower disease indices in 2020. Within each year, all classifiers were estimated to perform significantly better than a random classifier, except for the models at -1 and 1 DAI in 2020.

However, the accuracy when testing the best models trained on the entire data from each time point in 2020 on data from the corresponding equivalent time points in 2021 was low (Table 4.2). For the best models from 2, 6, 13, and 21 DAI trained

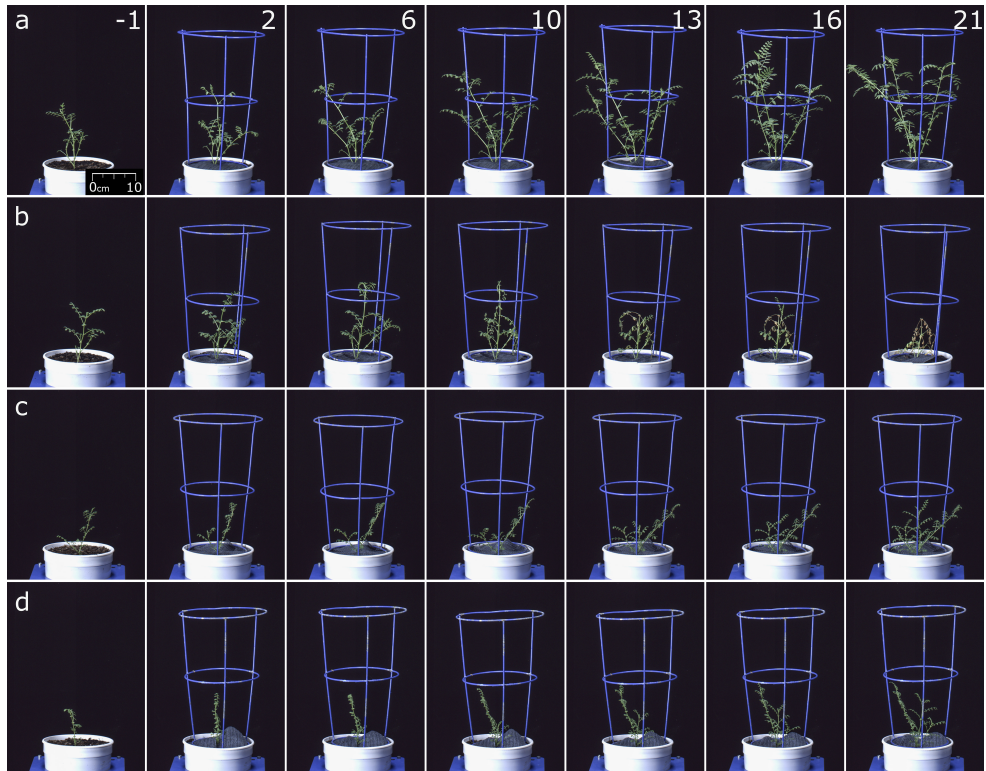


FIGURE 4.8: Side view images of plants in greenhouse from 2021 experiment, from -1 DAI to 21 DAI. a) = CVR484 control (DI = 0), b) = CVR484 infected (DI = 70), c) = WLD085 control (DI = 0), d) = WLD085 infected (DI = 0). Despite the earlier sowing date, WLD085 was smaller than the cultivars at the time of inoculation. DI = 70 was the highest observed DI for the entire experiment. The entire grid image was adjusted for exposure and color using Adobe Lightroom automatic settings.

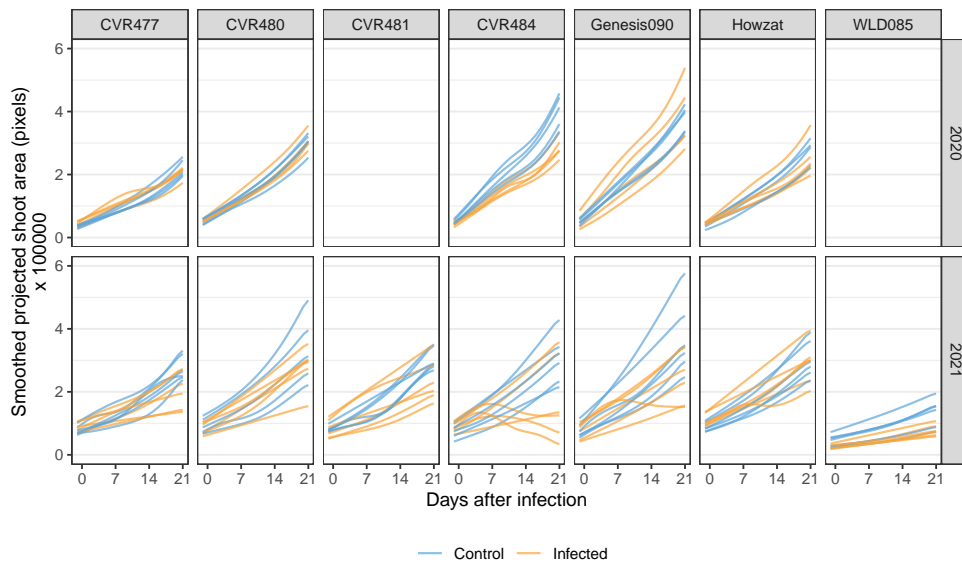


FIGURE 4.9: Smoothed PSA in greenhouse experiments in 2020 and 2021. Accessions CVR481 and WLD085 were not grown in 2020. Each line represents one pot. Treatment is indicated by color.

on the full dataset from 2020 and tested on the full dataset from 2021, the respective accuracies were only 54 %, 49 %, 51 %, and 42 %. Evaluating vice versa, the best models from 2, 6, 13 and 21 DAI trained on the full dataset from 2021 achieved respective accuracies of 52 %, 42 %, 50 %, and 50 % when applied to 2020 data, indicating a complete lack of transferability. The models were highly biased towards one treatment class or the other (Table 4.2). For DAI 13 and 21 of 2020 data, only control treatment was predicted. Similarly, for 6 DAI and 21 DAI of 2021, only control treatment was predicted. However, for 13 DAI of 2021 data, only infected treatment was predicted.

TABLE 4.2: Confusion matrices for early detection algorithms. The infection status at progressing DAI was predicted with models trained on hyperspectral data from the respective opposite year. Columns represent true values and rows represent predicted values.

	2020 Data		2021 Data	
	Infected	Control	Infected	Control
<i>2 DAI</i>				
Predicted: Infected	15	14	16	12
Predicted: Control	10	11	26	29
<i>6 DAI</i>				
Predicted: Infected	5	9	0	0
Predicted: Control	20	16	42	41
<i>13 DAI</i>				
Predicted: Infected	0	0	42	41
Predicted: Control	25	25	0	0
<i>21 DAI</i>				
Predicted: Infected	0	0	0	6
Predicted: Control	25	25	42	35

4.5.4 Prediction of disease index

Prediction of disease index with RGB image data

Of all the extracted traits, RGR_{7-14} and RGR_{14-21} showed the strongest correlation with the DI in both years, however only reaching a significant level in 2021 (Figure 4.10). Plants with a higher DI tended to show a reduced growth rate in the second and third week after inoculation. Both PSA_0 and PSA_7 showed a consistent, albeit non-significant, weak correlation to the DI, indicating that plants that were larger at infection were more strongly affected by the disease at the time of scoring.

A linear regression model was built using predictors PSA_0 , RGR_{7-14} , and RGR_{14-21} and compared with a RF model containing all extracted traits as predictors. In 5-fold cross-validation, the RF model achieved an estimated mean root mean squared error (RMSE) of 6.66 ± 0.27 in 2020 and an estimated mean RMSE of 12.03 ± 0.44 in 2021. In

comparison, the reduced linear model had an estimated mean RMSE of 5.78 ± 0.25 in 2020 and 12.71 ± 0.6 in 2021.

When training the linear and RF model on all data from 2020 and testing on all data from 2021, the linear model achieved an RMSE of 12.43 ($R^2 = 0.64$) while the RF model achieved an RMSE of 19.21 ($R^2 = 0.30$) (Figure 4.11). The opposite evaluation, that is, training on the entire data of 2021 and testing on 2020, resulted in an RMSE of 5.99 ($R^2 = 0.37$) for the linear model and an RMSE of 7.12 ($R^2 = 0.12$) for the RF model.

Prediction of disease index with hyperspectral data

The algorithm with the lowest mean RMSE in cross-validation for the prediction of disease index used non-smoothed, VNIR-only, non-binned, Pu-normalized second derivative data in a RF model in 2020. The cross-validation results for that algorithm were a mean RMSE of 6.44 ± 1.83 for 2020 data and 12.72 ± 2.16 for 2021 data (Supplementary Table 4.5). For 2021, the best algorithm used non-smoothed, VNIR-only, binned at double FWHM, not normalized, first derivative data in a PLSR model. The cross-validation results here were a mean RMSE of 7.34 ± 1.75 for 2020 data and 11.77 ± 2.25 for 2021 data (Table 4.5). For the final evaluation, the best algorithm developed with 2020 data was fit to the entire 2020 data and then tested on the 2021 data. The resulting RMSE was 21.08 ($R^2 = 0.02$) (Figure 4.11). The opposite way of evaluation, training the best algorithm found for 2021 data on all data from that year and then testing on 2020 data resulted in an RMSE of 8.08 ($R^2 = 0.00$), indicating that these full spectrum hyperspectral models were not transferable.

Influence of processing steps and learning algorithms on DI prediction results

For the prediction of DI from 2020 data, only the choice of learning algorithm had a significant effect on the RMSE achieved in cross-validation, but none of the data processing steps (Table 4.3). Random forest models performed best for 2020 data. However, for 2021 data, all processing steps except smoothing and the inclusion of SWIR data had a significant effect on RMSE, and so did the choice of learning algorithm. The results indicate that the spectral region of SWIR does not contribute to the prediction of DI.

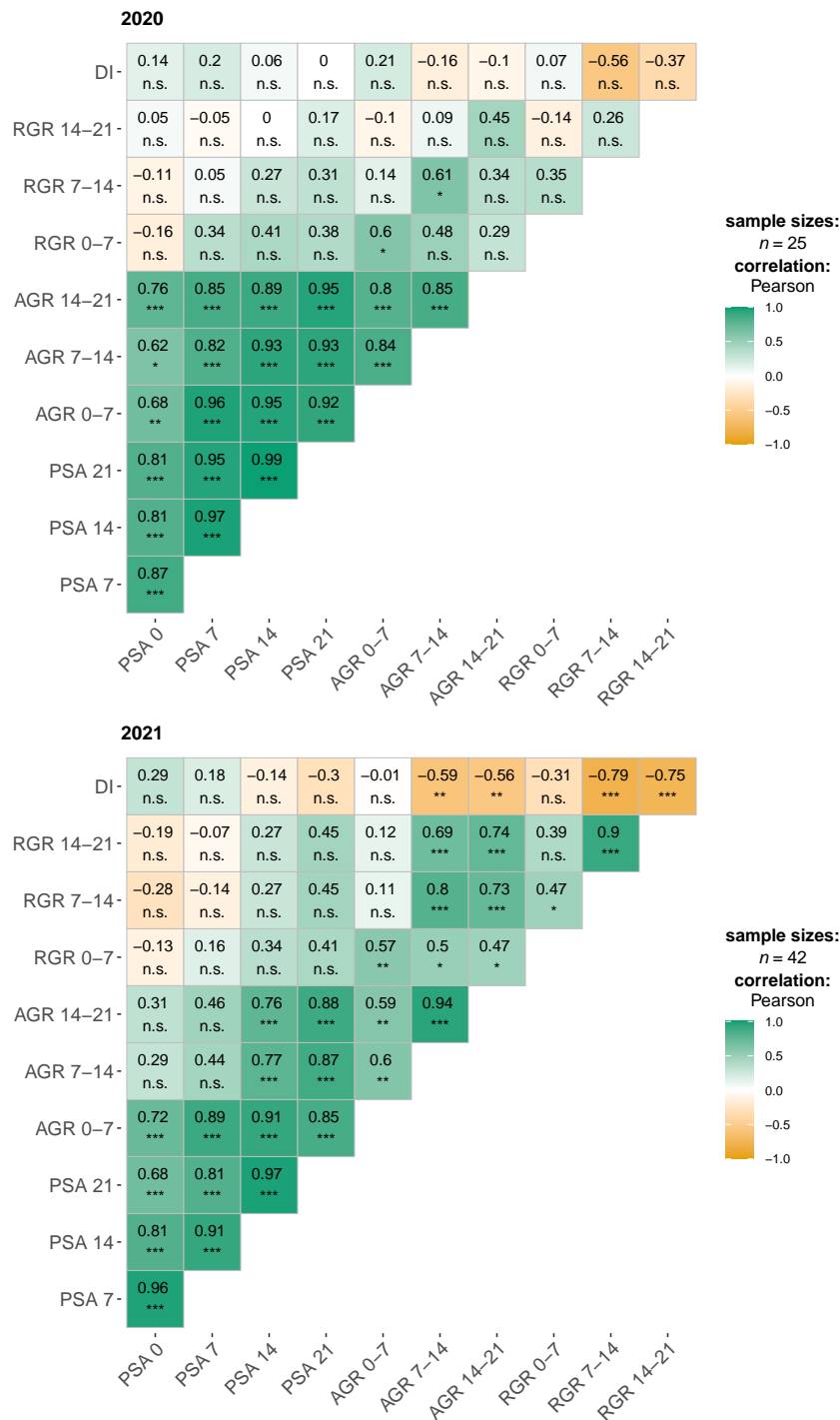
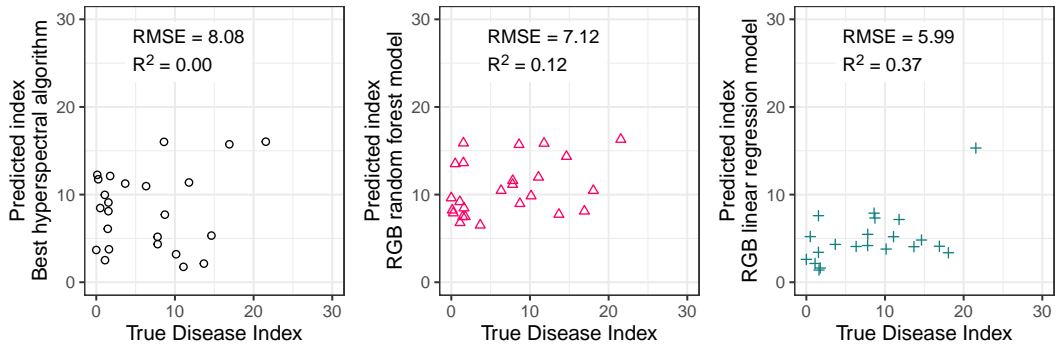


FIGURE 4.10: Disease index correlation matrices for traits extracted from RGB images for experiments in 2020 and 2021. n.s. = non-significant, * = significant at $p < 0.05$, ** = significant at $p < 0.01$, *** = significant at $p < 0.001$ (Adjustment = Holm).

Disease indices of 2020 predicted with models trained on 2021 data



Disease indices of 2021 predicted with models trained on 2020 data

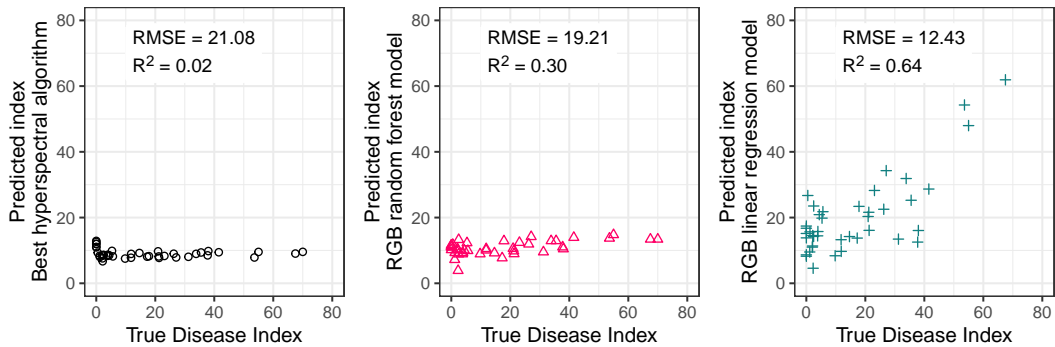


FIGURE 4.11: Predicted disease indices for 2020 (top row) and 2021 (bottom row) compared to ground truth of respective year, predicted with the respective best 1) hyperspectral algorithm (left column, black circles), 2) RGB trait RF model (middle column, pink triangles), 3) RGB trait linear regression model (right column, turquoise crosses). The models were trained on the full datasets of the respective other year. Axis limits are adjusted to match observed disease indices within each year, they were higher in 2021 than in 2020.

TABLE 4.3: Influence of processing steps on DI prediction performance. RMSE \pm standard deviation from 5 repeats and 5 fold CV within each experiment grouped by the respective step is shown.

Pipeline Step	2020 RMSE	2021 RMSE
<i>Binning</i>		
Full spectrum	7.86 ± 2.47	14.84 ± 4.2
FWHM binned	8.06 ± 2.5	15.09 ± 4.2
Double FWHM binned	8.02 ± 2.42	15.64 ± 4.77
<i>Derivation</i>		
None	8.05 ± 2.45	15.15 ± 4.49
First	7.96 ± 2.51	14.56 ± 4.03
Second	7.85 ± 2.45	15.91 ± 4.51
<i>Normalization</i>		
None	8 ± 2.37	15.74 ± 4.56
Pu	7.95 ± 2.56	14.64 ± 4.19
<i>Learning algorithm</i>		
PLSR	8.97 ± 2.77	13.72 ± 4.15
RF	6.86 ± 1.89	14.86 ± 3.46
SVM	8.1 ± 2.18	16.99 ± 4.87
<i>Smoothing</i>		
Raw	7.96 ± 2.48	15.21 ± 4.38
Smoothed	8.03 ± 2.43	15.13 ± 4.5
<i>VNIR + SWIR</i>		
VNIR + SWIR	7.97 ± 2.5	15.13 ± 4.23
VNIR only	7.99 ± 2.43	15.25 ± 4.59

4.6 Discussion

4.6.1 Low disease pressure in the greenhouse

In general and compared to outdoor disease tests (Chapters 3 and 5, Figure 5.4 and 5.5), the disease pressure in the greenhouse was low (Figure 4.7). The observation of exclusively low disease indices (< 25) during the first experiment in 2020 led us to adapt the inoculation protocol for the next experiment. We used larger mini-domes to prevent contact of plants with the inside of the cups and doubled the period under the cups to 48 h in 2021. This may have contributed to the higher disease indices in the experiment in 2021 (Jhorar, Butler, and Mathauda, 1998). However, the ranking of the genotypes according to their DI was consistent with the variety guides, the results of the outdoor screens (Chapter 3), and between both greenhouse experiments, although the genotypic differences were not significant in 2020. The low disease pressure could have decreased the differences in spectral response, thereby leading to an underestimation of prediction performance that may be achieved with a more natural disease expression. In a study on early detection of potato late blight, plants that had not reached severe disease by the end of the study were removed from the analysis (Gold et al., 2020b). With a larger contrast between treatments, better prediction may be achieved.

4.6.2 Full spectrum early detection models were not transferable between experiments

Within each year, infection could be detected as early as 2 DAI, suggesting that metabolic changes may be detected before the appearance of visible symptoms. The estimated accuracies in 2021 were generally better, which may have been due to increased disease pressure and consequently larger differences between the treatment groups. In 2021, even the classifier that was trained on data from before the inoculation, -1 DAI, performed significantly better than a random classifier, indicating that there was a systematic difference between the two groups not due to inoculation, potentially caused by the imaging times of the plants. In 2021, all non-infected plants were imaged before the infected plants to avoid cross-contamination. The imaging of each group took approximately 1.5 hours, and this temporal separation between the groups might explain the discriminatory power of the classifier on the day before the inoculation. These results also cast doubt on the estimated accuracy that was achieved for later days after inoculation for the 2021 experiment. In 2020 however, no such temporal separation was performed; plants from both treatment groups were mixed during imaging.

When transferring trained models between experiments, none of the detection models performed better than a random classifier. This may be due to multiple reasons. There is a risk of overfitting when using hyperspectral data and training on few experimental units, known as the curse of dimensionality ($n \gg p$), since there

were only 50 pots in 2020 and 84 pots in 2021, but the full spectrum hyperspectral data had 710 bands after merging VNIR and SWIR data (Table 4.1) (Lowe, Harrison, and French, 2017). Even when binning at double FWHM, the number of predictors (117) still exceeded the number of observations. Furthermore, the low spatial resolution in relation to the size of the leaflets will have led to mixed pixels, potentially confounding the average plant spectra (Figures 4.3 and 4.6). The biases of the models towards either infected or control treatment may have also been due to differences in disease pressure between the years and systematic differences in imaging time between the treatments in 2021 (Table 4.2). The disease indices were lower in 2020 than in 2021, which may explain that no pots were predicted to be infected after 6 DAI for 2020 data (Figure 4.7). As the differences in disease indices were low in 2020, the predictions for 2021 data may have been randomly biased towards either infected treatment at 13 DAI or control treatment at 6 and 21 DAI (Table 4.2).

4.6.3 RGB-based growth rates are stable predictors for disease indices

Longitudinal traits derived from RGB outperformed hyperspectral sensors for the prediction of disease indices. The transferability of the linear regression model using PSA_0 , RGR_{7-14} , and RGR_{14-21} as input was the highest compared to the best hyperspectral model. Whether full spectrum data or only VNIR data were used did not make a consistent difference. The advantage of RGB-derived traits may be due to the longitudinal dimension that allows normalization of genotype growth habits and can represent the response to the disease, as observed in Chapter 3. The same drawbacks of the measured hyperspectral data as discussed for early detection may also apply for the prediction of DI, that is, high dimensionality, low spatial resolution, and mixed pixels. For example, the best regression algorithm for 2020 was an RF model with 394 predictors fit to 25 observational units, which may explain overfitting and low transferability to the second experiment. However, dimensionality reduction techniques, such as spectral binning or PLSR, did not improve the performance of the models consistently either (Table 4.3).

4.6.4 Perspectives

Ensuring high disease pressure and avoiding cross-contamination

The disease pressure may be strengthened by increasing the concentration of spores in the inoculum (Chen, McPhee, and Muehlbauer, 2005). Another option to increase disease pressure may be to use growth rooms instead of a greenhouse, where constant high humidity and temperatures conducive to disease can be maintained (Pande et al., 2011; Newman et al., 2021). Cross-contamination was observed in one experiment that was performed but was excluded from the analysis for this study. In this experiment, an RCBD was used that could have led the non-infected and infected plants to touch and thereby cause cross-infection. In both of the studies considered here, no signs of cross-contamination were observed. In 2020, the infected and non-infected plants

were fully spatially separated, and in 2021, a split-unit design was used. Therefore, careful separation of infected and non-infected plants is required. Conversely, the same ordering of the imaging of the treatments for the sake of separation will result in the confounding of treatment differences with any systematic difference between the first and second imaging periods.

Potential approaches to increase suitability of hyperspectral data

Spatial resolution The spatial resolution of both the VNIR and SWIR cameras was too low to resolve individual chickpea leaflets, and pixels that have mixed background and foreground reflectance were unavoidable despite the use of a strict semantic segmentation classifier. Such mixed pixels can be removed with erosion, whereby pixels are removed at the outer edges of the foreground segments of the plant are removed (Moghimi et al., 2018; Paulus and Mahlein, 2020).

However, the spatial resolution in this experiment did not allow erosion as even when using the smallest kernel possible (3×3), many leaflets were completely eroded. This would leave too few pixels, especially for the SWIR data that had the lowest spatial resolution (Figure 4.3, Table 4.1). Ideally, the spatial resolution should be increased, for example by reducing the imaging distance. In a situation where closed canopies, not single plants, are monitored, mixed pixels caused by small leaflets would not be an issue and HSI may be more suitable (Chapter 5).

3D correction Another possible option to improve the quality of hyperspectral data is 3D correction, a pre-processing step that can address the influence of the angle of different parts of the plant on the reflectance (Paulus and Mahlein, 2020). Such a correction requires simultaneous construction of a 3D plant model while HSI is performed. It is possible that a 3D correction of HSI could improve the predictive performance of the early detection severity prediction algorithms, but again, higher spatial resolution would be required.

Further analysis algorithms Further analysis methods for the hyperspectral data that may be attempted include Standard Normal Variate (SNV) normalization and neural networks (NN) as learning algorithms (Liu, personal communication). As the normalization and learning algorithms that were tested in this thesis had significant influences on the results of the analysis, it is possible that implementing further steps such as SNV and NN may positively influence the results.

Furthermore, the learning algorithms (RF, SVM, and PLSR) were used individually in this thesis. However, it is possible to stack learning algorithms to combine the advantages of multiple models, and such ensemble modeling was proposed for hyperspectral data analysis (Moghimi, Yang, and Marchetto, 2018).

Longitudinal analysis A promising approach to better use the HSI data would be to consider the progression over the course of the infection. So far, only the HSI data

acquired on the day of scoring were considered for the predictions of severity. More feature extraction and longitudinal analysis of HSI data need to be performed. It has been proposed to apply dimensionality reduction to entire sets of time series HSI (Dorrepaal, Malegori, and Gowen, 2016). Other approaches that have been performed are pooling of timepoints and aggregating observations by the coinciding disease severity or averaging spectra over the measured timepoints (Section 4.3.3) (Ziheng Feng et al., 2021; Zhang et al., 2022; Gold et al., 2020b; Wei et al., 2021).

Wet lab ground-truthing The approach of this study was to use hyperspectral data to predict disease scores. However, the disease scores are derived from RGB information perceived by the human eye, which may favor the RGB sensors and forfeit the advantages of hyperspectral sensors. Instead of predicting disease scores, a different approach would be to remotely sense metabolites associated with the infection such as presented in Table 1.2. Such an approach would require ground truthing of metabolite levels in the wet lab, not only visual scoring (Brugger et al., 2021; Kuska et al., 2018).

4.6.5 Study outcomes in relation to research aims

1. Development of sensor-based phenotyping methods to score disease severity in a chickpea breeding program The disease pressure in the greenhouse experiments was not sufficient for fine discrimination of genotypes, which would be required for selection. In 2020, no significant genotypic differences in DI were observed at all and in 2021, only the genotypes at the extremes showed significant differences in DI (Figure 4.7). Despite varying resistance ratings in sowing guides, cultivars Howzat and Genesis090 did not show significant differences in either year, unlike in the disease nursery (Chapter 3, Figure 3) and in the field (Figure 5.4). Therefore, the priority for supporting breeding programs with sensor-based methods in greenhouse screens should be on improving experimental design and inoculation protocols (Newman et al., 2021). Before choosing an approach for greenhouse-based screens, further validation under higher disease pressure and comparison to improved hyperspectral data need to be performed.

2. Identification of within-scale and cross-scale functional resistance components Based on the predictive power for DI, weekly relative growth-rates after infection were suitable candidate traits, indicating that RGB time course imaging may be suitable for supporting selection. These results are consistent with Chapter 3.

4.7 Conclusion

We showed that intermediate traits extracted from time-series RGB images performed better than single time point hyperspectral images acquired on the day of scoring for the prediction of *Ascochyta* blight disease indices of greenhouse-grown chickpeas.

Disease indices were negatively correlated with the relative growth rates derived from RGB two to three weeks after inoculation. Models for the prediction of disease indices and for the early detection of infection trained on full spectrum hyperspectral data were essentially not transferrable to unseen independent data. After experiencing cross-infection, low disease pressure and possible temporal effects from imaging, we narrowed the design space for greenhouse experiments to using split-units in combination with large mini-dome inoculation for 48 h, and imaging of all treatments together while ensuring that cross-infection did not occur. We showed that time-series RGB is a suitable candidate for supporting *Ascochyta* blight disease screens in the greenhouse, but more research towards feature extraction from hyperspectral data, in particular over the longitudinal dimension and at higher spatial resolution, is required. This may lead to the detection of AB-specific features and transferable models.

4.8 Data availability

The data and code required to reproduce these results is available via

- https://github.com/FCTanner/ab_hsi_phenotyping
- <https://projects.pawsey.org.au/appf-tpa-0521-ph-ua-tpa-tanner-chickpea/index.html>
- <https://projects.pawsey.org.au/appf-tpa-0588-ph-ua-tpa-tanner-chickpea/index.html>

4.9 References

- Angelica Galieni et al. (Mar. 2022). “Surveying soil-borne disease development on wild rocket salad crop by proximal sensing based on high-resolution hyperspectral features.” In: *Scientific Reports* 12.1. MAG ID: 4220983416, pp. 5098–5098. DOI: 10.1038/s41598-022-08969-5.
- Arens, Nadja et al. (2016). “Non-invasive presymptomatic detection of *Cercospora beticola* infection and identification of early metabolic responses in sugar beet”. In: *Frontiers in Plant Science* 7.September, pp. 1–14. ISSN: 1664462X. DOI: 10.3389/fpls.2016.01377.
- Bar, Ido (Oct. 2019). *Whole Genome Sequencing of Ascochyta rabiei Isolates*. original-date: 2017-07-18T23:36:46Z. URL: https://github.com/IdoBar/A_rabiei_WGS_analysis (visited on 11/14/2022).
- Blake, Sara (2022). *2022 South Australia Pulse Variety Disease Guide*. Tech. rep. PIRSA, SARDI. URL: https://pir.sa.gov.au/__data/assets/pdf_file/0020/386102/pulse_variety_disease_guide_2022.pdf.
- Bradski, G (2000). “The OpenCV Library”. In: *Dr. Dobb’s Journal of Software Tools*.

- Brien, Chris et al. (2020). "Smoothing and extraction of traits in the growth analysis of noninvasive phenotypic data". In: *Plant Methods* 16.1. Publisher: BioMed Central, pp. 1–21. ISSN: 17464811. DOI: 10.1186/s13007-020-00577-6. URL: <https://doi.org/10.1186/s13007-020-00577-6>.
- Brugger, Anna et al. (2021). "Spectral signatures in the UV range can be combined with secondary plant metabolites by deep learning to characterize barley–powdery mildew interaction". In: *Plant Pathology* 70.7, pp. 1572–1582. ISSN: 13653059. DOI: 10.1111/ppa.13411.
- Calderón, Rocío, Juan A. Navas-Cortés, and Pablo J. Zarco-Tejada (2015). "Early detection and quantification of verticillium wilt in olive using hyperspectral and thermal imagery over large areas". In: *Remote Sensing* 7.5. ISBN: 3467695493, pp. 5584–5610. ISSN: 20724292. DOI: 10.3390/rs70505584.
- Chen, W., K. E. McPhee, and F. J. Muehlbauer (2005). "Use of a mini-dome bioassay and grafting to study resistance of chickpea to *Ascochyta* blight". In: *Journal of Phytopathology* 153.10, pp. 579–587. ISSN: 09311785. DOI: 10.1111/j.1439-0434.2005.01022.x.
- Conrad, Anna O et al. (2020). "Machine Learning-Based Presymptomatic Detection of Rice Sheath Blight Using Spectral Profiles". In: *Plant Phenomics* 2020. Publisher: American Association for the Advancement of Science (AAAS) ISBN: 2643-6515, pp. 1–10. DOI: 10.34133/2020/8954085.
- Dorrepaal, Ronan, Cristina Malegori, and Aoife Gowen (Apr. 2016). "Tutorial: Time Series Hyperspectral Image Analysis". EN. In: *Journal of Near Infrared Spectroscopy* 24.2. Publisher: SAGE Publishing, pp. 89–107. ISSN: 1751-6552. URL: <https://opg.optica.org/jnirs/abstract.cfm?uri=jnirs-24-2-89> (visited on 11/27/2022).
- Felipe de Mendiburu and Muhammad Yaseen (2020). *agricolae: Statistical Procedures for Agricultural Research*. URL: <https://cran.r-project.org/package=agricolae>.
- Fernando Emiliano Romero Galvan et al. (Oct. 2022). "Scalable early detection of grapevine virus infection with airborne imaging spectroscopy". In: MAG ID: 4303474663. DOI: 10.1101/2022.10.04.510827.
- Gold, Kaitlin M et al. (2020a). "Hyperspectral Measurements Enable Pre-Symptomatic Detection and Differentiation of Contrasting Physiological Effects of Late Blight and Early Blight in Potato". In: *Remote Sensing* 12.2. Publisher: MDPI AG ISBN: 2072-4292, p. 286. DOI: 10.3390/rs12020286.
- Gold, Kaitlin M. et al. (June 2020b). "Investigating potato late blight physiological differences across potato cultivars with spectroscopy and machine learning." In: *Plant Science* 295. MAG ID: 2985102654, p. 110316. DOI: 10.1016/j.plantsci.2019.110316.
- GRDC (2016). "Chickpeas Northern Region - GrowNotes™". In: 53.9. arXiv: 1011.1669v3 ISBN: 9788578110796, pp. 1689–1699. ISSN: 1098-6596. DOI: 10.1017/CB09781107415324.004.

- GRDC (2017). *GRDC: Chickpea Southern Region - GrowNotes™*. Vol. 53. arXiv: 1011.1669v3 Issue: 9 ISSN: 1098-6596. ISBN: 978-85-7811-079-6. DOI: 10.1017/CB09781107415324.004.
- Harris, Charles R et al. (Sept. 2020). “Array programming with {NumPy}”. In: *Nature* 585.7825. Publisher: Springer Science and Business Media [LLC], pp. 357–362. DOI: 10.1038/s41586-020-2649-2. URL: <https://doi.org/10.1038/s41586-020-2649-2>.
- Heim, René H. J. et al. (June 2018). “Detecting myrtle rust (*Austropuccinia psidii*) on lemon myrtle trees using spectral signatures and machine learning”. In: *Plant Pathology* 67.5. MAG ID: 2793166416, pp. 1114–1121. DOI: 10.1111/ppa.12830.
- Hennessy, Andrew, Kenneth Clarke, and Megan Lewis (Jan. 2020). “Hyperspectral Classification of Plants: A Review of Waveband Selection Generalisability”. In: *Remote Sensing* 12.1, p. 113. ISSN: 2072-4292. DOI: 10.3390/rs12010113. URL: <https://www.mdpi.com/2072-4292/12/1/113>.
- James, Gareth et al. (2013). *An Introduction to Statistical Learning*. Vol. 103. Series Title: Springer Texts in Statistics Publication Title: Synthesis Lectures on Mathematics and Statistics Issue: 4 ISSN: 19381751. New York, NY: Springer New York. ISBN: 978-1-4614-7137-0. DOI: 10.1007/978-1-4614-7138-7. URL: <http://link.springer.com/10.1007/978-1-4614-7138-7>.
- Jhorar, O P, D R Butler, and S S Mathauda (1998). “Effects of leaf wetness duration , relative humidity , light and dark on infection and sporulation by *Didymella rabiei*”. In: pp. 586–594.
- Karatzoglou, Alexandros, Alex Smola, and Kurt Hornik (2022). *kernelab: Kernel-based machine learning lab*. manual. URL: <https://CRAN.R-project.org/package=kernelab>.
- Kuhn, Max and Hadley Wickham (2020). *Tidymodels: a collection of packages for modeling and machine learning using tidyverse principles*. URL: <https://www.tidymodels.org>.
- Kuska, Matheus T. et al. (July 2018). “Screening of Barley Resistance Against Powdery Mildew by Simultaneous High-Throughput Enzyme Activity Signature Profiling and Multispectral Imaging”. en. In: *Frontiers in Plant Science* 9, p. 1074. ISSN: 1664-462X. DOI: 10.3389/fpls.2018.01074. URL: <https://www.frontiersin.org/article/10.3389/fpls.2018.01074/full> (visited on 04/17/2023).
- Liu, H (2020). *appf_toolbox*. Publication Title: GitHub repository. URL: https://github.com/Harwis/appf_toolbox.
- Lowe, Amy, Nicola Harrison, and Andrew P. French (2017). “Hyperspectral image analysis techniques for the detection and classification of the early onset of plant disease and stress”. In: *Plant Methods* 13.1. Publisher: BioMed Central, pp. 1–12. ISSN: 17464811. DOI: 10.1186/s13007-017-0233-z.
- Mahlein, A.-K. et al. (2018). “Hyperspectral Sensors and Imaging Technologies in Phytopathology: State of the Art”. In: *Annual Review of Phytopathology* 56.1, pp. 535–558. ISSN: 0066-4286. DOI: 10.1146/annurev-phyto-080417-050100.

- Moghimi, Ali, Ce Yang, and Peter M. Marchetto (2018). "Ensemble Feature Selection for Plant Phenotyping: A Journey from Hyperspectral to Multispectral Imaging". In: *IEEE Access* 6. Publisher: IEEE, pp. 56870–56884. ISSN: 21693536. DOI: 10.1109/ACCESS.2018.2872801.
- Moghimi, Ali et al. (2018). "A novel approach to assess salt stress tolerance in wheat using hyperspectral imaging". In: *Asian Journal of Pharmaceutical and Clinical Research* 9.August, pp. 1–17. ISSN: 24553891. DOI: 10.3389/fpls.2018.01182.
- Newman, Toby E. et al. (2021). "Identification of novel sources of resistance to ascochyta blight in a collection of wild cicer accessions". In: *Phytopathology* 111.2, pp. 369–379. ISSN: 19437684. DOI: 10.1094/PHYTO-04-20-0137-R.
- Oerke, Erich Christian, Marlene Leucker, and Ulrike Steiner (2019). "Sensory assessment of *Cercospora beticola* sporulation for phenotyping the partial disease resistance of sugar beet genotypes". In: *Plant Methods* 15.1. Publisher: BioMed Central, pp. 1–12. ISSN: 17464811. DOI: 10.1186/s13007-019-0521-x. URL: <https://doi.org/10.1186/s13007-019-0521-x>.
- Oerke, Erich-Christian et al. (Oct. 2016). "Hyperspectral phenotyping of the reaction of grapevine genotypes to *Plasmopara viticola*." In: *Journal of Experimental Botany* 67.18. MAG ID: 2513191602, pp. 5529–5543. DOI: 10.1093/jxb/erw318.
- Pande, S. et al. (2011). "Development of screening techniques and identification of new sources of resistance to *Ascochyta* blight disease of chickpea". In: *Australasian Plant Pathology* 40.2, pp. 149–156. ISSN: 08153191. DOI: 10.1007/s13313-010-0024-8.
- Patil, Indrajeet (2021). "Visualizations with statistical details: The ggstatsplot approach". In: *Journal of Open Source Software* 6.61. Publisher: The Open Journal, p. 3167. DOI: 10.21105/joss.03167. URL: <https://doi.org/10.21105/joss.03167>.
- Paulus, Stefan and Anne Katrin Mahlein (2020). "Technical workflows for hyperspectral plant image assessment and processing on the greenhouse and laboratory scale". In: *GigaScience* 9.8. Publisher: Oxford University Press ISBN: 0000000310, pp. 1–10. ISSN: 2047217X. DOI: 10.1093/gigascience/giaa090.
- Pedregosa, F et al. (2011). "Scikit-learn: Machine Learning in {P}ython". In: *Journal of Machine Learning Research* 12, pp. 2825–2830.
- Poblete, Tomas et al. (Sept. 2021). "Discriminating *Xylella fastidiosa* from *Verticillium dahliae* infections in olive trees using thermal- and hyperspectral-based plant traits". In: *Isprs Journal of Photogrammetry and Remote Sensing* 179. MAG ID: 3192010693, pp. 133–144. DOI: 10.1016/j.isprsjprs.2021.07.014.
- Pu, Ruiliang et al. (2012). "Discrimination of seagrass species and cover classes with in situ hyperspectral data". In: *Journal of Coastal Research* 28.6, pp. 1330–1344. ISSN: 07490208. DOI: 10.2112/JCOASTRES-D-11-00229.1.
- R Core Team (2022). *R: A Language and Environment for Statistical Computing*. Place: Vienna, Austria. URL: <https://www.r-project.org/>.
- Raman, Rosy et al. (2022). "Genome-Wide Association Analyses Track Genomic Regions for Resistance to *Ascochyta rabiei* in Australian Chickpea Breeding

- Germplasm". In: *Frontiers in Plant Science* 13. ISSN: 1664-462X. URL: <https://www.frontiersin.org/articles/10.3389/fpls.2022.877266> (visited on 11/27/2022).
- Savitzky, Abraham. and M. J. E. Golay (July 1964). "Smoothing and Differentiation of Data by Simplified Least Squares Procedures." en. In: *Analytical Chemistry* 36.8, pp. 1627–1639. ISSN: 0003-2700, 1520-6882. DOI: 10.1021/ac60214a047. URL: <https://pubs.acs.org/doi/abs/10.1021/ac60214a047> (visited on 07/25/2022).
- Stevens, Antoine and Leonardo Ramirez-Lopez (2020). *An introduction to the prospectr package*. URL: <https://cran.r-project.org/web/packages/prospectr/vignettes/prospectr.html>.
- team, The pandas development (Feb. 2020). *pandas-dev/pandas: Pandas*. DOI: 10.5281/zenodo.3509134. URL: <https://doi.org/10.5281/zenodo.3509134>.
- The GIMP Development Team (2020). *GNU Image Manipulation Program (GIMP)*. URL: <https://www.gimp.org>.
- Van Rossum, Guido (2020). *The Python Library Reference, release 3.8.2*. Python Software Foundation.
- Wei, Xing et al. (July 2021). "Identifying Optimal Wavelengths as Disease Signatures Using Hyperspectral Sensor and Machine Learning". In: *Remote Sensing* 13.14. MAG ID: 3186446746, p. 2833. DOI: 10.3390/rs13142833.
- Wickham, Hadley (2016). *ggplot2: Elegant Graphics for Data Analysis*. Springer-Verlag New York. ISBN: 978-3-319-24277-4. URL: <https://ggplot2.tidyverse.org>.
- Wickham, Hadley et al. (2019). "Welcome to the {tidyverse}". In: *Journal of Open Source Software* 4.43, p. 1686. DOI: 10.21105/joss.01686.
- Wright, Marvin N. and Andreas Ziegler (2017). "ranger: A fast implementation of random forests for high dimensional data in C++ and R". In: *Journal of Statistical Software* 77.1, pp. 1–17. DOI: 10.18637/jss.v077.i01.
- York, Larry M. (2019). "Functional phenomics: An emerging field integrating high-throughput phenotyping, physiology, and bioinformatics". In: *Journal of Experimental Botany* 70.2, pp. 379–386. ISSN: 14602431. DOI: 10.1093/jxb/ery379.
- Yu, Kang et al. (2018). "Hyperspectral Canopy Sensing of Wheat Septoria Tritici Blotch Disease". eng. In: *Frontiers in Plant Science* 9. Publisher: Frontiers Media S.A. ISBN: 1664-462X, p. 1195. DOI: 10.3389/fpls.2018.01195. URL: <https://pubmed.ncbi.nlm.nih.gov/30174678>.
- Zarco-Tejada, P. J. et al. (2018). "Previsual symptoms of *Xylella fastidiosa* infection revealed in spectral plant-trait alterations". In: *Nature Plants* 4.7. Publisher: Springer US, pp. 432–439. ISSN: 20550278. DOI: 10.1038/s41477-018-0189-7. URL: <http://dx.doi.org/10.1038/s41477-018-0189-7>.
- Zhang, Chongyuan, Weidong Chen, and Sindhuja Sankaran (2019). "High-throughput field phenotyping of *Ascochyta* blight disease severity in chickpea". In: *Crop Protection* 125. March. Publisher: Elsevier Ltd, p. 104885. ISSN: 02612194. DOI: 10.1016/j.cropro.2019.104885. URL: <https://doi.org/10.1016/j.cropro.2019.104885>.

-
- Zhang, Jinnuo et al. (Dec. 2022). "Rice bacterial blight resistant cultivar selection based on visible/near-infrared spectrum and deep learning". In: *Plant Methods* 18.1, p. 49. ISSN: 1746-4811. DOI: 10.1186/s13007-022-00882-2. URL: <https://plantmethods.biomedcentral.com/articles/10.1186/s13007-022-00882-2>.
- Ziheng Feng et al. (Dec. 2021). "Monitoring Wheat Powdery Mildew Based on Hyperspectral, Thermal Infrared, and RGB Image Data Fusion". In: *Sensors* 22.1. MAG ID: 4200064788, pp. 31–31. DOI: 10.3390/s22010031.

4.10 Supplementary material

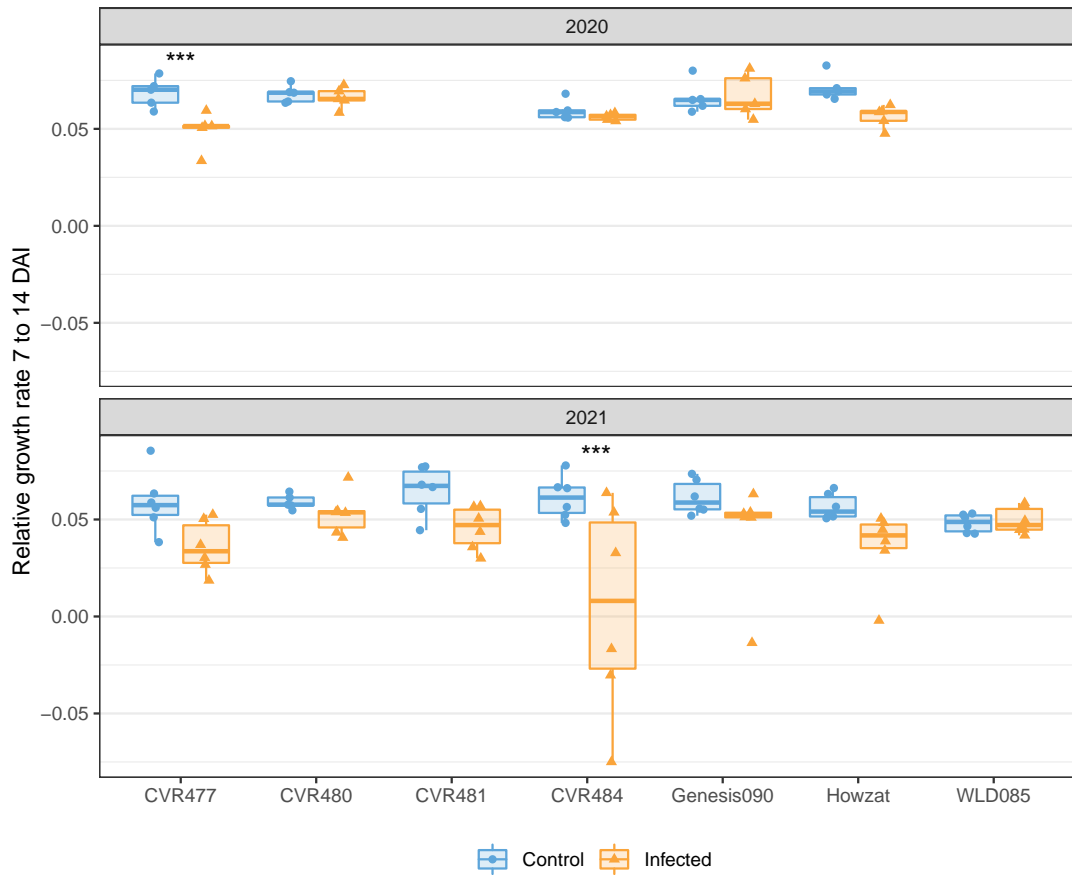


FIGURE 4.12: Relative growth rates 7 - 14 DAI. Significant differences are marked with asterisks (***) = $p < 0.001$). Accessions CVR481 and WLD085 were not grown in 2020.

TABLE 4.4: P-values for genotypic, treatment, and interaction effect on scores and measured traits. Where interaction terms are significant, the main effects are omitted. DI was only examined for genotypic effects on infected plants, therefore the other effects are NA.

Trait	Year	Genotype	Treatment	Genotype x Treatment
DI	2020	0.082	NA	NA
DI	2021	0.001	NA	NA
<i>AGR</i> ₀₋₇	2020	—	—	0.037
<i>AGR</i> ₀₋₇	2021	< 0.001	0.160	0.574
<i>AGR</i> ₇₋₁₄	2020	< 0.001	0.009	0.179
<i>AGR</i> ₇₋₁₄	2021	< 0.001	< 0.001	0.275
<i>AGR</i> ₁₄₋₂₁	2020	—	—	0.031
<i>AGR</i> ₁₄₋₂₁	2021	< 0.001	< 0.001	0.359
<i>PSA</i> ₀	2020	0.006	0.546	0.333
<i>PSA</i> ₀	2021	< 0.001	0.877	0.272
<i>PSA</i> ₇	2020	< 0.001	0.916	0.085
<i>PSA</i> ₇	2021	< 0.001	0.553	0.566
<i>PSA</i> ₁₄	2020	< 0.001	0.279	0.108
<i>PSA</i> ₁₄	2021	< 0.001	0.007	0.636
<i>PSA</i> ₂₁	2020	< 0.001	0.059	0.059
<i>PSA</i> ₂₁	2021	< 0.001	< 0.001	0.533
<i>RGR</i> ₀₋₇	2020	< 0.001	0.236	0.360
<i>RGR</i> ₀₋₇	2021	< 0.001	0.099	0.077
<i>RGR</i> ₇₋₁₄	2020	—	—	0.009
<i>RGR</i> ₇₋₁₄	2021	—	—	0.025
<i>RGR</i> ₁₄₋₂₁	2020	—	—	0.039
<i>RGR</i> ₁₄₋₂₁	2021	0.017	< 0.001	0.080

TABLE 4.5: Cross-validation results for prediction of DI with hyperspectral data and longitudinal traits extracted from RGB data. RMSE \pm standard deviation from 5 repeats and 5 fold cross-validation within each experiment is shown. The top five algorithms including pre-processing steps were selected within each year and then also tested in cross-validation on data from the opposite year.

Binning	Smoothing	Sensors	Normalization	Derivative	Model	RMSE 2020	RMSE 2021
<i>Best hyperspectral algorithms 2020</i>							
Full spectrum	Raw	VNIR only	Pu	Second	RF	6.44 ± 1.83	12.72 ± 2.16
Full spectrum	Raw	VNIR + SWIR	Pu	None	RF	6.47 ± 1.7	13.58 ± 3
Full spectrum	Smoothed	VNIR + SWIR	Pu	None	RF	6.53 ± 1.7	13.46 ± 3.03
Full spectrum	Raw	VNIR only	None	Second	RF	6.55 ± 1.69	14.02 ± 2.02
FWHM binned	Raw	VNIR + SWIR	Pu	None	RF	6.58 ± 1.78	13.41 ± 2.9
<i>Best hyperspectral algorithms 2021</i>							
Double FWHM binned	Raw	VNIR only	None	First	PLSR	7.34 ± 1.75	11.77 ± 2.25
Full spectrum	Raw	VNIR only	Pu	First	RF	6.89 ± 1.9	12.18 ± 2.16
Double FWHM binned	Raw	VNIR only	Pu	First	PLSR	6.97 ± 2.27	12.2 ± 2.28
FWHM binned	Raw	VNIR only	Pu	First	PLSR	7.99 ± 2.66	12.38 ± 3.03
FWHM binned	Raw	VNIR only	Pu	First	RF	6.89 ± 1.89	12.39 ± 2.25
<i>Longitudinal RGB traits</i>							
Full RF model	—	—	—	—	—	6.66 ± 0.27	12.03 ± 0.44
Reduced linear model	—	—	—	—	—	5.78 ± 0.25	12.71 ± 0.6

TABLE 4.6: Accuracy (\pm standard deviation) of early detection of AB at each imaging time point with the best respective algorithm, estimated with 5-fold CV with 5 repeats. The p-value relates to the cross-validation performance compared to a random classifier.

DAI	Binning	Smoothing	Sensors	Normalization	Derivative	Model	Accuracy	P-value
<i>2020</i>								
-1	Double FWHM binned	Raw	VNIR only	Pu	Second	SVM	49 % \pm 16 %	= 0.527
1	Double FWHM binned	Raw	VNIR only	None	Second	SVM	54 % \pm 16 %	= 0.097
2	Double FWHM binned	Raw	VNIR only	Pu	Second	RF	62 % \pm 12 %	< 0.001
3	FWHM binned	Raw	VNIR only	Pu	Second	RF	64 % \pm 12 %	< 0.001
6	Full spectrum	Raw	VNIR only	None	Second	SVM	62 % \pm 14 %	= 0.001
8	Double FWHM binned	Raw	VNIR only	None	None	SVM	67 % \pm 15 %	< 0.001
10	Double FWHM binned	Raw	VNIR only	Pu	Second	SVM	64 % \pm 15 %	< 0.001
13	FWHM binned	Smoothed	VNIR + SWIR	Pu	None	SVM	71 % \pm 9 %	< 0.001
15	Double FWHM binned	Raw	VNIR + SWIR	None	None	RF	69 % \pm 14 %	< 0.001
17	FWHM binned	Raw	VNIR + SWIR	None	Second	RF	72 % \pm 11 %	< 0.001
20	FWHM binned	Smoothed	VNIR + SWIR	None	None	RF	60 % \pm 13 %	= 0.002
21	Full spectrum	Raw	VNIR only	None	Second	RF	59 % \pm 12 %	= 0.003
<i>2021</i>								
-1	Full spectrum	Raw	VNIR + SWIR	None	First	SVM	71 % \pm 11 %	< 0.001
2	Full spectrum	Raw	VNIR + SWIR	Pu	First	SVM	72 % \pm 12 %	< 0.001
6	Full spectrum	Raw	VNIR + SWIR	Pu	First	SVM	72 % \pm 12 %	< 0.001
9	Full spectrum	Raw	VNIR + SWIR	None	First	SVM	78 % \pm 10 %	< 0.001
13	Full spectrum	Raw	VNIR + SWIR	None	First	SVM	78 % \pm 9 %	< 0.001
16	Full spectrum	Raw	VNIR + SWIR	None	None	RF	73 % \pm 11 %	< 0.001
21	Full spectrum	Raw	VNIR + SWIR	None	Second	SVM	76 % \pm 12 %	< 0.001

Chapter 5

Prediction of Ascochyta blight damage on field-grown chickpea using lidar and hyperspectral data

5.1 Declarations

Statement of Authorship

Title of Chapter	Prediction of Ascochyta blight damage on field-grown chickpea using lidar and hyperspectral data
Publication Details	Unpublished and unsubmitted work written in manuscript style

Principal Author

Name of Principal Author	Florian Tanner
Contribution to the Paper by the Candidate	Conception, Knowledge, Experimentation, Analysis, Drafting. Performed experiment in 2022, analysed data, wrote manuscript.
Overall percentage Certification	80% This paper reports on original research I conducted during the period of my Higher Degree by Research candidature and is not subject to any obligations or contractual agreements with a third party that would constrain its inclusion in this thesis. I am the primary author of this paper.
Signature	
Date	2022-11-22

Co-Author Contributions

By signing the Statement of Authorship, each author certifies that:

- the candidate's stated contribution to the publication is accurate (as detailed above);
- permission is granted for the candidate to include the publication in the thesis; and
- the sum of all co-author contributions is equal to 100% less the candidate's stated contribution.

Name of Co-Author	Andrew Hennessy
Contribution to the Paper	Analysis: Pre-processing of hyperspectral and lidar data
Signature	
Date	24/11/2022

Name of Co-Author	Jennifer Davidson
Contribution to the Paper	Conception, Review of Manuscript and Visual Scoring
Signature	
Date	24/11/22

Name of Co-Author	Darren Plett
Contribution to the Paper	Conception and Data Acquisition
Signature	
Date	24/11/2022

Name of Co-Author	Kenneth Clarke
Contribution to the Paper	Conception, Data Acquisition and Review of Manuscript
Signature	
Date	November 22, 2022

Name of Co-Author	Bettina Berger
Contribution to the Paper	Conception and Review of Manuscript
Signature	
Date	November 22, 2022

5.2 Abstract

Evaluation of *Ascochyta* blight damage in the field is required for resistance breeding of chickpea. However, such screens are currently dependent on human visual scoring and limited in precision and throughput. Here, we tested the potential of a ground-based phenotyping platform carrying hyperspectral and lidar sensors to predict visual scores of *Ascochyta* blight damage to various genotypes grown in field plots and trays. We evaluated the specificity of the methods by including soil salinity as a second stress. We show that measuring a general response to plant stress in the visible to near-infrared spectral region can accurately replicate a ranking of genotypes according to their visual scores of damage on unseen data from an independent experiment ($\rho = 0.89$). Distinction between infected and fungicide-protected plots was possible with near perfect accuracy estimated in cross-validation within a season and the distinction between (a) infected, (b) fungicide-protected, and (c) fungicide-protected and salinity-treated trays achieved an accuracy of 75 % estimated in within-season cross-validation. This study serves as a proof of concept for using sensor-based phenotyping to screen genetic material for *Ascochyta* blight resistance in the field, showing that visual scores of damage can be predicted, but that methods need to be supervised for specificity.

5.3 Introduction

5.3.1 Field disease screening

Field disease screenings are an important part of the breeding process to evaluate whether resistance is effective under farming conditions (Niks et al., 2019). This is particularly important for *Ascochyta* blight (AB) resistance, which can occasionally differ between seedling stage and adult plant stage (Garg et al., 2018). Resistance that is detected in seedlings needs to be confirmed in adult plants by quantifying signs and symptoms in the field. Traditionally, signs and symptoms are evaluated visually, which can limit accuracy and throughput (Bock et al., 2020). These limitations can be addressed with sensor-based phenotyping methods that have the potential to increase genetic gain in breeding programs (Chapter 1) (Araus et al., 2018).

5.3.2 Sensor-based disease phenotyping in the field

Compared to sensor-based phenotyping in controlled environments, the deployment of sensor technology in the field, especially in the context of biotic stress trials, is still less common (Araus and Cairns, 2014). This can be attributed to a set of challenges, including passive illumination that influences spectral measurements, spatial variability in the field, and exposure to secondary biotic or abiotic stressors other than the target pathogen (Araus and Cairns, 2014). To bring the sensors to the plant, many dedicated ground-based and aerial vehicles have been designed (Xu and Li,

2022). Ground-based vehicles can offer the advantages of higher spatial resolution due to the proximity of the sensors to the plants, higher payload for heavy sensors, and the option of shading and active illumination. These advantages come at the cost of lower throughput compared to aerial platforms. For very high throughput and measurements at field scale, aircraft or satellite-based measurements can be used (Zarco-Tejada et al., 2018; Poblete et al., 2021).

5.3.3 Related work

Sensor - based screening of necrotrophic fungi in the field

Necrotrophic fungi cause the formation of necrotic lesions and sporulation followed by more widespread necrosis of plant tissue. These signs and symptoms can be targets for sensor-based phenotyping with RGB cameras, but generally require a high spatial resolution, which excludes the use of high-flying aerial platforms (Chapter 2). In the case of maize Northern Leaf Blight, RGB images acquired with a telephoto lens from a drone flying at a low altitude of 6 m over the canopy provided enough spatial resolution to measure lesion size, as the lesions of Northern Leaf Blight reach a size of 1 cm in width and 5 cm in length within a few weeks after infection (Wiesner-Hanks et al., 2019; Wiesner-Hanks et al., 2018; DeChant et al., 2017). Contrary to that, *Cercospora* Leaf Blight of sugar beet causes small lesions between 2 and 5 mm in diameter. In a field trial with this plant-pathosystem, the size and density of the spots could only be detected from a ground-based phenotyping platform, but not from an airborne hexacopter. Due to the lower resolution of the data from the airborne platform, the only trait that could be extracted from the images was green fraction. The traits measured on the ground could predict the visual scores of *Cercospora* Leaf Spot with lower root mean squared error (RMSE) (Jay et al., 2020).

Instead of directly measuring morphological features such as green fraction or necrotic lesions, using average reflectance data over whole observational units is another approach and can be achieved by either averaging the foreground reflectance of imaging data or using non-imaging spectroscopy. For example, the reflectance at canopy level (1.5 m above the canopy) of wheat affected by *Septoria tritici* blotch was measured with a non-imaging spectrometer (Yu et al., 2018). This pathogen causes necrosis and sporulation which were rated visually on the top three leaf layers. Multiple vegetation indices (VI) related to biomass, chlorophyll content, and water content were negatively correlated with visual scores, while Structure Insensitive Pigment Index (SIPI) and Plant Senescence Reflectance Index (PSRI) were positively correlated with visual scores. Toward the latter stages of disease progression, an overall reduction in reflectance was observed in the green spectrum in the infected plots and was attributed to a reduction in chlorophyll content caused by chlorosis and necrosis (Yu et al., 2018). More studies employing spectroscopy in the field are discussed in Section 4.3.2 and include wheat powdery mildew (Ziheng Feng et al., 2021) and soil-borne pathogens of wild rocket (Angelica Galieni et al., 2022).

5.3.4 Research opportunities

Considerations and applications for AB screens

AB can cause necrotic lesions on all above-ground plant parts and sporulation on the surface of the lesions. When lesions occur on stems, stem breakage can occur, which leads to a reduction of biomass and yield loss (Pande et al., 2005). These signs and symptoms must be measured to select genotypes with high levels of resistance. Suitable sensors to measure these signs and symptoms include light detection and ranging (lidar) sensors for the loss of biomass and imaging sensors for the degree of necrosis and sporulation (Chapter 2).

Sensor-based phenotyping of AB screens of chickpea under field conditions has been performed previously in trials examining the efficacy of fungicides. Plots were imaged from a drone over three seasons between 2016 and 2018 with multiple sensors at different flight heights on different days after planting (Zhang, Chen, and Sankaran, 2019). Multiple VI and canopy temperature were used to predict visual scores that were recorded on a 1 to 9 scale and correlation coefficients between 0.35 and 0.81 were reported. In addition to the aerial data, leaf-level reflectance data were also collected with a leaf-clip spectroradiometer in the spectral range between 350 and 2500 nm in 2018. From a total of 1024 recorded bands, 14 wavebands were selected using the Least Absolute Shrinkage and Selection Operator (LASSO) variable selection method. The selected bands could predict the disease score in a linear model with a correlation coefficient of $r = 0.71$ at 36 days after planting and $r = 0.73$ at 50 days after planting. However, this was not an improvement compared to the prediction of disease index when simply using the normalized difference vegetation index (NDVI) measured from a drone, which resulted in $r = 0.73$ at 36 days after planting and $r = 0.72$ at 50 days after planting (Zhang, Chen, and Sankaran, 2019). This indicates that when the average reflectance per plot is used for predicting *Ascochyta* blight disease severity, simple vegetation indices that can be acquired at high throughput may be sufficient.

Specificity of stress detection in the field

To reliably identify a stress and distinguish it from other stresses, sensor-based methods must have high specificity (Anderegg et al., 2019). Spatial variability in the field, abiotic stresses, and secondary pathogens can mask the effects of the fungus or lead to false positive detection. In managed field trials, this can be controlled to some extent (Jay et al., 2020). In a farming context where early detection of AB may be used as a management tool, specificity is important so that fungicides are applied only where needed. Spectroscopy is a promising tool for distinguishing biotic stresses, as shown with contact spectroscopy on potato infected with either *Phytophthora infestans* or *Alternaria solani* and aerial imaging of olive trees infected with either *Verticillium dahliae* or *Xylella fastidiosa* (Poblete et al., 2021; Gold et al., 2020a).

Salinity is an important abiotic stress in chickpeas and can cause a reduction in plant height and plant biomass in the vegetative stage in the greenhouse and a

reduction in seed yield in the field (Atieno et al., 2017; Flowers et al., 2010). Symptoms of salinity stress caused by ion accumulation in the shoot include chlorosis, early senescence, and necrosis of the leaves (Carillo et al., 2011; Atieno et al., 2021). Therefore, both observations of optical properties and estimates of plant biomass can be suitable for judging salinity tolerance and detecting the stress (Stoddard et al., 2006; Maliro et al., 2008). Due to the symptoms of senescence/necrosis and loss of healthy biomass that are comparable between salinity stress and AB, salinity stress was chosen for this study to evaluate whether the developed AB detection method is specific and capable of distinguishing between symptoms of AB and salinity stress.

5.3.5 Aims of this study

We evaluated the potential of using a ground-based phenotyping platform with hyperspectral and lidar sensors to detect AB compared to non-infected plants, fungicide protected plants, and to distinguish the specific AB stress from salinity stress. Furthermore, the possibility of predicting the percentage of area diseased (PAD) scores in infected plots and trays was evaluated.

5.4 Materials and methods

5.4.1 Experimental design

2020 Field experiment The South Australian Research and Development Institute (SARDI) conducted AB field screens in Kingsford, South Australia in the 2020 season (34°33'15.5"S 138°46'57.8"E). In total, nine genotypes were screened (CVR020, CVR021, CVR022, CVR478, CVR479, CVR481, CVR482, Genesis090, Howzat). All genotypes are anonymized here in line with the other chapters except for the control cultivars Genesis090 (moderately susceptible to AB) and Howzat (very susceptible to AB) (Raman et al., 2022; Blake, 2022). Four plots per treatment and genotype combination were grown in a randomized complete block design in 7 m long plots with six rows of plants. All plots were infected with stubble containing unspecified *A. rabiei* isolates and exposed to three treatments: (i) Nil, (ii) fortnightly Chlorothalonil, and (iii) strategically applied Veritas (Azoxystrobin + Tebuconazole, Adama, Australia) (Figure 5.1). Accessions CVR021, Genesis090 and Howzat were also screened in a separate experiment with treatments (i), (ii), (iii), and additionally (iv) strategically applied Chlorothalonil and (v) strategically applied Aviator (Bixafen + Prothioconazole, Bayer Crop Science, Australia). The plants were seeded on 2020-06-06, infected on 2020-07-22 (46 days after sowing (DAS)), scored on 2020-10-15 (85 days after infection (DAI)), and imaged on 2020-10-20 (90 DAI). For treatment details, see Supplementary Table 5.6.

2022 Tray experiment In the 2022 season, three accessions (Genesis090, CVR484, and WLD085) were grown in draining trays of 420 mm length, 320 mm width, and 130 mm height in the same experimental setup as described in Chapter 3. Briefly, 20 seeds per

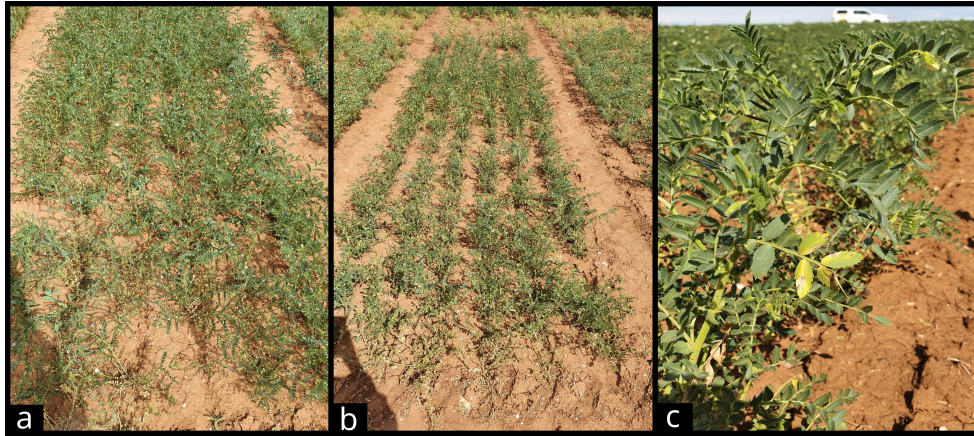


FIGURE 5.1: Plots and lesions in 2020 field experiment imaged on 2020-09-16 (56 DAI) (used with permission from Sara Blake). a = *cv.* Howzat + fortnightly Chlorothalonil (ii), b = *cv.* Howzat + Nil treatment (i), c = Leaf lesions on unknown cultivar.

tray were seeded in Van Schaik's Bio Gro soil mix (Bio Gro Pty Ltd., Mount Gambier, South Australia) on 2022-06-08, placed on a sandy soil layer, infected with a spore suspension of *A. rabiei* on 2022-07-19 (40 DAS), scored on 2022-09-14 (58 DAI) and imaged on 2022-09-15 (59 DAI) (Figure 5.2). The inoculum had a concentration of 1×10^6 pycnidiospores ml^{-1} of isolate 16CUR018 (collected on *cv.* Genesis090 in Curyo, Victoria, Australia in 2016) and surfactant Tween 20 (0.01%) (Merck Pty Ltd.) and was sprayed to runoff (Bar, 2019). The same isolate was used in Chapters 3 and 4. Three treatments were applied to 4 replicates in a split plot design: (i) inoculation, (ii) no inoculation and treatment with Chlorothalonil (Bravo Weather Stik, Syngenta Crop Protection, 720 g l^{-1} applied at 40 ml per tray), and (iii) no inoculation, application of saline solution and treatment with Chlorothalonil (same as described for (ii)). Soil salinization was performed at the same time as inoculation (40 DAS) by applying 3.3 l of 60 mM NaCl solution to each tray with a watering can. Salinization was repeated with the same volume of 60 mM NaCl solution on 28 DAI and with the same volume, but with a concentration of 120 mM on 42 DAI. Fungicide treatment was carried out the day before inoculation, 21 DAI, 28 DAI and 44 DAI (Supplementary Table 5.6).

5.4.2 Data acquisition

The plots were visually scored by an expert pathologist for PAD per plot or tray. The plots and trays were phenotyped using a ground-based field phenotyping platform (Field Explorer / TraitSeeker, *CropTraits*; *Phenokey*) carrying hyperspectral cameras with active illumination (Table 5.1) and a lidar sensor (SICK LMS400-1000, SICK, USA).

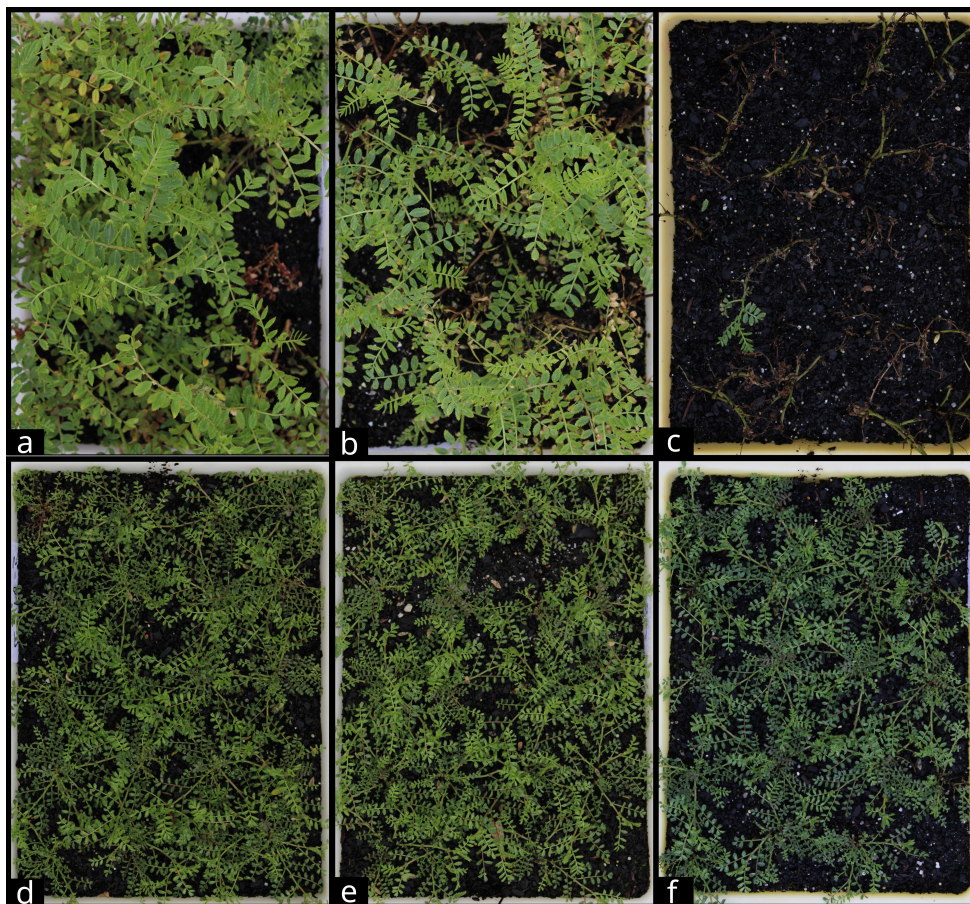


FIGURE 5.2: Trays in 2020 field experiment imaged on 2022-09-16 (60 DAI) a = *cv.* Howzat + no inoculation and treatment with Chlorothalonil (ii) (0 PAD), b = *cv.* Howzat + no inoculation, application of saline solution and treatment with Chlorothalonil (iii) (30 PAD), c = *cv.* Howzat + inoculation (i) (95 PAD), d = WLD085 + (ii) (0 PAD), e = WLD085 + (iii) (0 PAD), f = WLD085 + (i) (0 PAD).

TABLE 5.1: Specifications of hyperspectral cameras in Field Explorer.

Camera	Spectral range	Bands	FWHM
Specim FX10	397 - 1,004 nm	224	5.5 nm
Specim FX17	937 - 1,718 nm	112	16 nm

FWHM: Full Width at Half Maximum

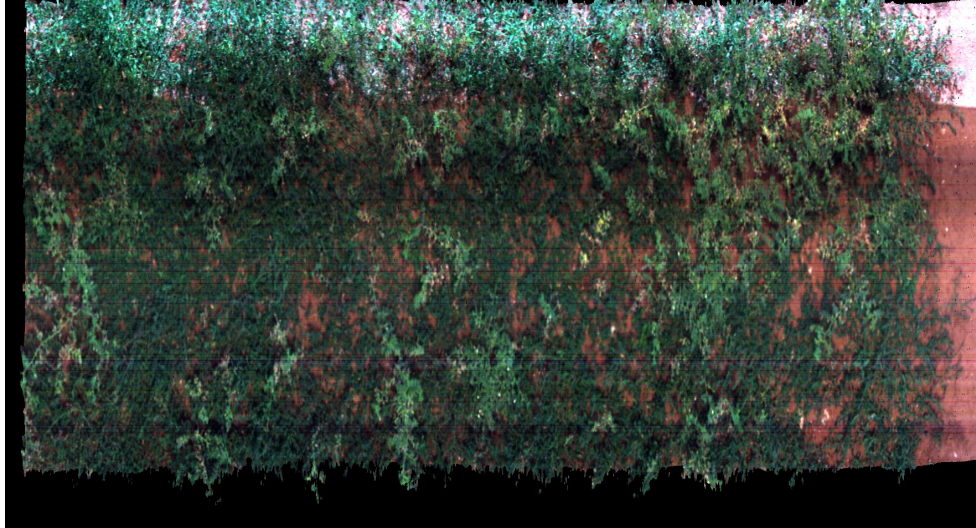


FIGURE 5.3: Reconstituted RGB image of a plot with low chickpea biomass and wireweed coverage.

5.4.3 Data analysis

Calibration and fusion of hyperspectral and lidar data

Hyperspectral data from VNIR and SWIR sensors were calibrated, fused, and merged with the point cloud derived from lidar data. In the 2020 season, the reflectance data was limited to plant material 10 cm or higher above the ground. This height threshold was implemented because large sections of the soil of the plots were covered with scrambling prostrate wireweed (*Polygonum aviculare subsp. aviculare*), particularly in plots where chickpeas were severely damaged and the ground was exposed (Figure 5.3).

Full spectrum hyperspectral data pre-processing

Following radiometric calibration and spatial segmentation, a series of smoothing, normalization, and binning steps were applied to the hyperspectral data as described in Chapter 4 (Paulus and Mahlein, 2020). The smoothing parameters and binwidths for spectral binning were adapted to the equipped sensors (Table 5.1). After visual inspection of the reflectance curves, the VNIR data were smoothed with a Savitzky-Golay filter with third polynomial order and a window length of seven, and the SWIR data were smoothed with a Savitzky-Golay filter with third order polynomial and a window length of nine. SWIR reflectance was adjusted to the baseline of the VNIR reflectance and the ends of the spectral range were limited to > 410 nm and < 1680 nm to remove noisy bands at the extremes of the range. Spectral binning was performed at both single and double FWHM of each sensor. The derivatives were calculated with a gap size of 1 and a window length of 9. Binning, smoothing, and derivation were performed using the packages `tidyverse` version 1.3.2 and `prospectr` version 0.2.6 for

R version 4.2.1 (Wickham et al., 2019; Stevens and Ramirez-Lopez, 2020; R Core Team, 2022). After smoothing and fusion of VNIR and SWIR data, Principal Component Analysis (PCA) was used to explore the dimensionality of the data and the sources of variation, using the `ggfortify` R version 0.4.14 package (Tang, Horikoshi, and Li, 2016).

Feature extraction from hyperspectral and lidar data

Ground cover per plot was estimated using lidar data thresholded by NDVI, and biomass was estimated from the volume of voxels in the point cloud (Supplementary Table 5.5). From the smoothed hyperspectral data, the following VI were calculated from specific wavebands: Modified Simple Ratio (MSR), Plant Senescence Reflectance Index (PSRI), Red Edge Modified Simple Ratio (REMSR / MRESR) and Structure Insensitive Pigment Index (SIPI). Additionally, the average reflectance was taken over all 307 bands to calculate the mean reflectance (MR) (Supplementary Table 5.5).

To evaluate the potential of using vegetation indices derived from RGB or multispectral sensors, four multispectral channels were emulated from hyperspectral data by averaging the raw reflectance within spectral ranges corresponding to typical ranges of RGB and multispectral sensors: 418 - 510 nm (blue), 490 - 580 nm (green), 573 - 645 nm (red), and 705 - 820 (NIR), (Zhang et al., 2017). From these averaged bands, the following VI were calculated: Enhanced Normalized Difference VI (ENDVI), Enhanced Vegetation Index (EVI), Excess Green Index (EXGI), Green Chromatic Coordinate (GCC), Green Red VI (GRVI), Modified Soil Adjusted VI (MSAVI), Normalized Difference VI (NDVI), Red Edge Normalized Difference VI (RENDVI), Red Edge Simple Ratio (SR), Green Red VI (VARI) (Supplementary Table 5.5).

Learning algorithms and model selection

Learning algorithms Both full spectrum reflectance data as well as ground cover and biomass were used for the prediction of PAD scores and the classification between fungicide and non-fungicide treatments. As in Chapter 4, random forest (RF), support vector machines (SVM), and partial least squares regression / - discriminant analysis (PLSR / PLS-DA) were used as learning algorithms for regression and classification analyses. In addition, least absolute shrinkage and selection operator (LASSO) with and without a correlation filter of 0.7 were tested for regression (James et al., 2013; Li et al., 2019).

Model selection The models were trained with five repeats of five - fold cross - validation using the `tidymodels` framework for each year (Kuhn and Wickham, 2020). Regression models were evaluated based on the estimated RMSE and squared Pearson's correlation coefficient (R^2), and classification models were evaluated based on the estimated accuracy and Cohen's kappa (κ). The best algorithms within each

year were selected, trained on the entire data set of the season, and evaluated on the data from the opposite season. The models for the prediction of PAD were only trained on the data from the infected trays and plots. As there were only 11 recorded infected trays in 2022, no regression models were trained on this year's data.

The training data for the classification task from the 2020 data contained only two classes of treatment, *i.e.* (i) Fungicide treated and (ii) non-fungicide treated. The data from the 2022 season instead contained three treatment classes: (i) Infected, (ii) non-infected and fungicide treated, (iii) non-infected, fungicide treated and salinity treated. In the evaluation of the final models, a predicted classification was considered correct if the infection status was predicted successfully, regardless of salinity treatment (Table 5.3).

The influence of the pre-processing steps (Smoothing, VNIR and SWIR fusion, Normalization, Derivation, Binning) and learning algorithms (LASSO, LASSO with 0.7 correlation filter, RF, SVM, PLSR for regression; RF, SVM and PLSDA for classification) on cross-validation (CV) results within each year was examined by analysis of variance (Chapter 4).

Feature selection

Variable importance was determined by permutation in RF models as described in Chapter 3. In the case of PAD score prediction, a linear least squares regression model with the most important trait as predictor was trained and in the case of classification between treatments, a multinomial regression model, again with the most important trait as predictor was trained (Li et al., 2019; Gregorutti, Michel, and Saint-Pierre, 2017).

Analysis of treatment and genotypic effects on PAD scores

The effects of fungicide treatment on PAD scores as well as genotypic effects within the nil-treated plots were examined as described in Chapter 3 by analysis of variance and comparison of Tukey Honest Significant Differences, implemented in the `agricolae` R package (Felipe de Mendiburu and Muhammad Yaseen, 2020).

5.5 Results

5.5.1 Visual scoring of AB damage

2020 season

PAD scores in untreated plots The PAD scores for the 2020 plots that were not treated with fungicides ranged from 2 to 90 % and there were significant genotypic differences (Figure 5.4). The susceptible control genotype *cv.* Howzat had an average score of 74.4 % AB damage over eight plots and the most resistant screened genotype CVR021 had an average score of 9.4 % over four plots.

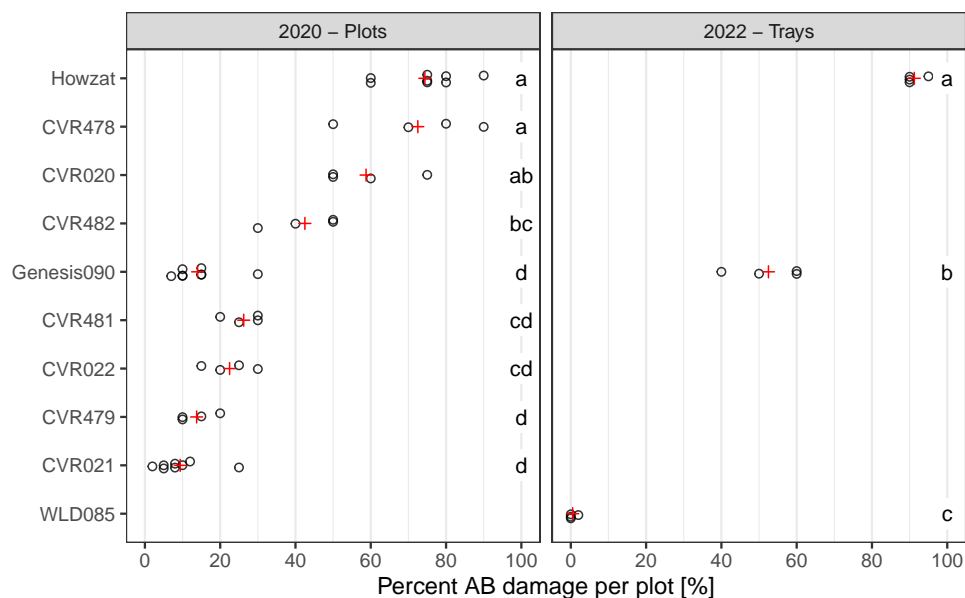


FIGURE 5.4: Visually rated percent AB damage for the non-fungicide treated plots in 2020 and non-fungicide treated trays in 2022. Black dots indicate individual plots / trays and red crosses indicate the mean PAD. Letters indicate groups where pairwise comparisons are significantly different at $\alpha = 0.05$, within each year.

Treatment effects on PAD scores Only the fortnightly Chlorothalonil treatment could fully prevent AB damage in 2020. AB damage was still observed under strategic application of Aviator, Veritas, or Chlorothalonil (Figure 5.5). Therefore, only the fortnightly Chlorothalonil treatment was chosen as control treatment for the disease detection algorithm in 2020.

2022 season

Genotypic effects in untreated trays In the trays in 2022, all three genotypes showed significantly different AB damage under the infection treatment. Howzat scored highest with a mean PAD score of 91.25 %, Genesis090 scored in the middle with a mean PAD score of 52.5 %, and WLD085, the candidate resistant *C. reticulatum* accession, scored lowest with a mean PAD score of 0.5 %. Only one out of four trays of WLD085 showed any signs or symptoms of AB, confirming the resistance of this genotype (Figure 5.4, Chapter 3).

Treatment effects The infected trays had significantly higher PAD scores than both the salt and fungicide-treated and the fungicide-treated trays (Figure 5.4). However, both fungicide-only and fungicide and salinity treated trays were given visual scores of more than zero in a concealed test where the rater was not aware of genotype and treatment. Three of the twelve fungicide-protected trays were rated as showing

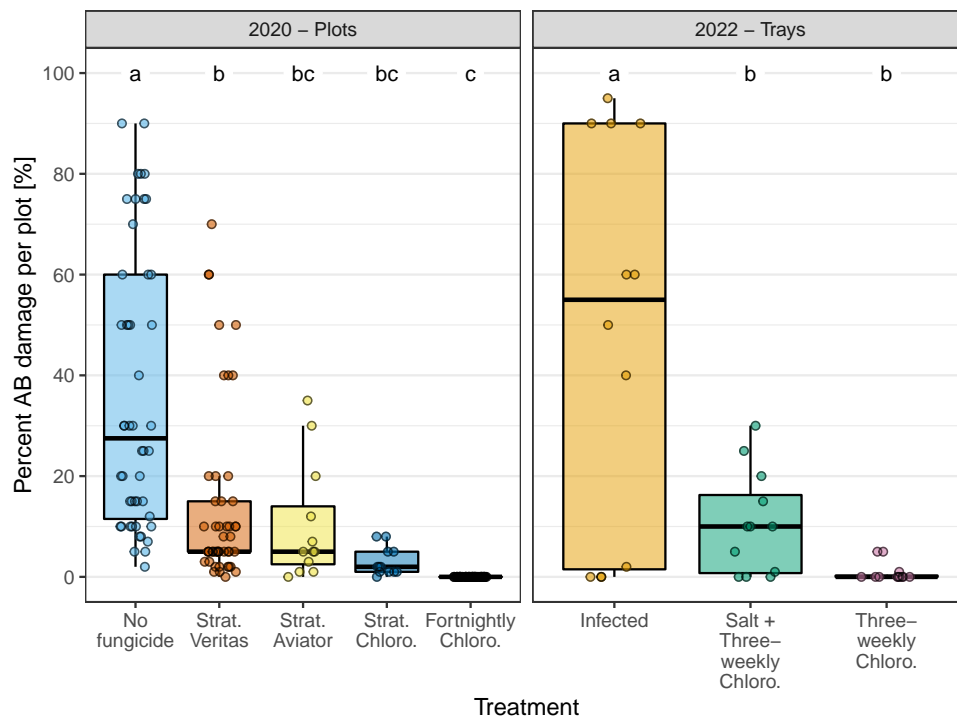


FIGURE 5.5: Visually scored Percent AB Damage under different treatments. Chloro. = Chlorothalonil, Strat. = Strategic. Letters indicate groups where pairwise comparisons are significantly different at $\alpha = 0.05$, within each year.

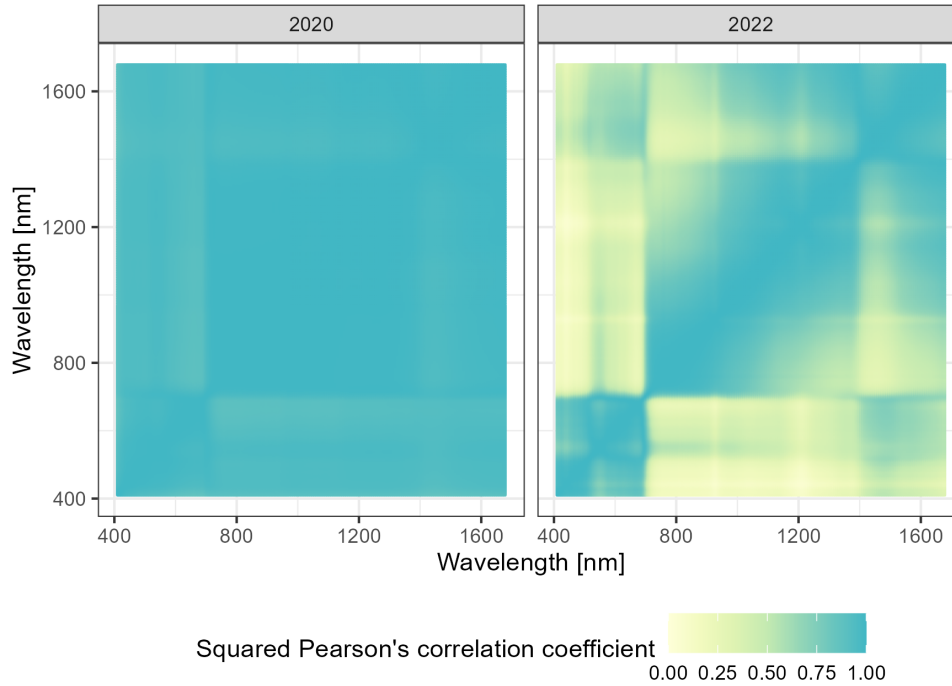


FIGURE 5.6: Symmetric correlation matrix between reflectance at individual bands for smoothed hyperspectral data within each season. For the 2020 data, two treatments (fortnightly Chlorothalonil and No-fungicide) are included and for the 2022 data, all treatments are included.

minimal AB damage of 5 % or less, and nine of the salinity-treated but fungicide-protected trays were rated as showing varying degrees of AB damage up to 30 % (Figure 5.5).

5.5.2 Exploratory analysis of hyperspectral data

In both seasons, the smoothed hyperspectral data showed high autocorrelation and redundant features across both fortnightly chlorothalonil treated and non-fungicide treated plots, reaching near-perfect correlation across all bands in the 2020 season (Figure 5.6). In 2022, the VIS region of the trays (sub 700 nm) showed a lower correlation to the near-infrared region (between 700 and 1300 nm). The correlation between the VIS and NIR - SWIR region was even lower when only the infected trays were considered (Figure 5.9). Principal component analysis (PCA) could capture a large fraction of the variation within the spectral data in few components for both seasons (Figure 5.7). For the 2020 data, the first and second PC represented 98.31 % and 1 % of the variation in the spectral data, respectively, and strong clustering of the treatments was apparent. In the 2022 season, the first two components represented 75.87 % and 16.86 % of the variation, respectively, and the three treatments did not show the same level of clustering as the 2020 data.

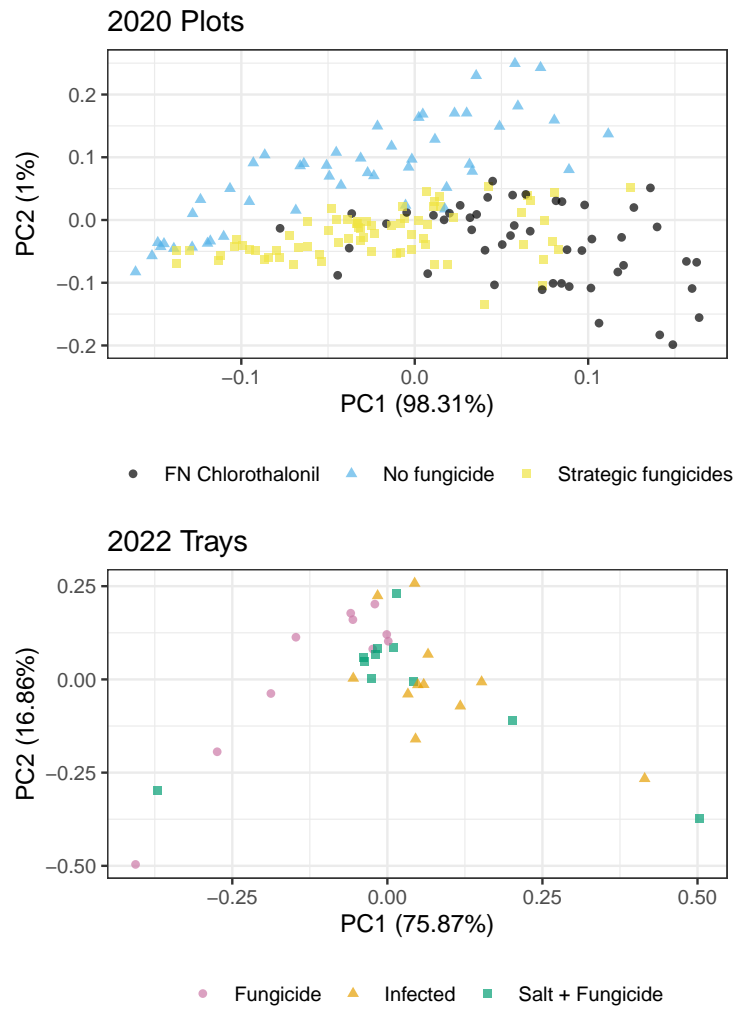


FIGURE 5.7: Principal component analysis of smoothed spectral data within each season. Treatments are highlighted by shape and color. For the 2020 season, all three strategic fungicide treatments (Aviator, Veritas, Chlorothalonil) are displayed as a single group.

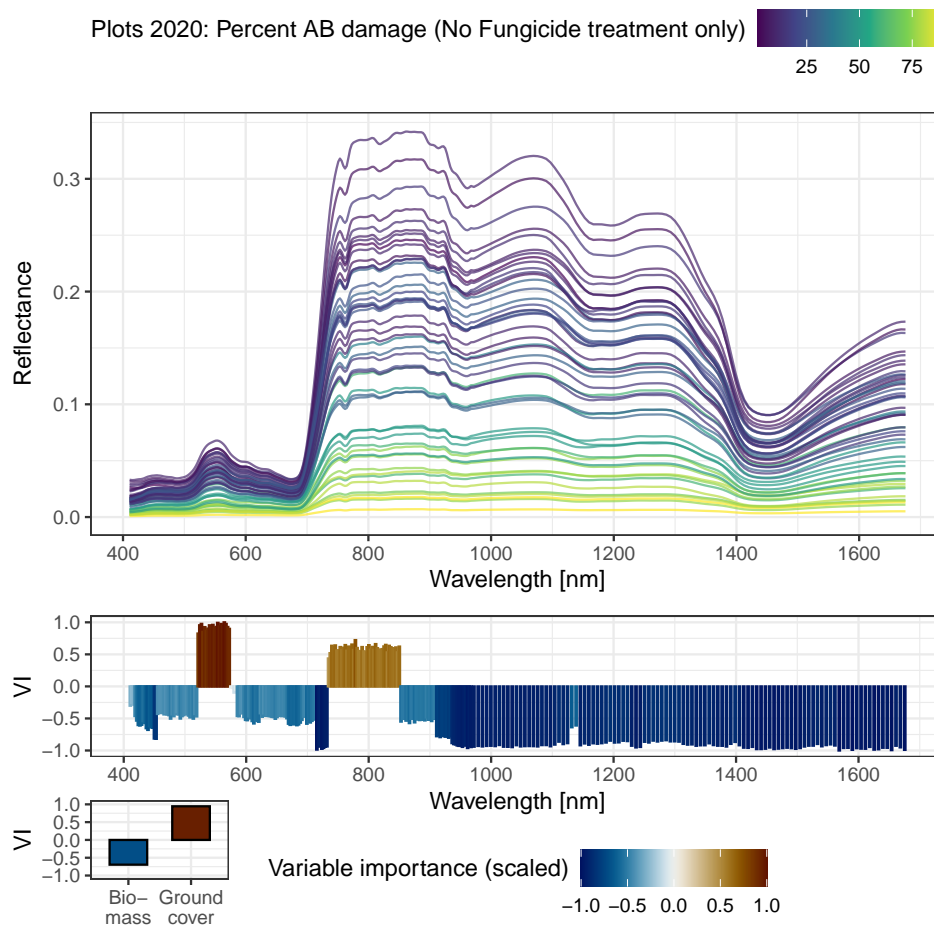


FIGURE 5.8: Thin lines represent smoothed reflectance for plots not treated with fungicides with PAD scores indicated as color (upper panel). Waveband and lidar-based trait importance (VI) for prediction of PAD based on permutation in 500 random forest models is shown in lower panel.

5.5.3 Prediction of AB damage

Regression using full spectrum hyperspectral data The best estimated prediction of PAD scores with full spectrum hyperspectral data (Figure 5.8) for the 2020 season was achieved using the second derivative of non-normalized raw reflectance data, binned at double FWHM, in a random forest model. The estimated RMSE \pm standard deviation was 9.27 ± 2.14 ($R^2 = 0.89 \pm 0.07$). When testing this algorithm on the data from trays of 2022 (Figure 5.9), an RMSE of 31.32 ($R^2 = 0.51$) was achieved (Table 5.2). Due to the trimodal distribution of the observed scores, Spearman's rank correlation coefficient was also calculated for the between-year evaluation ($\rho = 0.74$) (Figure 5.4). Each step of the pre-processing pipeline except for the inclusion of SWIR data had a significant influence on the results of the within-year CV in 2020 (Supplementary Table 5.4).

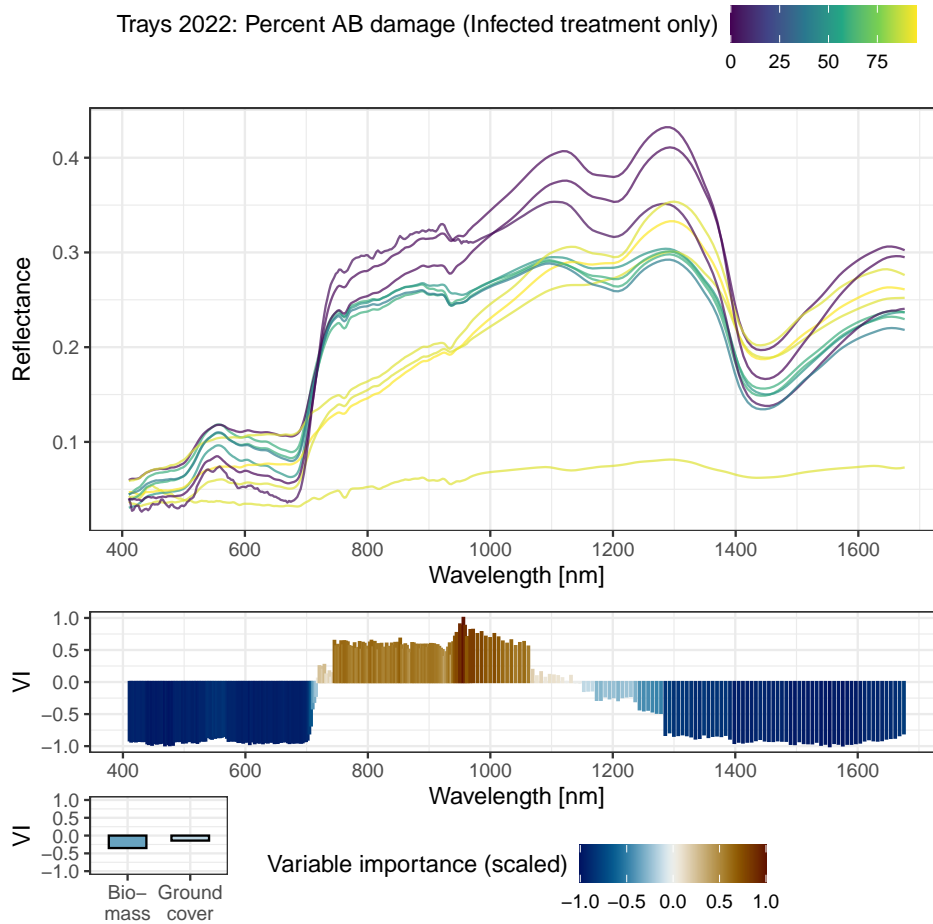


FIGURE 5.9: Thin lines represent smoothed reflectance for infected trays with PAD scores indicated as color (upper panel). Waveband and lidar-based trait variable importance (VI) for prediction of PAD based on permutation in 500 random forest models is shown in lower panel.

TABLE 5.2: Between-year PAD score prediction validation results of a random forest model trained on processed full spectrum hyperspectral data (Full spectrum model), linear regression model trained on reflectance at 792 nm (Single band model) and a linear regression model trained on EVI (EVI model). Model RMSE, squared Pearson's correlation coefficient (R^2) and Spearman's rank correlation coefficient (ρ) are reported. No models were trained on 2022 data.

Validation	Full spectrum model	Single band model (792 nm)	EVI model
2020 model, 2022 data	RMSE = 31.32 $R^2 = 0.51$ $\rho = 0.74$	RMSE = 41.18 $R^2 = 0.68$ $\rho = 0.89$	RMSE = 27.35 $R^2 = 0.70$ $\rho = 0.77$
2022 model, 2020 data	—	—	—

Variable extraction for regression The important spectral regions for the prediction of PAD scores in 2020 ranged from 520 to 570 nm and from 740 to 850 nm (Figure 5.8). Bands within and between these two spectral regions were strongly correlated ($r > 0.99$) (Figure 5.6). Furthermore, the lidar-derived ground cover was important for the prediction of PAD scores. The region between 740 and 850 nm was also important for the prediction in 2022 (Figure 5.9). Therefore, a simple linear regression model with a center wavelength of 792 nm as the only predictor was evaluated in cross-validation for 2020 data ($RMSE = 13.02 \pm 0.54$, $R^2 = 0.81 \pm 0.02$), and then trained on the entire data of 2020 and tested on 2022 data ($RMSE = 41.18$, $R^2 = 0.68$, $\rho = 0.89$) (Table 5.2).

Vegetation indices for regression Due to the high collinearity between wavebands, the extracted vegetation indices were also strongly autocorrelated. For the infected plots in 2020, the correlation coefficients of all extracted indices with PAD scores ranged between absolute values of ($r = 0.7$ and $r = 0.9$). The strongest correlations were EVI ($r = -0.9$), ExGI ($r = -0.89$) and MSAVI ($r = -0.89$), which are correlated with plant vigor (Huete et al., 2002; M. Woebbecke et al., 1995; Larrinaga and Brotons, 2019; Qi et al., 1994). Out of all the extracted traits, only PSRI showed a positive correlation with PAD scores ($r = 0.72$), this index is correlated with leaf senescence (Merzlyak et al., 1999). Mean reflectance (MR) had a correlation of -0.88 with PAD scores (Figures 5.8 5.9). All of these correlations were significant at $p < 0.05$. In the 2022 season, PAD scores were also strongly correlated with vegetation indices, but that year the correlations were not significant, possibly because only 11 trays were recorded. EVI again showed the strongest correlation to PAD scores on the trays ($r = -0.84$), followed by MSAVI, SR, and RENDVI (all $r = -0.83$). MR had a correlation of -0.67 to PAD scores. As in 2020, the only index with a positive correlation to PAD scores was PSRI ($r = 0.11$). In cross-validation within 2020 data, EVI achieved an RMSE of 12.2 ± 0.50 , $R^2 = 0.83 \pm 0.02$. When the EVI linear regression model was trained on all data of 2020 and applied to 2022 data, the results were $RMSE = 27.4$, $R^2 = 0.7$, $\rho = 0.77$ (Table 5.2).

5.5.4 Treatment classification

Classification using full spectrum hyperspectral data The best algorithm to distinguish non-fungicide treated plots from those treated fortnightly with Chlorothalonil in 2020 used the first derivative of normalized raw full spectrum data in an SVM model, achieving an estimated accuracy of $99.6 \% \pm 1.5 \%$. When training on the entire data from 2020 and applying the model to 2022 data, the accuracy was 34.4% ($\kappa = 0.00$, Table 5.3). As for the regression model, all preprocessing steps and the choice of learning algorithm had a significant influence on the CV performance of the classifiers, except for the inclusion of SWIR data (Supplementary Table 5.4). The best algorithm to distinguish salt and fungicide treated, fungicide-only treated, and infected trays in 2022 used raw reflectance VNIR-only data in a random forest model, achieving an estimated accuracy of $70.1 \% \pm 15.0 \%$ (Figure 5.11). Applying the trained

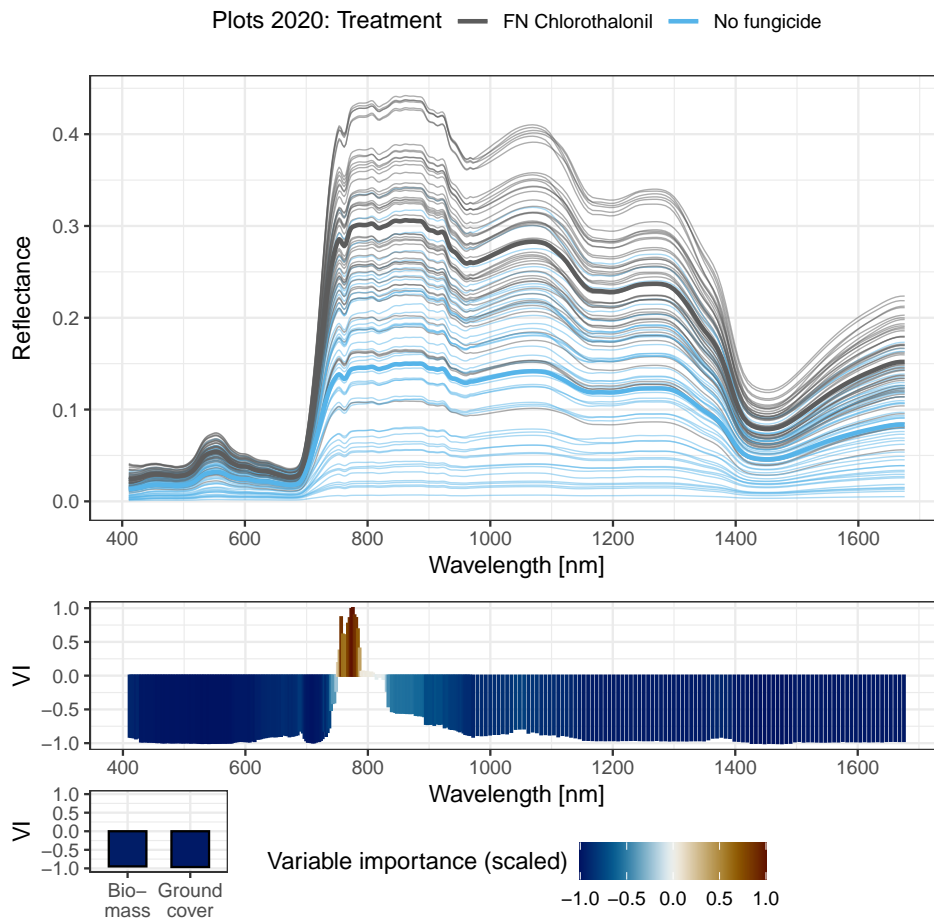


FIGURE 5.10: Smoothed reflectance of all plots used for the treatment classifier in 2020 and feature importance. Thin lines represent smoothed reflectance for individual plots with treatment indicated as color (upper panel), with the average for each treatment overlaid as a thick line. Waveband and lidar-based trait importance (VI) for prediction of PAD based on permutation in 500 random forest models is shown in lower panel.

model from 2022 to 2020 data resulted in an accuracy of 72.9 % ($\kappa = 0.458$, Table 5.3). The selection of learning algorithm and all preprocessing steps except smoothing all had a significant influence on the CV results of classifiers trained on 2022 data (Supplementary Table 5.4).

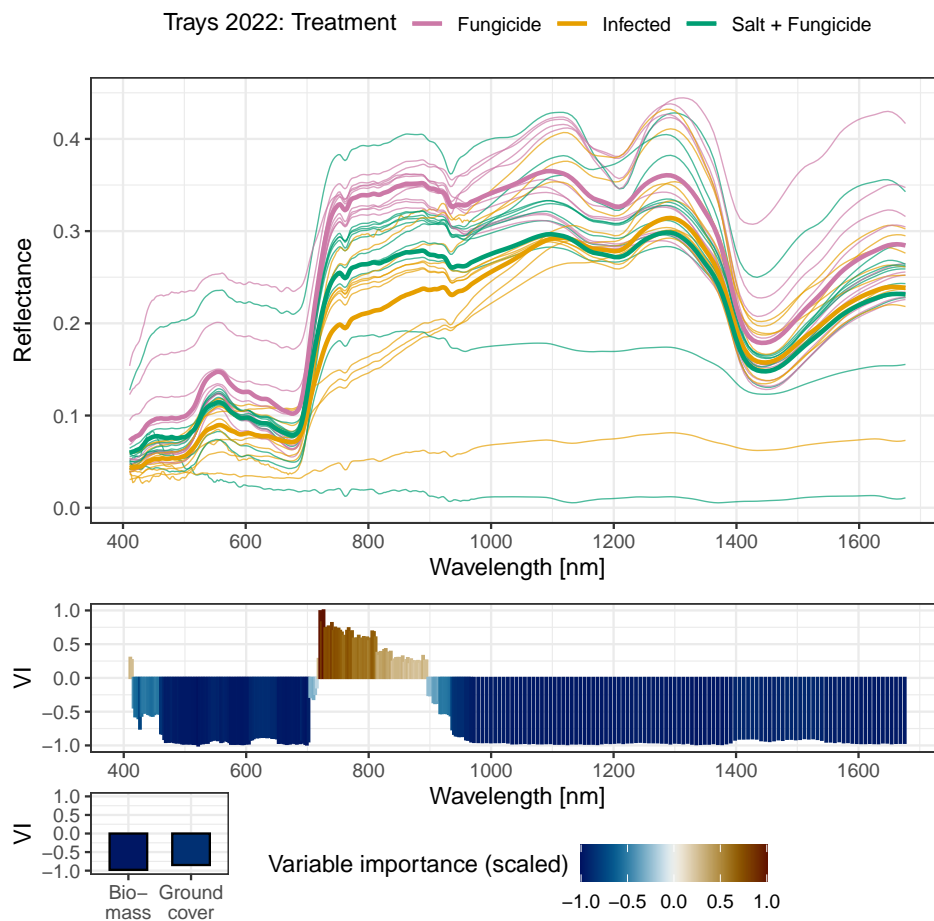


FIGURE 5.11: Smoothed reflectance of all plots used for the treatment classifier in 2022 and feature importance. Thin lines represent smoothed reflectance for individual trays with treatment indicated as color (upper panel), with the average for each treatment overlaid as a thick line. Waveband and lidar-based trait importance (VI) for prediction of PAD based on permutation in 500 random forest models is shown in lower panel.

TABLE 5.3: Upper table shows treatment predictions for 2020 data made with models trained on 2022 data, both with a single band model (logistic regression with reflectance at 756 nm as predictor) and full spectrum model. Predictions that were considered correct are highlighted green and predictions that are considered wrong are highlighted red. Overall accuracy and Cohen's κ are reported. The lower table shows the opposite validation, prediction for 2022 made with models trained on 2020 data.

<i>2022 models predicting 2020 data</i>	Plots + FN chlorothalonil	Plots without fungicide
Single band model (756 nm): Accuracy = 81.2 %, $\kappa = 0.63$		
Predicted: Trays + Infected	11	41
Predicted: Trays + Fungicide	22	1
Predicted: Trays + Salt + Fungicide	15	6
Full spectrum model (VNIR, RF): Accuracy = 72.9 %, $\kappa = 0.46$		
Predicted: Trays + Infected	25	47
Predicted: Trays + Fungicide	23	1
Predicted: Trays + Salt + Fungicide	0	0

<i>2020 models predicting 2022 data</i>	Trays: Infected	Trays: Fungicide	Trays: Salt + Fungicide
Single band model (756 nm): Accuracy = 71.9 %, $\kappa = 0.30$			
Predicted: Plots + FN chlorothalonil	7	10	9
Predicted: Plots without fungicide	4	0	2
Full spectrum model (VNIR + SWIR, SVM): Accuracy = 34.4 %, $\kappa = 0.00$			
Predicted: Plots + FN chlorothalonil	0	0	0
Predicted: Plots without fungicide	11	10	11

Variable extraction for classification The most important spectral region for classification of fungicide-treated and untreated plots in 2020 was between 756 and 784 nm (Figure 5.10). In 2022, the important region was between 721 and 811 nm with greater importance towards shorter wavelengths (Figure 5.11). The reflectance at an intermediate wavelength of 756 nm was chosen as the only predictor. This band had a Pearson correlation greater than 0.99 with the bands where importance was highest at 776 and 726 nm, respectively, for each year. The classifiers trained on that individual band achieved estimated accuracies of 81.8 % \pm 1.5 % in 2020 and 74.5 % \pm 3.2 % in 2022. The prediction of data from 2022 with the model trained on 2020 data achieved an accuracy of 71.9 % ($\kappa = 0.301$). Testing the algorithm from 2022 on 2020 data resulted in an accuracy of 81.2 % ($\kappa = 0.625$) (Table 5.3).

5.6 Discussion

5.6.1 General discussion

PAD scores The performance of the genotypes in the infected and nil-treated subsets was consistent throughout the growing seasons and in experiments in other environments (Chapters 3 and 4). Cv. Howzat performed the worst, cv. Genesis090 showed moderate susceptibility and the candidate resistance of the wild accession WLD085 was confirmed (Figure 5.4). Concerning the treatment effects on PAD scores, only the fortnightly chlorothalonil treatment could completely prevent AB in plots in 2020, but not the strategic applications of fungicides before rain events. Therefore, frequent fungicide applications are required for complete disease management. Despite such frequent applications, the fungicide-protected trays in 2022 were also rated positive for AB symptoms. It is possible that there was a small amount of cross-infection from the infected trays facilitated by favorable environmental conditions in the nursery, despite the fungicide treatment and spatial separation of the trays (Chapter 3). Among the fungicide-protected trays, those that also received salt treatments had slightly higher PAD scores (Figure 5.5). While this difference was not significant, it may be explained by three factors. (i) The salt-treated trays could have been more cross-contaminated than the non-salt-treated trays by chance or (ii) the plants could have been stressed by the salt treatment and therefore been more susceptible to cross-infection (Bostock, Pye, and Roubtsova, 2014). Another potential explanation is (iii) false positive scoring, in which salt damage could have been interpreted as AB damage, as the scoring was performed as a concealed trial with respect to the treatment (Figure 5.2).

Hyperspectral imaging of chickpea AB interaction in the field High autocorrelation between bands was observed in 2020 across the entire measured spectrum and within 400 to 700 nm in 2022, consistent with published literature and Chapter 4 (Hennessy, Clarke, and Lewis, 2020). The lower correlation of the wavelengths longer than 700 nm with the other bands in 2022 may be explained by trays with overall low reflectance across the entire spectrum and infected trays that showed a less steep

red edge section (Figure 5.11). In the cross-validation of all classification and regression models trained on hyperspectral data in 2020, there was no significant effect of including SWIR data, probably due to the high correlation with bands in the VNIR region (Figure 5.6). However, all other processing steps, as well as the choice of learning algorithm, had significant influences on cross-validation performance, except for smoothing for the classifier in 2022. The correlation between VNIR and SWIR bands was lower in 2022, which could be the reason that the inclusion of SWIR bands had a significant negative effect on the CV treatment classification results (Supplementary Table 5.4). These results confirm the influence of hyperspectral data preprocessing methods and learning algorithms on the success of the treatment classification and disease severity prediction. Therefore, the methods need to be chosen carefully (Hennessy, Clarke, and Lewis, 2020; Paulus and Mahlein, 2020; Heim et al., 2018; Wei et al., 2021).

Prediction of PAD An accurate ranking of genotypes grown in 2022 according to their PAD was achieved with a linear model trained on the reflectance of plots from a single waveband at 792 nm from 2020 ($\rho = 0.89$). This linear model performed similarly to one trained on EVI when evaluated on R^2 , with EVI performing better based on RMSE, while the single band achieved better results based on ρ . The lower RMSE when using EVI may be due to the normalization step when calculating this vegetation index (Supplementary Table 5.5). Both the single band model and the EVI model performed better than the model trained on full spectrum data, indicating that dimensionality reduction improves transferrability of the model. The band at 792 nm was chosen as predictor because it shared high importance in both seasons (Figures 5.8, 5.9). The band is located between the red edge region and NIR plateau and is related to the collapse of the leaf cell structure (Malthus and Madeira, 1993; Hennessy, Clarke, and Lewis, 2020). In the 2020 season, the greenness and lidar-based groundcover were important in addition to the red edge / NIR region. As the segmentation of plant material is performed using sensor fusion with lidar and no correction for soil reflectance needs to be performed, the green brightness can represent the ratio of healthy plant tissue to necrotic plant tissue in the remaining plant material (Gitelson et al., 2002). Stem breakage caused by AB leads to a loss of biomass up to a complete absence of plants in heavily diseased plots, which might explain the importance of the trait Ground cover for the prediction of PAD. Ground cover, however measured by RGB image segmentation, not lidar, was also found to be an important predictor for disease index classes of pots in Chapter 3.

Treatment classification The CV performance of the full spectrum model within the 2020 season was almost perfect with more than 99 % accuracy, but the full model had no predictive power for the 2022 data ($\kappa = 0$), a clear sign of overfitting that is a strong risk in situations where the number of predictors exceeds the number of observations (Table 5.3) (James et al., 2013). In contrast, the full spectrum model trained on 2022

showed a lower within-year estimated CV accuracy (70 %) than the between-year accuracy (72.9 %, $\kappa = 0.46$), potentially due to the smaller training data set. In 2020, the important spectral bands for classification were limited to the red edge region between 756 nm and 784 nm, indicating that capturing a general plant stress response expressed as a reduction in reflectance in the red edge region is sufficient to distinguish between fungicide-treated and nil-treated plots (Figure 5.10) (Clevers et al., 2002). When a third treatment was included in 2022, a larger spectral region from 721 to 811 nm contributed to model performance, indicating that there are differences in the spectral response of plants to AB and salt stress (Figure 5.11) (Lowe, Harrison, and French, 2017; Moghimi, Yang, and Marchetto, 2018). Lidar-based traits in themselves did not contribute to treatment classification accuracy in either season, but sensor fusion enabled limitation of the spectral measures to the plant material and elimination of background signals.

Specificity and sensor suitability Despite the larger region of variable importance for classification between three treatments in 2022, the specificity of treatment classification was low and the spectral response to salt stress and infection was similar, as shown in the clustering of treatments in PCA, the reflectance curves, and the lower estimated classification accuracy of 70 % compared to an estimated accuracy of 99 % when only distinguishing between nil-treated and fungicide protected plots (Figures 5.7, 5.10 and 5.11). However, there was still more evidence of differences in the spectral response between salt and infection treatment, as no salinity was predicted with the full spectrum model trained on 2022 data applied to 2020 data, unlike the single band model (Table 5.3).

The specificity of detection may be improved by limiting the influence of secondary stresses in controlled trials, or using human supervision when in doubt, as suggested for *Cercospora* Leaf Spot on sugar beet (Jay et al., 2020). Alternatively, increased specificity via sensor technology may be achieved by the addition of high-resolution RGB sensors to the phenotyping platform, which would allow to detect lesions with the methods developed in Chapter 3. Specific distinction between two biotic stresses was also shown to be possible in the controlled environment with contact spectrometry (Gold et al., 2020b) and even using imaging spectroscopy from an airplane (Poblete et al., 2021) (Section 4.3.2).

Lidar sensors facilitate the semantic segmentation and limit the reflectance measurements to the remaining plant material; this task would be more difficult if only spectral measurements were available. The results of whether lidar-based traits themselves are useful compared to spectral measurements alone were inconclusive and should be investigated in future field trials (Figure 5.8). In the investigation of within-year variable importance, ground cover was only important for the prediction of PAD in 2020, possibly due to the presence of the sprawling weeds. Lidar-based traits were not important for the other season. An alternative vector for measuring average plot-level reflectance could be aerial platforms to increase the throughput, but this

would limit the ability to perform 3D reconstruction, reflectance from the soil would need to be controlled for, and lesion detection would likely not be possible due to low spatial resolution.

5.6.2 Study outcomes in relation to research aims

1. Development of sensor-based phenotyping methods to score disease severity in a chickpea breeding program Breeding selection may be supported using simple sensors that can measure reflectance in the RGB and the VNIR spectrum. At plot-level, that reflectance may also be measured with higher throughput by mounting such sensors on UAVs. However, specificity to AB stress cannot be guaranteed when using simple vegetation indices. Therefore, the following options exist to support breeding with sensor-based methods in the field with simple vegetation indices. (i) Secondary stresses need to be removed, (ii) human supervision of the methods can be used to recognize secondary stresses, (iii) sensor-based methods need to be developed further for higher specificity.

2. Identification of within-scale and cross-scale functional resistance components At the field scale, single band reflectance at 792 nm or EVI were suitable candidate traits for prediction of DI. However, it is implausible that they are functional resistance components due to their non-specificity as shown in the tray experiments in 2022. No time-series measurements were performed for the field-scale, therefore no relative growth rates in response to inoculation (promising potential resistance components in Chapter 3 and 4) could be derived and compared to the single time point spectral traits.

5.7 Conclusion

In summary, we showed that spectral measurements in the VNIR region of chickpeas affected by *Ascochyta* blight in the field can accurately rank genotypes according to their visual scores. The transferability of AB damage prediction and treatment classification models could be increased by selecting features from full spectrum hyperspectral data such as simple vegetation indices or single waveband reflectance. The best ranking of unseen data from an independent experiment was achieved with a least squares regression model trained on the reflectance from a single band at 792 nm ($\rho = 0.89$). Treatment classification models using a single band at 756 nm achieved accuracies of 71.9 % and 81.2 % in between-year validation. However, the specificity of stress detection was not very high, as the chosen feature was a general plant stress response. The results for classification accuracy should be confirmed in additional trials, as salt treatment was only included in one of the two seasons. Ground cover and biomass estimates derived from lidar data seemed not to be important for treatment classification and prediction of PAD scores, but enabled 3D reconstruction of the

plant material and, thus, improved the spectral data. Similarly, the inclusion of SWIR data did not improve treatment classification and prediction of PAD scores. Our methods open up the possibility of predicting Ascochyta blight damage with simple spectral indices in field trials where secondary stresses can be mitigated. As average plot-level indices were suitable predictors, data acquisition may be simplified from using ground-based hyperspectral measurements to using multispectral sensors on airborne platforms that would achieve increased throughput at a lower cost. However, more work is needed to increase the specificity of the methods by including multi-environment, multi-year data.

5.8 Acknowledgements

Technical assistance was provided by the field team of the South Australian Research and Development Institute (SARDI) Clare field team, Scientific Officer Sara Blake of SARDI Urrbrae who ran the field experiment in 2020, and technical officer Marzena Krysinska-Kaczmarek of SARDI Urrbrae who provided *A. rabiei* isolates for the 2022 tray experiment.

5.9 Data availability

The data and code required to reproduce these results are available via

- https://github.com/FCTanner/ab_field_phenotyping
- <https://projects.pawsey.org.au/appf-tpa-0556-fe-sardi-davidson-chickpeas-turretfield/index.html>

5.10 COVID-19 impact statement

Screens of field experiments could not be conducted in the seasons 2021 and 2022 due to COVID-19 restrictions. To substitute for this, an experiment using tray-grown plants to simulate full canopies was carried out in 2022. These trays could be imaged on campus.

5.11 References

Anderegg, Jonas et al. (2019). "In-Field Detection and Quantification of Septoria Tritici Blotch in Diverse Wheat Germplasm Using Spectral–Temporal Features". In: *Frontiers in Plant Science* 10.October, pp. 1–19. ISSN: 1664462X. DOI: 10.3389/fpls.2019.01355.

- Angelica Galieni et al. (Mar. 2022). "Surveying soil-borne disease development on wild rocket salad crop by proximal sensing based on high-resolution hyperspectral features." In: *Scientific Reports* 12.1. MAG ID: 4220983416, pp. 5098–5098. DOI: 10.1038/s41598-022-08969-5.
- Araus, José Luis and Jill E. Cairns (2014). "Field high-throughput phenotyping: The new crop breeding frontier". In: *Trends in Plant Science* 19.1, pp. 52–61. ISSN: 13601385. DOI: 10.1016/j.tplants.2013.09.008.
- Araus, José Luis et al. (2018). "Translating High-Throughput Phenotyping into Genetic Gain". In: *Trends in Plant Science* 23.5, pp. 451–466. ISSN: 13601385. DOI: 10.1016/j.tplants.2018.02.001.
- Atieno, Judith et al. (2017). "Exploring genetic variation for salinity tolerance in chickpea using image-based phenotyping". In: *Scientific Reports* 7.1. Publisher: Springer US, pp. 1–11. ISSN: 20452322. DOI: 10.1038/s41598-017-01211-7. URL: <http://dx.doi.org/10.1038/s41598-017-01211-7>.
- Atieno, Judith et al. (2021). "Novel Salinity Tolerance Loci in Chickpea Identified in Glasshouse and Field Environments". In: *Frontiers in Plant Science* 12. ISSN: 1664-462X. URL: <https://www.frontiersin.org/articles/10.3389/fpls.2021.667910> (visited on 11/22/2022).
- Bar, Ido (Oct. 2019). *Whole Genome Sequencing of Ascochyta rabiei Isolates*. original-date: 2017-07-18T23:36:46Z. URL: https://github.com/IdoBar/A_rabiei_WGS_analysis (visited on 11/14/2022).
- Blake, Sara (2022). *2022 South Australia Pulse Variety Disease Guide*. Tech. rep. PIRSA, SARDI. URL: https://pir.sa.gov.au/__data/assets/pdf_file/0020/386102/pulse_variety_disease_guide_2022.pdf.
- Bock, Clive H. et al. (Dec. 2020). "From visual estimates to fully automated sensor-based measurements of plant disease severity: status and challenges for improving accuracy". In: *Phytopathology Research* 2.1. Publisher: Phytopathology Research, p. 9. ISSN: 2524-4167. DOI: 10.1186/s42483-020-00049-8. URL: <https://phytopatholres.biomedcentral.com/articles/10.1186/s42483-020-00049-8>.
- Bostock, Richard M., Matthew F. Pye, and Tatiana V. Roubtsova (2014). "Predisposition in plant disease: exploiting the nexus in abiotic and biotic stress perception and response". eng. In: *Annual Review of Phytopathology* 52, pp. 517–549. ISSN: 1545-2107. DOI: 10.1146/annurev-phyto-081211-172902.
- Carillo, Petronia et al. (Sept. 2011). *Salinity Stress and Salt Tolerance*. en. Publication Title: Abiotic Stress in Plants - Mechanisms and Adaptations. IntechOpen. ISBN: 978-953-307-394-1. DOI: 10.5772/22331. URL: <https://www.intechopen.com/state.item.id> (visited on 11/22/2022).
- Chen, Jing M. (Sept. 1996). "Evaluation of Vegetation Indices and a Modified Simple Ratio for Boreal Applications". In: *Canadian Journal of Remote Sensing* 22.3. Publisher: Taylor & Francis _eprint: <https://doi.org/10.1080/07038992.1996.10855178>, pp. 229–242. ISSN: 0703-8992. DOI: 10.1080/07038992.1996.10855178. URL: <https://doi.org/10.1080/07038992.1996.10855178> (visited on 08/11/2022).

- Clevers, J. G. P. W. et al. (Jan. 2002). "Derivation of the red edge index using the MERIS standard band setting". In: *International Journal of Remote Sensing* 23.16. Publisher: Taylor & Francis _eprint: <https://doi.org/10.1080/01431160110104647>, pp. 3169–3184. ISSN: 0143-1161. DOI: 10.1080/01431160110104647. URL: <https://doi.org/10.1080/01431160110104647> (visited on 10/24/2022).
- CropTraits. URL: <https://www.croptraits.com.au/#TraitSeeker> (visited on 11/21/2022).
- D. M. Woebbecke et al. (1995). "Color Indices for Weed Identification Under Various Soil, Residue, and Lighting Conditions". en. In: *Transactions of the ASAE* 38.1, pp. 259–269. ISSN: 2151-0059. DOI: 10.13031/2013.27838. URL: <http://elibrary.asabe.org/abstract.asp??JID=3&AID=27838&CID=t1995&v=38&i=1&T=1> (visited on 08/16/2022).
- DeChant, Chad et al. (Nov. 2017). "Automated Identification of Northern Leaf Blight-Infected Maize Plants from Field Imagery Using Deep Learning". In: *Phytopathology*® 107.11. Publisher: Scientific Societies, pp. 1426–1432. ISSN: 0031-949X. DOI: 10.1094/PHYTO-11-16-0417-R. URL: <https://apsjournals.apsnet.org/doi/10.1094/PHYTO-11-16-0417-R> (visited on 10/21/2022).
- Ehammer, Andrea et al. (Oct. 2010). "Statistical derivation of fPAR and LAI for irrigated cotton and rice in arid Uzbekistan by combining multi-temporal RapidEye data and ground measurements". In: ed. by Christopher M. U. Neale and Antonino Maltese, p. 782409. DOI: 10.1117/12.864796.
- ENDVI. URL: <https://maxmax.com/endvi.htm> (visited on 03/17/2022).
- Felipe de Mendiburu and Muhammad Yaseen (2020). *agricolae: Statistical Procedures for Agricultural Research*. URL: <https://cran.r-project.org/package=agricolae>.
- Flowers, Timothy J. et al. (2010). "Salt sensitivity in chickpea". In: *Plant, Cell and Environment* 33.4, pp. 490–509. ISSN: 01407791. DOI: 10.1111/j.1365-3040.2009.02051.x.
- Garg, Tosh et al. (2018). "Identification of QTLs for resistance to Fusarium wilt and Ascochyta blight in a recombinant inbred population of chickpea (*Cicer arietinum* L.)" In: *Euphytica* 214.3. Publisher: Springer Netherlands, pp. 1–11. ISSN: 15735060. DOI: 10.1007/s10681-018-2125-3. URL: <https://doi.org/10.1007/s10681-018-2125-3>.
- Gitelson, Anatoly A., Yoram J. Kaufman, and Mark N. Merzlyak (Dec. 1996). "Use of a green channel in remote sensing of global vegetation from EOS-MODIS". In: *Remote Sensing of Environment* 58.3. Publisher: Elsevier, pp. 289–298. ISSN: 00344257. DOI: 10.1016/S0034-4257(96)00072-7. URL: <https://linkinghub.elsevier.com/retrieve/pii/S0034425796000727>.
- Gitelson, Anatoly A. et al. (2002). "Novel algorithms for remote estimation of vegetation fraction". In: *Remote Sensing of Environment* 80.1, pp. 76–87. ISSN: 00344257. DOI: 10.1016/S0034-4257(01)00289-9.
- Gold, Kaitlin M. et al. (June 2020a). "Investigating potato late blight physiological differences across potato cultivars with spectroscopy and machine learning." In:

- Plant Science* 295. MAG ID: 2985102654, p. 110316. DOI: 10.1016/j.plantsci.2019.110316.
- Gold, Kaitlin M et al. (2020b). "Investigating potato late blight physiological differences across potato cultivars with spectroscopy and machine learning". In: *Plant Science* 295. Publisher: Elsevier BV ISBN: 0168-9452, p. 110316. DOI: 10.1016/j.plantsci.2019.110316.
- Gregorutti, Baptiste, Bertrand Michel, and Philippe Saint-Pierre (May 2017). "Correlation and variable importance in random forests". en. In: *Statistics and Computing* 27.3, pp. 659–678. ISSN: 1573-1375. DOI: 10.1007/s11222-016-9646-1. URL: <https://doi.org/10.1007/s11222-016-9646-1> (visited on 08/19/2022).
- Haboudane, Driss et al. (Aug. 2002). "Integrated narrow-band vegetation indices for prediction of crop chlorophyll content for application to precision agriculture". en. In: *Remote Sensing of Environment* 81.2-3, pp. 416–426. ISSN: 00344257. DOI: 10.1016/S0034-4257(02)00018-4. URL: <https://linkinghub.elsevier.com/retrieve/pii/S0034425702000184> (visited on 08/10/2022).
- Heim, René H. J. et al. (June 2018). "Detecting myrtle rust (*Austropuccinia psidii*) on lemon myrtle trees using spectral signatures and machine learning". In: *Plant Pathology* 67.5. MAG ID: 2793166416, pp. 1114–1121. DOI: 10.1111/ppa.12830.
- Hennessy, Andrew, Kenneth Clarke, and Megan Lewis (Jan. 2020). "Hyperspectral Classification of Plants: A Review of Waveband Selection Generalisability". In: *Remote Sensing* 12.1, p. 113. ISSN: 2072-4292. DOI: 10.3390/rs12010113. URL: <https://www.mdpi.com/2072-4292/12/1/113>.
- Huete, A et al. (Nov. 2002). "Overview of the radiometric and biophysical performance of the MODIS vegetation indices". en. In: *Remote Sensing of Environment*. The Moderate Resolution Imaging Spectroradiometer (MODIS): a new generation of Land Surface Monitoring 83.1, pp. 195–213. ISSN: 0034-4257. DOI: 10.1016/S0034-4257(02)00096-2. URL: <https://www.sciencedirect.com/science/article/pii/S0034425702000962> (visited on 08/10/2022).
- James, Gareth et al. (2013). *An Introduction to Statistical Learning*. Vol. 103. Series Title: Springer Texts in Statistics Publication Title: Synthesis Lectures on Mathematics and Statistics Issue: 4 ISSN: 19381751. New York, NY: Springer New York. ISBN: 978-1-4614-7137-0. DOI: 10.1007/978-1-4614-7138-7. URL: <http://link.springer.com/10.1007/978-1-4614-7138-7>.
- Jay, S. et al. (Aug. 2020). "Scoring Cercospora Leaf Spot on Sugar Beet: Comparison of UGV and UAV Phenotyping Systems". In: *Plant Phenomics* 2020. Publisher: American Association for the Advancement of Science (AAAS) ISBN: 2643-6515, pp. 1–18. ISSN: 2643-6515. DOI: 10.34133/2020/9452123. URL: <https://spj.sciencemag.org/journals/plantphenomics/2020/9452123/>.
- Kuhn, Max and Hadley Wickham (2020). *Tidymodels: a collection of packages for modeling and machine learning using tidyverse principles*. URL: <https://www.tidymodels.org>.

- Larrinaga, Asier R. and Lluís Brotons (2019). "Greenness indices from a low-cost UAV imagery as tools for monitoring post-fire forest recovery". In: *Drones* 3.1, pp. 1–16. ISSN: 2504446X. DOI: 10.3390/drones3010006.
- Li, Jiating et al. (Nov. 2019). "Principal variable selection to explain grain yield variation in winter wheat from features extracted from UAV imagery". In: *Plant Methods* 15.1, p. 123. ISSN: 1746-4811. DOI: 10.1186/s13007-019-0508-7. URL: <https://doi.org/10.1186/s13007-019-0508-7> (visited on 08/15/2022).
- Lowe, Amy, Nicola Harrison, and Andrew P. French (2017). "Hyperspectral image analysis techniques for the detection and classification of the early onset of plant disease and stress". In: *Plant Methods* 13.1. Publisher: BioMed Central, pp. 1–12. ISSN: 17464811. DOI: 10.1186/s13007-017-0233-z.
- M. Woebbecke, D. et al. (1995). "Color Indices for Weed Identification Under Various Soil, Residue, and Lighting Conditions". In: *Transactions of the ASAE* 38.1. Place: St. Joseph, MI Publisher: ASAE, pp. 259–269. ISSN: 0001-2351. DOI: 10.13031/2013.27838. URL: <https://elibrary.asabe.org/abstract.asp?aid=27838&t=3>.
- Maliro, Moses F. A. et al. (Feb. 2008). "Sampling strategies and screening of chickpea (*Cicer arietinum* L.) germplasm for salt tolerance". In: *Genetic Resources and Crop Evolution* 55.1, pp. 53–63. ISSN: 1573-5109. DOI: 10.1007/s10722-007-9214-9. URL: <https://doi.org/10.1007/s10722-007-9214-9> (visited on 08/09/2022).
- Malthus, Tim J. and Ana Carla Madeira (1993). "High resolution spectroradiometry: Spectral reflectance of field bean leaves infected by *Botrytis fabae*". In: *Remote Sensing of Environment* 45.1, pp. 107–116. ISSN: 00344257. DOI: 10.1016/0034-4257(93)90086-D.
- Merzlyak, Mark N. et al. (May 1999). "Non-destructive optical detection of pigment changes during leaf senescence and fruit ripening". In: *Physiologia Plantarum* 106.1, pp. 135–141. ISSN: 0031-9317. DOI: 10.1034/j.1399-3054.1999.106119.x. URL: <http://www.scopus.com/inward/record.url?scp=0033004343&partnerID=8YFLogxK> (visited on 08/10/2022).
- Moghimi, Ali, Ce Yang, and Peter M. Marchetto (2018). "Ensemble Feature Selection for Plant Phenotyping: A Journey from Hyperspectral to Multispectral Imaging". In: *IEEE Access* 6. Publisher: IEEE, pp. 56870–56884. ISSN: 21693536. DOI: 10.1109/ACCESS.2018.2872801.
- Niks, R.E. et al. (Mar. 2019). *Breeding crops with resistance to diseases and pests*. The Netherlands: Wageningen Academic Publishers. ISBN: 978-90-8686-328-0. DOI: 10.3920/978-90-8686-882-7. URL: <https://www.wageningenacademic.com/doi/book/10.3920/978-90-8686-882-7>.
- Pande, S. et al. (2005). "Ascochyta blight of chickpea (*Cicer arietinum* L.): a review of biology, pathogenicity, and disease management". In: *Australian Journal of Agricultural Research* 56.4, p. 317. ISSN: 0004-9409. DOI: 10.1071/AR04143. URL: <http://www.publish.csiro.au/?paper=AR04143>.
- Paulus, Stefan and Anne Katrin Mahlein (2020). "Technical workflows for hyperspectral plant image assessment and processing on the greenhouse and laboratory

- scale". In: *GigaScience* 9.8. Publisher: Oxford University Press ISBN: 0000000310, pp. 1–10. ISSN: 2047217X. DOI: 10.1093/gigascience/giaa090.
- Phenokey. en. URL: <https://www.phenokey.com/applications/rover-based-field-phenotyping> (visited on 10/21/2022).
- Poblete, Tomas et al. (Sept. 2021). "Discriminating *Xylella fastidiosa* from *Verticillium dahliae* infections in olive trees using thermal- and hyperspectral-based plant traits". In: *Isprs Journal of Photogrammetry and Remote Sensing* 179. MAG ID: 3192010693, pp. 133–144. DOI: 10.1016/j.isprsjprs.2021.07.014.
- Qi, J. et al. (May 1994). "A modified soil adjusted vegetation index". en. In: *Remote Sensing of Environment* 48.2, pp. 119–126. ISSN: 0034-4257. DOI: 10.1016/0034-4257(94)90134-1. URL: <https://www.sciencedirect.com/science/article/pii/0034425794901341> (visited on 08/10/2022).
- R Core Team (2022). *R: A Language and Environment for Statistical Computing*. Place: Vienna, Austria. URL: <https://www.r-project.org/>.
- Raman, Rosy et al. (2022). "Genome-Wide Association Analyses Track Genomic Regions for Resistance to *Ascochyta rabiei* in Australian Chickpea Breeding Germplasm". In: *Frontiers in Plant Science* 13. ISSN: 1664-462X. URL: <https://www.frontiersin.org/articles/10.3389/fpls.2022.877266> (visited on 11/27/2022).
- Rouse Jr, J W et al. (1973). "Monitoring vegetation systems in the Great Plains with ERTS". In: *Third Earth Resources Technology Satellite-1 Symposium: Section AB. Technical presentations*. Vol. 1, p. 309.
- Sims, Daniel A and John A Gamon (Aug. 2002). "Relationships between leaf pigment content and spectral reflectance across a wide range of species, leaf structures and developmental stages". en. In: *Remote Sensing of Environment* 81.2, pp. 337–354. ISSN: 0034-4257. DOI: 10.1016/S0034-4257(02)00010-X. URL: <https://www.sciencedirect.com/science/article/pii/S003442570200010X> (visited on 08/10/2022).
- Stevens, Antoine and Leonardo Ramirez-Lopez (2020). *An introduction to the prospectr package*. URL: <https://cran.r-project.org/web/packages/prospectr/vignettes/prospectr.html>.
- Stoddard, F. L. et al. (2006). "Screening techniques and sources of resistance to abiotic stresses in cool-season food legumes". In: *Euphytica* 147.1-2, pp. 167–186. ISSN: 00142336. DOI: 10.1007/s10681-006-4723-8.
- Tang, Yuan, Masaaki Horikoshi, and Wenxuan Li (2016). "ggfortify: Unified interface to visualize statistical result of popular R packages". In: *The R Journal* 8.2, pp. 474–485. DOI: 10.32614/RJ-2016-060. URL: <https://doi.org/10.32614/RJ-2016-060>.
- Wei, Xing et al. (July 2021). "Identifying Optimal Wavelengths as Disease Signatures Using Hyperspectral Sensor and Machine Learning". In: *Remote Sensing* 13.14. MAG ID: 3186446746, p. 2833. DOI: 10.3390/rs13142833.
- Wickham, Hadley et al. (2019). "Welcome to the {tidyverse}". In: *Journal of Open Source Software* 4.43, p. 1686. DOI: 10.21105/joss.01686.
- Wiesner-Hanks, Tyr et al. (Dec. 2018). "Image set for deep learning: field images of maize annotated with disease symptoms". In: *BMC Research Notes* 11.1, p. 440. ISSN:

- 1756-0500. DOI: 10.1186/s13104-018-3548-6. URL: <https://bmccresnotes.biomedcentral.com/articles/10.1186/s13104-018-3548-6>.
- Wiesner-Hanks, Tyr et al. (2019). "Millimeter-Level Plant Disease Detection From Aerial Photographs via Deep Learning and Crowdsourced Data". eng. In: *Frontiers in Plant Science* 10. Publisher: Frontiers Media S.A. ISBN: 1664-462X, p. 1550. DOI: 10.3389/fpls.2019.01550. URL: <https://pubmed.ncbi.nlm.nih.gov/31921228>.
- Xu, Rui and Changying Li (June 2022). "A Review of High-Throughput Field Phenotyping Systems: Focusing on Ground Robots". en. In: *Plant Phenomics 2022*, pp. 1–20. ISSN: 2643-6515. DOI: 10.34133/2022/9760269. URL: <https://spj.sciencemag.org/journals/plantphenomics/2022/9760269/> (visited on 08/03/2022).
- Yu, Kang et al. (2018). "Hyperspectral Canopy Sensing of Wheat Septoria Tritici Blotch Disease". eng. In: *Frontiers in Plant Science* 9. Publisher: Frontiers Media S.A. ISBN: 1664-462X, p. 1195. DOI: 10.3389/fpls.2018.01195. URL: <https://pubmed.ncbi.nlm.nih.gov/30174678>.
- Zarco-Tejada, P. J. et al. (2018). "Previsual symptoms of Xylella fastidiosa infection revealed in spectral plant-trait alterations". In: *Nature Plants* 4.7. Publisher: Springer US, pp. 432–439. ISSN: 20550278. DOI: 10.1038/s41477-018-0189-7. URL: <http://dx.doi.org/10.1038/s41477-018-0189-7>.
- Zhang, Chongyuan, Weidong Chen, and Sindhuja Sankaran (2019). "High-throughput field phenotyping of Ascochyta blight disease severity in chickpea". In: *Crop Protection* 125.March. Publisher: Elsevier Ltd, p. 104885. ISSN: 02612194. DOI: 10.1016/j.cropro.2019.104885. URL: <https://doi.org/10.1016/j.cropro.2019.104885>.
- Zhang, Jian et al. (2017). "Crop classification and LAI estimation using original and resolution-reduced images from two consumer-grade cameras". In: *Remote Sensing* 9.10. ISSN: 20724292. DOI: 10.3390/rs9101054.
- Ziheng Feng et al. (Dec. 2021). "Monitoring Wheat Powdery Mildew Based on Hyperspectral, Thermal Infrared, and RGB Image Data Fusion". In: *Sensors* 22.1. MAG ID: 4200064788, pp. 31–31. DOI: 10.3390/s22010031.

5.12 Supplementary material

TABLE 5.4: Influence of hyperspectral data processing and learning algorithms. Mean RMSE \pm standard deviation of CV results for the PAD prediction models from 2020 and the mean AUC ROC \pm standard deviation for treatment classification models of 2020 and 2022 are shown.

Pipeline Step	2020 RMSE	2020 ROC AUC	2022 ROC AUC
Binning			
Full spectrum	13.94 \pm 5.1	0.98 \pm 0.03	0.79 \pm 0.14
FWHM binned	13.63 \pm 4.12	0.98 \pm 0.03	0.8 \pm 0.14
Double FWHM binned	13.84 \pm 4.29	0.98 \pm 0.04	0.78 \pm 0.15
Derivation			
None	13.93 \pm 4.37	0.98 \pm 0.04	0.8 \pm 0.15
First	14.28 \pm 5.24	0.99 \pm 0.01	0.79 \pm 0.13
Second	13.11 \pm 3.93	0.98 \pm 0.03	0.78 \pm 0.14
Learning algorithm			
LASSO	12.81 \pm 3.09	—	—
LASSO + Cor. filter	18.13 \pm 6.65	—	—
PLSR / PLSDA	12.44 \pm 3.15	1 \pm 0.01	0.78 \pm 0.14
RF	12.89 \pm 3.82	0.97 \pm 0.05	0.81 \pm 0.14
SVM	13.92 \pm 3.65	0.99 \pm 0.03	0.77 \pm 0.15
Normalization			
None	12.18 \pm 3.54	0.97 \pm 0.05	0.81 \pm 0.14
Pu	15.25 \pm 4.81	1 \pm 0.01	0.77 \pm 0.15
Sensors			
VNIR + SWIR	13.84 \pm 4.49	0.98 \pm 0.03	0.78 \pm 0.15
VNIR only	13.76 \pm 4.56	0.98 \pm 0.04	0.8 \pm 0.14
Smoothing			
Raw	13.76 \pm 4.56	0.99 \pm 0.03	0.79 \pm 0.14
Smoothed	13.93 \pm 4.39	0.98 \pm 0.04	0.8 \pm 0.15

TABLE 5.5: Low-level traits extracted from average hyperspectral data and lidar at plot level.

Abbreviation	Trait	Equation	Reference
<i>Extracted from lidar data</i>			
BM	Biomass > 10 cm	Sum of plant voxel volumes	<i>CropTraits</i>
GC	Ground cover	$\frac{\text{CoveredGround}}{\text{ScannedSurface}}$	<i>CropTraits</i>
<i>Vegetation indices</i>			
ENDVI	Enhanced Normalized Difference VI	$\frac{(NIR+Green)-(2 \times Blue)}{(NIR+Green)+(2 \times Blue)}$	<i>ENDVI</i>
EVI	Enhanced Vegetation Index	$2.5 * \frac{(NIR-Red)}{(NIR+6*Red+7.5*Blue+1)}$	Huete et al., 2002
ExGI	Excess Green Index	$2 * Green - Red + Blue$	M. Woebbecke et al., 1995
GCC	Green Chromatic Coordinate	$\frac{(Green)}{(Blue+Green+Red)}$	D. M. Woebbecke et al., 1995
GRVI	Green Red VI	$\frac{(Green-Red)}{(Green+Red)}$	Rouse Jr et al., 1973
MR	Mean Reflectance	$\frac{\sum_{R=R_{411}}^{R_{1676}} R}{307}$	
MSAVI	Modified Soil Adjusted VI	$\frac{2NIR+1-\sqrt{(2NIR+1)^2-8(NIR-Red)}}{2}$	Qi et al., 1994
MSR	Modified Simple Ratio	$\frac{(R800/R670)-1}{\sqrt{(R800/R670+1)}}$	Chen, 1996
NDVI	Normalized Difference VI	$\frac{(NIR-Red)}{(NIR+Red)}$	Rouse Jr et al., 1973
PSRI	Plant Senescence Reflectance Index	$\frac{R680-R500}{R750}$	Merzlyak et al., 1999; Yu et al., 2018
REMSR	Red Edge Modified Simple Ratio (MRESR)	$\frac{R750-R445}{R705-R445}$	Sims and Gamon, 2002
RENDVI	Red Edge Normalized Difference VI	$\frac{(NIR-RedEdge)}{(NIR+RedEdge)}$	Gitelson, Kaufman, and Merzlyak, 1996
SIPI	Structure Insensitive Pigment Index	$\frac{R800-R445}{R800+R680}$	Haboudane et al., 2002; Yu et al., 2018
SR	Red Edge Simple Ratio	$\frac{(NIR)}{(RedEdge)}$	Ehammer et al., 2010
VARI	Green Red VI	$\frac{(Green-Red)}{(Blue+Green+Red)}$	Gitelson et al., 2002

TABLE 5.6: Details and timing of treatments (i) to (v) applied to 2020 plots and treatments (i) to (iii) applied to trays in 2022.

	Treatment	DAI	Details
<i>2020 plots</i>			
i	Nil (only infection)	0	Infection from stubble
ii	Fortnightly Chlorothalonil720®	Fortnightly	720 g l ⁻¹ chlorothalonil applied at 2 l ha ⁻¹
iii	Strategic Veritas®	43, 56, 71, 91	200 g l ⁻¹ tebuconazole plus 120 g l ⁻¹ azoxystrobin, Adama, Australia, applied at 1 l ha ⁻¹
iv	Strategic Chlorothalonil720®	43, 56, 71, 91	720 g l ⁻¹ chlorothalonil applied at 2 l ha ⁻¹
v	Strategic AviatorXpro®	43, 56, 71, 91	150 g l ⁻¹ prothioconazole plus 75 g l ⁻¹ bixafen, Bayer Crop Science, Australia, applied at 600 ml ha ⁻¹)
<i>2022 trays</i>			
i	Inoculation	0	
ii	Bravo Weather Stik®	-1, 21, 28, 44	720 g l ⁻¹ chlorothalonil applied at 40 ml per tray (Syngenta Crop Protection)
iii _i	Bravo Weather Stik®	-1, 21, 28, 44	720 g l ⁻¹ chlorothalonil applied at 40 ml per tray (Syngenta Crop Protection)
iii _{ii}	Salinity	0, 28	3.3 l of 60 mM NaCl solution
iii _{iii}	Salinity	42	3.3 l of 120 mM NaCl solution

Chapter 6

Discussion

6.1 Discussion structure

This integrated discussion chapter contains a synthesis of the previous thesis chapters with the aim of establishing logical links between the chapters and providing a high-level analysis and interpretation. The first section provides a connected overview of the thesis chapters with summarised study aims and key results. The key outcomes across the study environments are discussed in the next section. Then, the overall significance, limitations, and disciplinary implications of the work are presented and perspectives for future research and deployment of the methods are discussed.

6.2 Thesis overview

The aim of this thesis was to develop sensor-based phenotyping methods to contribute to genetic gain for chickpea *Ascochyta* blight (AB) resistance breeding. In Chapter 1, chickpea production and AB impacts are introduced and opportunities for sensor-based phenotyping for resistance breeding are identified as (i) prediction of disease severity scores and (ii) measurement of resistance components. A literature review (Chapter 2) explores the potential of sensor technology to measure specific signs and symptoms of plant disease, that is, changes to primary and secondary metabolism, chlorosis and necrosis, thermal energy dissipation, and growth of the pathogen. Suitable sensors for measuring chickpea and *A. rabiei* interactions were identified as RGB, fluorescence and hyperspectral imaging, and light detection and ranging (lidar). In the following three experimental chapters, most of these sensors were tested in nursery disease screens (Chapter 3: RGB and multispectral), controlled environment (Chapter 4: RGB and hyperspectral), and in the field (Chapter 5: lidar and hyperspectral).

In Chapter 3, methods were developed to complement visual scoring in a disease resistance screen run on chickpea and wild relatives grown outdoors in pots, which is part of a breeding program. We showed that features extracted from time course RGB imaging combined with spatial and longitudinal modeling can accurately predict disease score classes on unseen data across three seasons (accuracies of 72.46 %, 80.97 %, 65.48 %, κ of 0.50, 0.59, 0.43), performing better than traits extracted from multispectral imaging.

In the following Chapter 4, the automated phenotyping system at The Plant Accelerator® was used to image plants grown in the greenhouse with the aim of identifying hyperspectral features for early detection of disease and identifying RGB- and hyperspectral based methods to predict disease indices. Low disease pressure was observed and impacted the results. Early disease detection algorithms were not transferable between the two experiments, performing no better than random classifiers. For the prediction of disease indices (DI), relative growth rates derived from RGB data performed better than single time point hyperspectral data. A pipeline to evaluate the impact of pre-processing methods of smoothing, normalization, derivation, and spectral binning on the DI prediction performance was developed and it was shown that (a) pre-processing significantly influenced the results and (b) inclusion of short wave infrared (SWIR) data with visible near-infrared (VNIR) data did not improve performance compared to VNIR alone.

In Chapter 5, a ground-based phenotyping platform (Field Explorer) was deployed in the field and hyperspectral and lidar data were used to distinguish infected untreated plots from infected fungicide treated plots as well as to predict disease scores. The same methods were applied to a second season where plants were grown in trays and a second stress, salinity, was introduced to evaluate the detection methods for specificity to AB. It was shown that a general spectral plant stress response in the VNIR region can accurately distinguish the fungicide and nil treatments in the field, but that the classification accuracy decreases when a secondary stress is included. For the prediction of DI, a model trained on features from the field data achieved a ρ of 0.89 for ranking the genotypes grown in trays, showing high transferability.

6.3 Thesis outcomes

6.3.1 Key outcomes

Symptoms of chickpea AB can be measured with imaging sensors

Relating to research aim two of this thesis (Identification of within-scale and cross-scale functional resistance components), the following two symptoms could be measured using RGB-based imaging: Lesion formation and reduction of healthy plant biomass caused by stem breakage. This would not have been possible with a comparable throughput by visual assessment alone. Although lesion detection only achieved F1-scores of 0.27 and 0.30 on unseen image data, the method could still provide estimates that were useful for distinguishing non-infected and infected pots with accuracies of more than 90% in 2021 and more than 75% in 2022 (Chapter 3, Figure 3.5). The detection of lesions showed promise and may be further improved with better data acquisition and detection algorithms.

Image-based estimates of chickpea shoot biomass that could be used to calculate growth rates were achievable both in the glasshouse using an automated multiangle imaging system, and in outdoor-grown chickpeas with topview imaging alone. In

summary, this means that sensor-based phenotyping is a suitable method for measuring the interaction of *A. rabiei* and chickpea and evaluating resistance, especially as there is potential to measure further plant-pathogen interactions (Chapter 2, Section 6.4.2).

RGB-imaging based growth rates are suitable for prediction for DI

Of the measured symptoms, the time-series derived growth rates were suitable to predict DI in the greenhouse, where R^2 of 0.64 (RMSE = 12.43) and R^2 of 0.37 (RMSE = 5.99) were achieved for the respective between-year validations (Chapter 4, Figure 4.11). Growth rates were also able to predict DI classes in the nursery, where a classifier achieved accuracies of 72.46 %, 80.97 %, 65.48 %, (κ of 0.50, 0.59, 0.43) (Table 3.4). In both environments, growth rates performed better than all other traits that were tested. Such growth rates have previously been used to quantify salt tolerance in chickpea in the greenhouse using the same automated imaging system as in Chapter 4, but have not yet been applied for chickpea AB in glasshouse and outdoors (Atieno et al., 2017; Atieno et al., 2021).

A possible advantage of the RGB-derived growth rates over spectral traits in the nursery was that they could consider disease progression over time. In the case of the nursery, they allowed the determination of critical phenotypic stages and were used to normalize for disease pressure differences between the years. However, only simple longitudinal trait extraction was performed for the multispectral imaging in the nursery. So far, the only extracted traits for that experiment were area under the curve (AUC) traits. In the greenhouse, no longitudinal trait extraction from hyperspectral data was performed at all; only single time point hyperspectral data from the day of scoring was tested for the prediction of DI. The AUC traits in the nursery as well as single time point hyperspectral data in the greenhouse had lower DI prediction performance than RGB - based growth rates, but it is possible that they could achieve higher performance if the longitudinal aspect was integrated (Section 4.3.3). Recently, time course spectroscopy was performed for potato late blight and peanut stem rot, where time course measurements were pooled and aggregated by visual disease severity rather than time points (Wei et al., 2021; Gold et al., 2020b; Ziheng Feng et al., 2021). Another recent approach was averaging of spectra from multiple timepoints, which has been done for wheat powdery mildew and rice bacterial blight (Zhang et al., 2022).

In the field, no imaging over time was performed, yet single time point data still provided a good prediction of AB damage, possibly due to the broad range of observed damage or the data quality achieved with the Field Explorer.

Lesion detection enables early detection of disease

Early detection of AB infection was attempted in the glasshouse and in the nursery. In the glasshouse, this was done by classifying infected versus non-infected plants

with hyperspectral data at single imaging time points at increasing days after infection (DAI) (Chapter 4). To determine the earliest timepoint at which classification between infected versus fungicide-treated pots was possible in the nursery, both vegetation indices and the RGB-derived traits collected until that timepoint were tested in incremental steps. In both the glasshouse and nursery, the early classification within trials resulted in acceptable accuracies (Figure 3.7 and Section 4.5.3). However, the classifiers that used spectral data showed low transferability between trials in both environments. Factors that negatively influenced the results may have been (a) overfitting of spectral models, (b) small amounts of cross-infection in the nursery, (c) systematic differences other than infection in the glasshouse (i.e. split imaging times), and (d) very low disease pressure in the glasshouse. A better classification accuracy and transferability between trials in the nursery was achieved by using the presence of three or more lesions as the only criterion.

In the field (Chapter 5), early detection was not attempted as imaging was only performed once at the time of scoring. At that time point, a general stress response in the red edge to near-infrared (NIR) spectral region (756 - 782 nm) was sufficient to distinguish between infected and fungicide-protected control treatment. These bands overlap with important bands selected in another study which predicted AB disease severity scores using proximal spectrometry (Zhang, Chen, and Sankaran, 2019).

However, all models built in this chapter struggled to distinguish between salinity stressed and infected trays, which indicates that biotic and abiotic non-AB stressors should be minimised in the experimental design. In the field, a complete control of secondary stressors is unrealistic, therefore, the specificity of the phenotyping methods also needs to be increased. This could potentially be achieved by including more wavebands, sensor fusion, integrating lesion detection, or using human supervision (Jay et al., 2020; Poblete et al., 2021; Gold et al., 2020a).

Hyperspectral models are significantly influenced by the choice of pre-processing steps and learning algorithms

In both the greenhouse (Section 4.5.4) and the field (Sections 5.5.3 and 5.5.4), pre-processing steps of hyperspectral data including smoothing, derivation, normalization, and binning as well as the choice of learning algorithms had a significant influence on the performance of the prediction of scores and classification of treatments. These results are consistent with the literature and imply that pre-processing methods need to be considered carefully (Hennessy, Clarke, and Lewis, 2020; Paulus and Mahlein, 2020; Heim et al., 2018; Wei et al., 2021).

Conservative growth may be a resistance mechanism

In the greenhouse, PSA at the time of infection was weakly positively correlated with DI (Figure 4.10) and in the nursery, a similar trend for the correlation between FGCC at the time of scoring with DI was observed (Figure 3.4). This indicates that conservative

growth, in particular within the wild species compared to the cultivars, may be a resistance mechanism. Conservative growth as a resistance mechanism can have an associated metabolic cost (Karasov et al., 2017). Should such a slow-growing genotype be used as a source of resistance, yield may be negatively impacted.

6.4 Perspectives

6.4.1 Summarised recommendations for deployment

Based on the results for the sensors, environments, and vectors that were tested in this thesis, we make the following recommendations for the deployment of sensor-based phenotyping methods to glasshouse, nursery, and field. Section 6.4.2 further covers the limitations and possible improvements of these recommendations.

Recommendations for deployment to nursery disease screens

For the goal of high throughput screens of genetic material on pot scale, top view RGB time course imaging is a suitable method as DI classes of independent unseen data over three seasons could be accurately predicted with growth rates derived from topview imaging. The focus for further development of the methods should be on data acquisition, such as increasing spatial resolution, eliminating shading, optimizing experimental design and positioning systems to identify pots and assign regions of interest automatically. This could be achieved with an improved ground-based phenotyping platform or a fixed gantry system.

Recommendations for deployment to glasshouse disease screens

If screens are undertaken in the glasshouse, time course RGB imaging-based growth rates are also a suitable tool for the prediction of DI. Using an automated conveyor-belt-based system offers the opportunity to completely automate the data acquisition. Unlike in the field, the issue in the glasshouse would not be data acquisition, but the creation of suitable environmental conditions, as high disease pressure needs to be created and cross-infection needs to be prevented. If such a robust inoculation procedure can be developed, the consistency and comparability of disease development across experiments could be improved.

Recommendations for deployment to field disease screens

The prediction of PAD in the field was highly accurate by simply using the reflectance of plant material at a band in the NIR region (792 nm) as a predictor. The use of a dedicated ground-based phenotyping platform such as the Field Explorer provided high quality sensor data, allowing the reflectance measurements to be limited to the chickpea plant material by sensor fusion with lidar data. This way, the reflectance of ground-covering weeds could be excluded from the measurements.

If the chickpea canopy cover is high enough, for example earlier in the season before the disease has damaged the crop or under generally lower disease pressure, average plot reflectance of chickpea infected with AB may also be measurable well enough from a UAV with multispectral sensors, as shown by Zhang, Chen, and Sankaran, 2019. This would offer a comparatively easy option for deployment. If specificity is a concern, for example, when secondary stresses may influence growth rates and simple spectral stress responses, lesion detection or spectral features such as those important for the discrimination of salinity-stressed and infected trays could be included in the imaging. For both the ground-based and potential aerial-based approach, more research and repeated experiments on field plots, not trays, are required.

6.4.2 Summarised recommendations for further research

Application of other sensor technologies

The selection of sensors for each environment in this thesis was constrained by time and the availability of platforms for each of the environments. However, other promising sensor technology exists to measure interactions between host plants and necrotrophic fungi, although they are often not as readily available and usable. One such option identified in Chapter 1 (Table 1.2) and Section 2.2.3 is chlorophyll fluorescence imaging which could enable detection of changes in primary metabolism, necrosis, and chlorosis, potentially before visual symptoms. This has been successfully shown at high throughput in the field using sun-induced chlorophyll fluorescence for predicting disease severity on olive trees infected with *Xylella fastidiosa* (Section 2.2.3) (Zarco-Tejada et al., 2018). Alternatively, at close range, fluorescence imaging may potentially be used to detect the autofluorescence of the palisade parenchyma occurring before hypersensitive response. Another proximal sensing option would be optical coherence tomography (OCT), with which the induced changes to leaf cell structure could be measured on individual leaves in the field using a backpack-based system (Lee et al., 2019; Ravichandran et al., 2016). Furthermore, high resolution hyperspectral measurements may be coupled with metabolic profiling to potentially identify signatures of secondary plant metabolites involved in resistance (Brugger et al., 2021; Arens et al., 2016). While the proximal sensing options are likely not suitable for high throughput screens by themselves and are difficult to deploy to the field (Section 2.2.4), they may be used to identify functional traits that could be measured across environments with simpler technology (Simko, Jimenez-Berni, and Sirault, 2017; Eeuwijk et al., 2019).

As only a single year of field screens with large-scale plots was performed, validation of lidar sensors and time course imaging should be performed, and RGB sensors should be included to evaluate RGB derived growth rates as a predictor in the field.

Exploration of trait extraction

To further develop the methods from this thesis, more research is required both for the extraction of low-level traits and intermediate traits, as well as exploring the suitability of deep learning approaches to directly predict disease scores from sensor data. A next step in the analysis could be to consider the experiments as multi-environment trials and extract higher order traits (Malosetti, Ribaut, and Eeuwijk, 2013; Eeuwijk et al., 2019).

Low-level trait extraction Especially for the imaging performed in the nursery, more research is needed for the low-level trait extraction from RGB and spectral data. Concerning RGB images, both the lesion detection and biomass estimation should be improved. The lesion detection algorithm may benefit from annotating more training data or using different object detection algorithms (Wiesner-Hanks et al., 2019). The biomass estimates could be improved if 3D plant structure was considered in the nursery as well, not only FGCC. Either of these approaches would benefit from improved data acquisition in terms of higher spatial resolution and illumination. Concerning spectral data, additional feature selection approaches and vegetation indices should be tested for the glasshouse and field. Alternatively, data augmentation of hyperspectral data might improve the issue of high dimensionality where only few observations are possible (Hennessy, Clarke, and Lewis, 2020).

Intermediate trait extraction The intermediate trait extraction depends on spatio-temporal modeling of the low-level traits, for which multiple approaches exist that should be examined in more detail (Roth et al., 2021; Brien et al., 2020; Pérez-Valencia et al., 2022). More focus should be placed on the extraction of intermediate traits from spectral data. While intermediate traits such as growth rates and time until lesion appearance were derived from RGB data, the only longitudinal traits extracted from multispectral images in this thesis were AUC traits, and the hyperspectral data in the glasshouse was not modelled over time at all. Neither AUC traits from the nursery nor single time point hyperspectral data in the greenhouse could match the DI prediction performance of RGB - based growth rates, but it is possible that they could do so if the longitudinal aspect was integrated (Dorrepaal, Malegori, and Gowen, 2016).

Trait normalization Across experiments, high genotypic variation in plant growth habits was observed, particularly in the wild *Cicer* relatives but also within the cultivar germplasm (Figure 1.3). This will have led to increased variation in the measured traits relating to plant biomass, and may have also influenced the other measured traits. The approach to mitigate the effect in Chapter 4 was to sow the wild relative species earlier than the cultivars, but even that did not result in a comparable projected shoot area (Figures 4.8 and 4.9). A similar effect was observed in the nursery, where no mitigation was performed (Figure 3). Fine-tuning the sowing dates according to expected growth habits could be one approach to normalise the growth habit, but the differences in

developmental stages could in turn influence the plant-pathogen interaction (Develey-Rivière and Galiana, 2007). Other than finely tuning sowing dates, normalizing plant traits to early development stages may be another option, for example with the Digital Adjustment of Plant Development (DAPD) method (Lozano-Claros et al., 2020).

Caveats of trait extraction Manual trait extraction was performed for all environments, both for low-level and intermediate traits. One risk of such manual trait extraction is that the study turns into ‘recreational phenotyping’ or ‘stamp-collecting’, meaning that everything that can be measured is collected without any value proposition (Rebetzke et al., 2019). Another risk is wasting valuable information from the sensor data by reducing it to traits that are chosen based on assumptions. Instead of attempting to manually define traits, the sensor data could be used in deep learning to predict target traits directly (Baker et al., 2018; Weiss, Jacob, and Duveiller, 2020; Sperschneider, 2019). However, the manual extraction of functional traits provided explainability and the option to select for the traits in breeding programs directly (Section 1.2.5). There was also evidence that simplifying the models to single growth rates or single reflectance bands improved the transferability of the models between experiments. Explainable machine learning methods offer the opportunity to use iterations of trait extraction and deep learning to narrow down mechanisms (Baker et al., 2018; Nagasubramanian et al., 2019; Ghosal et al., 2018).

Direct selection for sensor-based traits

Visual disease scores of *Ascochyta* blight of chickpea have been shown to correlate well with field resistance, that is, yield under disease pressure (Davidson, personal communication). Therefore, we used the prediction of scores as a benchmark for the evaluation of the sensor-based methods developed in this thesis. However, it is not necessary to use the traits that are extracted from sensor-based measurements to predict the disease scores that are then selected for. Instead, the sensor-based traits may be selected for directly as they can indicate resistance components. The consensus in the literature seems to be to eventually move from visual scoring to sensor-based phenotyping or at least combine both methods for the evaluation of plant resistance, including for AB of chickpea (Araus et al., 2018; Bock et al., 2020; Ford et al., 2022). Ultimately, the methods need to be evaluated based on genetic gain in terms of field resistance.

6.5 Significance and implications of research

Worldwide, yield losses and fungicide use in chickpea due to AB are high. Breeding for resistance is an economically and ecologically sustainable way to improve chickpea cultivars and contribute to global food security (Foyer et al., 2016; Jha et al., 2022). The methods developed here can contribute to genetic gain in breeding programs by increasing precision, throughput, and the range of measurable symptoms of the

disease. To my knowledge, sensor-based phenotyping has not been applied for breeding of chickpea for AB resistance so far. We showed that RGB-imaging-derived growth rates can predict disease severity both in the glasshouse and in less controlled conditions in the nursery. Therefore, this work can help alleviate the prevalent "field phenotyping bottleneck" for biotic stresses (Araus et al., 2018). Our lesion detection methods may be applied as a tool to screen for resistance by increasing specificity and measuring resistance components, but also as a tool for early detection of disease in the field, which may be used to guide precision agriculture. Many other diseases that cause necrotic lesions and reduced growth rates exist for other crops. Our methods may be transferable to such host-pathosystems and the transfer would be facilitated by our use of low-cost sensors combined with free, open-source software. The multi-year, multi-scale data that were collected for this thesis were published for further method development. In particular, the set of 86,792 time course topview RGB images gathered outside at pot level across three seasons and annotated with visual disease scores provides a valuable resource. Overall, the work presented in this thesis can contribute to the development of resistant cultivars, not only for chickpea AB, but also other crops and other diseases.

6.6 Conclusion

The research in this thesis identified suitable sensor-based phenotyping methods to evaluate chickpea AB resistance. Time-series RGB imaging was used to identify critical growth rates and allows for method transfer between seasons by normalizing for varying disease pressure and disease progression. The methods have been shown to work across two greenhouse experiments and three seasons of outdoor disease screens. Additionally, pathways for automating the sensor-based screens were proposed. Furthermore, the research has narrowed the experimental design space for hyperspectral imaging of single plants in the greenhouse, enabling further research on the identification of spectral features. Accurate early detection of disease has been achieved with lesion detection algorithms which may guide precision agriculture for targeted fungicide applications. Together, the methods have the potential to increase genetic gain of chickpea resistance breeding programs and can inform the design of phenotyping methods more broadly for other crops. Easy adoption and further development of the methods is possible, as simple RGB sensors and free and open-source software were used.

6.7 References

Araus, José Luis et al. (2018). "Translating High-Throughput Phenotyping into Genetic Gain". In: *Trends in Plant Science* 23.5, pp. 451–466. ISSN: 13601385. DOI: 10.1016/j.tplants.2018.02.001.

- Arens, Nadja et al. (2016). "Non-invasive presymptomatic detection of *Cercospora beticola* infection and identification of early metabolic responses in sugar beet". In: *Frontiers in Plant Science* 7.September, pp. 1–14. ISSN: 1664462X. DOI: 10.3389/fpls.2016.01377.
- Atieno, Judith et al. (2017). "Exploring genetic variation for salinity tolerance in chickpea using image-based phenotyping". In: *Scientific Reports* 7.1. Publisher: Springer US, pp. 1–11. ISSN: 20452322. DOI: 10.1038/s41598-017-01211-7. URL: <http://dx.doi.org/10.1038/s41598-017-01211-7>.
- Atieno, Judith et al. (2021). "Novel Salinity Tolerance Loci in Chickpea Identified in Glasshouse and Field Environments". In: *Frontiers in Plant Science* 12. ISSN: 1664-462X. URL: <https://www.frontiersin.org/articles/10.3389/fpls.2021.667910> (visited on 11/22/2022).
- Baker, Ruth E. et al. (2018). "Mechanistic models versus machine learning, a fight worth fighting for the biological community?" In: *Biology Letters* 14.5, pp. 1–4. ISSN: 1744957X. DOI: 10.1098/rsbl.2017.0660.
- Bock, Clive H. et al. (Dec. 2020). "From visual estimates to fully automated sensor-based measurements of plant disease severity: status and challenges for improving accuracy". In: *Phytopathology Research* 2.1. Publisher: Phytopathology Research, p. 9. ISSN: 2524-4167. DOI: 10.1186/s42483-020-00049-8. URL: <https://phytopatholres.biomedcentral.com/articles/10.1186/s42483-020-00049-8>.
- Brien, Chris et al. (2020). "Smoothing and extraction of traits in the growth analysis of noninvasive phenotypic data". In: *Plant Methods* 16.1. Publisher: BioMed Central, pp. 1–21. ISSN: 17464811. DOI: 10.1186/s13007-020-00577-6. URL: <https://doi.org/10.1186/s13007-020-00577-6>.
- Brugger, Anna et al. (2021). "Spectral signatures in the UV range can be combined with secondary plant metabolites by deep learning to characterize barley–powdery mildew interaction". In: *Plant Pathology* 70.7, pp. 1572–1582. ISSN: 13653059. DOI: 10.1111/ppa.13411.
- Develey-Rivière, Marie-Pierre and Eric Galiana (Aug. 2007). "Resistance to pathogens and host developmental stage: a multifaceted relationship within the plant kingdom". en. In: *New Phytologist* 175.3, pp. 405–416. ISSN: 0028-646X, 1469-8137. DOI: 10.1111/j.1469-8137.2007.02130.x. URL: <https://onlinelibrary.wiley.com/doi/10.1111/j.1469-8137.2007.02130.x> (visited on 04/18/2023).
- Dorrepaal, Ronan, Cristina Malegori, and Aoife Gowen (Apr. 2016). "Tutorial: Time Series Hyperspectral Image Analysis". EN. In: *Journal of Near Infrared Spectroscopy* 24.2. Publisher: SAGE Publishing, pp. 89–107. ISSN: 1751-6552. URL: <https://opg.optica.org/jnirs/abstract.cfm?uri=jnirs-24-2-89> (visited on 11/27/2022).
- Eeuwijk, Fred A. van et al. (2019). "Modelling strategies for assessing and increasing the effectiveness of new phenotyping techniques in plant breeding". In: *Plant Science* 282.December 2017. Publisher: Elsevier, pp. 23–39. ISSN: 18732259. DOI: 10.1016/j.plantsci.2018.06.018. URL: <https://doi.org/10.1016/j.plantsci.2018.06.018>.

- Ford, Rebecca et al. (Oct. 2022). *Panel Discussion*. Wagga Wagga, NSW, Australia.
- Foyer, Christine H. et al. (2016). "Neglecting legumes has compromised human health and sustainable food production". In: *Nature Plants* 2.8. Publisher: Macmillan Publishers Limited, pp. 1–10. ISSN: 2055026X. DOI: 10.1038/NPLANTS.2016.112. URL: <http://dx.doi.org/10.1038/nplants.2016.112>.
- Ghosal, Sambuddha et al. (May 2018). "An explainable deep machine vision framework for plant stress phenotyping". In: *Proceedings of the National Academy of Sciences* 115.18. Publisher: Proceedings of the National Academy of Sciences, pp. 4613–4618. DOI: 10.1073/pnas.1716999115. URL: <https://www.pnas.org/doi/abs/10.1073/pnas.1716999115> (visited on 12/15/2022).
- Gold, Kaitlin M et al. (2020a). "Hyperspectral Measurements Enable Pre-Symptomatic Detection and Differentiation of Contrasting Physiological Effects of Late Blight and Early Blight in Potato". In: *Remote Sensing* 12.2. Publisher: MDPI AG ISBN: 2072-4292, p. 286. DOI: 10.3390/rs12020286.
- Gold, Kaitlin M. et al. (June 2020b). "Investigating potato late blight physiological differences across potato cultivars with spectroscopy and machine learning." In: *Plant Science* 295. MAG ID: 2985102654, p. 110316. DOI: 10.1016/j.plantsci.2019.110316.
- Heim, René H. J. et al. (June 2018). "Detecting myrtle rust (*Austropuccinia psidii*) on lemon myrtle trees using spectral signatures and machine learning". In: *Plant Pathology* 67.5. MAG ID: 2793166416, pp. 1114–1121. DOI: 10.1111/ppa.12830.
- Hennessy, Andrew, Kenneth Clarke, and Megan Lewis (Jan. 2020). "Hyperspectral Classification of Plants: A Review of Waveband Selection Generalisability". In: *Remote Sensing* 12.1, p. 113. ISSN: 2072-4292. DOI: 10.3390/rs12010113. URL: <https://www.mdpi.com/2072-4292/12/1/113>.
- Jay, S. et al. (Aug. 2020). "Scoring Cercospora Leaf Spot on Sugar Beet: Comparison of UGV and UAV Phenotyping Systems". In: *Plant Phenomics* 2020. Publisher: American Association for the Advancement of Science (AAAS) ISBN: 2643-6515, pp. 1–18. ISSN: 2643-6515. DOI: 10.34133/2020/9452123. URL: <https://spj.sciencemag.org/journals/plantphenomics/2020/9452123/>.
- Jha, Uday C. et al. (2022). "Breeding and Genomics Interventions for Developing Ascochyta Blight Resistant Grain Legumes". In: *International Journal of Molecular Sciences* 23.4. ISSN: 14220067. DOI: 10.3390/ijms23042217.
- Karasov, Talia L. et al. (Apr. 2017). "Mechanisms to Mitigate the Trade-Off between Growth and Defense". In: *The Plant Cell* 29.4, pp. 666–680. ISSN: 1040-4651. DOI: 10.1105/tpc.16.00931. URL: <https://www.ncbi.nlm.nih.gov/pmc/articles/PMC5435432/> (visited on 12/09/2022).
- Lee, Junsoo et al. (2019). "On-Field in situ Inspection for Marssonina Coronaria Infected Apple Blotch Based on Non-Invasive Bio-Photonic Imaging Module". In: *IEEE Access* 7, pp. 148684–148691. ISSN: 21693536. DOI: 10.1109/ACCESS.2019.2946388.
- Lozano-Claros, Diego et al. (Dec. 2020). "Developmental normalization of phenomics data generated by high throughput plant phenotyping systems". en. In: *Plant*

- Methods* 16.1, p. 111. ISSN: 1746-4811. DOI: 10.1186/s13007-020-00653-x. URL: <https://plantmethods.biomedcentral.com/articles/10.1186/s13007-020-00653-x> (visited on 04/18/2023).
- Malosetti, Marcos, Jean-Marcel Ribaut, and Fred A. van Eeuwijk (2013). "The statistical analysis of multi-environment data: modeling genotype-by-environment interaction and its genetic basis". en. In: *Frontiers in Physiology* 4. ISSN: 1664-042X. DOI: 10.3389/fphys.2013.00044. URL: <http://journal.frontiersin.org/article/10.3389/fphys.2013.00044/abstract> (visited on 07/08/2022).
- Nagasubramanian, Koushik et al. (2019). "Plant disease identification using explainable 3D deep learning on hyperspectral images". In: *Plant Methods* 15.1. Publisher: BioMed Central, pp. 1–10. ISSN: 17464811. DOI: 10.1186/s13007-019-0479-8. URL: <https://doi.org/10.1186/s13007-019-0479-8>.
- Paulus, Stefan and Anne Katrin Mahlein (2020). "Technical workflows for hyperspectral plant image assessment and processing on the greenhouse and laboratory scale". In: *GigaScience* 9.8. Publisher: Oxford University Press ISBN: 0000000310, pp. 1–10. ISSN: 2047217X. DOI: 10.1093/gigascience/giaa090.
- Poblete, Tomas et al. (Sept. 2021). "Discriminating *Xylella fastidiosa* from *Verticillium dahliae* infections in olive trees using thermal- and hyperspectral-based plant traits". In: *Isprs Journal of Photogrammetry and Remote Sensing* 179. MAG ID: 3192010693, pp. 133–144. DOI: 10.1016/j.isprsjprs.2021.07.014.
- Pérez-Valencia, Diana M. et al. (2022). "A two-stage approach for the spatio-temporal analysis of high-throughput phenotyping data". In: *Scientific Reports* 12.1. Publisher: Nature Publishing Group UK ISBN: 4159802206, pp. 1–16. ISSN: 2045-2322. DOI: 10.1038/s41598-022-06935-9. URL: <https://doi.org/10.1038/s41598-022-06935-9>.
- Ravichandran, Naresh Kumar et al. (2016). "In vivo monitoring on growth and spread of gray leaf spot disease in capsicum annum leaf using spectral domain optical coherence tomography". In: *Journal of Spectroscopy* 2016. ISSN: 23144939. DOI: 10.1155/2016/1093734.
- Rebetzke, G. J. et al. (2019). "Review: High-throughput phenotyping to enhance the use of crop genetic resources". In: *Plant Science* 282. June 2018. Publisher: Elsevier, pp. 40–48. ISSN: 18732259. DOI: 10.1016/j.plantsci.2018.06.017. URL: <https://doi.org/10.1016/j.plantsci.2018.06.017>.
- Roth, Lukas et al. (2021). "Phenomics data processing: A plot-level model for repeated measurements to extract the timing of key stages and quantities at defined time points". In: *Field Crops Research* 274. October. ISSN: 03784290. DOI: 10.1016/j.fcr.2021.108314.
- Simko, Ivan, Jose A. Jimenez-Berni, and Xavier R.R. Sirault (2017). "Phenomic approaches and tools for phytopathologists". In: *Phytopathology* 107.1, pp. 6–17. ISSN: 0031949X. DOI: 10.1094/PHYTO-02-16-0082-RW.

- Sperschneider, Jana (2019). "Machine learning in plant–pathogen interactions: empowering biological predictions from field scale to genome scale". In: *New Phytologist*. ISSN: 14698137. DOI: 10.1111/nph.15771.
- Wei, Xing et al. (July 2021). "Identifying Optimal Wavelengths as Disease Signatures Using Hyperspectral Sensor and Machine Learning". In: *Remote Sensing* 13.14. MAG ID: 3186446746, p. 2833. DOI: 10.3390/rs13142833.
- Weiss, M., F. Jacob, and G. Duveiller (2020). "Remote sensing for agricultural applications: A meta-review". In: *Remote Sensing of Environment* 236. August 2019. Publisher: Elsevier, p. 111402. ISSN: 00344257. DOI: 10.1016/j.rse.2019.111402. URL: <https://doi.org/10.1016/j.rse.2019.111402>.
- Wiesner-Hanks, Tyr et al. (Dec. 2019). "Millimeter-Level Plant Disease Detection From Aerial Photographs via Deep Learning and Crowdsourced Data". In: *Frontiers in Plant Science* 10. December, pp. 1–11. ISSN: 1664-462X. DOI: 10.3389/fpls.2019.01550. URL: <https://www.frontiersin.org/article/10.3389/fpls.2019.01550/full>.
- Zarco-Tejada, P. J. et al. (2018). "Previsual symptoms of *Xylella fastidiosa* infection revealed in spectral plant-trait alterations". In: *Nature Plants* 4.7. Publisher: Springer US, pp. 432–439. ISSN: 20550278. DOI: 10.1038/s41477-018-0189-7. URL: <http://dx.doi.org/10.1038/s41477-018-0189-7>.
- Zhang, Chongyuan, Weidong Chen, and Sindhuja Sankaran (2019). "High-throughput field phenotyping of *Ascochyta* blight disease severity in chickpea". In: *Crop Protection* 125. March. Publisher: Elsevier Ltd, p. 104885. ISSN: 02612194. DOI: 10.1016/j.cropro.2019.104885. URL: <https://doi.org/10.1016/j.cropro.2019.104885>.
- Zhang, Jinnuo et al. (Dec. 2022). "Rice bacterial blight resistant cultivar selection based on visible/near-infrared spectrum and deep learning". In: *Plant Methods* 18.1, p. 49. ISSN: 1746-4811. DOI: 10.1186/s13007-022-00882-2. URL: <https://plantmethods.biomedcentral.com/articles/10.1186/s13007-022-00882-2>.
- Ziheng Feng et al. (Dec. 2021). "Monitoring Wheat Powdery Mildew Based on Hyperspectral, Thermal Infrared, and RGB Image Data Fusion". In: *Sensors* 22.1. MAG ID: 4200064788, pp. 31–31. DOI: 10.3390/s22010031.